



**Journal of
Mechanics of
Materials and Structures**

Volume 9, No. 2

March 2014



JOURNAL OF MECHANICS OF MATERIALS AND STRUCTURES

msp.org/jomms

Founded by Charles R. Steele and Marie-Louise Steele

EDITORIAL BOARD

ADAIR R. AGUIAR University of São Paulo at São Carlos, Brazil
KATIA BERTOLDI Harvard University, USA
DAVIDE BIGONI University of Trento, Italy
IWONA JASIUK University of Illinois at Urbana-Champaign, USA
THOMAS J. PENCE Michigan State University, USA
YASUhide SHINDO Tohoku University, Japan
DAVID STEIGMANN University of California at Berkeley

ADVISORY BOARD

J. P. CARTER University of Sydney, Australia
R. M. CHRISTENSEN Stanford University, USA
G. M. L. GLADWELL University of Waterloo, Canada
D. H. HODGES Georgia Institute of Technology, USA
J. HUTCHINSON Harvard University, USA
C. HWU National Cheng Kung University, Taiwan
B. L. KARIHALOO University of Wales, UK
Y. Y. KIM Seoul National University, Republic of Korea
Z. MROZ Academy of Science, Poland
D. PAMPLONA Universidade Católica do Rio de Janeiro, Brazil
M. B. RUBIN Technion, Haifa, Israel
A. N. SHUPIKOV Ukrainian Academy of Sciences, Ukraine
T. TARNAI University Budapest, Hungary
F. Y. M. WAN University of California, Irvine, USA
P. WRIGGERS Universität Hannover, Germany
W. YANG Tsinghua University, China
F. ZIEGLER Technische Universität Wien, Austria

PRODUCTION production@msp.org

SILVIO LEVY Scientific Editor


Cover photo: Mando Gomez, www.mandolux.com

See msp.org/jomms for submission guidelines.

JoMMS (ISSN 1559-3959) at Mathematical Sciences Publishers, 798 Evans Hall #6840, c/o University of California, Berkeley, CA 94720-3840, is published in 10 issues a year. The subscription price for 2014 is US\$555/year for the electronic version, and \$710/year (+\$60, if shipping outside the US) for print and electronic. Subscriptions, requests for back issues, and changes of address should be sent to MSP.

JoMMS peer-review and production is managed by EditFLOW[®] from Mathematical Sciences Publishers.

PUBLISHED BY

 **mathematical sciences publishers**
nonprofit scientific publishing

<http://msp.org/>

© 2014 Mathematical Sciences Publishers

PLANE WAVES AT THE BOUNDARY OF TWO MICROPOLAR THERMOELASTIC SOLIDS WITH DISTINCT CONDUCTIVE AND THERMODYNAMIC TEMPERATURES

RAJNEESH KUMAR, MANDEEP KAUR AND SATISH C. RAJVANSHI

The present investigation is concerned with wave propagation at an interface of two different micropolar thermoelastic solid half-spaces with distinct conductive and thermodynamic temperatures. Reflection and transmission phenomena of plane waves impinging obliquely at a plane interface between two different micropolar thermoelastic solid half-spaces with two temperatures are investigated. The incident wave is assumed to be striking at the plane interface after propagating through one of the micropolar generalized thermoelastic solids with two temperatures. Amplitude ratios of the various reflected and transmitted waves are obtained in closed form and it is found that these are functions of the angle of incidence and frequency, and are affected by the elastic properties of the media. Micropolarity and two-temperature effects are shown on these amplitude ratios for a specific model. Results of some earlier workers have also been deduced from the present investigation.

1. Introduction

The theory of micropolar elasticity introduced and developed by Eringen [1966] has aroused much interest in recent years because of its possible utility in investigating the deformation properties of solids for which classical theory is inadequate. Micropolar theory is believed to be particularly useful in investigating material consisting of bar-like molecules, which exhibit microrotational effects and can support body and surface couples. A micropolar continuum is a collection of interconnected particles in the form of small rigid bodies undergoing both translational and rotational motions. The force at a point of the surface element of a body is completely characterized by the force stress vector and couple stress vector at that point.

The linear theory of micropolar thermoelasticity was developed by extending the theory of micropolar continua to include thermal effects. A comprehensive review of the subject was given in [Eringen 1970; 1999; Nowacki 1981]. Tauchert et al. [1968] also derived the basic equations of the linear theory of micropolar coupled thermoelasticity. Dost and Tabarrok [1978] presented the generalized thermoelasticity by using Green and Lindsay theory. Chandrasekharaiah [1986] developed a heat flux-dependent micropolar thermoelasticity. Boschi and Ieşan [1973] extended a generalized theory of micropolar thermoelasticity that permits the transmission of heat as thermal waves at finite speeds.

Thermoelasticity with two temperatures is one of the nonclassical theories of the thermoelasticity of elastic solids. The main difference between this theory and the classical theory is the thermal dependence.

MSC2010: 74A10, 74J05.

Keywords: micropolar thermoelastic solid, conductive and thermodynamic temperatures, elastic waves, reflection coefficient, transmission coefficient.

Chen and Williams [1968] and Chen et al. [1969] formulated a theory of heat conduction in deformable bodies. This depends on two distinct temperatures, the conductive temperature Φ and thermodynamic temperature T . Chen et al. [1969] suggested that the difference between these two temperatures is proportional to the heat supply. These two temperatures may be equal under certain conditions for time-independent situations. However, for time-dependent problems relating to wave propagation, these two temperatures are, in general, different, regardless of the presence of a heat supply. The two temperatures and the strain are found to have representation in the form of a traveling wave pulse, a response which occurs instantaneously throughout the body [Boley and Tolins 1962]. Warren and Chen [1973] investigated wave propagation in the two-temperature theory of thermoelasticity.

Youssef [2006] presented a new theory of generalized thermoelasticity by taking into account the theory of heat conduction in deformable bodies, which depends on distinct conductive and thermodynamic temperatures. He also established a uniqueness theorem for the equation of two-temperature generalized linear thermoelasticity for a homogeneous and isotropic body. Recently, Puri and Jordan [2006] studied the propagation of plane waves under two temperatures. Youssef and Al-Lehaibi [2007] and Youssef and Al-Harby [2007] investigated various problems on the basis of two-temperature thermoelasticity with a relaxation time and showed that the obtained results are qualitatively different when compared to those in the case of one-temperature thermoelasticity. Magaña and Quintanilla [2009] investigated the uniqueness and growth of the solution in two-temperature generalized thermoelastic theories. Mukhopadhyay and Kumar [2009] studied thermoelastic interaction in two-temperature generalized thermoelasticity in an infinite medium with a cylindrical cavity. Various investigators have studied problems in two temperatures, for example, [Kaushal et al. 2010; Kumar and Mukhopadhyay 2010; El-Karamany 2011; El-Karamany and Ezzat 2011; Kaushal et al. 2011].

Various authors have investigated the problems of reflection and transmission at the boundary surface of micropolar elastic solid half-spaces, for example, [Tomar and Gogna 1992; 1995a; 1995b; Hsia and Cheng 2006; Hsia et al. 2007; Kumar and Barak 2007; Kumar et al. 2008a; 2008b].

In this paper, we study the problem of reflection and transmission of plane waves at an interface of two different micropolar generalized thermoelastic solid half-spaces with two temperatures. Micropolarity and two-temperature effects are depicted graphically on the amplitude ratios for the incidence of various plane waves, that is, longitudinal displacement waves (LD waves), thermal waves (T waves), and transverse displacement waves coupled with transverse microrotational waves (CD-I and CD-II waves).

2. Basic equations

Following [Eringen 1966; Ezzat and Awad 2010], the field equations in an isotropic, homogeneous, micropolar elastic medium in the context of the generalized theory of thermoelasticity with two temperatures, without body forces, body couples, or heat sources, are given by

$$(\lambda + 2\mu + K)\nabla(\nabla \cdot \vec{u}) - (\mu + K)\nabla \times (\nabla \times \vec{u}) + K(\nabla \times \vec{\phi}) - \nu \nabla T = \rho \frac{\partial^2 \vec{u}}{\partial t^2}, \quad (1)$$

$$(\alpha + \beta + \gamma)\nabla(\nabla \cdot \vec{\phi}) - \gamma \nabla \times (\nabla \times \vec{\phi}) + K(\nabla \times \vec{u}) - 2K\vec{\phi} = \rho j \frac{\partial^2 \vec{\phi}}{\partial t^2}, \quad (2)$$

$$K^* \nabla^2 \Phi = \rho c^* \left(\frac{\partial T}{\partial t} + \tau_0 \frac{\partial^2 T}{\partial t^2} \right) + \nu T_0 \left(\frac{\partial}{\partial t} + \tau_0 \frac{\partial^2}{\partial t^2} \right) (\nabla \cdot \vec{u}), \quad (3)$$

where

$$T = (1 - a\nabla^2)\Phi,$$

and the constitutive relations are

$$t_{ij} = \lambda u_{r,r} \delta_{ij} + \mu(u_{i,j} + u_{j,i}) + K(u_{j,i} - \epsilon_{ijr} \phi_r) - \nu(1 - a\nabla^2)\Phi \delta_{ij}, \quad (4)$$

$$m_{ij} = \alpha \phi_{r,r} \delta_{ij} + \beta \phi_{i,j} + \gamma \phi_{j,i}, \quad i, j, r = 1, 2, 3, \quad (5)$$

where λ and μ are Lamé's constants; K , α , β , and γ are micropolar constants; t_{ij} are the components of the stress tensor; m_{ij} are the components of couple stress tensor; \vec{u} and $\vec{\phi}$ are the displacement and microrotation vectors; δ_{ij} is the Kronecker delta; ρ is the density; ϵ_{ijr} is the alternating symbol; j is the microinertia; K^* is the thermal conductivity; c^* is the specific heat at constant strain; τ_0 is the relaxation time; T is the deviation of the thermodynamic temperature from the reference temperature; Φ is the deviation of the conductive temperature from the reference temperature; T_0 is the reference temperature; a is the two-temperature parameter; and $\nu = (3\lambda + 2\mu + K)\alpha_T$, where α_T is the coefficient of linear thermal expansion.

The necessary and sufficient conditions for the internal energy to be nonnegative as given in [Eringen 1970] are

$$0 \leq (3\lambda + 2\mu + K), \quad 0 \leq \mu, \quad 0 \leq K, \quad 0 \leq 3\alpha + 2\gamma, \quad -\gamma \leq \beta \leq \gamma, \quad 0 \leq \gamma.$$

3. Formulation of the problem

We consider a homogeneous, isotropic, micropolar, thermoelastic solid half-space with two temperatures (medium M_2) lying over another homogeneous, isotropic, micropolar, thermoelastic solid half-space with two temperatures (medium M_1). The rectangular Cartesian coordinate system $Ox_1x_2x_3$ having origin on the surface $x_3 = 0$ with the x_3 -axis pointing vertically into the medium M_1 is introduced. Quantities in medium M_2 are denoted with a bar, while those in medium M_1 have no bar.

We consider the two-dimensional problem in the x_1x_3 -plane, so that the displacement vector \vec{u} and microrotation vector $\vec{\phi}$ for the solid medium M_1 are taken as

$$\vec{u} = (u_1(x_1, x_3), 0, u_3(x_1, x_3)), \quad \vec{\phi} = (0, \phi_2(x_1, x_3), 0). \quad (6)$$

For convenience, the following nondimensional quantities are introduced:

$$\begin{aligned} x'_1 &= \frac{\omega^* x_1}{c_1}, & x'_3 &= \frac{\omega^* x_3}{c_1}, & u'_1 &= \frac{\rho \omega^* c_1}{\nu T_0} u_1, & u'_3 &= \frac{\rho \omega^* c_1}{\nu T_0} u_3, & \phi'_2 &= \frac{\rho c_1^2}{\nu T_0} \phi_2, \\ t' &= \omega^* t, & T' &= \frac{T}{T_0}, & \Phi' &= \frac{\Phi}{T_0}, & t'_{ij} &= \frac{1}{\nu T_0} t_{ij}, & m'_{ij} &= \frac{\omega^*}{c_1 \nu T_0} m_{ij}, \\ \tau'_0 &= \omega^* \tau_0, & a' &= \frac{\omega^{*2}}{c_1^2} a, \end{aligned} \quad (7)$$

where

$$\omega^* = \frac{\rho c^* c_1^2}{K^*}, \quad c_1^2 = \frac{\lambda + 2\mu + K}{\rho}.$$

The expressions relating the displacement components u_1 and u_3 to the potential functions ϕ and ψ in dimensionless form are taken as

$$u_1 = \frac{\partial \phi}{\partial x_1} - \frac{\partial \psi}{\partial x_3}, \quad u_3 = \frac{\partial \phi}{\partial x_3} + \frac{\partial \psi}{\partial x_1}. \quad (8)$$

Making use of (8) in (1)–(2) and with the aid of (6) and (7) (after suppressing the primes), we obtain

$$\nabla^2 \phi - (1 - a \nabla^2) \Phi - \frac{\partial^2 \phi}{\partial t^2} = 0, \quad (9)$$

$$\nabla^2 \psi + a_1 \phi_2 - a_2 \frac{\partial^2 \psi}{\partial t^2} = 0, \quad (10)$$

$$\nabla^2 \phi_2 - a_3 \nabla^2 \psi - a_4 \phi_2 - a_5 \frac{\partial^2 \phi_2}{\partial t^2} = 0, \quad (11)$$

$$\nabla^2 \Phi = a_6 \left(1 + \tau_0 \frac{\partial}{\partial t} \right) \frac{\partial}{\partial t} (1 - a \nabla^2) \Phi + a_7 \left(\frac{\partial}{\partial t} + \tau_0 \frac{\partial^2}{\partial t^2} \right) \nabla^2 \phi, \quad (12)$$

where

$$a_1 = \frac{K}{\mu + K}, \quad a_2 = \frac{\rho c_1^2}{\mu + K}, \quad a_3 = \frac{K c_1^2}{\gamma \omega^{*2}}, \quad a_4 = 2a_3, \quad a_5 = \frac{\rho \hat{j} c_1^2}{\gamma}, \quad a_6 = \frac{\rho c^* c_1^2}{K^* \omega^*}, \quad a_7 = \frac{v^2 T_0}{\rho K^* \omega^*},$$

and $\nabla^2 = \frac{\partial^2}{\partial x_1^2} + \frac{\partial^2}{\partial x_3^2}$ is the Laplacian operator.

4. Boundary conditions

The boundary conditions at the interface $x_3 = 0$ are requirements of the continuity of the normal stress component, the tangential stress component, the tangential couple stress component, the tangential displacement component, the normal displacement component, the microrotation component, and of the thermodynamic temperature and normal component of the heat flux. Mathematically these can be written as

$$t_{33} = \bar{t}_{33}, \quad t_{31} = \bar{t}_{31}, \quad m_{32} = \bar{m}_{32}, \quad u_1 = \bar{u}_1, \quad u_3 = \bar{u}_3, \quad \phi_2 = \bar{\phi}_2, \quad T = \bar{T}, \quad K^* \frac{\partial T}{\partial x_3} = \bar{K}^* \frac{\partial \bar{T}}{\partial x_3}. \quad (13)$$

5. Reflection and transmission

We consider LD waves, T waves, CD-I, and CD-II waves propagating through medium M_1 , which we designate as the region $x_3 > 0$, and incident at the plane $x_3 = 0$ with direction of propagation at angle θ_0 normal to the surface. Corresponding to each incident wave, we get reflected LD, T, CD-I, and CD-II waves in medium M_1 and transmitted LD, T, CD-I, and CD-II waves in medium M_2 , as shown in Figure 1. In order to solve (9)–(12), we assume solutions of the form

$$\{\phi, \Phi, \psi, \phi_2\} = \{\tilde{\phi}, \tilde{\Phi}, \tilde{\psi}, \tilde{\phi}_2\} e^{i\{k(x_1 \sin \theta - x_3 \cos \theta) - \omega t\}}, \quad (14)$$

where k is the wave number, ω the angular frequency, θ the angle of incidence, and $\phi, \Phi, \psi,$ and ϕ_2 arbitrary constants.

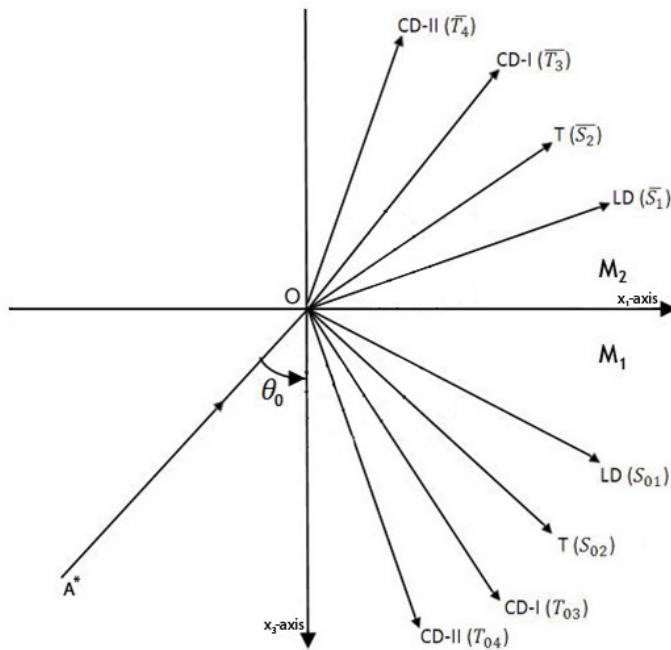


Figure 1. Geometry of the problem.

Making use of (14) in (9)–(12) yields

$$V^4 + D_1 V^2 + E_1 = 0, \tag{15}$$

$$V^4 + D_2 V^2 + E_2 = 0, \tag{16}$$

where

$$D_1 = \frac{-1 + (a - 1/\omega^2)a_6\omega^2(t/\omega + \tau_0) - a_7(t/\omega + \tau_0)}{a_6(t/\omega + \tau_0)}, \quad E_1 = \frac{1 - a\omega^2[a_7(t/\omega + \tau_0) + a_6(t/\omega + \tau_0)]}{a_6(t/\omega + \tau_0)},$$

$$D_2 = \left(\frac{a_1 a_3}{\omega^2 a_2} + 1\right) \frac{1}{(a_4/\omega^2 - a_5)} - \frac{1}{a_2}, \quad E_2 = \frac{1}{(a_5 - a_4/\omega^2)a_2},$$

and $V^2 = \omega^2/k^2$.

Equations (15) and (16) are quadratic in V^2 , therefore the roots of these equations give four values of V^2 . Corresponding to each value of V^2 in (15), there exist two types of waves in medium M_1 which are, in decreasing order of their velocities, a LD and a T wave. Similarly, corresponding to each value of V^2 in (16), there exist two types of waves in medium M_1 , a CD-I and a CD-II wave. Let V_1 and V_2 be the velocities of the reflected LD and T waves, respectively, and V_3 and V_4 be the velocities of the reflected CD-I and CD-II waves in medium M_1 , respectively.

In view of (14), the appropriate solutions of (9)–(12) for mediums M_1 and M_2 are assumed in the following forms.

For medium M_1 :

$$\{\phi, \Phi\} = \sum_{i=1}^2 \{1, f_i\} [S_{0i} e^{\iota\{k_i(x_1 \sin \theta_{0i} - x_3 \cos \theta_{0i}) - \omega_i t\}} + P_i], \quad (17)$$

$$\{\psi, \phi_2\} = \sum_{j=3}^4 \{1, f_j\} [T_{0j} e^{\iota\{k_j(x_1 \sin \theta_{0j} - x_3 \cos \theta_{0j}) - \omega_j t\}} + P_j]. \quad (18)$$

Medium M_2 :

$$\{\bar{\phi}, \bar{\Phi}\} = \sum_{i=1}^2 \{1, \bar{f}_i\} [\bar{S}_i e^{\iota\{\bar{k}_i(x_1 \sin \bar{\theta}_i - x_3 \cos \bar{\theta}_i) - \bar{\omega}_i t\}}], \quad (19)$$

$$\{\bar{\psi}, \bar{\phi}_2\} = \sum_{j=3}^4 \{1, \bar{f}_j\} [\bar{T}_j e^{\iota\{\bar{k}_j(x_1 \sin \bar{\theta}_j - x_3 \cos \bar{\theta}_j) - \bar{\omega}_j t\}}], \quad (20)$$

where

$$P_i = S_i e^{\iota\{k_i(x_1 \sin \theta_i + x_3 \cos \theta_i) - \omega_i t\}}, \quad P_j = T_j e^{\iota\{k_j(x_1 \sin \theta_j + x_3 \cos \theta_j) - \omega_j t\}},$$

$$f_i = \frac{\omega^2(1 - 1/V_i^2)}{1 + a\omega^2/V_i^2}, \quad f_j = \frac{-\omega^2(a_2 - 1/V_j^2)}{a_1},$$

and S_{0i} and T_{0j} are the amplitudes of the incident LD and T waves, and CD-I and CD-II waves, respectively. S_i and T_j are the amplitudes of the reflected LD and T waves, and CD-I and CD-II waves, respectively, and \bar{S}_i and \bar{T}_j are the amplitudes of the transmitted LD and T waves, and CD-I and CD-II waves, respectively.

In order to satisfy the boundary conditions, we use the following extension of Snell's law:

$$\frac{\sin \theta_0}{V_0} = \frac{\sin \theta_1}{V_1} = \frac{\sin \theta_2}{V_2} = \frac{\sin \theta_3}{V_3} = \frac{\sin \theta_4}{V_4} = \frac{\sin \bar{\theta}_1}{\bar{V}_1} = \frac{\sin \bar{\theta}_2}{\bar{V}_2} = \frac{\sin \bar{\theta}_3}{\bar{V}_3} = \frac{\sin \bar{\theta}_4}{\bar{V}_4}, \quad (21)$$

where

$$k_1 V_1 = k_2 V_2 = k_3 V_3 = k_4 V_4 = \bar{k}_1 \bar{V}_1 = \bar{k}_2 \bar{V}_2 = \bar{k}_3 \bar{V}_3 = \bar{k}_4 \bar{V}_4 = \omega, \quad \text{at } x_3 = 0. \quad (22)$$

Making use of the values of ϕ , ψ , Φ , and ϕ_2 from (17)–(20) in boundary conditions (13), and with the aid of (4)–(8), using (21) and (22), we obtain a system of eight nonhomogeneous equations which can be written as

$$\sum_{j=1}^8 a_{ij} Z_j = Y_i \quad (i = 1, 2, 3, 4, 5, 6, 7, 8), \quad (23)$$

where

$$a_{1i} = \left(d_1 + d_2 \left(1 - \frac{V_i^2}{V_0^2} \sin^2 \theta_0 \right) \right) \frac{\omega^2}{V_i^2} + (1 - \tau_1 \omega) \left(1 + a \frac{\omega^2}{V_i^2} \right) f_i,$$

$$a_{1j} = d_2 \frac{\omega^2}{V_j V_0} \sin \theta_0 \sqrt{1 - \frac{V_j^2}{V_0^2} \sin^2 \theta_0},$$

$$\begin{aligned}
a_{15} &= -\left[\left(\bar{d}_1 + \bar{d}_2\left(1 - \frac{\bar{V}_1^2}{V_0^2}\sin^2\theta_0\right)\right)\frac{\omega^2}{\bar{V}_1^2} + \bar{p}_0(1 - \bar{\tau}_1\iota\omega)\left(1 + \bar{a}\frac{\omega^2}{\bar{V}_1^2}\right)\bar{f}_1\right], \\
a_{16} &= -\left[\left(\bar{d}_1 + \bar{d}_2\left(1 - \frac{\bar{V}_2^2}{V_0^2}\sin^2\theta_0\right)\right)\frac{\omega^2}{\bar{V}_2^2} + \bar{p}_0(1 - \bar{\tau}_1\iota\omega)\left(1 + \bar{a}\frac{\omega^2}{\bar{V}_2^2}\right)\bar{f}_2\right], \\
a_{17} &= -\bar{d}_2\frac{\omega^2}{\bar{V}_3V_0}\sin\theta_0\sqrt{1 - \frac{\bar{V}_3^2}{V_0^2}\sin^2\theta_0}, \quad a_{18} = -\bar{d}_2\frac{\omega^2}{\bar{V}_4V_0}\sin\theta_0\sqrt{1 - \frac{\bar{V}_4^2}{V_0^2}\sin^2\theta_0}, \\
a_{2i} &= -(2d_4 + d_5)\frac{\omega^2}{V_iV_0}\sin\theta_0\sqrt{1 - \frac{V_i^2}{V_0^2}\sin^2\theta_0}, \\
a_{2j} &= \left(d_4\frac{\omega^2}{V_j^2}\left(1 - 2\frac{V_j^2}{V_0^2}\sin^2\theta_0\right) + d_5\frac{\omega^2}{V_j^2}\left(1 - \frac{V_j^2}{V_0^2}\sin^2\theta_0\right)\right) - d_5f_j, \\
a_{25} &= (2\bar{d}_4 + \bar{d}_5)\frac{\omega^2}{\bar{V}_1V_0}\sin\theta_0\sqrt{1 - \frac{\bar{V}_1^2}{V_0^2}\sin^2\theta_0}, \quad a_{26} = (2\bar{d}_4 + \bar{d}_5)\frac{\omega^2}{\bar{V}_2V_0}\sin\theta_0\sqrt{1 - \frac{\bar{V}_2^2}{V_0^2}\sin^2\theta_0}, \\
a_{27} &= -\left[\bar{d}_4\frac{\omega^2}{\bar{V}_3^2}\left(1 - 2\frac{\bar{V}_3^2}{V_0^2}\sin^2\theta_0\right) + \bar{d}_5\left(\frac{\omega^2}{\bar{V}_3^2}\left(1 - \frac{\bar{V}_3^2}{V_0^2}\sin^2\theta_0\right) - \bar{f}_3\right)\right], \\
a_{28} &= -\left[\bar{d}_4\frac{\omega^2}{\bar{V}_4^2}\left(1 - 2\frac{\bar{V}_4^2}{V_0^2}\sin^2\theta_0\right) + \bar{d}_5\left(\frac{\omega^2}{\bar{V}_4^2}\left(1 - \frac{\bar{V}_4^2}{V_0^2}\sin^2\theta_0\right) - \bar{f}_4\right)\right], \\
a_{3i} &= 0, \quad a_{3j} = \iota\frac{\omega}{V_j}\sqrt{1 - \frac{V_j^2}{V_0^2}\sin^2\theta_0}f_j, \quad a_{35} = a_{36} = 0, \quad a_{37} = \iota\frac{\omega}{\bar{V}_3}p_1\sqrt{1 - \frac{\bar{V}_3^2}{V_0^2}\sin^2\theta_0}\bar{f}_3, \\
a_{38} &= \iota\frac{\omega}{\bar{V}_4}p_1\sqrt{1 - \frac{\bar{V}_4^2}{V_0^2}\sin^2\theta_0}\bar{f}_4, \\
a_{4i} &= \iota\frac{\omega}{V_0}\sin\theta_0, \quad a_{4j} = -\iota\frac{\omega}{V_j}\sqrt{1 - \frac{V_j^2}{V_0^2}\sin^2\theta_0}, \\
a_{45} &= a_{46} = -\iota\frac{\omega}{V_0}\sin\theta_0, \quad a_{47} = -\iota\frac{\omega}{\bar{V}_3}\sqrt{1 - \frac{\bar{V}_3^2}{V_0^2}\sin^2\theta_0}, \quad a_{48} = -\iota\frac{\omega}{\bar{V}_4}\sqrt{1 - \frac{\bar{V}_4^2}{V_0^2}\sin^2\theta_0}, \\
a_{5i} &= \iota\frac{\omega}{V_i}\sqrt{1 - \frac{V_i^2}{V_0^2}\sin^2\theta_0}, \quad a_{5j} = \iota\frac{\omega}{V_0}\sin\theta_0, \\
a_{55} &= \iota\frac{\omega}{\bar{V}_1}\sqrt{1 - \frac{\bar{V}_1^2}{V_0^2}\sin^2\theta_0}, \quad a_{56} = \iota\frac{\omega}{\bar{V}_2}\sqrt{1 - \frac{\bar{V}_2^2}{V_0^2}\sin^2\theta_0}, \quad a_{57} = a_{58} = -\iota\frac{\omega}{V_0}\sin\theta_0, \\
a_{6i} &= 0, \quad a_{6j} = f_j, \quad a_{65} = a_{66} = 0, \quad a_{67} = -\bar{f}_3, \quad a_{68} = -\bar{f}_4, \\
a_{7i} &= \left(1 + a\frac{\omega^2}{V_i^2}\right)f_i, \quad a_{7j} = 0, \quad a_{75} = -\left(1 + \bar{a}\frac{\omega^2}{\bar{V}_1^2}\right)\bar{f}_1, \quad a_{76} = -\left(1 + \bar{a}\frac{\omega^2}{\bar{V}_2^2}\right)\bar{f}_2, \quad a_{77} = a_{78} = 0,
\end{aligned}$$

$$\begin{aligned}
a_{8i} &= \iota \frac{\omega}{V_i} \left(1 + a \frac{\omega^2}{V_i^2} \right) \sqrt{1 - \frac{V_i^2}{V_0^2} \sin^2 \theta_0 f_i}, \quad a_{8j} = 0, \\
a_{85} &= \iota p_2 \frac{\omega}{\bar{V}_1} \left(1 + \bar{a} \frac{\omega^2}{\bar{V}_1^2} \right) \sqrt{1 - \frac{\bar{V}_1^2}{V_0^2} \sin^2 \theta_0 \bar{f}_1}, \\
a_{86} &= \iota p_2 \frac{\omega}{\bar{V}_2} \left(1 + \bar{a} \frac{\omega^2}{\bar{V}_2^2} \right) \sqrt{1 - \frac{\bar{V}_2^2}{V_0^2} \sin^2 \theta_0 \bar{f}_2}, \quad a_{87} = a_{88} = 0, \\
\bar{p}_0 &= \frac{\bar{v}}{v}, \quad d_1 = \frac{\lambda}{\rho c_1^2}, \quad d_2 = \frac{(2\mu + K)}{\rho c_1^2}, \quad d_4 = \frac{\mu}{\rho c_1^2}, \quad d_5 = \frac{K}{\rho c_1^2}, \quad p_1 = \frac{\bar{\gamma}}{\gamma}, \quad p_2 = \frac{K_1^*}{K^*}, \\
\bar{d}_1 &= \frac{\bar{\lambda}}{\rho c_1^2}, \quad \bar{d}_2 = \frac{(2\bar{\mu} + \bar{K})}{\rho c_1^2}, \quad \bar{d}_4 = \frac{\bar{\mu}}{\rho c_1^2}, \quad \bar{d}_5 = \frac{\bar{K}}{\rho c_1^2}.
\end{aligned} \tag{24}$$

In (24), $i = 1, 2$ and $j = 3, 4$, and

$$Z_1 = \frac{S_1}{A^*}, \quad Z_2 = \frac{S_2}{A^*}, \quad Z_3 = \frac{T_3}{A^*}, \quad Z_4 = \frac{T_4}{A^*}, \quad Z_5 = \frac{\bar{S}_1}{A^*}, \quad Z_6 = \frac{\bar{S}_2}{A^*}, \quad Z_7 = \frac{\bar{T}_3}{A^*}, \quad Z_8 = \frac{\bar{T}_4}{A^*}. \tag{25}$$

(1) For an incident LD wave:

$$\begin{aligned}
A^* &= S_{01}, \quad S_{02} = T_{03} = T_{04} = 0, \quad Y_1 = -a_{11}, \quad Y_2 = a_{21}, \quad Y_3 = a_{31} = 0, \\
Y_4 &= -a_{41}, \quad Y_5 = a_{51}, \quad Y_6 = a_{61} = 0, \quad Y_7 = -a_{71}, \quad Y_8 = a_{81}.
\end{aligned}$$

(2) For an incident T wave:

$$\begin{aligned}
A^* &= S_{02}, \quad S_{01} = T_{03} = T_{04} = 0, \quad Y_1 = -a_{12}, \quad Y_2 = a_{22}, \quad Y_3 = a_{32} = 0, \\
Y_4 &= -a_{42}, \quad Y_5 = a_{52}, \quad Y_6 = a_{62} = 0, \quad Y_7 = -a_{72}, \quad Y_8 = a_{82}.
\end{aligned}$$

(3) For an incident CD-I wave:

$$\begin{aligned}
A^* &= T_{03}, \quad S_{01} = S_{02} = T_{04} = 0, \quad Y_1 = a_{13}, \quad Y_2 = -a_{23}, \quad Y_3 = a_{33}, \\
Y_4 &= a_{43}, \quad Y_5 = -a_{53}, \quad Y_6 = -a_{63}, \quad Y_7 = a_{73} = 0, \quad Y_8 = a_{83} = 0.
\end{aligned}$$

(4) For an incident CD-II wave:

$$\begin{aligned}
A^* &= T_{04}, \quad S_{01} = S_{02} = T_{03} = 0, \quad Y_1 = a_{14}, \quad Y_2 = -a_{24}, \quad Y_3 = a_{34}, \\
Y_4 &= a_{44}, \quad Y_5 = -a_{54}, \quad Y_6 = -a_{64}, \quad Y_7 = a_{74} = 0, \quad Y_8 = a_{84} = 0,
\end{aligned}$$

where Z_1, Z_2, Z_3 , and Z_4 are the amplitude ratios of the reflected LD, T, and coupled CD-I and CD-II waves in the medium M_1 , and Z_5, Z_6, Z_7 , and Z_8 are the amplitude ratios of the transmitted LD, T, and coupled CD-I and CD-II waves in medium M_2 .

6. Particular cases

Case I. If the two-temperature parameters vanish, that is, $a = 0$ and $\bar{a} = 0$ in (23), then we obtain the amplitude ratios at the interface of the two micropolar thermoelastic solid half-spaces with the following changed values of a_{ij} :

$$\begin{aligned}
 a_{1i} &= \left(d_1 + d_2 \left(1 - \frac{V_i^2}{V_0^2} \sin^2 \theta_0 \right) \right) \frac{\omega^2}{V_i^2} + (1 - \tau_1 \iota \omega) f_i, \\
 a_{15} &= - \left[\left(\bar{d}_1 + \bar{d}_2 \left(1 - \frac{\bar{V}_1^2}{V_0^2} \sin^2 \theta_0 \right) \right) \frac{\omega^2}{\bar{V}_2^2} + \bar{p}_0 (1 - \bar{\tau}_1 \iota \bar{\omega}_1) \bar{f}_1 \right], \\
 a_{16} &= - \left[\left(\bar{d}_1 + \bar{d}_2 \left(1 - \frac{\bar{V}_2^2}{V_0^2} \sin^2 \theta_0 \right) \right) \frac{\omega^2}{\bar{V}_2^2} + \bar{p}_0 (1 - \bar{\tau}_1 \iota \bar{\omega}_2) \bar{f}_2 \right], \\
 a_{7i} &= f_i, \quad a_{75} = -\bar{f}_1, \quad a_{76} = -\bar{f}_2, \quad a_{8i} = \iota \frac{\omega}{V_i} \sqrt{1 - \frac{V_i^2}{V_0^2} \sin^2 \theta_0} f_i, \\
 a_{85} &= \iota p_2 \frac{\omega}{\bar{V}_1} \sqrt{1 - \frac{\bar{V}_1^2}{V_0^2} \sin^2 \theta_0} \bar{f}_1 \quad a_{86} = \iota p_2 \frac{\omega}{\bar{V}_2} \sqrt{1 - \frac{\bar{V}_2^2}{V_0^2} \sin^2 \theta_0} \bar{f}_2.
 \end{aligned} \tag{26}$$

Case II. By neglecting the thermal effect and the two-temperature effect in (23), the amplitude ratios at the interface of the two micropolar elastic solid half-spaces are given by

$$\sum_{j=1}^6 a_{ij} Z_j = Y_i \quad (i = 1, 2, 3, 4, 5, 6),$$

where the values of a_{ij} are given by

$$\begin{aligned}
 a_{1i} &= 0, \quad a_{11} = \left(d_1 + d_2 \left(1 - \frac{V_1^2}{V_0^2} \sin^2 \theta_0 \right) \right) \frac{\omega^2}{V_1^2}, \quad a_{12} = d_2 \frac{\omega^2}{V_3 V_0} \sin \theta_0 \sqrt{1 - \frac{V_3^2}{V_0^2} \sin^2 \theta_0}, \\
 a_{13} &= d_2 \frac{\omega^2}{V_4 V_0} \sin \theta_0 \sqrt{1 - \frac{V_4^2}{V_0^2} \sin^2 \theta_0}, \quad a_{14} = - \left[\left(\bar{d}_1 + \bar{d}_2 \left(1 - \frac{\bar{V}_1^2}{V_0^2} \sin^2 \theta_0 \right) \right) \frac{\omega^2}{\bar{V}_1^2} \right], \\
 a_{15} &= -\bar{d}_2 \frac{\omega^2}{\bar{V}_3 V_0} \sin \theta_0 \sqrt{1 - \frac{\bar{V}_3^2}{V_0^2} \sin^2 \theta_0}, \quad a_{16} = -\bar{d}_2 \frac{\omega^2}{\bar{V}_4 V_0} \sin \theta_0 \sqrt{1 - \frac{\bar{V}_4^2}{V_0^2} \sin^2 \theta_0}, \\
 a_{21} &= -(2d_4 + d_5) \frac{\omega^2}{V_1 V_0} \sin \theta_0 \sqrt{1 - \frac{V_1^2}{V_0^2} \sin^2 \theta_0}, \\
 a_{22} &= \left(d_4 \frac{\omega^2}{V_3^2} \left(1 - 2 \frac{V_3^2}{V_0^2} \sin^2 \theta_0 \right) + d_5 \frac{\omega^2}{V_3^2} \left(1 - \frac{V_3^2}{V_0^2} \sin^2 \theta_0 \right) \right) - d_5 f_3, \\
 a_{23} &= \left(d_4 \frac{\omega^2}{V_4^2} \left(1 - 2 \frac{V_4^2}{V_0^2} \sin^2 \theta_0 \right) + d_5 \frac{\omega^2}{V_4^2} \left(1 - \frac{V_4^2}{V_0^2} \sin^2 \theta_0 \right) \right) - d_5 f_4, \\
 a_{24} &= (2\bar{d}_4 + \bar{d}_5) \frac{\omega^2}{\bar{V}_1 V_0} \sin \theta_0 \sqrt{1 - \frac{\bar{V}_1^2}{V_0^2} \sin^2 \theta_0},
 \end{aligned}$$

$$\begin{aligned}
a_{25} &= -\left[\bar{d}_4 \frac{\omega^2}{\bar{V}_2^2} \left(1 - 2 \frac{\bar{V}_2^2}{V_0^2} \sin^2 \theta_0\right) + \bar{d}_5 \left(\frac{\omega^2}{\bar{V}_2^2} \left(1 - \frac{\bar{V}_2^2}{V_0^2} \sin^2 \theta_0\right) - \bar{f}_3\right)\right], \\
a_{26} &= -\left[\bar{d}_4 \frac{\omega^2}{\bar{V}_3^2} \left(1 - 2 \frac{\bar{V}_3^2}{V_0^2} \sin^2 \theta_0\right) + \bar{d}_5 \left(\frac{\omega^2}{\bar{V}_3^2} \left(1 - \frac{\bar{V}_3^2}{V_0^2} \sin^2 \theta_0\right) - \bar{f}_4\right)\right], \\
a_{31} &= 0, \quad a_{32} = \iota \frac{\omega}{V_3} \sqrt{1 - \frac{V_3^2}{V_0^2} \sin^2 \theta_0} f_3, \quad a_{33} = \iota \frac{\omega}{V_4} \sqrt{1 - \frac{V_4^2}{V_0^2} \sin^2 \theta_0} f_4, \\
a_{34} &= 0, \quad a_{35} = \iota \frac{\omega}{V_3} p_1 \sqrt{1 - \frac{\bar{V}_3^2}{V_0^2} \sin^2 \theta_0} \bar{f}_3, \quad a_{36} = \iota \frac{\omega}{V_4} p_1 \sqrt{1 - \frac{\bar{V}_4^2}{V_0^2} \sin^2 \theta_0} \bar{f}_4, \\
a_{41} &= \iota \frac{\omega}{V_0} \sin \theta_0, \quad a_{42} = -\iota \frac{\omega}{V_3} \sqrt{1 - \frac{V_3^2}{V_0^2} \sin^2 \theta_0}, \quad a_{43} = -\iota \frac{\omega}{V_4} \sqrt{1 - \frac{V_4^2}{V_0^2} \sin^2 \theta_0}, \\
a_{44} &= -\iota \frac{\omega}{V_0} \sin \theta_0, \quad a_{45} = -\iota \frac{\omega}{\bar{V}_3} \sqrt{1 - \frac{\bar{V}_3^2}{V_0^2} \sin^2 \theta_0}, \quad a_{46} = -\iota \frac{\omega}{\bar{V}_4} \sqrt{1 - \frac{\bar{V}_4^2}{V_0^2} \sin^2 \theta_0}, \\
a_{51} &= \iota \frac{\omega}{V_1} \sqrt{1 - \frac{V_1^2}{V_0^2} \sin^2 \theta_0}, \quad a_{52} = a_{53} = \iota \frac{\omega}{V_0} \sin \theta_0, \quad a_{54} = \iota \frac{\omega}{\bar{V}_1} \sqrt{1 - \frac{\bar{V}_1^2}{V_0^2} \sin^2 \theta_0}, \\
a_{55} &= a_{56} = -\iota \frac{\omega}{V_0} \sin \theta_0, \\
a_{61} &= 0, \quad a_{62} = f_3, \quad a_{63} = f_4, \quad a_{64} = 0, \quad a_{65} = -\bar{f}_3, \quad a_{66} = -\bar{f}_4.
\end{aligned} \tag{27}$$

V_1 is the velocity of the reflected P wave and

$$Z_1 = \frac{S_1}{A^*}, \quad Z_2 = \frac{T_3}{A^*}, \quad Z_3 = \frac{T_4}{A^*}, \quad Z_4 = \frac{\bar{S}_1}{A^*}, \quad Z_5 = \frac{\bar{T}_3}{A^*}, \quad Z_6 = \frac{\bar{T}_4}{A^*}, \tag{28}$$

where Z_1 , Z_2 , and Z_3 are the amplitude ratios of the reflected P and coupled CD-I and CD-II waves in medium M_1 , and Z_5 , Z_6 , and Z_7 are the amplitude ratios of the transmitted P and coupled CD-I and CD-II waves in medium M_2 .

The above results are similar to those obtained by Tomar and Gogna [1995a; 1995b], changing the dimensionless quantities into physical quantities.

Case III. By neglecting the micropolarity effect in medium M_2 , we obtain amplitude ratios at the interface of the micropolar thermoelastic solid with two temperatures and the thermoelastic solid with two temperatures as

$$\sum_{j=1}^7 a_{ij} Z_j = Y_i \quad (i = 1, 2, 3, 4, 5, 6, 7),$$

where

$$a_{1i} = \left(d_1 + d_2 \left(1 - \frac{V_i^2}{V_0^2} \sin^2 \theta_0 \right) \right) \frac{\omega^2}{V_i^2} + (1 - \tau_1 \iota \omega) \left(1 + a \frac{\omega^2}{V_i^2} \right) f_i,$$

$$a_{1j} = d_2 \frac{\omega^2}{V_j V_0} \sin \theta_0 \sqrt{1 - \frac{V_j^2}{V_0^2} \sin^2 \theta_0},$$

$$a_{15} = - \left[\left(\bar{d}_1 + \bar{d}_2 \left(1 - \frac{\bar{V}_1^2}{V_0^2} \sin^2 \theta_0 \right) \right) \frac{\omega^2}{\bar{V}_1^2} + \bar{p}_0 (1 - \bar{\tau}_1 \iota \omega) \left(1 + \bar{a} \frac{\omega^2}{\bar{V}_1^2} \right) \bar{f}_1 \right],$$

$$a_{16} = - \left[\left(\bar{d}_1 + \bar{d}_2 \left(1 - \frac{\bar{V}_2^2}{V_0^2} \sin^2 \theta_0 \right) \right) \frac{\omega^2}{\bar{V}_2^2} + \bar{p}_0 (1 - \bar{\tau}_1 \iota \omega) \left(1 + \bar{a} \frac{\omega^2}{\bar{V}_2^2} \right) \bar{f}_2 \right],$$

$$a_{17} = - \bar{d}_2 \frac{\omega^2}{\bar{V}_3 V_0} \sin \theta_0 \sqrt{1 - \frac{\bar{V}_3^2}{V_0^2} \sin^2 \theta_0},$$

$$a_{2i} = -(2d_4 + d_5) \frac{\omega^2}{V_i V_0} \sin \theta_0 \sqrt{1 - \frac{V_i^2}{V_0^2} \sin^2 \theta_0},$$

$$a_{2j} = \left(d_4 \frac{\omega^2}{V_j^2} \left(1 - 2 \frac{V_j^2}{V_0^2} \sin^2 \theta_0 \right) + d_5 \frac{\omega^2}{V_j^2} \left(1 - \frac{V_j^2}{V_0^2} \sin^2 \theta_0 \right) \right) - d_5 f_j,$$

$$a_{25} = (2\bar{d}_4 + \bar{d}_5) \frac{\omega^2}{\bar{V}_1 V_0} \sin \theta_0 \sqrt{1 - \frac{\bar{V}_1^2}{V_0^2} \sin^2 \theta_0},$$

$$a_{26} = (2\bar{d}_4 + \bar{d}_5) \frac{\omega^2}{\bar{V}_2 V_0} \sin \theta_0 \sqrt{1 - \frac{\bar{V}_2^2}{V_0^2} \sin^2 \theta_0},$$

$$a_{27} = -\bar{d}_4 \frac{\omega^2}{\bar{V}_3^2} \left(1 - 2 \frac{\bar{V}_3^2}{V_0^2} \sin^2 \theta_0 \right),$$

$$a_{3i} = 0, \quad a_{3j} = \iota \frac{\omega}{V_j} \sqrt{1 - \frac{V_j^2}{V_0^2} \sin^2 \theta_0} f_j, \quad a_{35} = a_{36} = a_{37} = 0, \quad ,$$

$$a_{4i} = \iota \frac{\omega}{V_0} \sin \theta_0, \quad a_{4j} = -\iota \frac{\omega}{V_i} \sqrt{1 - \frac{V_j^2}{V_0^2} \sin^2 \theta_0}, \quad a_{45} = a_{46} = -\iota \frac{\omega}{V_0} \sin \theta_0,$$

$$a_{47} = -\iota \frac{\omega}{\bar{V}_3} \sqrt{1 - \frac{\bar{V}_3^2}{V_0^2} \sin^2 \theta_0}, \quad a_{5i} = \iota \frac{\omega}{V_i} \sqrt{1 - \frac{V_i^2}{V_0^2} \sin^2 \theta_0},$$

$$a_{5j} = \iota \frac{\omega}{V_0} \sin \theta_0, \quad a_{55} = \iota \frac{\omega}{\bar{V}_1} \sqrt{1 - \frac{\bar{V}_1^2}{V_0^2} \sin^2 \theta_0}, \quad a_{56} = \iota \frac{\omega}{\bar{V}_2} \sqrt{1 - \frac{\bar{V}_2^2}{V_0^2} \sin^2 \theta_0}, \quad a_{57} = -\iota \frac{\omega}{V_0} \sin \theta_0,$$

$$a_{6i} = \left(1 + a \frac{\omega^2}{V_i^2} \right) f_i, \quad a_{6j} = 0, \quad a_{65} = - \left(1 + \bar{a} \frac{\omega^2}{\bar{V}_1^2} \right) \bar{f}_1, \quad a_{66} = - \left(1 + \bar{a} \frac{\omega^2}{\bar{V}_2^2} \right) \bar{f}_2, \quad a_{67} = 0,$$

$$\begin{aligned}
 a_{7i} &= \iota \frac{\omega}{V_i} \left(1 + a \frac{\omega^2}{V_i^2} \right) \sqrt{1 - \frac{V_i^2}{V_0^2} \sin^2 \theta_0} f_i, & a_{7j} &= 0, & a_{75} &= \iota p_2 \frac{\omega}{\bar{V}_1} \left(1 + \bar{a} \frac{\omega^2}{\bar{V}_1^2} \right) \sqrt{1 - \frac{\bar{V}_1^2}{V_0^2} \sin^2 \theta_0} \bar{f}_1, \\
 a_{76} &= \iota p_2 \frac{\omega}{\bar{V}_2} \left(1 + \bar{a} \frac{\omega^2}{\bar{V}_2^2} \right) \sqrt{1 - \frac{\bar{V}_2^2}{V_0^2} \sin^2 \theta_0} \bar{f}_2, & a_{77} &= 0,
 \end{aligned} \tag{29}$$

and

$$Z_1 = \frac{S_1}{A^*}, \quad Z_2 = \frac{S_2}{A^*}, \quad Z_3 = \frac{T_3}{A^*}, \quad Z_4 = \frac{T_4}{A^*}, \quad Z_5 = \frac{\bar{S}_1}{A^*}, \quad Z_6 = \frac{\bar{S}_2}{A^*}, \quad Z_7 = \frac{\bar{T}_3}{A^*},$$

where $Z_1, Z_2, Z_3,$ and Z_4 are the amplitude ratios of the reflected LD, T, and coupled CD-I and CD-II waves in medium M_1 , and $Z_5, Z_6,$ and Z_7 are the amplitude ratios of the transmitted LD, T, and SV (transverse) waves in medium M_2 .

Subcase (a). By taking $\bar{a} = 0$, we obtain amplitude ratios at the interface of the micropolar thermoelastic solid with two temperatures and the thermoelastic solid. The values of a_{ij} are from (29), with the following changes:

$$\begin{aligned}
 a_{15} &= - \left[\left(\bar{d}_1 + \bar{d}_2 \left(1 - \frac{\bar{V}_1^2}{V_0^2} \sin^2 \theta_0 \right) \right) \frac{\omega^2}{\bar{V}_1^2} + \bar{p}_0 (1 - \bar{\tau}_1 \iota \omega) \bar{f}_1 \right], \\
 a_{16} &= - \left[\left(\bar{d}_1 + \bar{d}_2 \left(1 - \frac{\bar{V}_2^2}{V_0^2} \sin^2 \theta_0 \right) \right) \frac{\omega^2}{\bar{V}_2^2} + \bar{p}_0 (1 - \bar{\tau}_1 \iota \omega) \bar{f}_2 \right], \\
 a_{65} &= -\bar{f}_1, \quad a_{66} = -\bar{f}_2, \\
 a_{75} &= \iota p_2 \frac{\omega}{\bar{V}_1} \sqrt{1 - \frac{\bar{V}_1^2}{V_0^2} \sin^2 \theta_0} \bar{f}_1, \quad a_{76} = \iota p_2 \frac{\omega}{\bar{V}_2} \sqrt{1 - \frac{\bar{V}_2^2}{V_0^2} \sin^2 \theta_0} \bar{f}_2.
 \end{aligned}$$

Case IV. If the upper medium M_2 is neglected and in the absence of two-temperature effect, we obtain the amplitude ratios at the free surface of micropolar generalized thermoelastic solid half-space as

$$\sum_{j=1}^4 a_{ij} Z_j = Y_i \quad (i = 1, 2, 3, 4), \tag{30}$$

where the values of a_{ij} are given by

$$\begin{aligned}
 a_{1i} &= \left(d_1 + d_2 \left(1 - \frac{V_i^2}{V_0^2} \sin^2 \theta_0 \right) \right) \frac{\omega^2}{V_i^2} + (1 - \tau_1 \iota \omega) f_i, & a_{1j} &= d_2 \frac{\omega^2}{V_j V_0} \sin \theta_0 \sqrt{1 - \frac{V_j^2}{V_0^2} \sin^2 \theta_0}, \\
 a_{2i} &= -(2d_4 + d_5) \frac{\omega^2}{V_i V_0} \sin \theta_0 \sqrt{1 - \frac{V_i^2}{V_0^2} \sin^2 \theta_0}, \\
 a_{2j} &= \left(d_4 \frac{\omega^2}{V_j^2} \left(1 - 2 \frac{V_j^2}{V_0^2} \sin^2 \theta_0 \right) + d_5 \frac{\omega^2}{V_j^2} \left(1 - \frac{V_j^2}{V_0^2} \sin^2 \theta_0 \right) \right) - d_5 f_j,
 \end{aligned}$$

$$a_{3i} = 0, \quad a_{3j} = \iota \frac{\omega}{V_j} \sqrt{1 - \frac{V_j^2}{V_0^2} \sin^2 \theta_0} f_j, \quad a_{4i} = \iota \frac{\omega}{V_i} \sqrt{1 - \frac{V_i^2}{V_0^2} \sin^2 \theta_0} f_i, \quad a_{4j} = 0,$$

and

$$Z_1 = \frac{S_1}{A^*}, \quad Z_2 = \frac{S_2}{A^*}, \quad Z_3 = \frac{T_3}{A^*}, \quad Z_4 = \frac{T_4}{A^*}, \quad (31)$$

where Z_1 , Z_2 , Z_3 , and Z_4 are the amplitude ratios of the reflected LD, T, and coupled CD-I and CD-II waves in medium M_1 .

The above results are in agreement with those obtained by Singh and Kumar [1998], changing the dimensionless quantities into physical quantities.

7. Numerical results and discussion

For numerical computations, we take the following values of the relevant parameters for both the half-spaces.

Following Eringen [1984], the values of the micropolar constants for medium M_1 are taken as

$$\begin{aligned} \lambda &= 9.4 \times 10^{10} \text{ Nm}^{-2}, & \mu &= 4.0 \times 10^{10} \text{ Nm}^{-2}, & K &= 1.0 \times 10^{10} \text{ Nm}^{-2}, \\ \gamma &= 7.79 \times 10^{-10} \text{ N}, & j &= 0.002 \times 10^{-17} \text{ m}^2, & \rho &= 1.74 \times 10^3 \text{ Kgm}^{-3}, \end{aligned}$$

and the thermal parameters for medium M_1 are taken as

$$\begin{aligned} T_0 &= 0.298 \text{ K}, & \nu &= 0.268 \times 10^8 \text{ Nm}^{-2} \text{ K}^{-1}, & c^* &= 0.104 \times 10^4 \text{ Jkg}^{-1} \text{ K}^{-1}, & a &= 0.3 \text{ m}^2, \\ K^* &= 1.7 \times 10^2 \text{ Jm}^{-1} \text{ s}^{-1} \text{ K}^{-1}, & \omega &= 1, & \tau_0 &= 0.813 \times 10^{-12} \text{ s}. \end{aligned}$$

Following Gauthier [1982], the values of the micropolar constants for medium M_2 are taken as

$$\begin{aligned} \bar{\lambda} &= 7.59 \times 10^{10} \text{ Nm}^{-2}, & \bar{\mu} &= 0.00189 \times 10^{13} \text{ Nm}^{-2}, & \bar{j} &= 0.00196 \times 10^{-16} \text{ m}^2, \\ \bar{K} &= 0.0149 \times 10^{10} \text{ Nm}^{-2}, & \bar{\gamma} &= 2.68 \times 10^{-7} \text{ N}, & \bar{\rho} &= 2.19 \times 10^3 \text{ Kgm}^{-3}. \end{aligned}$$

The thermal parameters for medium M_2 are taken to be of comparable magnitudes:

$$\begin{aligned} \bar{T}_0 &= 0.0296 \text{ K}, & \bar{\nu} &= 0.2603 \times 10^7 \text{ Nm}^{-2} \text{ K}^{-1}, & \bar{c}^* &= 0.921 \times 10^4 \text{ Jkg}^{-1} \text{ K}^{-1}, \\ \bar{K}^* &= 2.04 \times 10^2 \text{ Jm}^{-1} \text{ s}^{-1} \text{ K}^{-1}, & \bar{a} &= 0.1 \text{ m}^2, & \bar{\tau}_0 &= 0.713 \times 10^{-12} \text{ s}. \end{aligned}$$

In Figures 2–25, we represent with the solid line the incident wave for the micropolar thermoelastic solid with one relaxation time and two temperatures (NL1), with the small-dashed line the incident wave for the micropolar thermoelastic solid with one relaxation time (ZL1), with the dash-dot-dash line the incident wave for the thermoelastic solid with one relaxation time (TZL1), and with the large-dashed line the incident wave for the thermoelastic solid with one relaxation time and two temperatures (TL1).

7.1. Incident LD wave. Variations of amplitude ratios $|Z_i|$, $1 \leq i \leq 8$, with angle of incidence θ_0 , for incident LD waves are shown in Figures 2–9.

Figures 2 and 3 show that the values of the amplitude ratios $|Z_1|$ and $|Z_2|$ for ZL1 remain greater than the values for NL1 and that the values for TL1 remain greater than the values for TZL1 in the whole range. The values of $|Z_2|$ for NL1 are magnified by a factor of 10^2 . Figures 4 and 5 show that the values

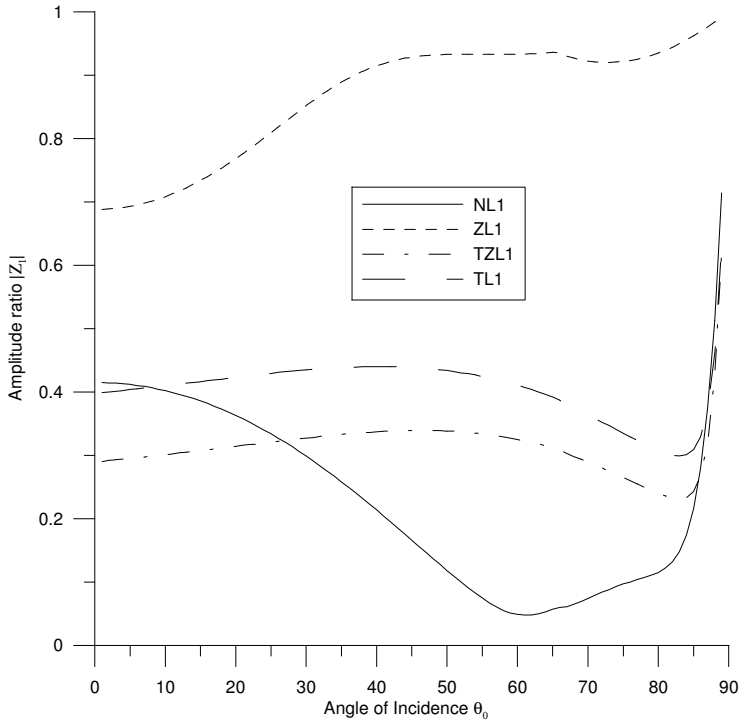


Figure 2. Variation of amplitude ratio with angle of incidence for LD wave.

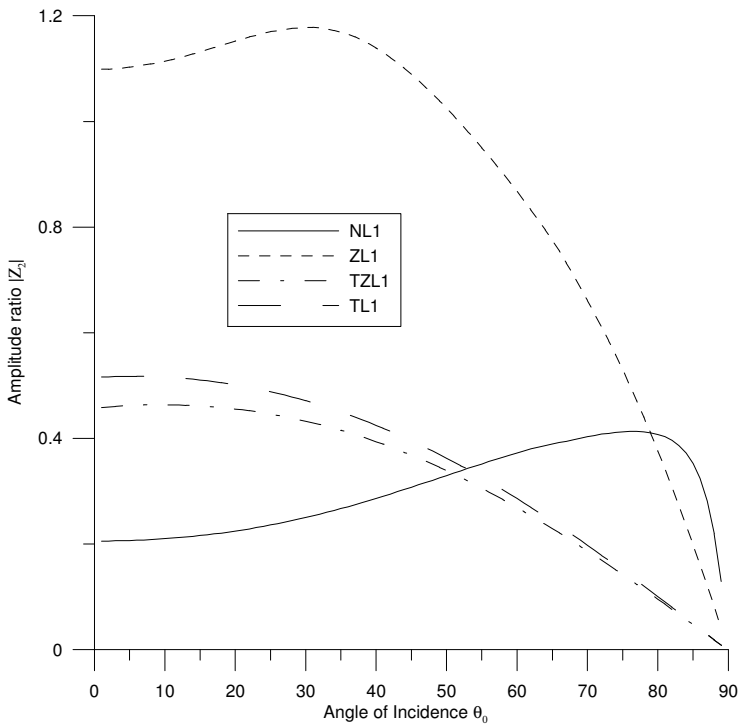


Figure 3. Variation of amplitude ratio with angle of incidence for LD wave.

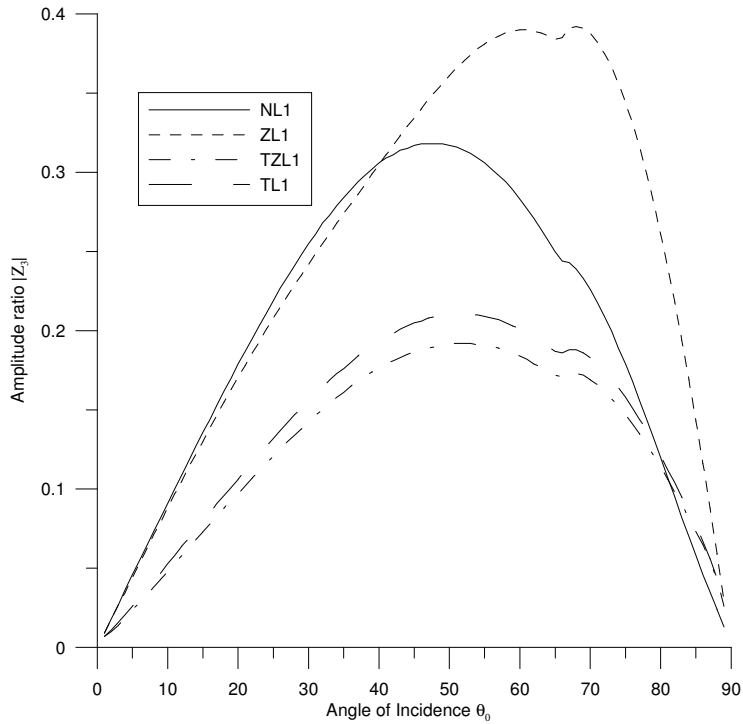


Figure 4. Variation of amplitude ratio with angle of incidence for LD wave.

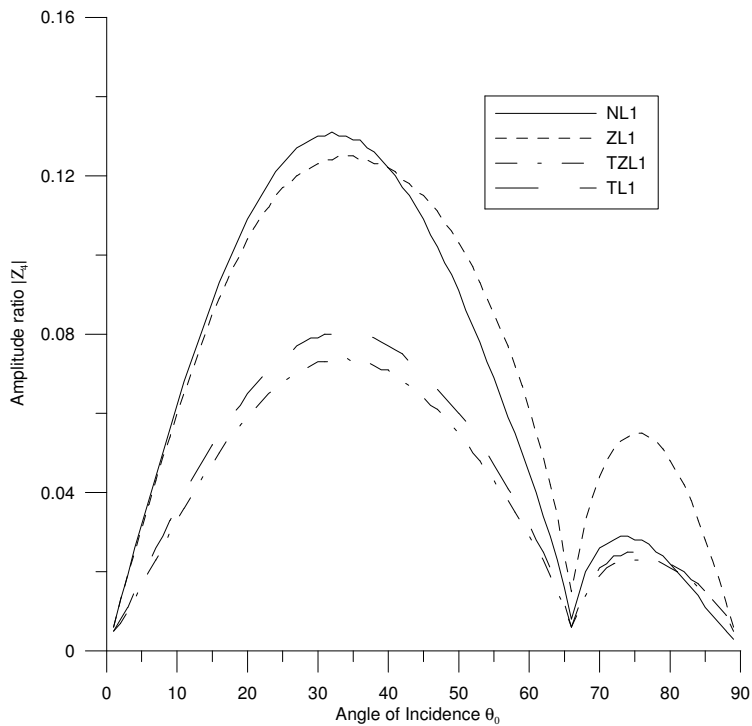


Figure 5. Variation of amplitude ratio with angle of incidence for LD wave.

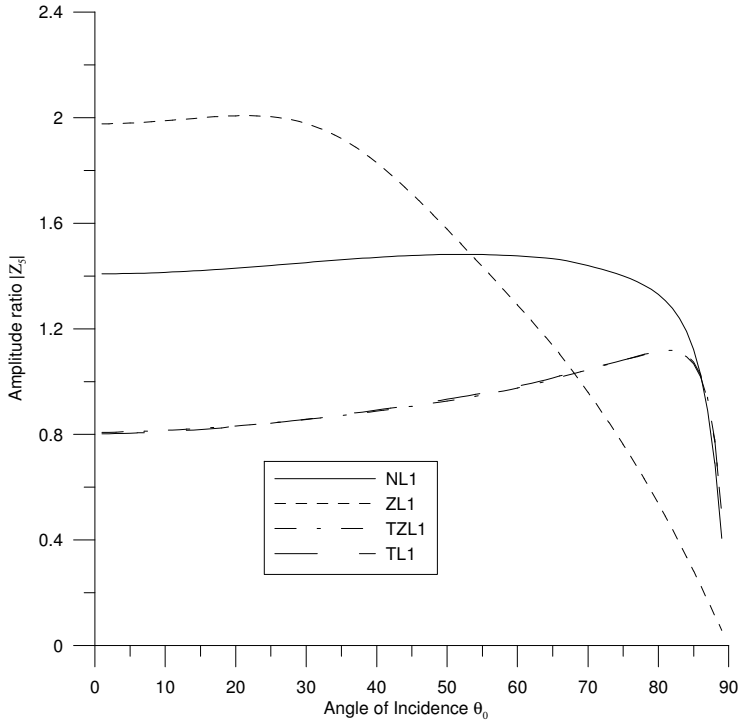


Figure 6. Variation of amplitude ratio with angle of incidence for LD wave.

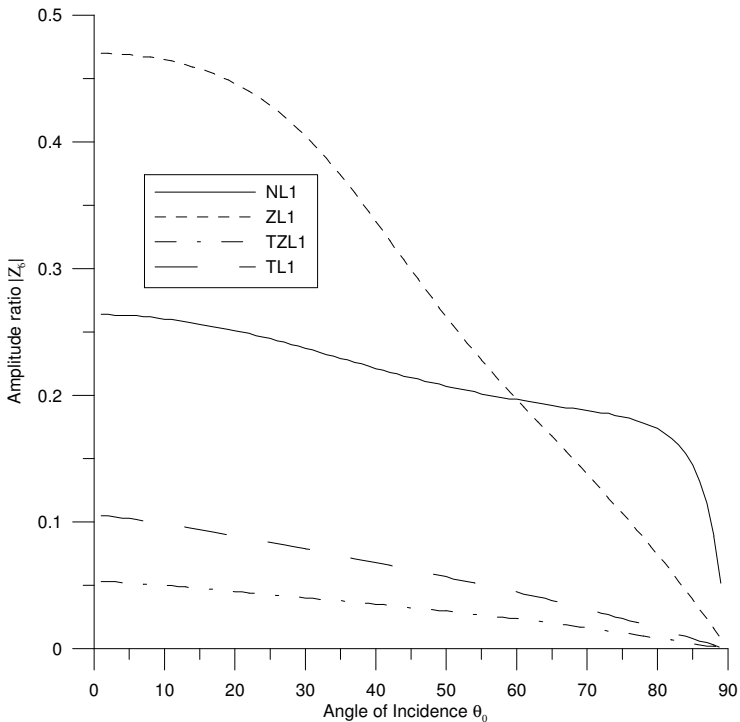


Figure 7. Variation of amplitude ratio with angle of incidence for LD wave.

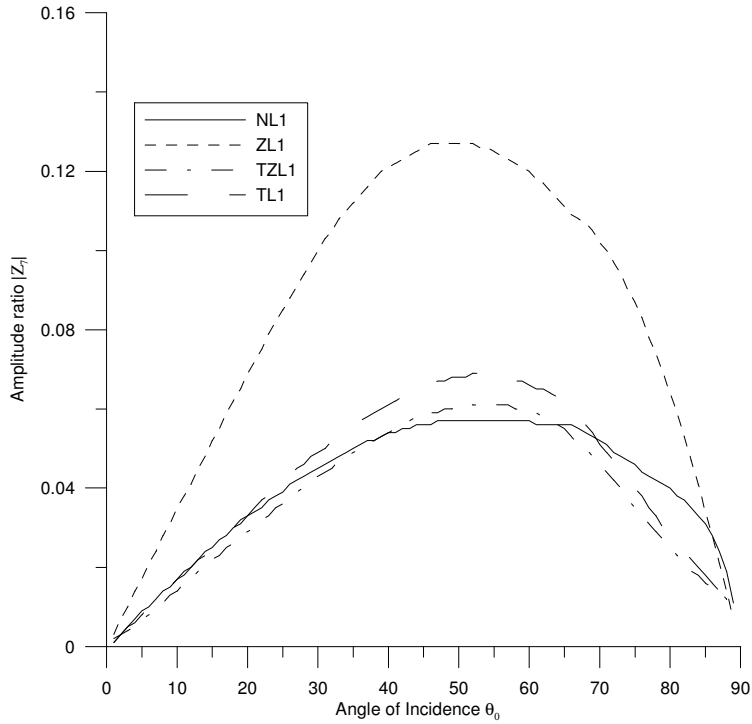


Figure 8. Variation of amplitude ratio with angle of incidence for LD wave.

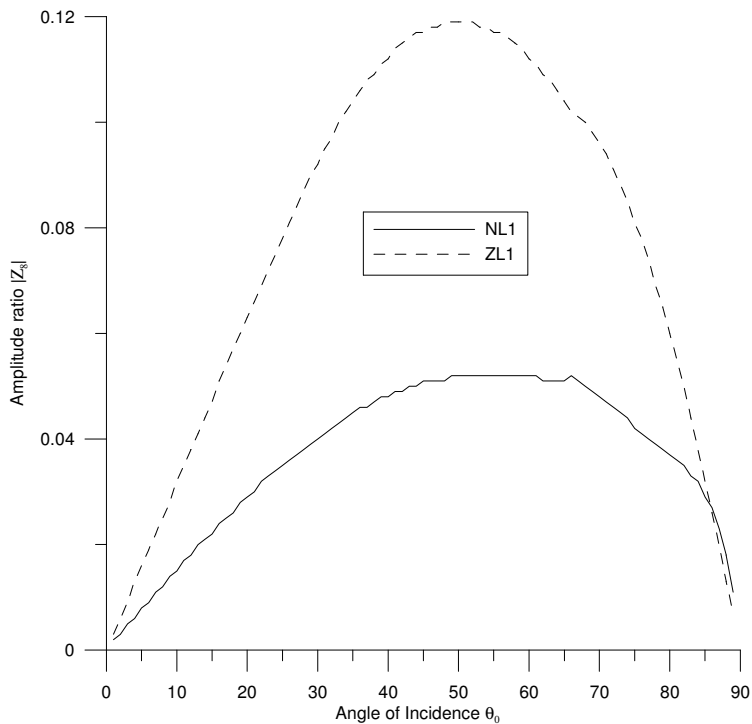


Figure 9. Variation of amplitude ratio with angle of incidence for LD wave.

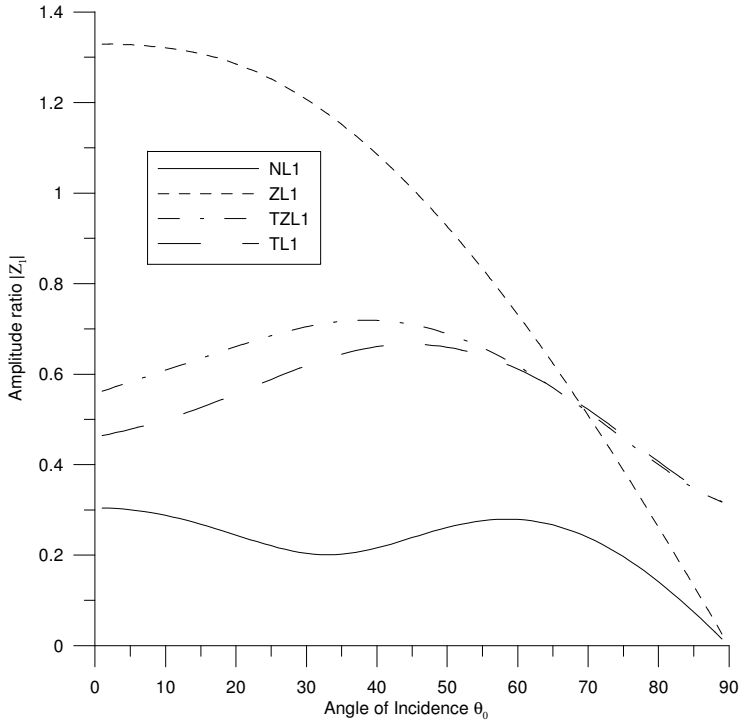


Figure 10. Variation of amplitude ratio with angle of incidence for T wave.

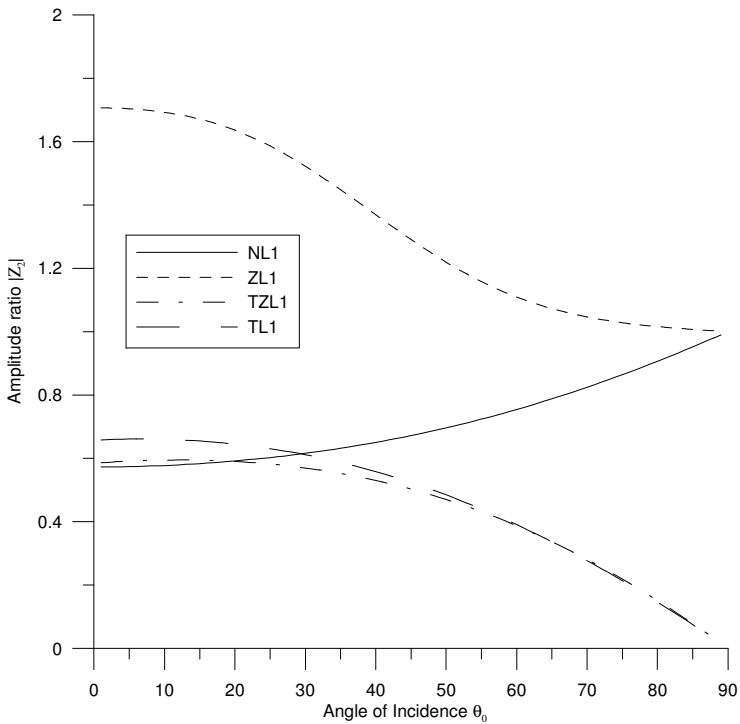


Figure 11. Variation of amplitude ratio with angle of incidence for T wave.

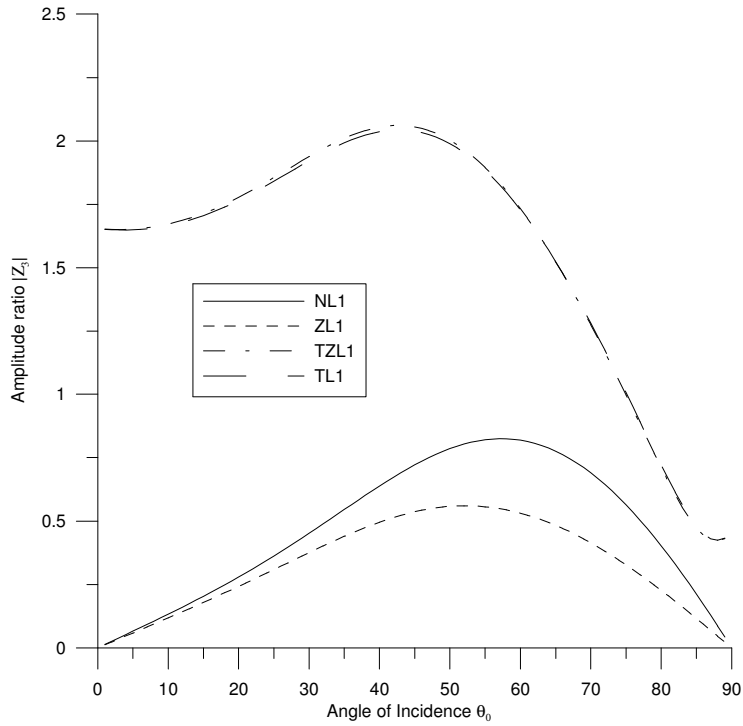


Figure 12. Variation of amplitude ratio with angle of incidence for T wave.

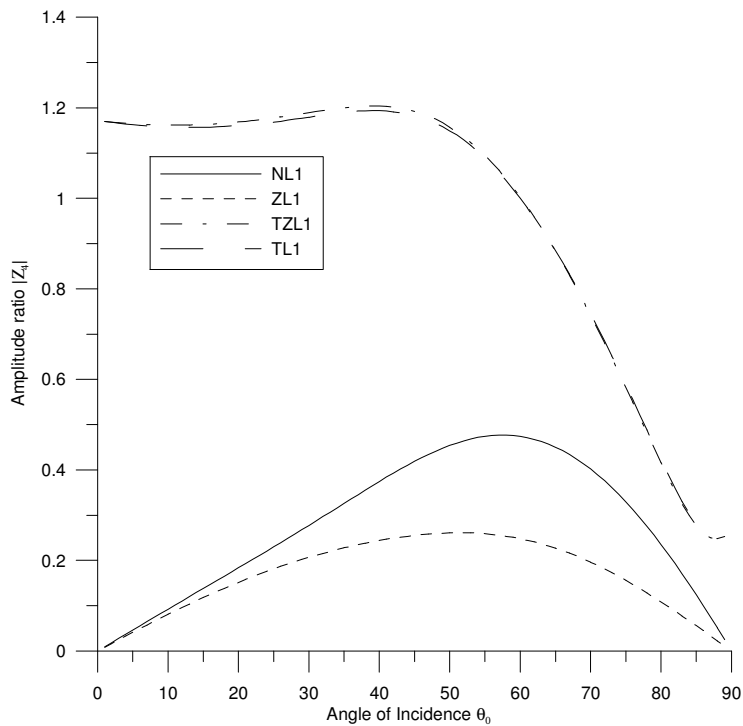


Figure 13. Variation of amplitude ratio with angle of incidence for T wave.

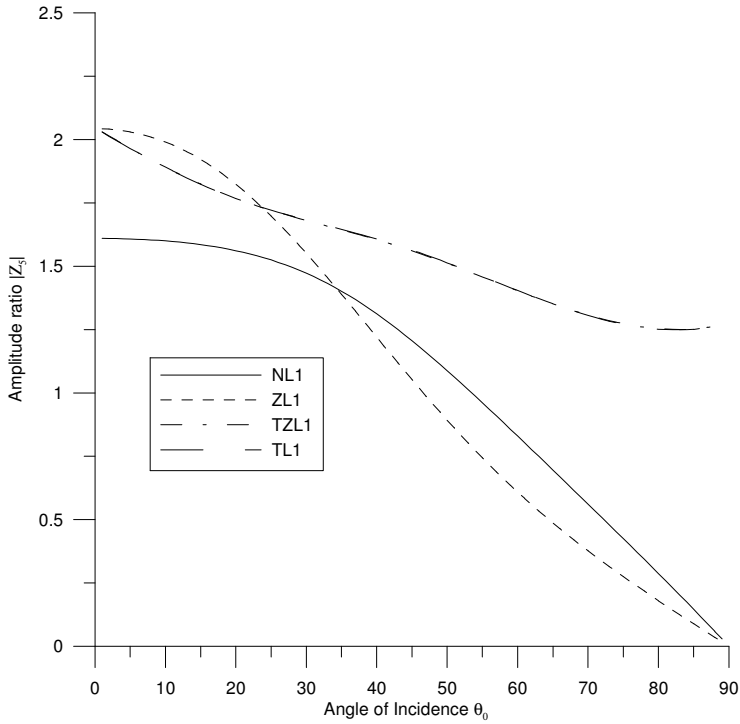


Figure 14. Variation of amplitude ratio with angle of incidence for T wave.

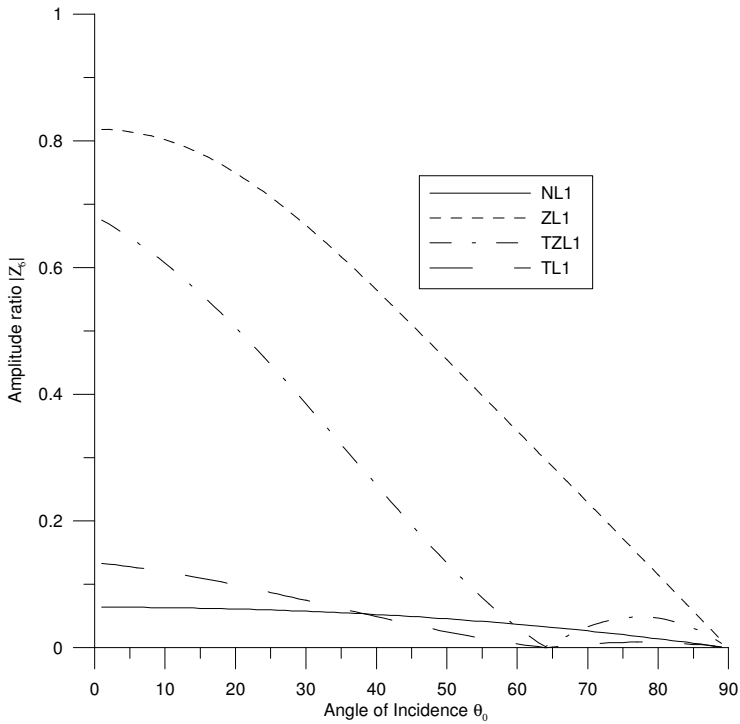


Figure 15. Variation of amplitude ratio with angle of incidence for T wave.

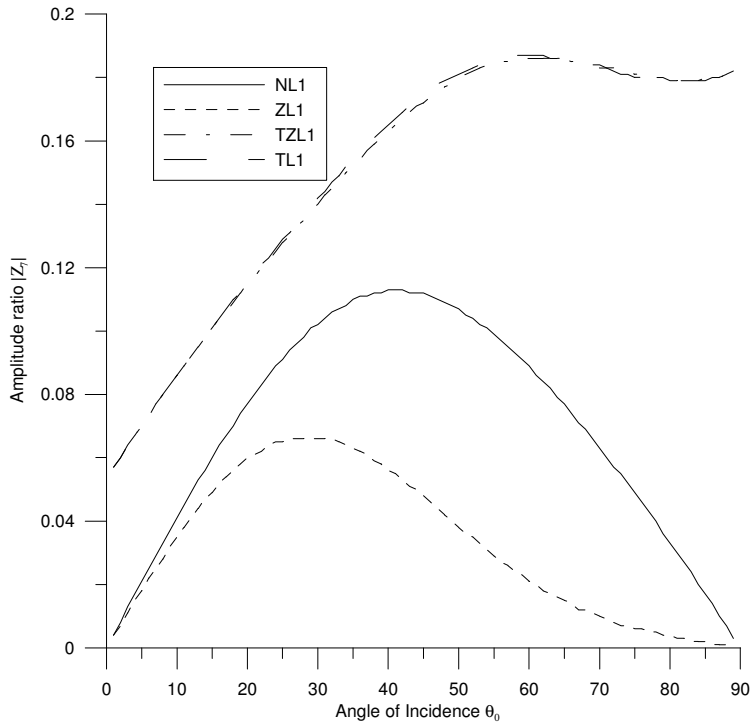


Figure 16. Variation of amplitude ratio with angle of incidence for T wave.

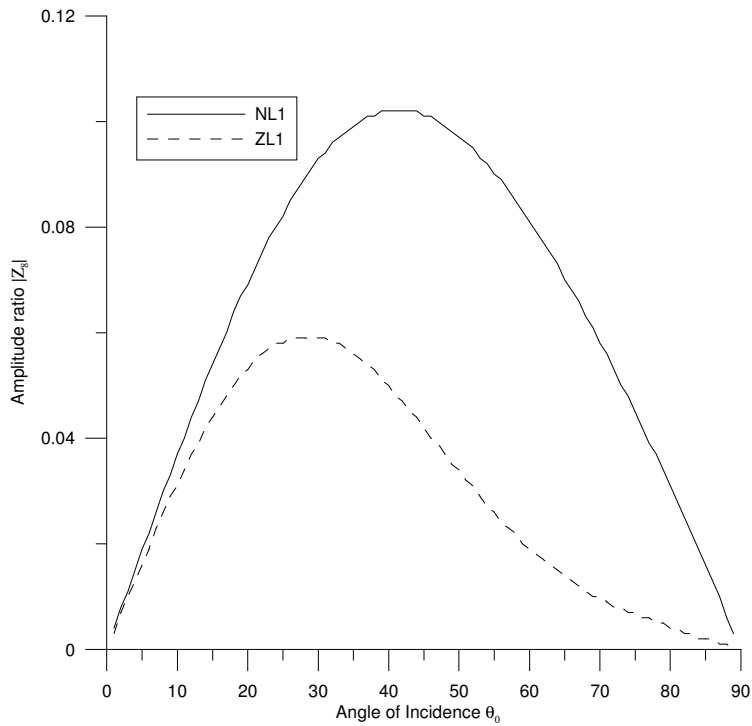


Figure 17. Variation of amplitude ratio with angle of incidence for T wave.

of $|Z_3|$ and $|Z_4|$ for NL1, ZL1, TZL1, and TL1 are oscillatory and the values for TL1 remain greater than the values for TZL1 in the whole range.

Figure 6 shows that the values of $|Z_5|$ for ZL1, TL1, and TZL1 increase in the whole range, except near the grazing incidence, where the values decrease sharply. Figure 7 shows that the values of $|Z_6|$ for NL1, ZL1, TL1, and TZL1 decrease in the whole range. The values of $|Z_6|$ for ZL1 and TL1 are magnified by a factor of 10 and for NL1 by 10^3 .

Notice from Figures 8 and 9 that the values of $|Z_7|$ and $|Z_8|$ for ZL1 remain greater than the values for NL1 in the whole range, except near the grazing incidence, where the values for NL1 are greater. The values of $|Z_7|$ for TZL1 and TL1 are magnified by a factor of 10.

7.2. Incident T wave. Variations of the amplitude ratios $|Z_i|$, $1 \leq i \leq 8$, with angle of incidence θ_0 , for incident T waves are shown in Figures 10–17.

Figure 10 shows that the values of $|Z_1|$ for ZL1 remain greater than the values for NL1 in the whole domain. The values of $|Z_1|$ for NL1, ZL1, TZL1, and TL1 are reduced by a factor of 10. It is evident from Figure 11 that the values of $|Z_2|$ for NL1 increase and those for ZL1, TZL1, and TL1 decrease in the whole range.

Figure 12 shows that the values of $|Z_3|$ for TL1 are greater than those for NL1, and the values for TZL1 are greater than those for ZL1, in the whole range. Figure 13 shows that the behavior of the variation of the amplitude ratio $|Z_4|$ is similar to that of $|Z_3|$ with a different magnitude. Figure 14 shows that the values of the amplitude ratio $|Z_5|$ for NL1 are greater than for ZL1, except in the range $0^\circ < \theta_0 < 33^\circ$, where the behavior is reversed.

Figure 15 shows that the values of $|Z_6|$ for NL1, ZL1, TZL1, and TL1 decrease in the whole range, while the values for TZL1 and TL1 follow an oscillatory pattern near the grazing incidence. The values of $|Z_6|$ for ZL1, TZL1, and TL1 and the values of $|Z_7|$ for TZL1 and TL1 are magnified by multiplying the original value by 10. It can be noticed from Figure 16 that values of $|Z_7|$ for NL1, ZL1, TZL1, and TL1 are oscillatory in the whole range. Figure 17 shows that the values of $|Z_8|$ for NL1 remain greater than the values for ZL1 in the whole range.

7.3. Incident CD-I wave. Variations of the amplitude ratios $|Z_i|$, $1 \leq i \leq 8$, with angle of incidence θ_0 , for incident CD-I waves are shown in Figures 18–25.

Figures 18 and 19 show that the values of the amplitude ratios $|Z_1|$ and $|Z_2|$ for NL1 and ZL1 oscillate, while the values for TZL1 and TL1 increase with increase in θ_0 . The values of $|Z_1|$ for TZL1 and NL1 remain greater than those for TL1 and ZL1, respectively, in the whole range. The values of $|Z_2|$ for NL1 are magnified by a factor of 10^2 .

Figures 20 and 21 show that the values of $|Z_3|$ and $|Z_4|$ for NL1 are greater than those for TL1, and the values for ZL1 are greater than those for TZL1, in the whole domain, which reveals the effect of micropolarity. Figures 22 and 23 show that the values of $|Z_5|$ and $|Z_6|$ for ZL1 remain greater than the values for NL1 in the whole range. The values of $|Z_6|$ for NL1 are magnified by a factor of 10^4 and for TL1 and TZL1 by a factor of 10.

It is shown in Figures 24 and 25 that the values of $|Z_7|$ and $|Z_8|$ for NL1 and ZL1 decrease in the whole range, except near $\theta_0 = 90^\circ$, where the values increase. The values of $|Z_7|$ for TL1 and TZL1 are magnified by a factor of 10^2 .

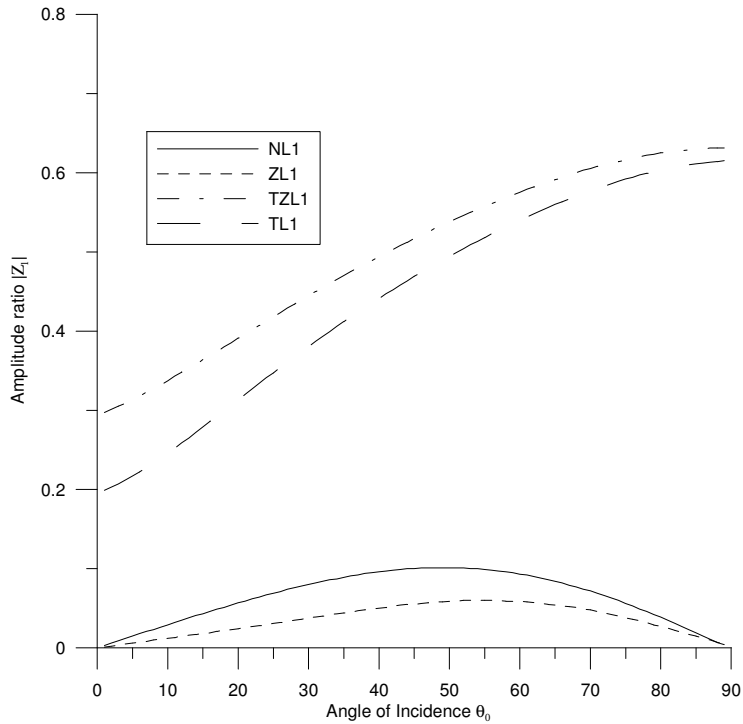


Figure 18. Variation of amplitude ratio with angle of incidence for CD-I wave.

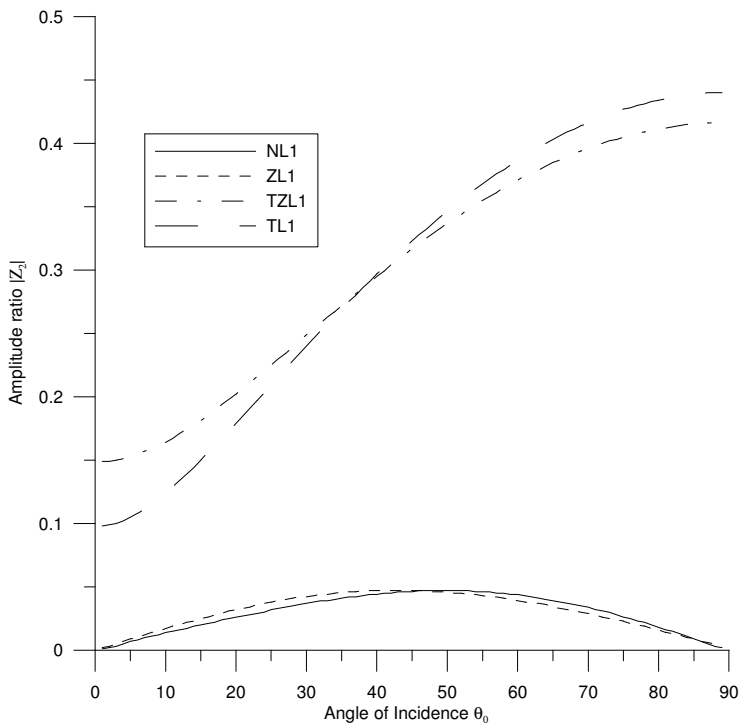


Figure 19. Variation of amplitude ratio with angle of incidence for CD-I wave.

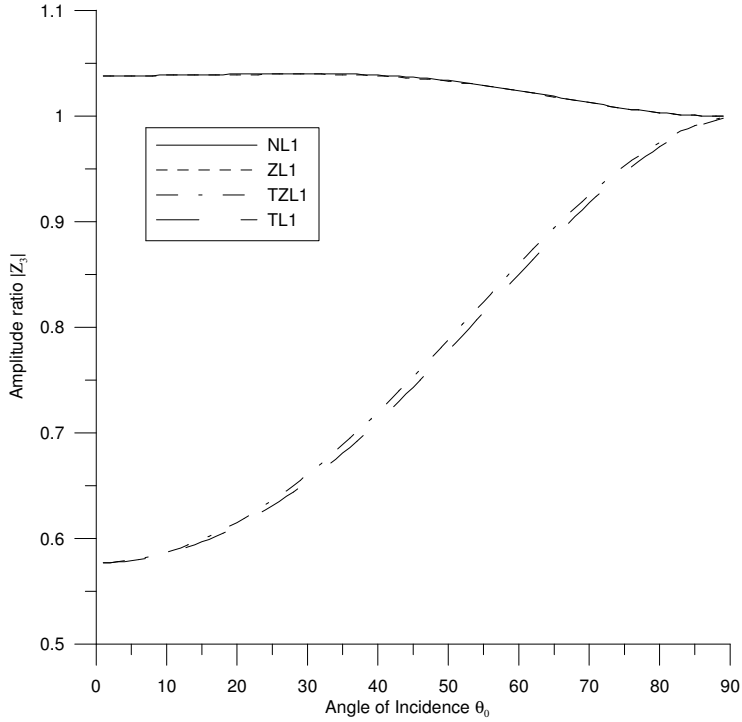


Figure 20. Variation of amplitude ratio with angle of incidence for CD-I wave.

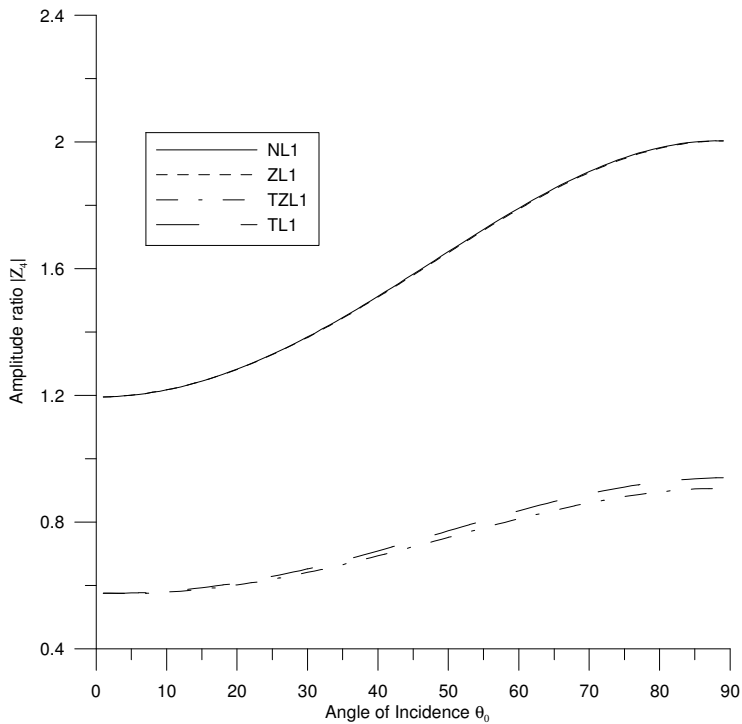


Figure 21. Variation of amplitude ratio with angle of incidence for CD-I wave.

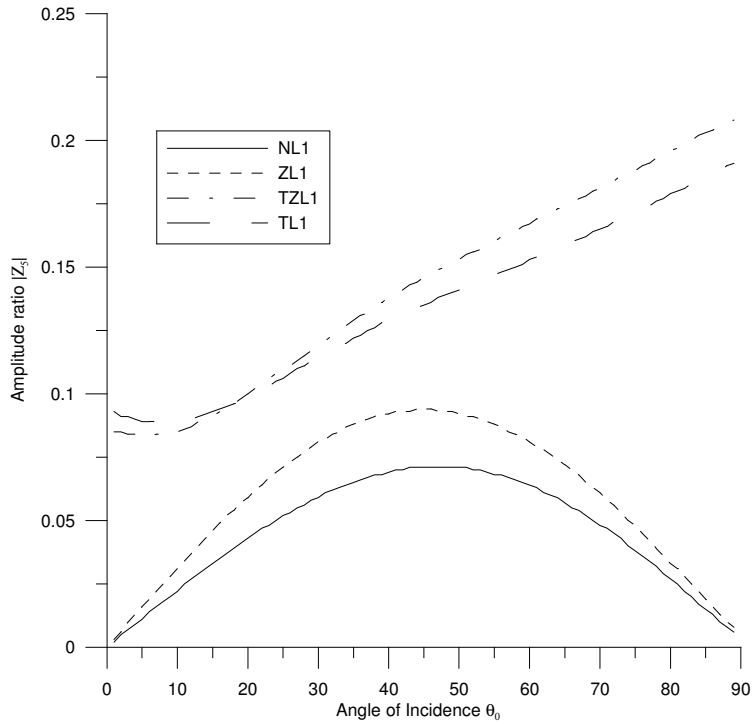


Figure 22. Variation of amplitude ratio with angle of incidence for CD-I wave.

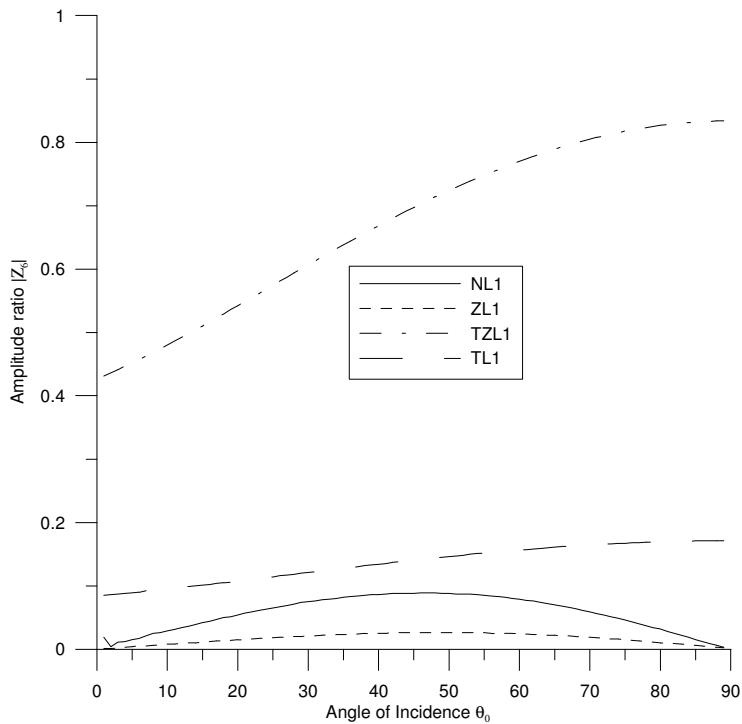


Figure 23. Variation of amplitude ratio with angle of incidence for CD-I wave.

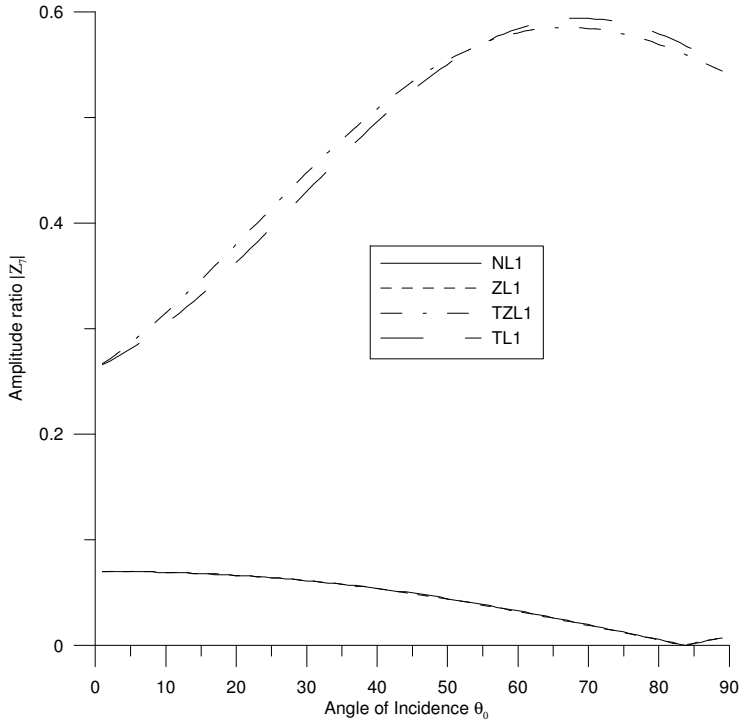


Figure 24. Variation of amplitude ratio with angle of incidence for CD-I wave.

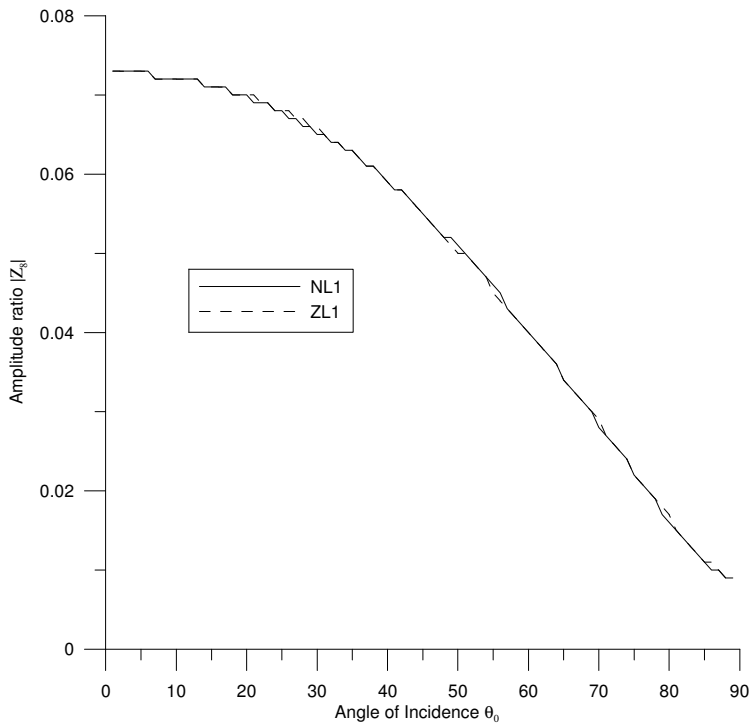


Figure 25. Variation of amplitude ratio with angle of incidence for CD-I wave.

8. Conclusion

The expressions for the reflection and transmission coefficients of various reflected and transmitted waves have been derived. When an LD wave is incident, the values of the amplitude ratios for NL1 and ZL1 follow an oscillatory pattern and the magnitudes of the amplitude ratios $|Z_i|$, $1 \leq i \leq 8$, for TL1 remain greater than the values for TZL1. When a T wave is incident, the values of $|Z_i|$; $i = 3, 4, 7, 8$ for NL1 remain more than the values for TL1 that reveals the effect of two temperatures. When a CD-I wave is incident the values of the amplitude ratios $|Z_1|$, $|Z_2|$, $|Z_5|$, $|Z_6|$, and $|Z_7|$ for TZL1 and TL1 remain greater than the values for ZL1 and NL1, respectively, due to the effect of micropolarity.

References

- [Boley and Tolins 1962] B. A. Boley and I. S. Tolins, “Transient coupled thermoelastic boundary value problems in the half-space”, *J. Appl. Mech.* **29**:4 (1962), 637–646.
- [Boschi and Ieşan 1973] E. Boschi and D. Ieşan, “A generalized theory of linear micropolar thermoelasticity”, *Meccanica (Milano)* **8**:3 (1973), 154–157.
- [Chandrasekharaiah 1986] D. S. Chandrasekharaiah, “Heat-flux dependent micropolar thermoelasticity”, *Int. J. Eng. Sci.* **24**:8 (1986), 1389–1395.
- [Chen and Williams 1968] P. J. Chen and W. O. Williams, “A note on non-simple heat conduction”, *Z. Angew. Math. Phys.* **19**:6 (1968), 969–970.
- [Chen et al. 1969] P. J. Chen, M. E. Gurtin, and W. O. Williams, “On the thermodynamics of non-simple elastic materials with two temperatures”, *Z. Angew. Math. Phys.* **20**:1 (1969), 107–112.
- [Dost and Tabarrok 1978] S. Dost and B. Tabarrok, “Generalized micropolar thermoelasticity”, *Int. J. Eng. Sci.* **16**:3 (1978), 173–183.
- [El-Karamany 2011] A. S. El-Karamany, “Two-temperature theory in linear micropolar thermoviscoelastic anisotropic solid”, *J. Therm. Stresses* **34**:9 (2011), 985–1000.
- [El-Karamany and Ezzat 2011] A. S. El-Karamany and M. A. Ezzat, “On the two-temperature Green–Naghdi thermoelasticity theories”, *J. Therm. Stresses* **34**:12 (2011), 1207–1226.
- [Eringen 1966] A. C. Eringen, “Linear theory of micropolar elasticity”, *J. Math. Mech.* **15**:6 (1966), 909–923.
- [Eringen 1970] A. C. Eringen, *Foundations of micropolar thermoelasticity* (Udine, 1970), CISM Courses and Lectures Series **23**, Springer, Vienna, 1970.
- [Eringen 1984] A. C. Eringen, “Plane waves in nonlocal micropolar elasticity”, *Int. J. Eng. Sci.* **22**:8–10 (1984), 1113–1121.
- [Eringen 1999] A. C. Eringen, *Microcontinuum field theories, I: Foundations and solids*, Springer, Berlin, 1999.
- [Ezzat and Awad 2010] M. A. Ezzat and E. S. Awad, “Constitutive relations, uniqueness of solution, and thermal shock application in the linear theory of micropolar generalized thermoelasticity involving two temperatures”, *J. Therm. Stresses* **33**:3 (2010), 226–250.
- [Gauthier 1982] R. D. Gauthier, “Experimental investigations on micropolar media”, Chapter 7, pp. 395–463 in *Mechanics of micropolar media*, edited by O. Brulin and R. K. T. Hsieh, World Scientific, Singapore, 1982.
- [Hsia and Cheng 2006] S.-Y. Hsia and J.-W. Cheng, “Longitudinal plane wave propagation in elastic-micropolar porous media”, *Jpn. J. Appl. Phys.* **45** (2006), 1743–1748.
- [Hsia et al. 2007] S.-Y. Hsia, S.-M. Chiu, C.-C. Su, and T.-H. Chen, “Propagation of transverse waves in elastic-micropolar porous semispaces”, *Jpn. J. Appl. Phys.* **46** (2007), 7399–7405.
- [Kaushal et al. 2010] S. Kaushal, N. Sharma, and R. Kumar, “Propagation of waves in generalized thermoelastic continua with two temperature”, *Int. J. Appl. Mech. Eng.* **15**:4 (2010), 1111–1127.
- [Kaushal et al. 2011] S. Kaushal, R. Kumar, and A. Miglani, “Wave propagation in temperature rate dependent thermoelasticity with two temperatures”, *Math. Sci. Quart. J.* **5**:2 (2011), 125–146.
- [Kumar and Barak 2007] R. Kumar and M. Barak, “Wave propagation in liquid-saturated porous solid with micropolar elastic skelton at boundary surface”, *Appl. Math. Mech. (English Ed.)* **28**:3 (2007), 337–349.

- [Kumar and Mukhopadhyay 2010] R. Kumar and S. Mukhopadhyay, “Effects of thermal relaxation time on plane wave propagation under two-temperature thermoelasticity”, *Int. J. Eng. Sci.* **48**:2 (2010), 128–139.
- [Kumar et al. 2008a] R. Kumar, N. Sharma, and P. Ram, “Interfacial imperfection on reflection and transmission of plane waves in anisotropic micropolar media”, *Theor. Appl. Fract. Mec.* **49**:3 (2008), 305–312.
- [Kumar et al. 2008b] R. Kumar, N. Sharma, and P. Ram, “Reflection and transmission of micropolar elastic waves at an imperfect boundary”, *Multidiscip. Model. Mater. Struct.* **4**:1 (2008), 15–36.
- [Magaña and Quintanilla 2009] A. Magaña and R. Quintanilla, “Uniqueness and growth of solutions in two-temperature generalized thermoelastic theories”, *Math. Mech. Solids* **14**:7 (2009), 622–634.
- [Mukhopadhyay and Kumar 2009] S. Mukhopadhyay and R. Kumar, “Thermoelastic interactions on two-temperature generalized thermoelasticity in an infinite medium with a cylindrical cavity”, *J. Therm. Stresses* **32**:4 (2009), 341–360.
- [Nowacki 1981] W. Nowacki, *Teoria niesymetrycznej sprężystości*, Państwowe Wydawnictwo Naukowe, Warsaw, 1981. In Polish; translated as *Theory of asymmetric elasticity*, Pergamon, Oxford, 1986.
- [Puri and Jordan 2006] P. Puri and P. M. Jordan, “On the propagation of harmonic plane waves under the two-temperature theory”, *Int. J. Eng. Sci.* **44**:17 (2006), 1113–1126.
- [Singh and Kumar 1998] B. Singh and R. Kumar, “Reflection of plane waves from the flat boundary of a micropolar generalized thermoelastic half-space”, *Int. J. Eng. Sci.* **36**:7–8 (1998), 865–890.
- [Tauchert et al. 1968] T. R. Tauchert, W. D. Claus, Jr., and T. Ariman, “The linear theory of micropolar thermoelasticity”, *Int. J. Eng. Sci.* **6**:1 (1968), 37–47.
- [Tomar and Gogna 1992] S. K. Tomar and M. L. Gogna, “Reflection and refraction of a longitudinal microrotational wave at an interface between two micropolar elastic solids in welded contact”, *Int. J. Eng. Sci.* **30**:11 (1992), 1637–1646.
- [Tomar and Gogna 1995a] S. K. Tomar and M. L. Gogna, “Reflection and refraction of coupled transverse and micro-rotational waves at an interface between two different micropolar elastic media in welded contact”, *Int. J. Eng. Sci.* **33**:4 (1995), 485–496.
- [Tomar and Gogna 1995b] S. K. Tomar and M. L. Gogna, “Reflection and refraction of longitudinal wave at an interface between two micropolar elastic solids in welded contact”, *J. Acoust. Soc. Am.* **97**:2 (1995), 822–830.
- [Warren and Chen 1973] W. E. Warren and P. J. Chen, “Wave propagation in the two temperature theory of thermoelasticity”, *Acta Mech.* **16**:1–2 (1973), 21–33.
- [Youssef 2006] H. M. Youssef, “Theory of two-temperature-generalized thermoelasticity”, *IMA J. Appl. Math.* **71**:3 (2006), 383–390.
- [Youssef and Al-Harby 2007] H. M. Youssef and A. H. Al-Harby, “State-space approach of two-temperature generalized thermoelasticity of infinite body with a spherical cavity subjected to different types of thermal loading”, *Arch. Appl. Mech.* **77**:9 (2007), 675–687.
- [Youssef and Al-Lehaibi 2007] H. M. Youssef and E. A. Al-Lehaibi, “State-space approach of two-temperature generalized thermoelasticity of one-dimensional problem”, *Int. J. Solids Struct.* **44**:5 (2007), 1550–1562.

Received 14 May 2013. Accepted 26 Dec 2013.

RAJNEESH KUMAR: rajneesh_kuk@rediffmail.com

Department of Mathematics, Kurukshetra University, Kurukshetra, Haryana 136119, India

MANDEEP KAUR: mandeep1125@yahoo.com

Department of Applied Sciences, Guru Nanak Dev Engineering College, Ludhiana, Punjab 141008, India

SATISH C. RAJVANSHI: satishrajvanshi@yahoo.com

Department of Applied Sciences, Gurukul Vidyapeeth, Institute of Engineering and Technology, Sector-7, Banur, District Patiala, Punjab 140601, India

DYNAMIC COMPRESSION OF SQUARE TUBE CELLULAR STRUCTURES

RYAN L. HOLLOMAN, KARTHIKEYAN KANDAN,
VIKRAM DESHPANDE AND HAYDN N. G. WADLEY

Aluminum cellular structures have been fabricated by combining a two-dimensional $[0^\circ/90^\circ]_2$ arrangement of square Al 6061-T6 alloy tubes with orthogonal tubes inserted in the out-of-plane direction. By varying the tube wall thickness, the resulting three-dimensional cellular structures had relative densities between 11 and 43%. The dynamic compressive response of the three-dimensional cellular structure, and the two-dimensional $[0^\circ/90^\circ]_2$ array and out-of-plane tubes from which they were constructed, have been investigated using a combination of instrumented Kolsky bar impact experiments, high-speed video imaging, and finite element analysis. We find the compression rate has no effect upon the strength for compression strain rates up to 2000 s^{-1} , despite a transition to higher-order buckling modes at high strain rates. The study confirms that a synergistic interaction between the colinear aligned and out-of-plane tubes, observed during quasistatic loading, extends to the dynamic regime. Finite element simulations, using a rate-dependent, piecewise linear strain hardening model with a von Mises yield surface and an equivalent plastic strain failure criterion, successfully predicted the buckling response of the structures, and confirmed the absence of strain-rate hardening in the three-dimensional cellular structure. The simulations also reveal that the ratio of the impact to back-face stress increased with strain rate and relative density, a result with significant implications for shock-load mitigation applications of these structures.

1. Introduction

Light sandwich-panel structures are widely used in stiffness-governed design, where large bending stresses must be supported with minimum elastic deflection [Allen 1969]. Since the flexural modulus of a sandwich panel increases with the square of its core thickness, the primary purpose of the core is to maintain separation of the face sheets at minimum mass [Vinson 1999]. By combining carbon fiber-reinforced polymer composite face sheets with lightweight Nomex and other polymeric cores, very high-flexural modulus structures have been developed for a variety of applications [Shahdin et al. 2009]. Advances in fabrication methods have led to the emergence of sandwich panels whose faces and cellular cores are made from high-strength metallic alloys based upon aluminum [Kooistra et al. 2004; Queheillalt et al. 2008], stainless steels [Ferri et al. 2006; Radford et al. 2007], and titanium [Queheillalt et al. 2000; Elzey and Wadley 2001; Moongkhamklang and Wadley 2010]. These sandwich structures also have high flexural strengths and moduli, and offer significant advantages over monolithic plates of equivalent mass in a variety of dynamic loading scenarios [Xue and Hutchinson 2004; Deshpande and Fleck 2005; Dharmasena et al. 2009; 2013; Wadley et al. 2013].

The benefits of metallic sandwich structures during localized impulsive loading arise from their high flexural strength and significant plastic strain energy dissipation. Some of the incident kinetic energy

Keywords: cellular structures, 6061 aluminum, impact testing, dynamic loads, material rate-dependence.

is stored as the plastic work of core compression, but for edge-clamped panels, a substantial fraction is also dissipated by plastic stretching of the core and face sheets [Zok et al. 2004]. Numerous cellular core topologies have been investigated for dynamic loading applications, including honeycombs with in-plane stretch-resistant square [Wadley et al. 2007] or triangular [Wei et al. 2008; Dharmasena et al. 2011] cells, as well as more-compressible prismatic topologies based upon corrugations (with stretch resistance in only one direction) [Rimoli et al. 2011]. Concepts such as flex honeycomb [Bitzer 1997, pp. 1–9] or lattice truss cores [Kooistra et al. 2008] have been proposed for curved sandwich panels, but these cores are significantly less stretch resistant.

The sandwich-panel approach is not widely used to mitigate automobile impacts. Instead this community has focused on crash box (tube) designs that absorb the kinetic energy during frontal vehicle impact [Hanssen et al. 2000b; 2001], and reduce force transmission to levels that remain below the injury threshold for vehicle occupants. An ideal crash box design provides close to theoretical plastic energy absorption at predictable (constant) force through progressive buckling and plastic deformation of the box/tube structure. However, the crush response of tubes is highly impact orientation-dependent [Abramowicz and Jones 1997; Pingle et al. 2011]. More-isotropic aluminum foams [Reyes 2008] and foam-filled tubes [Reid 1993; Baumeister et al. 1997; Hanssen et al. 2000a] have therefore received attention for these structural impact problems. These foam-based structures are highly compressible, and can undergo compression at nearly constant (plateau) stress to plastic strains of 60% or more, making them efficient impact energy absorbers. However, they possess little (or none) of the in-plane stretch resistance that is utilized in sandwich panel-based mitigation approaches.

The compressive stress versus strain response of cellular structures is frequently found to depend upon the rate of straining [Dannemann and Lankford 2000; Deshpande and Fleck 2000]. This can arise from material strain-rate hardening [Wadley et al. 2003], changes in the deformation modes of the cells [Maiti et al. 1984] and from inertial effects [Calladine and English 1984]. To eventually design a structure whose energy absorption and stress transfer are insensitive to the rate or direction of compression, it is necessary to understand the significance of each of these factors to the overall response. The objective of the study reported here is to investigate the dynamic crushing of a cellular structure made from a three-dimensional arrangement of square cross section, extruded tubes of a heat-treatable 6061 aluminum alloy, shown in Figure 1(a), that exhibits negligible strain-rate hardening. The structure contains $[0^\circ/90^\circ]_2$ oriented in-plane tubes that provide in-plane stretch resistance, while the through-thickness tubes resist compression in analogous fashion to that of a crash box design.

A recent study of the quasistatic compressive response of three-dimensional tube structures [Holloman et al. 2013] revealed a synergistic interaction between the in and out-of-plane tubes that enhanced the energy dissipated by the structure's component tubes. The compressive energy absorption was comparable to that of axially loaded tubes, but had superior stretch resistance [loc. cit.], and a more omnidirectional crush response than a collinear tube array. The study also showed that by using different wall thicknesses for the in-plane and through-thickness tubes, it was possible to independently control the in-plane stretch resistance and the through-thickness crush strength. The large nodal contact areas also improved load transfer within the core, and between the core and face sheets. The topology also afforded multifunctionality [Evans et al. 2001] such as cross-flow heat exchange via the open channels that extend within the structure [Tian et al. 2007]. The study described here investigates the dynamic out-of-plane compressive response of the same structures. The dynamic crushing resistance and collapse mode mechanisms are

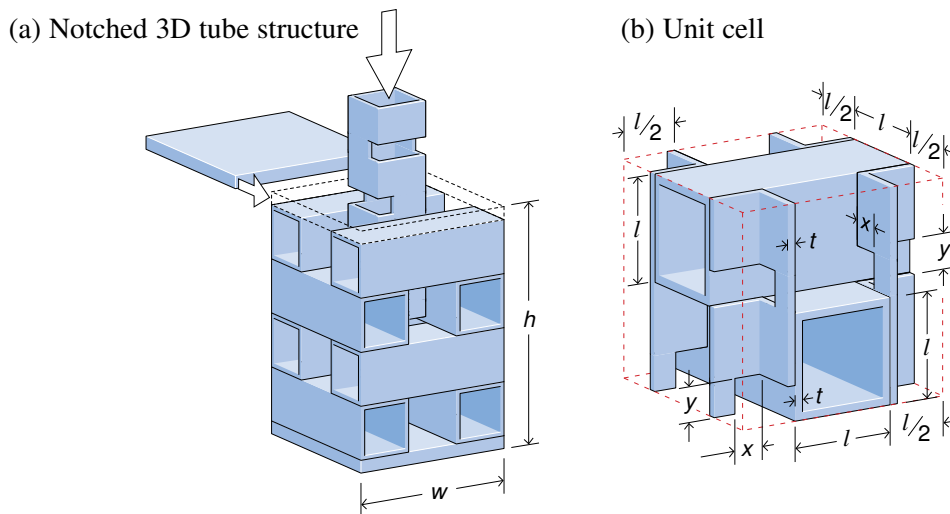


Figure 1. (a) A three-dimensional tube structure with the vertical tube notched to facilitate dip braze bonding. (b) The unit cell of the three-dimensional structure with the notch geometry incorporated. For all experiments reported here, $x = y = 6.35$ mm.

explored via direct-impact Kolsky bar experiments that utilize high-speed photography. Finite-element analysis is also used to investigate the dynamic deformation modes, and to estimate the stresses at the impact and distal faces of the structures.

2. Experimental protocols

2.1. Test structures. A two-dimensional structure was first assembled by laying down a colinear layer of 6061 aluminum alloy square tubes, each spaced a tube width apart. A second, similarly spaced, layer was then orthogonally placed on the first, and the assembly sequence repeated to create a $[0^\circ/90^\circ]_2$ structure. The three-dimensional topology, shown in [Figure 1\(a\)](#), was then assembled from the two-dimensional structure by inserting additional tubes in the out-of-plane (vertical) void space between the cross-ply oriented tubes. The out-of-plane tube was notched, as shown in [Figure 1\(a\)](#), to facilitate complete fluid penetration during subsequent dip brazing bonding and heat treatment [[Holloman et al. 2013](#)]. Since the notches affect the buckling response, additional three-dimensional samples were fabricated using regular out-of-plane tubes without notches. Samples consisting of just the regular and notched vertical tubes (called one-dimensional structures here) were also fabricated and tested. Following the dip brazing process, all the structures were slow-aged at room temperature for 96 hours to the T4 condition and then peak hardened (to the T6 condition) by heating to 163°C for 18 hours, followed by water quenching. [Figure 1\(a\)](#) shows that when the cellular tube structures are bonded to 4.76 mm thick face sheets, they have a large core-to-face-sheet interfacial area with potentially beneficial consequences for the robustness of intensely loaded panels. The structure's relative density, $\bar{\rho}$, given by the ratio of the volume occupied by metal to that of a unit cell — see [Figure 1\(b\)](#) — was calculated for each sample. A summary of the geometries and relative densities of the samples investigated is presented in [Table 1](#).

Topology	Sample core		In-plane		Out-of-plane		$\bar{\rho}$
	w (mm)	h (mm)	t (mm)*	l (mm)*	t (mm)*	l (mm)*	
1D	19.1	76.2	–	–	1.52	19.1	6.7**
2D	57.2	76.2	1.70	19.1	–	–	16.3
3D	57.2	76.2	1.45	19.1	1.45	19.1	20.1
3D	34.4	55.4	0.74	11.5	0.74	11.5	11.6
3D	57.2	76.2	3.47	19.1	3.47	19.1	42.7
1D unnotched	19.1	76.2	–	–	1.52	19.1	7.3**
3D unnotched	57.2	76.2	1.44	19.1	1.44	19.1	21.0

* Variability in the tube wall thickness resulted in reporting a mean value per sample with a standard deviation in tube wall thickness of ± 0.14 mm.

** Corresponds to relative density contribution to the three-dimensional structure.

Table 1. Tube core geometries (sample core widths and heights, w and h , and mean tube wall thicknesses, t , and tube widths, l) and relative densities ($\bar{\rho}$).

Tensile tests were previously performed on the tube wall alloy in postbrazed and peak-hardened condition [Holloman et al. 2013]. The experimental curve (measured at 25° C with a strain rate of 10^{-4} s^{-1}) is shown in Figure 2, and is later used to deduce the coefficients for a constitutive model for numerical simulation of the tube structures.

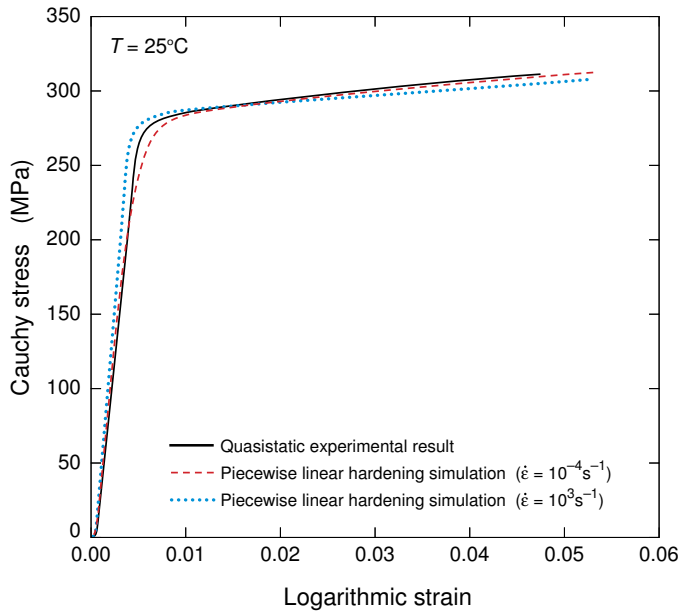


Figure 2. Measured tensile stress-strain relation for a sample of the 6061-T6 alloy extracted from a tube structure. The predicted responses of the constitutive model for strain rates of 10^{-4} and 10^3 s^{-1} are also shown.

2.2. Dynamic testing. The dynamic out-of-plane compressive response of the core structures was measured from a series of direct-impact Kolsky bar tests, where the force was measured on the sample's back face with a strain-gauged Kolsky [1949] bar while synchronously recording the strain with a high-speed video camera; see Figure 3. Each specimen was attached to the end of a stationary 2 m long, 7.62 cm diameter Kolsky bar using Loctite Super Glue. A striker projectile was accelerated with a gas gun towards the front face of the specimen, and the force transmitted by the sample was measured by diametrically opposed strain gauges placed 0.76 m from the impact end of the Kolsky bar. The striker diameter was equal to both the inner diameter of the gas gun barrel and the diameter of the Kolsky bar. The gas gun barrel measured 4.50 m in length; to achieve an impact velocity, v_0 , of less than or equal to 75 ms^{-1} , the projectile was positioned 3.2 m from the exit of the barrel. Higher velocities were achieved by placing the striker projectile 3.8 m from the gun barrel exit. All initial velocities were measured near the barrel exit using two sets of laser velocity gates as shown in Figure 3. That figure also defines all other relevant geometrical parameters of the test setup. The Kolsky bar was made from aluminum alloy 6082-T6, with yield strength 310 MPa and measured longitudinal elastic wave speed $c = 5108 \text{ ms}^{-1}$. A time window of $485.5 \mu\text{s}$ was therefore available for measurements before elastic reflections from the distal end of the Kolsky bar complicated interpretation.

The precision of the measurements was derived from multiple calibration tests. An example of one of the results is shown in Figure 4(a). The aluminum Kolsky bar was impacted by an aluminum projectile that had a diameter of 7.6 cm, a length of 54.0 cm, and a mass of 6124 g. In this example, it impacted the Kolsky bar with an initial (preimpact) velocity $v_0 = 7.3 \text{ ms}^{-1}$. Figure 4(a) sets time $t = 0$ as the first arrival of the stress pulse at the strain gauges, and shows that the rise time of the stress pulse at the gauge location was $35 \mu\text{s}$ for the bar/strain gauge system used here. This rise-time limitation only became significant at the highest impact velocities, where substantial specimen compression could occur within the first $5 \mu\text{s}$ after impact.

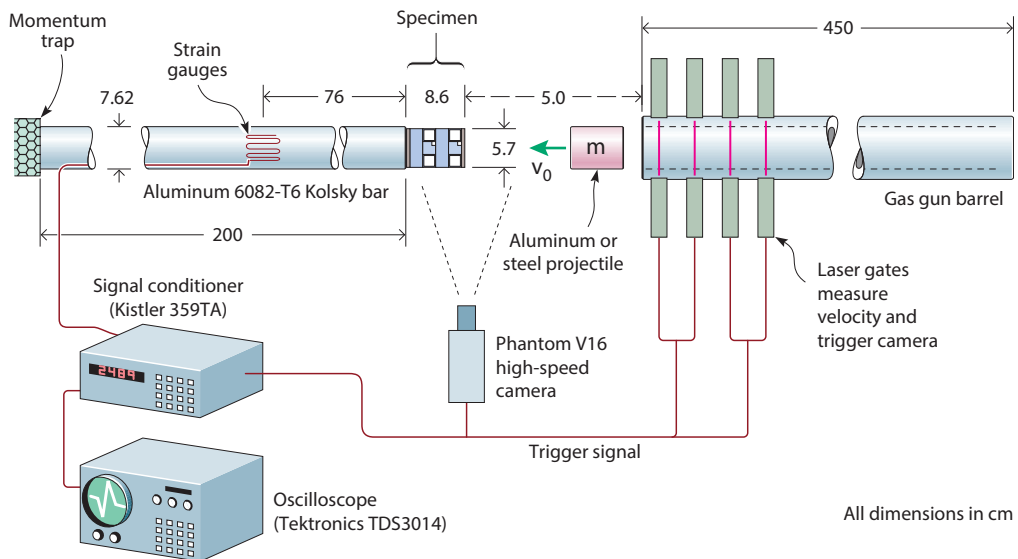


Figure 3. Schematic diagram of the Kolsky bar arrangement used for dynamic testing.

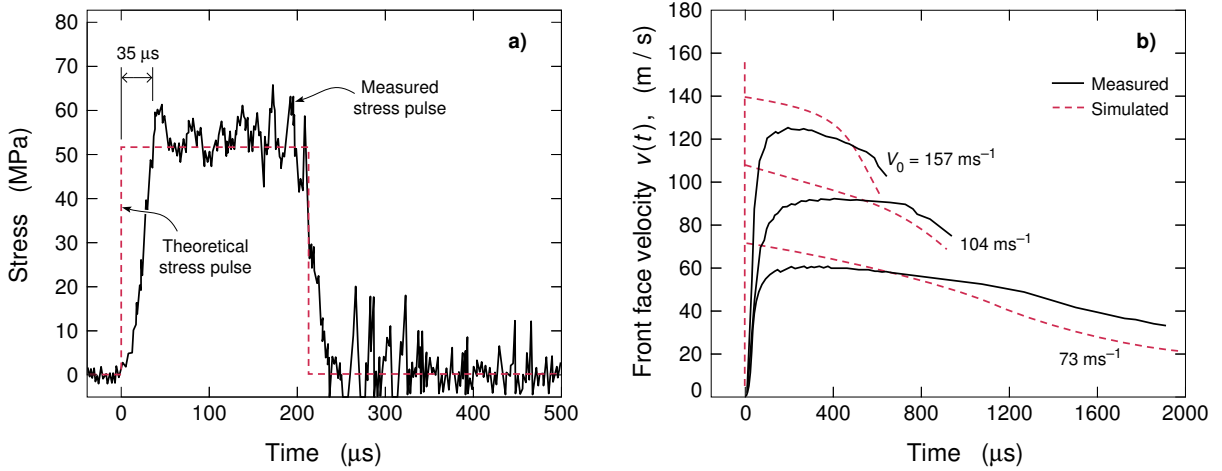


Figure 4. (a) Transmitted stress versus time history of the aluminum Kolsky bar following impact by a 54.0 cm long, 7.6 cm diameter aluminum striker with a mass of 6.124 kg and velocity $v_0 = 7.3 \text{ ms}^{-1}$. The axial stress in the aluminum Kolsky bar (predicted by one-dimensional elastic wave theory) was 51.3 MPa (the dashed curve). (b) The measured front-face velocity for a three-dimensional tube structure with $\bar{\rho} = 20.1\%$. Simulated data is also shown.

Elastic wave theory [Johnson 1972] gives the axial stress transferred to the aluminum Kolsky bar in this test as $\rho c v_0 / 2 = 51.3 \text{ MPa}$, where $\rho = 2755 \text{ kg}\cdot\text{m}^{-3}$ is the density and $c = 5108 \text{ ms}^{-1}$ is the extensional wave speed of the aluminum Kolsky bar. The predicted axial stress pulse—the red dotted curve in Figure 4(a)—is within 16% of the first stress measured peak (61.2 MPa), and is reasonably close to the average measured stress. The measured calibration test stress drops to zero at $t = 236 \mu\text{s}$, which corresponds to the arrival of the elastic stress pulse reflected from the free end of the striker.

Russell et al. [2010] have shown that the striker projectile kinetic energy governs the compressive strain of the crushable sample and the transient velocity imposed upon the impacted end of the specimen. For the samples tested here, impact experiments were performed at nominal impact velocities of 75, 100, and 150 ms^{-1} . A steel striker of mass $M = 2.5 \text{ kg}$ was used for impact velocities v_0 of 75 and 100 ms^{-1} . It imparted sufficient momentum to crush most of the samples beyond their densification strain. An aluminum striker of mass $M = 0.75 \text{ kg}$ was used for tests at impact velocity $v_0 \geq 150 \text{ ms}^{-1}$. High-speed video images of the samples were recorded using a Phantom V12 high-speed camera to measure the compression rate, to identify failure modes and to confirm that the striker kinetic energy was sufficient to provide a constant-velocity sample compression up to a nominal strain of at least 50%. Figure 4(b) shows a typical impact face velocity result for a three-dimensional structure with $\bar{\rho} = 20.1\%$; the front-face velocity rose quickly upon striker impact to a peak crushing velocity and then fell slowly during continued crushing. The actual crush velocity was always slightly less than that of the striker just prior to impact, and remained relatively constant during crushing to the densification strain. As the relative density was increased to $\bar{\rho} = 42.7\%$, constant velocity compression ceased at core compressions of 20% and the samples were not completely crushed even with the more-massive striker. In the results to follow, we designate each test by the incident impact velocity, v_0 , of the striker.

3. Finite element analysis protocols

Finite element (FE) techniques have been used to study the dynamic compression of one-, two-, and three-dimensional tubes. The aims of this aspect of the investigation were to

- (i) validate the analysis method by comparing the predicted and measured dynamic crush resistance of the tube structures,
- (ii) investigate the dynamic collapse mechanisms responsible for the mechanical responses of the cellular tube structures,
- (iii) determine the stresses imposed on the front (not experimentally measured), and
- (iv) rationalize the absence of strain rate strengthening of the structure.

3.1. The FE model. All the tests were analyzed using finite element simulations conducted using the explicit version of the commercial, nonlinear finite element package IMPETUS Afea Solver® [Hanssen and Olovsson 2013]. The geometry and relative density of the modeled tube specimens were designed to be the same as those of the measured specimens, reported in Table 1, but following the usual practice [Zok et al. 2005; Radford et al. 2007; Fyllingen et al. 2010], small imperfections (described below) were incorporated in the models to account for manufacturing defects, such as tube misalignment and tube wall thickness variability, seen in the tested specimens. The modeled sandwich structure geometry was merged with a modeled Kolsky bar of the same dimensions and with strain gauge placement as shown in Figure 3. The Kolsky bar model included a cylindrical gridded region, at the same location as the experimental strain gauges, where the axial displacements and forces could be inferred.

The FE models were constructed using cubic hexahedral elements. The meshing specifics are summarized in Table 2. A mesh sensitivity study indicated that an in-plane nodal spacing approximately equal to the tube wall thickness (t) was sufficient to provide converged solutions for impacts with tube core structures. One cubic hexahedral element was therefore used through the thickness of each tube wall. The nodes of the adjacent tubes were merged prior to the simulation, thus representing a perfect braze zone with no interface failure criterion [Holloman et al. 2013]. The contact formulation in the software is based on a penalty formulation. Simulations with uniform-wall-thickness models resulted in higher strengths than observed experimentally, and so imperfections to the geometries were introduced to trip buckling and better predict the stress-strain curves. The imperfections were modeled as a displacement of the lowest-order measured eigenmode to each tube wall. For most modeled structures the first-order eigenmode amplitude was set at 0.1 times the tube wall thickness; however, the unnotched tube structure required a larger amplitude imperfection (0.3 the tube wall thickness) to match the experiments.

All the simulations introduced a cylindrical projectile with the same dimensions and mass as the experimental projectile. An initial velocity (v_0) was applied to the simulated projectile that matched the measured projectile velocity recorded by the laser gates in the experiment. Conservation of momentum during the inelastic collision between the projectile and the specimen resulted in a decrease in projectile velocity, as shown in Figure 4(b).

3.2. Material properties. The experimentally recovered Cauchy stress-true strain response of the Al 6061-T6 alloy during uniaxial tensile testing is presented in Figure 2. The uniaxial Cauchy stress, σ ,

Topology	$\bar{\rho}$	Hexahedral elements		
		Cubic	Linear	Nodes
1D	6.7	2,176	–	88,958
2D	16.3	5,440	–	297,854
3D	20.1	7,264	–	403,838
3D	11.6	5,356	1,936	345,958
3D	42.7	4,592	–	253,294
1D, unnotched	7.3	450	–	28,192
3D, unnotched	21.0	2,240	450	205,376

Table 2. Tube geometries and velocity-time function values used during FE simulations.

versus true strain, ε , relation for an elastic-plastic material under uniaxial straining can be written

$$\varepsilon = \varepsilon_e + \varepsilon_p = \frac{\sigma}{E} + \varepsilon_p, \tag{1}$$

where ε_e and ε_p are the elastic and plastic components of the strain, respectively, and E is the Young’s modulus. Having performed the uniaxial tensile test, the true stress versus plastic strain curve was tabulated and used to determine an isotropic strain hardening relation needed for FE simulations. The transition from elastic to plastic behavior was set at a Cauchy stress of 230.7 MPa. This hardening tabulation was implemented in the IMPETUS Afea Solver using the general piecewise linear hardening constitutive model with optional thermal softening and strain-rate hardening. The yield stress of this model is defined in the form

$$\sigma_y = f(\varepsilon_{\text{eff}}) \left(1 - \left(\frac{T - T_0}{T_m - T_0} \right)^m \right) \left(1 + \frac{\dot{\varepsilon}_{\text{eff}}}{\dot{\varepsilon}_0} \right)^c, \tag{2}$$

where $f(\varepsilon_{\text{eff}})$ is the piecewise-linear hardening function of the effective deviatoric strain, which was obtained from the hardening curve behavior. The thermal softening component was defined by the current temperature, T , the reference temperature, T_0 , the melting temperature, T_m , and the thermal softening parameter, m . The strain-rate hardening component of (2) was defined by a reference strain rate, $\dot{\varepsilon}_0$, and a strain-rate hardening parameter, c . The coefficients used in conjunction with (2) to model the material are given in Table 3. The thermal softening and strain-rate hardening components made a negligible contribution to the yield stress. The yield strength was primarily defined by the piecewise linear hardening function $f(\varepsilon_{\text{eff}})$ modeled using a von Mises yield criterion with isotropic hardening. Using the material model described above, a uniaxial tensile test was simulated at room temperature for the measured strain rate and compared well to the measured Cauchy stress-logarithmic strain curve (Figure 2). The response at a strain rate of 10^3 s^{-1} is also shown, and confirms the modest strain-rate dependence of the alloy.

To account for softening created by tube wall fracture on the tensile side of severely buckled tubes, the Cockcroft–Latham failure criterion [Cockcroft and Latham 1968] was implemented for all the dynamic compression simulations. Failure was defined to occur when a damage parameter, D , reached unity. The damage parameter was calculated as

$$D = \frac{1}{W_c} \int_0^{\varepsilon_{\text{eff}}} \max(0, \sigma_1) d\varepsilon_{\text{eff}}, \tag{3}$$

Elastic constant and density			Strain rate hardening		Temperature softening and adiabatic heating			Fracture parameter
E (GPa)	ν	ρ (kg·m ⁻³)	ϵ_0 (s ⁻¹)	c	T_0 (K)	T_m (K)	m	W_c (MPa)
70.5	0.3	2700	$5 \cdot 10^{-4}$	0.001	293	893	1	85

Table 3. Material constants for AA6061-T6 tube wall material.

where σ_1 is the first principle stress. The critical damage parameter, $W_c = 85$ MPa, was obtained by fitting the simulated measured stress-strain response of a single laterally compressed tube tested in [Holloman et al. 2013]. The general node-splitting feature in the IMPETUS code was turned on. In this feature the damage variable is allowed to evolve without any change to the constitutive response of the Al 6061-T6 alloy until $D = 1$. At that instant, the Al 6061-T6 alloy is assumed to have failed and nodes of the elements where this failure has occurred are split apart.

4. Quasistatic core response

The quasistatic compressive responses of all the core structures investigated here have been investigated previously in [Holloman et al. 2013], and the key findings relevant to this study are summarized in Table 4, together with a summary of the dynamic results presented below. The relative density given to the one-dimensional tube samples corresponds to their contribution in a three-dimensional structure, Table 1. The compressive strengths of the one-dimensional (notched) and two-dimensional cores were 4.7 and 13.2 MPa, respectively. The addition of one and two-dimensional strengths (17.9 MPa) was less than the measured peak strength of the equivalent three-dimensional structure (20.8 MPa) with a relative density, $\bar{\rho} = 20.1\%$, indicating a substantial synergistic interaction between the colinear and vertical tubes during quasistatic loading. However, the mechanism responsible for the enhanced crush resistance of the fully integrated three-dimensional structure was not identified.

The volumetric energy absorption up to the core densification strain (ϵ_D) per unit volume,¹ E_v , and gravimetric energy absorption, $E_m = E_v / \bar{\rho} \rho_s$ (where ρ_s is the density of the aluminum alloy), are also given for each core in Table 4. The theoretical gravimetric energy absorption, E_m^* (the product of the compressive strength and densification strain divided by $\bar{\rho} \rho_s$), and the gravimetric energy-absorbing efficiency (E_m / E_m^*) are also summarized in Table 4. The energy-absorbing efficiency of the two-dimensional structures was low as a result of the unstable buckling response of the structure, making the two-dimensional core poorly suited for impact energy-absorption applications. All other structures exhibited energy-absorbed-per-unit-mass values near the upper bound for tubes [Holloman et al. 2013].

5. Dynamic compression results

We begin by examining the dynamic compression of the components (single-axial and two-dimensional tube arrays) of the three-dimensional cellular structure, and then investigate the fully integrated structure at three relative densities. Finite element analysis is used to resolve the tube collapse modes, identify the mechanism responsible for the synergistic effect, and estimate the impact-face pressure.

¹Defined as the area under the stress strain response until the onset of densification.

Topology	$\bar{\rho}$	v (ms ⁻¹)	σ_p (MPa)	ε_D	E_v (MJ/m ³)	E_m (J/g)	E_m^* (J/g)	E_m/E_m^*
1D notched tube	6.7	0	4.7	0.72	1.7	9.4	18.7	0.50
		72	2.6	0.65	1.0	5.5	9.2	0.59
		105	3.2	0.56	1.4	7.7	9.6	0.80
		157	3.0	0.68	2.3	12.7	10.9	1.16
1D tube	7.3	0	10.3	0.79	5.3	26.9	39.6	0.68
		73	10.2	0.77	1.9	9.6	37.2	0.26
		108	11.6	0.75	3.3	16.7	40.8	0.41
		157	11.2	0.72	4.3	21.8	37.1	0.58
2D [0/90°] ₂	16.3	0	13.2	0.64	1.2	2.7	19.2	0.14
		73	15.4	0.62	2.8	6.4	21.2	0.30
		104	13.4	0.59	4.3	9.7	17.3	0.56
		156	13.5	0.59	4.8	10.9	17.0	0.64
3D cellular structure	20.1	0	20.8	0.61	10.4	19.2	23.4	0.82
		73	18.2	0.59	8.4	15.5	18.2	0.85
		104	17.5	0.56	9.3	17.1	17.0	1.00
		157	17.2	0.56	8.8	16.2	16.6	0.98
3D cellular structure (unnotched)	21.0	0	27.1	0.63	12.5	22.0	30.1	0.73
		74	24.6	0.72	10.8	19.0	30.7	0.62
		108	21.8	0.66	10.5	18.5	24.5	0.75
		154	19.5	0.63	9.6	16.9	20.7	0.82
3D cellular structure	11.6	0	7.3	0.59	3.9	12.7	13.7	0.92
		72	7.0	0.73	2.8	8.9	16.3	0.55
		156	7.1	0.73	3.5	11.2	16.5	0.68
3D cellular structure	42.7	0	49.8	0.45	24.4	21.2	29.4	0.73
		73	53.2	–	–	–	–	–
		105	51.4	–	–	–	–	–
		157	56.6	–	–	–	–	–

Table 4. Measured mechanical properties (including relative density, $\bar{\rho}$, impact velocity, v , and compressive strength, σ_p) and energy absorption values (including volumetric energy absorption, E_v , gravimetric energy absorption, E_m , theoretical gravimetric energy absorption, E_m^* , and energy absorption efficiency, E_m/E_m^*) for tested tubular cellular structures.

5.1. Axially loaded tubes.

5.1.1. Notched tube response. The back-face pressure versus core strain responses of notched tubes impacted at the three velocities are given in Figure 5(b–d), and compared with the quasistatic result in Figure 5(a). The core strain, ε_c , for the impacted samples was defined as $\varepsilon_c = h^{-1} \int_0^t v(t) dt$, where $v(t)$ was the measured sandwich-panel impact-face velocity as a function of time t (measured from

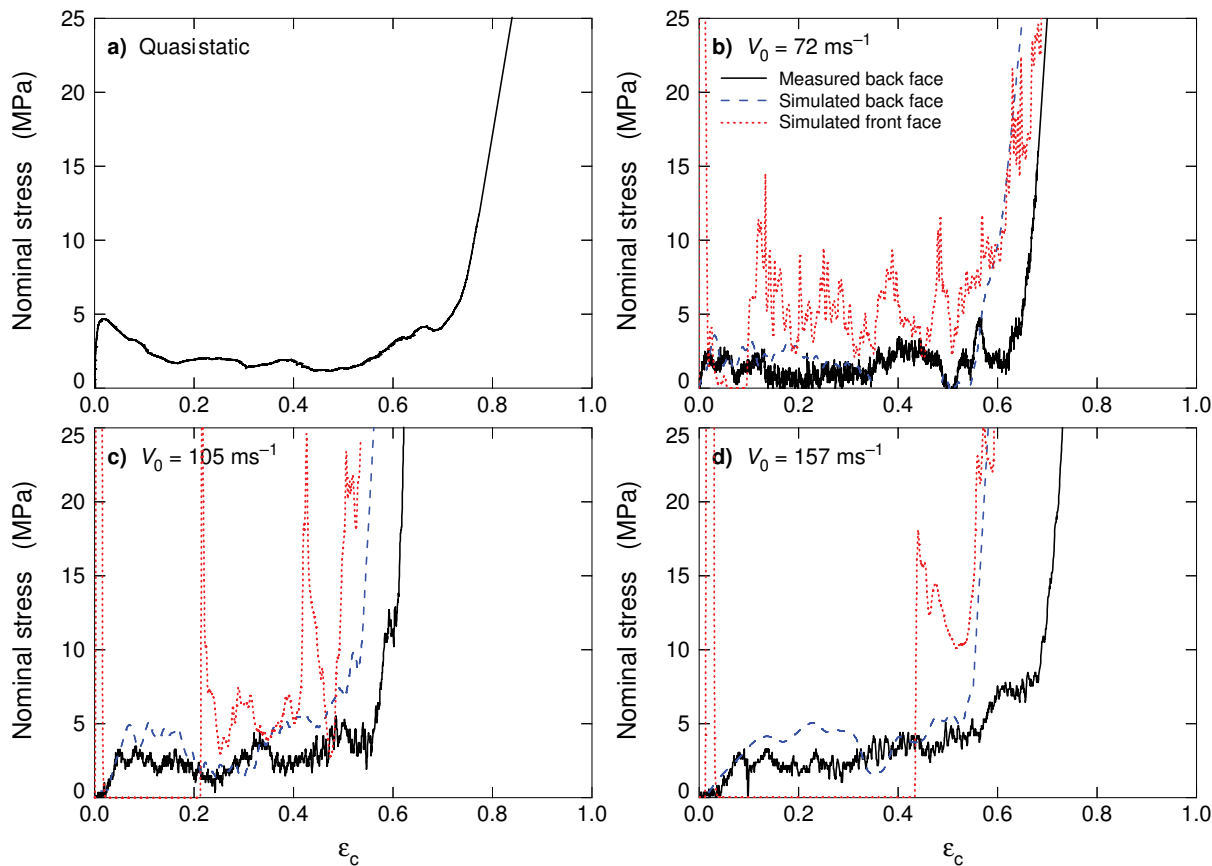


Figure 5. The measured and simulated back-face stress versus nominal compressive strain for a notched (one-dimensional) tube which contributed 6.7% to the relative density of a three-dimensional structure. (a) The quasistatic compression response followed by the responses after impact at (b) 72 ms^{-1} , (c) 105 ms^{-1} , and (d) 157 ms^{-1} . Simulation results are also shown for the specimens' front (impacted) face pressure.

the high-speed photographs), and h the initial core height (85.7 mm). The predicted back-face stress versus imposed nominal strain results are overlaid on the experimental data in Figure 5, and found to be in good agreement with the measured back-face stress. Under quasistatic loading, examination of Figure 5(a) shows a plateau-like stress versus strain response after an initial peak in compressive stress of $\sigma_p = 4.7 \text{ MPa}$. During dynamic impact at 72 ms^{-1} the stress-strain response remained plateau-like, as seen in Figure 5(b), but with a smaller initial stress peak of $2.9 \pm 0.3 \text{ MPa}$ for the three impact velocities; this is consistent with an absence of strain-rate (or inertial) hardening. However, after the initial peak in resistance, the measured and simulated flow stresses of the dynamically loaded samples gradually increased with strain, especially at the highest strain rate, and also exhibited several small additional stress peaks before the onset of densification (where the stress rose rapidly towards 25 MPa and beyond) at a strain $\varepsilon_D = 0.62 \pm 0.06$, which was less than the value of 0.72 measured under quasistatic deformation. These results are summarized in Table 4.

A sequence of high-speed video images and corresponding simulations for a notched tube impacted at $v_0 = 72 \text{ ms}^{-1}$ are shown in Figure 6. The initial strain suffered by the impacted tube occurred by axial plastic compression of the tube walls at the notches. However, after a small shortening period as the tube walls at the notch compressed, the initial peak in strength was reached as the tube began to buckle about a notch, see Figure 6(a). This was initiated at the right-hand notch (nearest to impact end of the tube) at

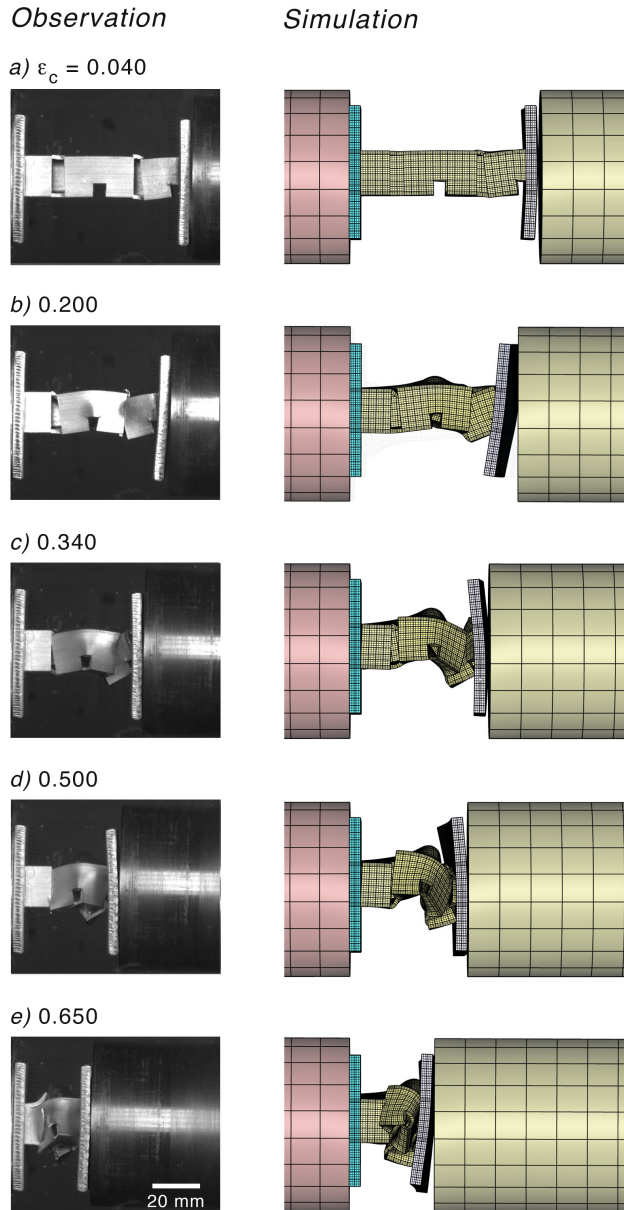


Figure 6. Observed and simulated deformation sequence for a (one-dimensional) notched tube specimen impacted at an initial velocity $v_0 = 72 \text{ ms}^{-1}$. Impact occurs on the right side of both the photographs and the FE simulations.

a nominal strain of slightly less than 0.04, and correlated well with the first stress peak in Figure 5(b). As the nominal strain increased, new notch buckling events progressed from notches at the impact end of the sample towards those at the distal end, see Figure 6(a and b). At a nominal strain of 0.34, the tube walls near all the notches had suffered significant buckling deflections, see Figure 6(c), and material near the impact end had rotated about the notch. Further axial compression resulted in fracture of the buckled tube wall at the most distal notch, and contact of the tube walls on either side of this notch, as in Figure 6(d). This self-contact coincided with stiffening of the structure, and a rise in compressive flow stress to 4.7 MPa at a nominal strain of 0.56; see Figure 5(b). This process then progressed from right to left along the tube, resulting in densification at $\varepsilon_D = 0.65$; see Figure 5(b).

If the four notches had buckled (without tube rotation) until tube wall contact was established across the 6.35 mm-wide notch, the axial displacement of the 76.2 mm-long tube would have been 25.4 mm, a strain of 33%. Since the densification strain was about twice this value, we conclude that the combination of tube rotation and axial compression of the tube walls between the notches contributed about the same level of strain as notch deformation to the densification limit. We note that simulation images compared well to those observed with the high-speed camera (see Figure 6). The comparison was best when the strain was below 0.300. Beyond this strain, tube rotations were increasingly difficult to precisely predict due to the global nature of failure, and its sensitivity to imperfections. The simulations verified that the strength was governed by buckling collapse of the tubes, and that this was initiated at the right-hand notch nearest to the impact.

Increasing the impact velocity resulted in a similar deformation sequence, but the degree of tube rotation decreased with increased impact velocity (see Figure 7). This was observed in both the experimental data and in the simulation. Since tube rotation is an inertially sensitive failure mode, and was active during the nominal plateau region of the crush response, its decrease with increase in impact velocity may be responsible for the more rapid rise in plateau flow stress as the impact velocity increased; see Figure 5(b–d). This would prolong axial tube compression (a harder mode) as opposed to tube rotation.

The total absorbed (plastically stored) energy per unit volume, E_v , was obtained from the area under the stress-strain curve shown in Figure 5(b). The integration was terminated at the densification strain, where the flow stress began to increase sharply due to material self-impingement. This gave a volumetric absorbed energy $E_v = 1.0 \text{ MJ/m}^3$. Dividing this by the core density, $\bar{\rho}_{\rho_s} = 0.067 \cdot 2.7 \text{ Mg}\cdot\text{m}^{-3} = 180.9 \text{ kg}\cdot\text{m}^{-3}$, gives a gravimetric absorbed energy, $E_m = 5.5 \text{ J/g}$. If the stress achieved at the first stress peak had remained constant until densification, the gravimetric absorbed energy would have been the theoretical limit of the structure, $E_m^* = 9.2 \text{ J/g}$. The notched one-dimensional structure impacted at $v_0 = 72 \text{ ms}^{-1}$ therefore had an energy absorption efficiency of 59.0%. The energy absorption and energy absorption efficiency of the tubes rose with impact velocity as the cores' peak strength also increased, see Table 4, and increased beyond unity (using the first stress peak to define the theoretical energy absorption) because of the gradual rise in plateau-region flow stress with strain in the most rapidly crushed samples. The FEA results slightly underpredicted the measured densification strains, most notably for the test at $v_0 = 157 \text{ ms}^{-1}$.

The simulations permit calculation of the front-face pressure for each test, and this is overlaid on the experimental and predicted back-face responses of Figure 5. The initial inelastic impact resulted in very large contact stresses on the front-face sheet, and a significant momentum transfer to the lighter sandwich structure, leading to its loss of contact with the striker. As the tube-crushing reaction forces

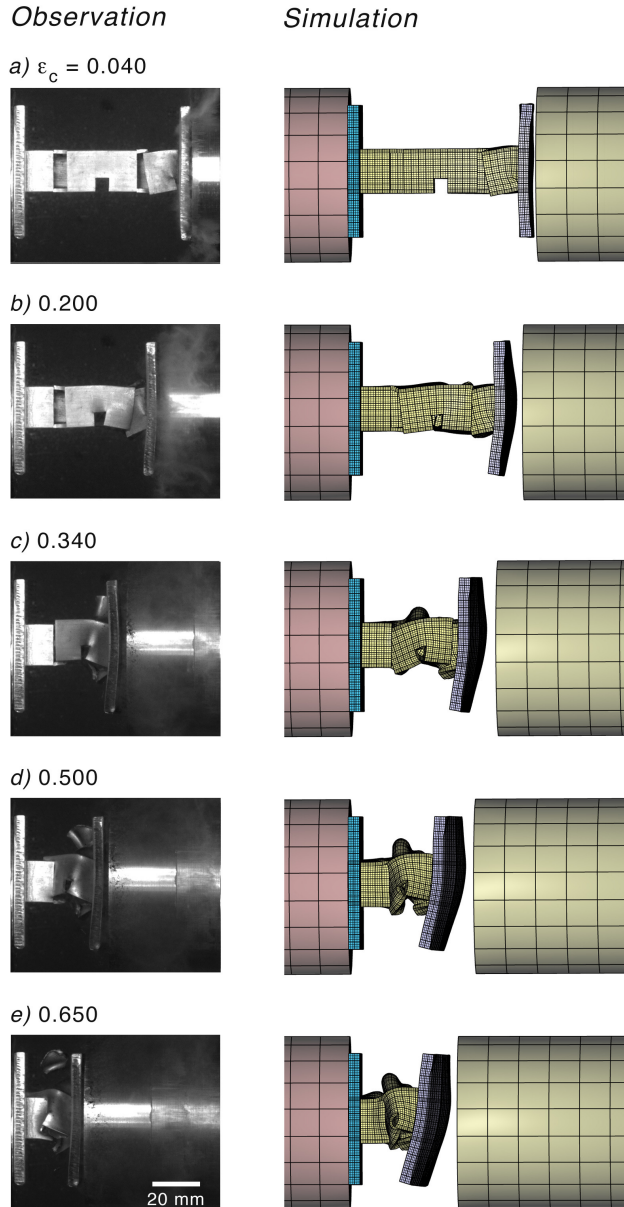


Figure 7. Experimentally observed and simulated deformation sequence for a notched (one-dimensional) tube specimen impacted at an initial velocity $v_0 = 157 \text{ ms}^{-1}$.

decelerated the impact face, the striker eventually recontacted the sample, and the stress once again increased. The repetition of this process is responsible for the series of stress peaks observed in the front-face stress-strain profiles, see [Figure 5](#).

5.1.2. Regular tube response. The impact response of the vertical tube without notches is shown in [Figure 8\(b–d\)](#), and compared with that measured during quasistatic testing in [Figure 8\(a\)](#). The initial

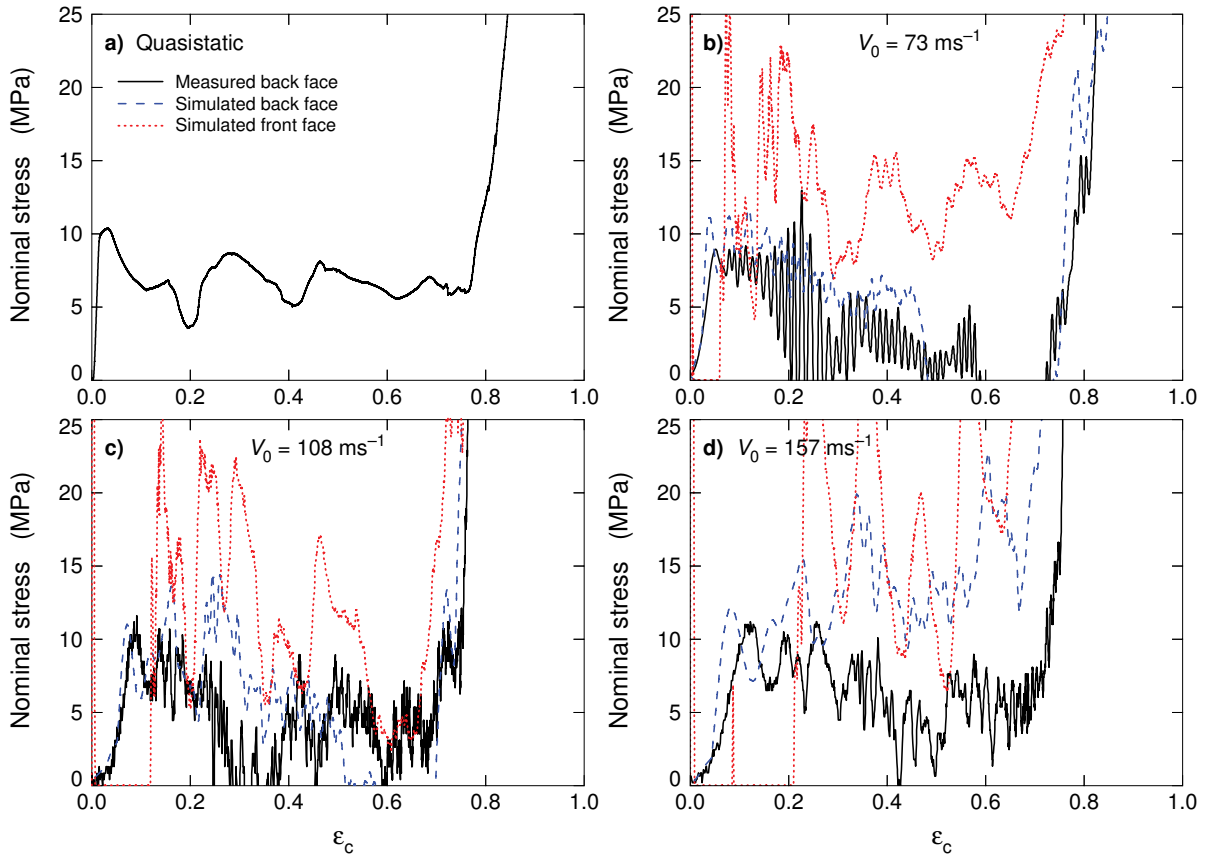


Figure 8. The measured and simulated back-face stress versus nominal compressive strain of an unnotched one-dimensional tube structure which contributed 7.3% to the relative density of the unnotched three-dimensional structure. (a) Quasistatic response, and for impacts at (b) 73 ms^{-1} , (c) 108 ms^{-1} , and (d) 157 ms^{-1} . Simulation results are also shown for the front face of the specimen.

peak stress was again unaffected by the impact velocity, but had a much higher value of $\sim 11 \text{ MPa}$ than that of a notched tube ($\sim 2.9 \text{ MPa}$). The flow stress then dropped with continued loading, exhibiting numerous stress oscillations, until the onset of densification at a very high densification strain, $\varepsilon_D = 0.8$. The simulated back-face stress-strain responses are compared to experimental results in [Figure 8](#), and are in reasonable agreement with the measurements considering the (small) experimental variability in the tube orientation. The measured peak strength and energy absorption for the samples are summarized in [Table 4](#). Even though the initial peak strength was about four times that of the notched structure, and it had a higher densification strain, the volumetric energy absorption was only about twice that of the notched structure because of the substantial fall in strength following the initial peak in stress, and the highly oscillatory plateau region's response.

High-speed video and simulated images of the collapse process are shown in [Figure 9](#). At low strains the tubes underwent plastic compression, and the initial peak in strength at $\varepsilon_c = 0.04\%$ was correlated with tube wall buckling; see [Figure 9\(a\)](#). This was followed by failure of the tube-front face bond, rotation of

the tube, and tube wall fracture at the apex of buckles; see [Figure 9\(b\)](#). This process continued resulting in fragmentation (and loss) of the tube walls. This delayed the onset of material self-impingement, and was the origin of the higher-than-normal densification strain; see [Figure 9\(e\)](#). The simulated damage progression in [Figure 9](#) also shows the significant tube rotation and fragmentation of the tube during

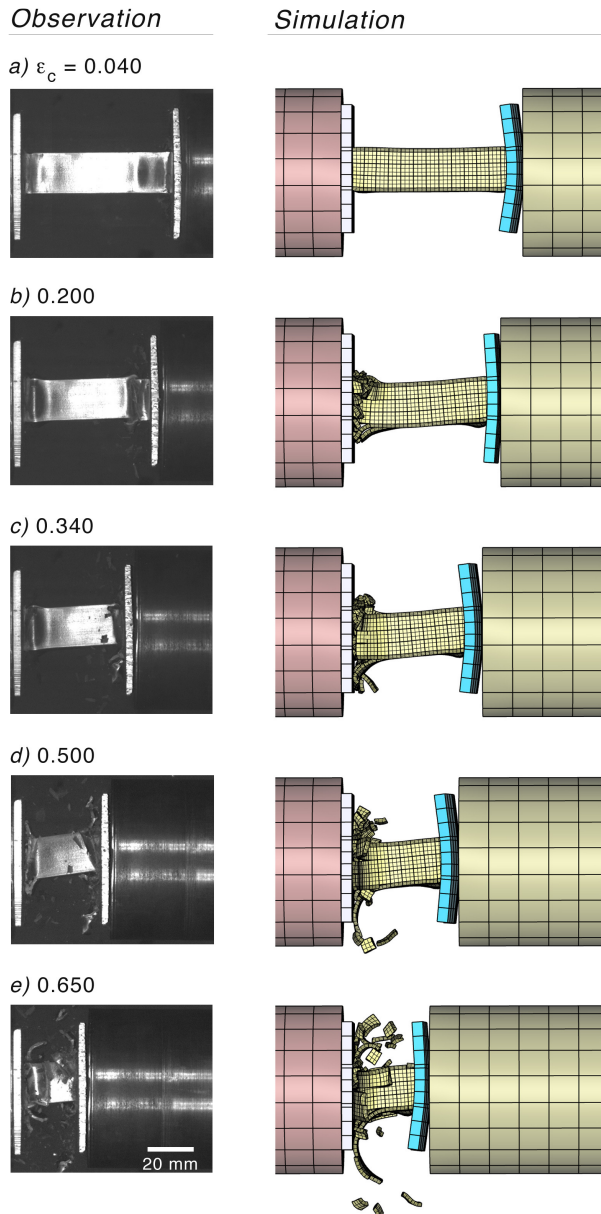


Figure 9. Observed and simulated deformation sequence for a one-dimensional tube specimen with a relative density of 7.3% and no notches impacted at an initial velocity $v_0 = 73 \text{ ms}^{-1}$.

dynamic loading² observed experimentally. The “spiky” character of the measured stress profile was also seen in the simulation, and the transient partial load drops were linked to tube fracture events. The progressive drop in flow stress with continued straining arose from continued fragmentation at the distal end of the tube until densification at a strain of 0.8.

5.2. Two-dimensional tube array. The measured and simulated compressive stress versus strain response of the dynamically tested two-dimensional structure is shown in Figure 10(b–d) and compared to the quasistatic result in Figure 10(a). The stress versus strain responses at all loading rates exhibit three peaks followed by densification. The initial peak stress, σ_p was again independent of loading rate, which is consistent with minimal strain-rate hardening. The load dropped after each peak in stress resulted

²The response of the tube was highly sensitive to small changes in its orientation. When tubes were perfectly aligned, progressive concertina plastic buckling of the tubes was observed. However, introduction of the small misalignments present in the experiments resulted in the modes shown in the figures.

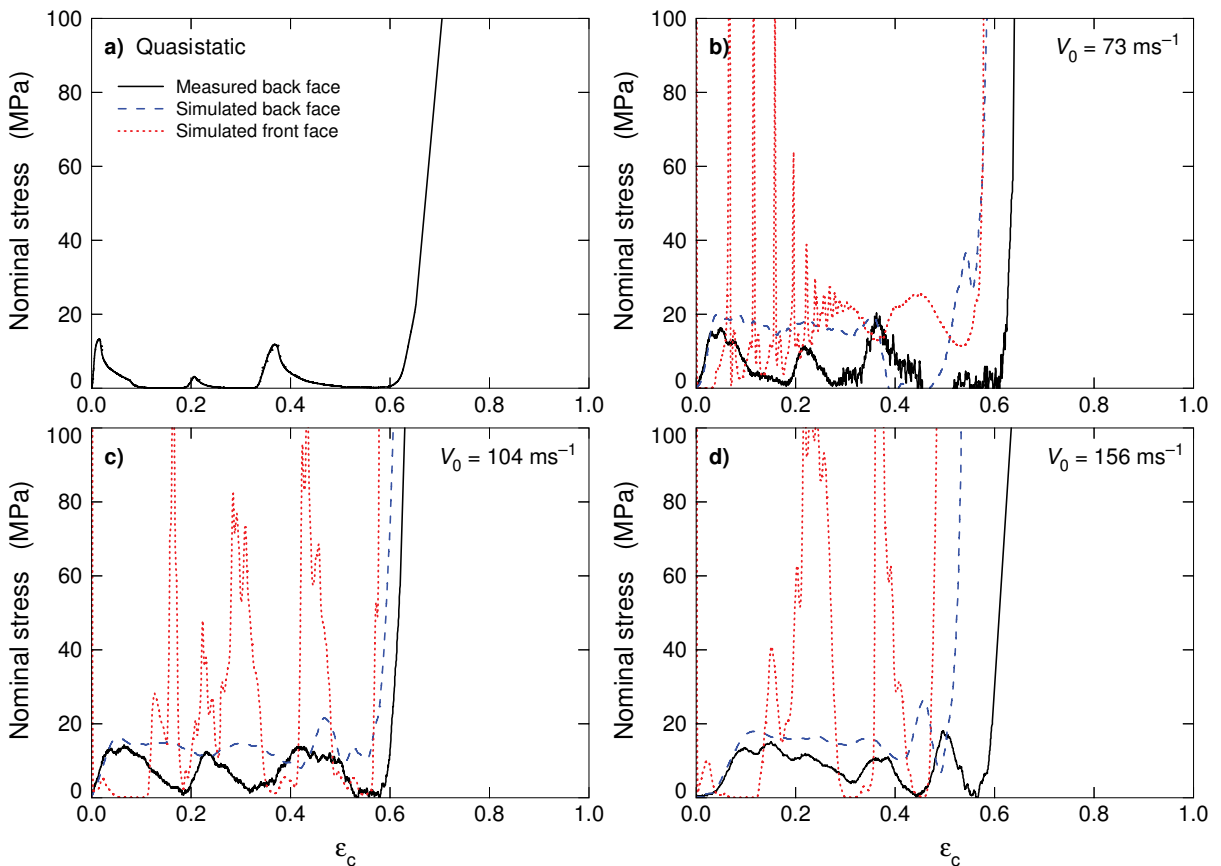


Figure 10. The measured and simulated dynamic stress versus normalized nominal strain responses of a two-dimensional tube structure with a relative density of 16.3%; (a) quasistatic response, and following impact at (b) 73 ms^{-1} , (c) 104 ms^{-1} , and (d) 156 ms^{-1} .

in low volumetric and gravimetric energy absorptions (Table 4), but these (and the energy absorption efficiency) increased with impact velocity because the stress drops decreased in amplitude at higher velocities (Figure 10).

High-speed video observations and simulations (Figure 11) indicate that the initial rise to the first stress peak was always correlated with the onset of a high-order (short wavelength) buckling mode of

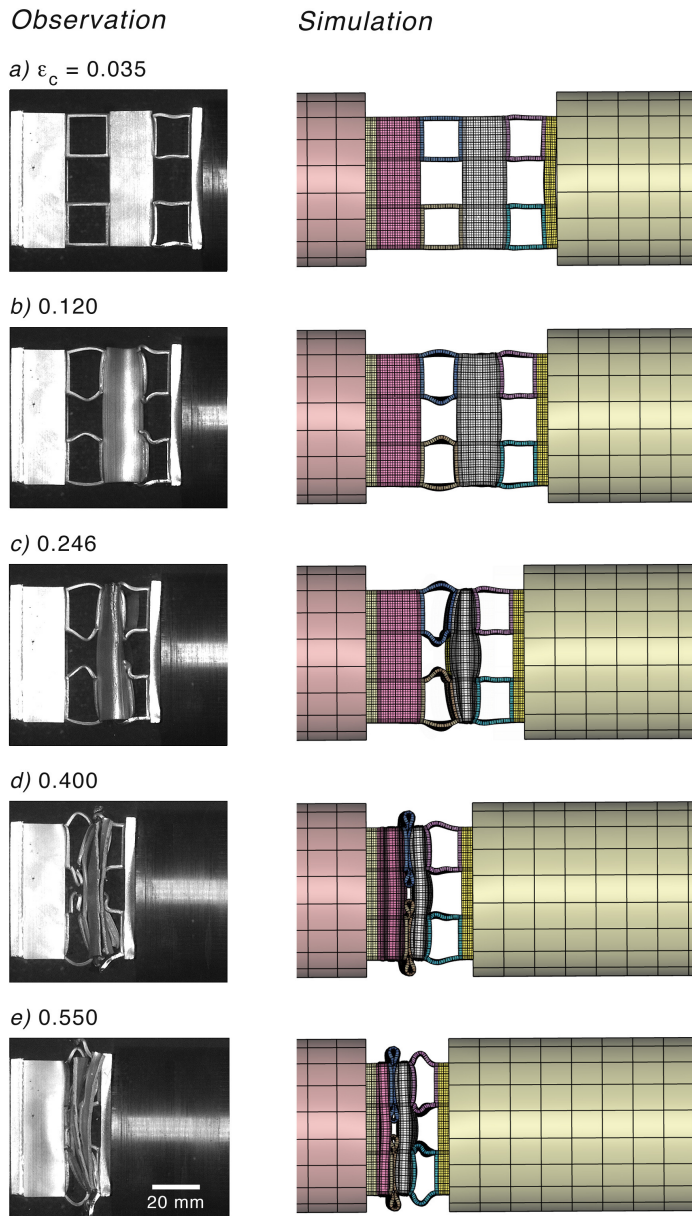


Figure 11. Observed and simulated deformation sequence for a two-dimensional specimen impacted at an initial velocity $v_0 = 73 \text{ ms}^{-1}$.

the axially aligned walls of the tube layer nearest the impacted face; see Figure 11(a and b). As the sample continued to undergo compression, the buckling behavior became impact velocity dependent. At an impact velocity of 73 ms^{-1} , buckling of the first-to-buckle (right-hand) layer stopped, as seen in Figure 11(b), and further strain was achieved by initiation of a low-order mode of buckling of the other three tube layers. As the compressive strain reached a value of about 0.2, the deformation localized into the tube layer second from the right in Figure 11(c), and the second peak in stress then corresponded to the collapse (aided by wall fracture) of this layer. The third stress peak corresponded to collapse of the tube layer third from the impacted end of the sample; see Figure 11(d). Collapse of the first impacted layer then coincided with the onset of densification at a strain of 0.62; see Figure 11(e). As the velocity of impact increased, the initial impact provided sufficient pressure to cause complete (but still high-order mode) buckling of the right-hand tube layer, and this collapse corresponded to the first peak in stress; see Figure 12(a and b). The other peaks then corresponded with the progressive collapse of the layers from right to left, as in Figure 12(c–e).

The simulated nominal stress versus applied nominal strain results shown in Figure 10(b–d) compared well with the experimental results. While the three peaks in stress are well predicted, the simulations do not fully capture the unloading instability, suggesting that the simulated tube wall fracture process is not completely captured by the approximate approach used here.

5.3. Three-dimensional tube cores.

5.3.1. Notched vertical tube response. The dynamic responses of the three-dimensional structures are shown in Figure 13(b–d) and are again compared to the quasistatic result in Figure 13(a). The three-dimensional cores' initial quasistatic peak strength, σ_p , was 20.9 MPa, while dynamically it was slightly less (varying from 17.2 to 18.2 MPa), and independent of impact velocity, see Table 4.³

In general, the dynamically deformed samples exhibited plateau-like compression responses with three small stress peaks like those associated with the sequential collapse of the two-dimensional in-plane tubes discussed above. The volumetric and gravimetric energy absorptions of the three-dimensional structures, seen in Table 4, were independent of compression rate. The average volumetric energy absorbed for the four loading rates was 9.2 MJ/m^3 . This significantly exceeded that for the average absorbed energy of 5.8 MJ/m^3 for the components of the three-dimensional system (one notched tube and the two-dimensional tube array, see Table 5). The energy absorption efficiency of the three-dimensional structure was independent of the compression rate, and varied between 82 and 100%. The high efficiency resulted in part from the rising background stress just before densification was reached. This high efficiency, combined with the plateau-like compressive stress-strain response to compressive strains of about 50%, indicates the three-dimensional tube structure to be well suited for impact-mitigation applications.

The rear-face pressure responses from the finite element simulations were in good agreement with the measurements at the lowest impact velocity; see Figure 13(b). During quasistatic loading, three stress peaks were superimposed on a constant stress plateau response; see Figure 13(a). However, during dynamic loading, the third peak occurred on a rising background stress response and was most pronounced

³The difference in strength was consistent with small tube misalignments which have a significant effect upon the small samples tested here. To illustrate, Figure 14(a) shows a high-speed video image of the sample tested at $v_0 = 73 \text{ ms}^{-1}$, and reveals that one of the in-plane tubes' side-walls (at the top right of the sample) was not in full contact with the underlying in-plane tube wall, causing it to prematurely fail.

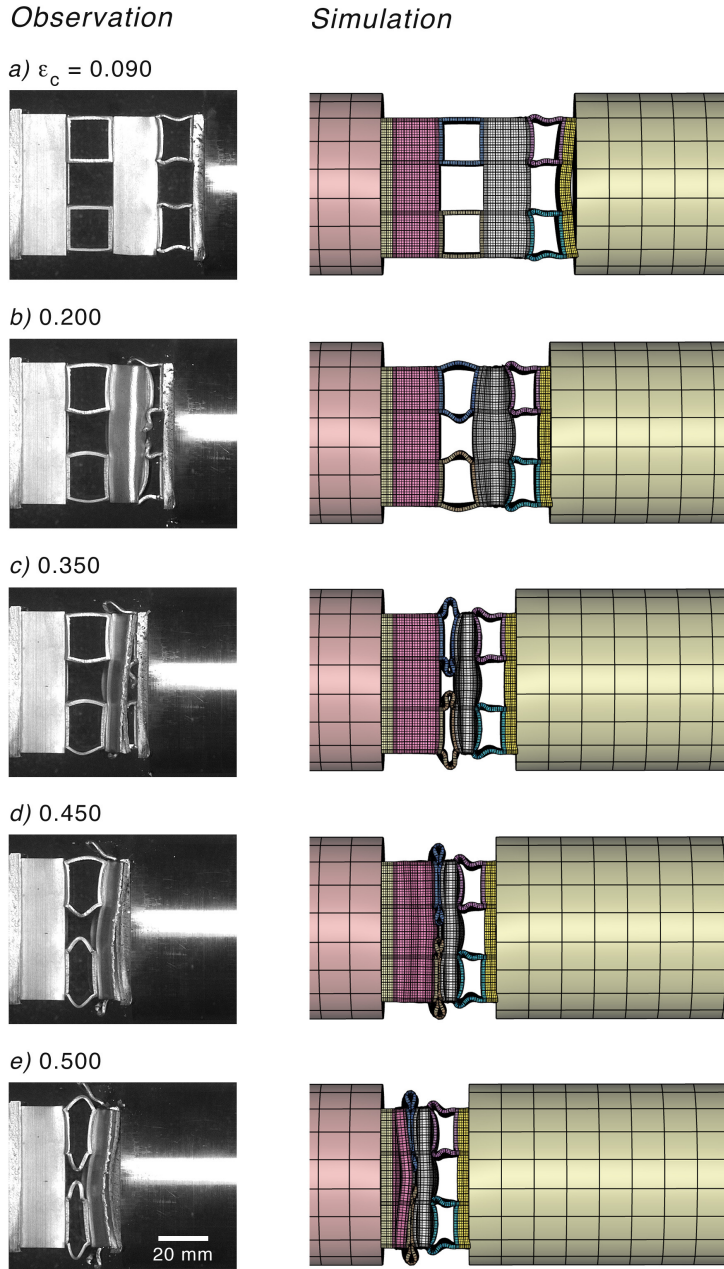


Figure 12. Observed and simulated deformation sequence for a two-dimensional specimen impacted at an initial velocity $v_0 = 156 \text{ ms}^{-1}$.

in the sample tested at the highest impact velocity; see [Figure 13\(d\)](#). This rising background stress was a characteristic of the vertical notched tube response; see [Figure 5\(c and d\)](#). A rise in predicted stress during the plateau response was also observed, but, for the two most rapidly loaded samples, exceeded that measured beyond a core strain of 20%. The small drops in flow stress after each peak were correlated

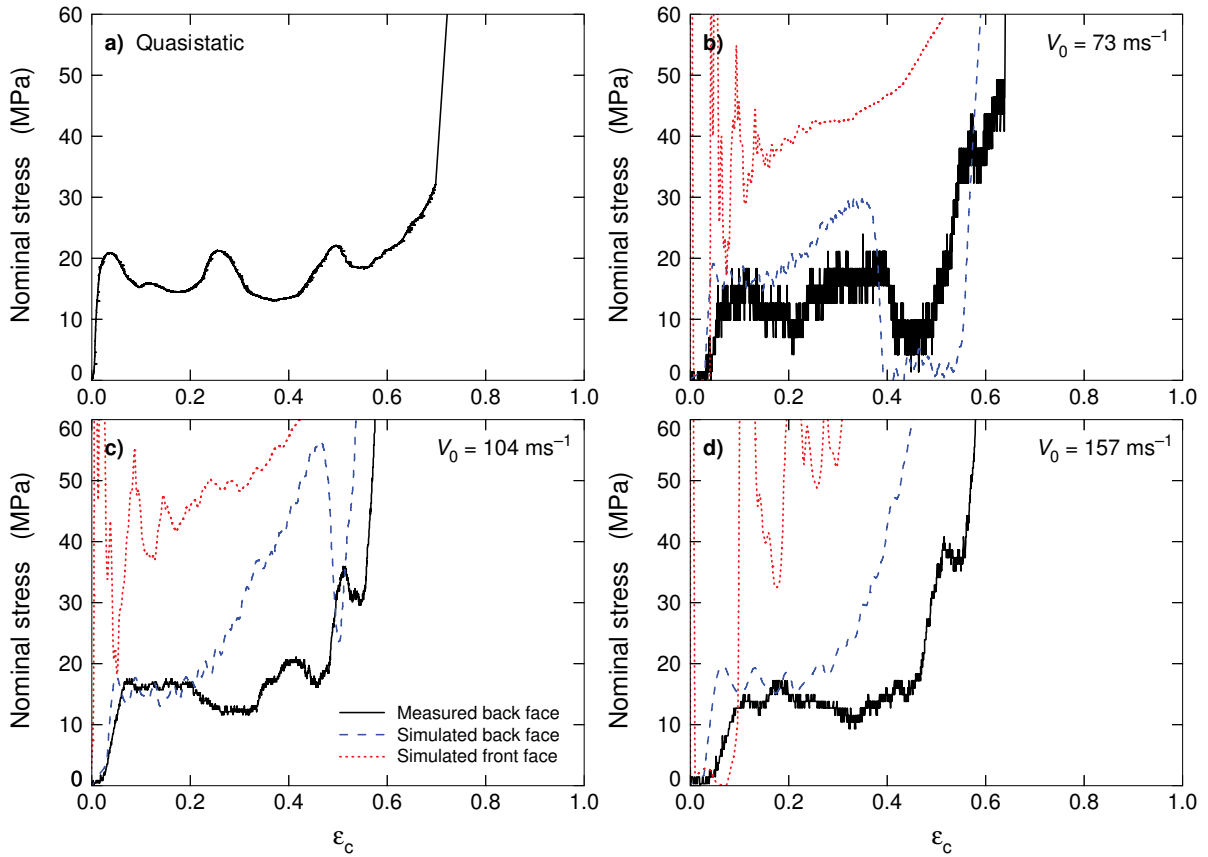


Figure 13. The measured and simulated dynamic stress versus nominal strain responses of a three-dimensional tube structure (containing notched out-of-plane tubes) with a relative density of 20.1%. (a) Quasistatic response, and after impact at (b) 73 ms^{-1} , (c) 104 ms^{-1} , and (d) 157 ms^{-1} .

with the buckling instability and fracture of the walls of one of the collapsing tube layers of the four tube layer, $[0/90^\circ]_2$ in-plane tube system.

The collapse mechanisms were investigated by examining a sequence of high-speed video images and finite element analyses. The result for an impact at $v_0 = 73 \text{ ms}^{-1}$ is shown in Figure 14. The initial peak in stress occurred at a strain of 0.10; see Figure 13(b). From the experimental observations shown in Figure 14(b) this was correlated with both notch-induced out-of-plane tube collapse and the initiation of buckling of the in-plane tube walls, and was identical to the mechanism previously observed at quasistatic strain rates [Holloman et al. 2013]. By using the FEA postprocessor to make the in-plane tubes transparent after a simulation, as Figure 15(a), we see that by a core strain of 0.04, the notched tube had begun to buckle at the two notches nearest the impacted face. We were also able to confirm that notch-tripped buckling of the out-of-plane tube was coincident with in-plane buckling, a result consistent with the earlier observations that the components (single-axial and two-dimensional tube arrays) of the three-dimensional cellular structure also buckled at the same strain (4%).

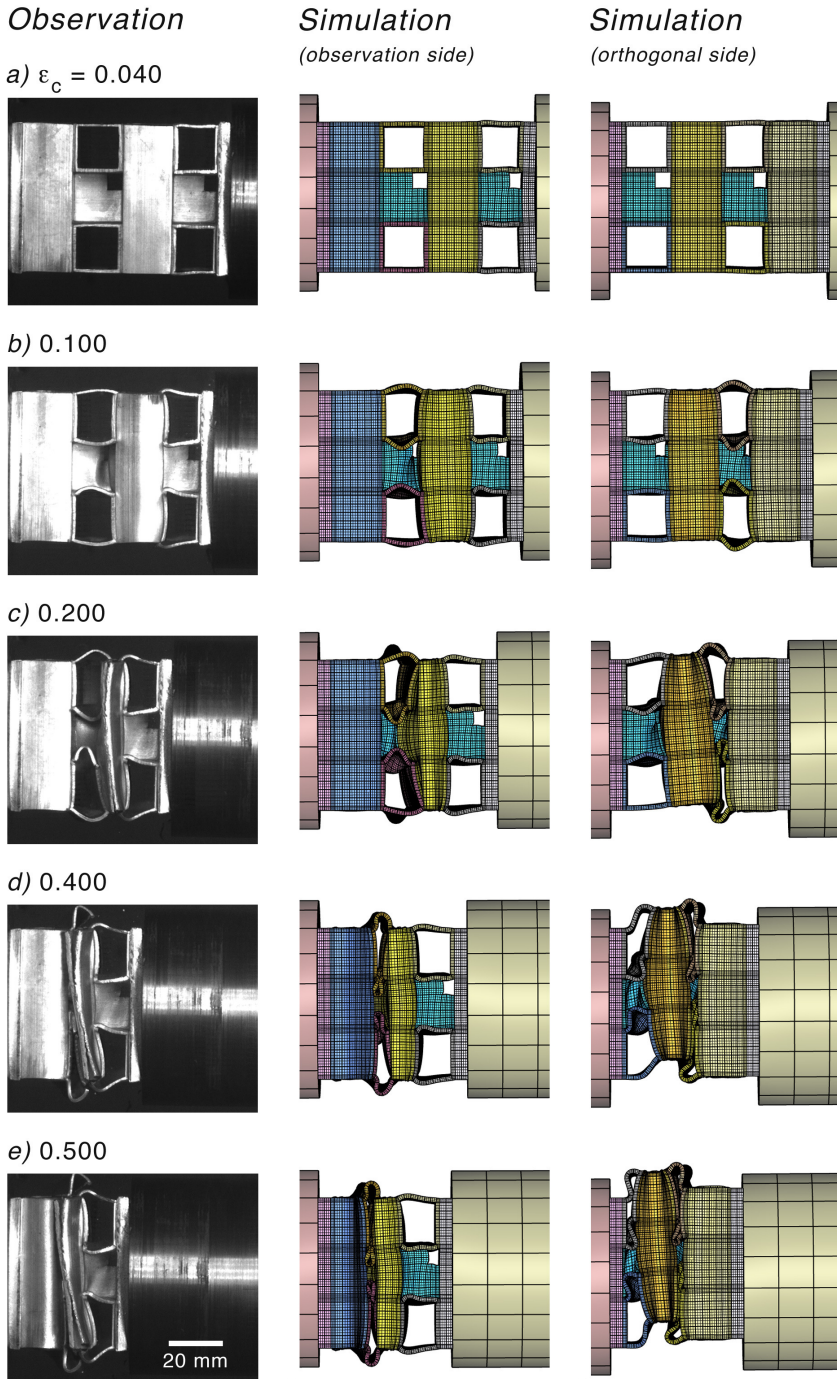
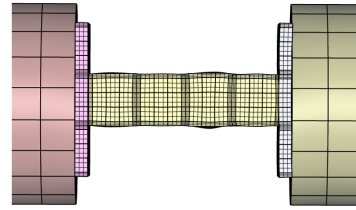
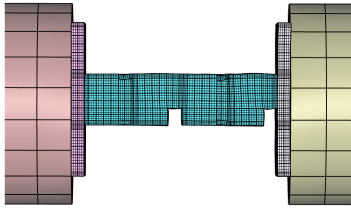
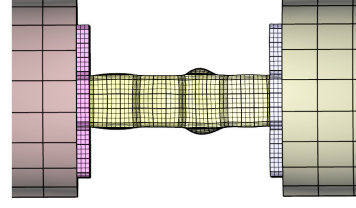
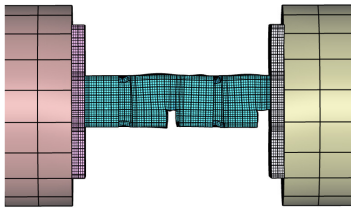


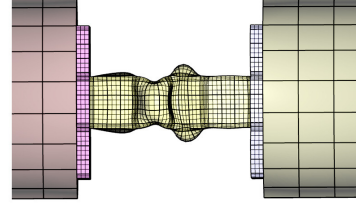
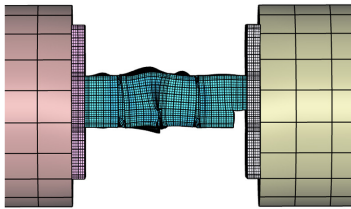
Figure 14. Observed and simulated deformation sequence for a three-dimensional specimen with a relative density of 20.1% after impact at an initial velocity $v_0 = 73 \text{ ms}^{-1}$. Two sides of the simulated FE model are shown to more clearly reveal the deformation sequence.

*Notched 3d structure**Un-notched 3d structure*a) $\varepsilon_c = 0.040$ 

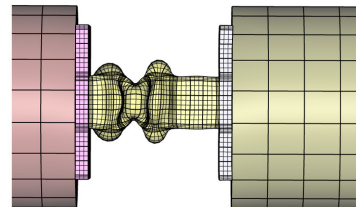
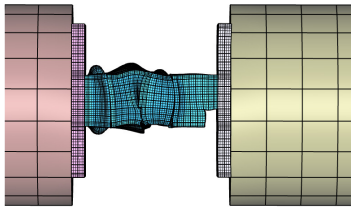
b) 0.100



c) 0.200



d) 0.340



e) 0.500

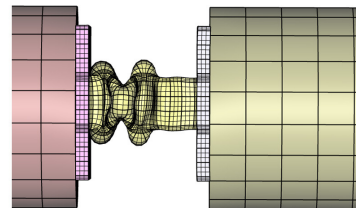
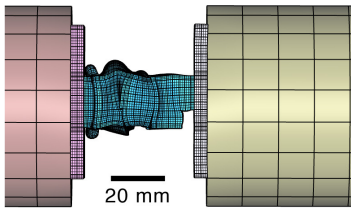


Figure 15. Deformation sequence showing the three-dimensional notched and un-notched structures when the colinear tubes have been made transparent to show the collapse mode of the axial aligned tubes following impact at an initial velocity $v_0 = 73 \text{ ms}^{-1}$.

Topology	$\sum \bar{\rho}$	v (ms ⁻¹)	$\sum \sigma_p$ (MPa)	E_v (MJ/m ³)	E_m (J/g)
Notched 1D tube with 2D core	23.0	0	17.9	2.8	5.2
		72	17.4	4.4	8.2
		105	17.3	7.2	13.3
		157	16.8	8.9	16.4
Unnotched 1D tube with 2D core	23.6	0	23.2	6.1	9.5
		73	25.1	4.8	8.5
		108	25.6	8.7	15.4
		157	25.6	11.5	20.3

Table 5. Summed responses of one and two-dimensional cores (including the sum of the relative densities, $\bar{\rho}$, the impact velocity, v , and the sum of the compressive strengths, σ_p). (The sums of the one and two-dimensional cores do not match the measured relative density of the three-dimensional core because of variability in tube wall thickness resulting from the extrusion process and an effect of the braze layer.)

Further compression beyond the initial stress peak resulted in the flow stress softening to a strain of $\sim 20\%$. The high-speed video images and the simulations, shown in [Figure 14\(c\)](#), indicate this corresponded with continued buckling of the second in-plane tube layer from the strike face, consistent with observations of the two-dimensional in-plane structure at this impact rate; see [Figure 11\(a\)](#). Collapse of the second layer, rather than that nearest the strike face, appears to have resulted from its higher-order buckling mode, which requires a higher stress to continue collapse. Following this softening, the tested structure hardened to a second stress peak at a strain of 0.38 followed by a sharp drop in stress at a strain of 0.41. The mechanism responsible for the structures' rapid stress drop can be seen by comparing the high-speed images and simulations in [Figure 14\(c and d\)](#). It resulted from the buckling collapse of the third layer of tubes from the strike face. The orthogonal simulated view of the collapse process in [Figure 14](#) also reveals a significant lateral (transverse shear) displacement as the axial strain increased to 0.4. The simulations also revealed that the second and fourth notches from the impact face contributed to the shearing of the second and fourth in-plane tube layers. This mechanism is not apparent in the high-speed video images due to the orientation of the specimen. Further collapse of the structure resulted in core densification (with additional shear of the second and fourth in-plane tube layers) as the fourth in-plane layer and the first in-plane tube layer buckled at $\epsilon_D = 0.61$.

It is interesting to note that as the impact velocity increased, the transverse (shear) displacement was reduced, and at the highest impact velocity the structure collapsed axially with no transverse displacement; this was observed by both experiment and simulation ([Figure 16](#)). This change in deformation mode appears to be linked with the collapse of the vertical notched tube which during isolated testing (see [Figures 6 and 7](#)), exhibited significant rotation and transverse displacement at low velocities, but deformed in a more axial manner at the highest impact velocity. To investigate this we show the simulated deformation sequence of the axial tubes of the three-dimensional sample tests conducted at 73 and 157 ms⁻¹ in [Figure 17](#). It can be seen that a significant lateral deformation accompanies the low-velocity test, but at high velocities, the sample progressively collapsed with no transverse motion.

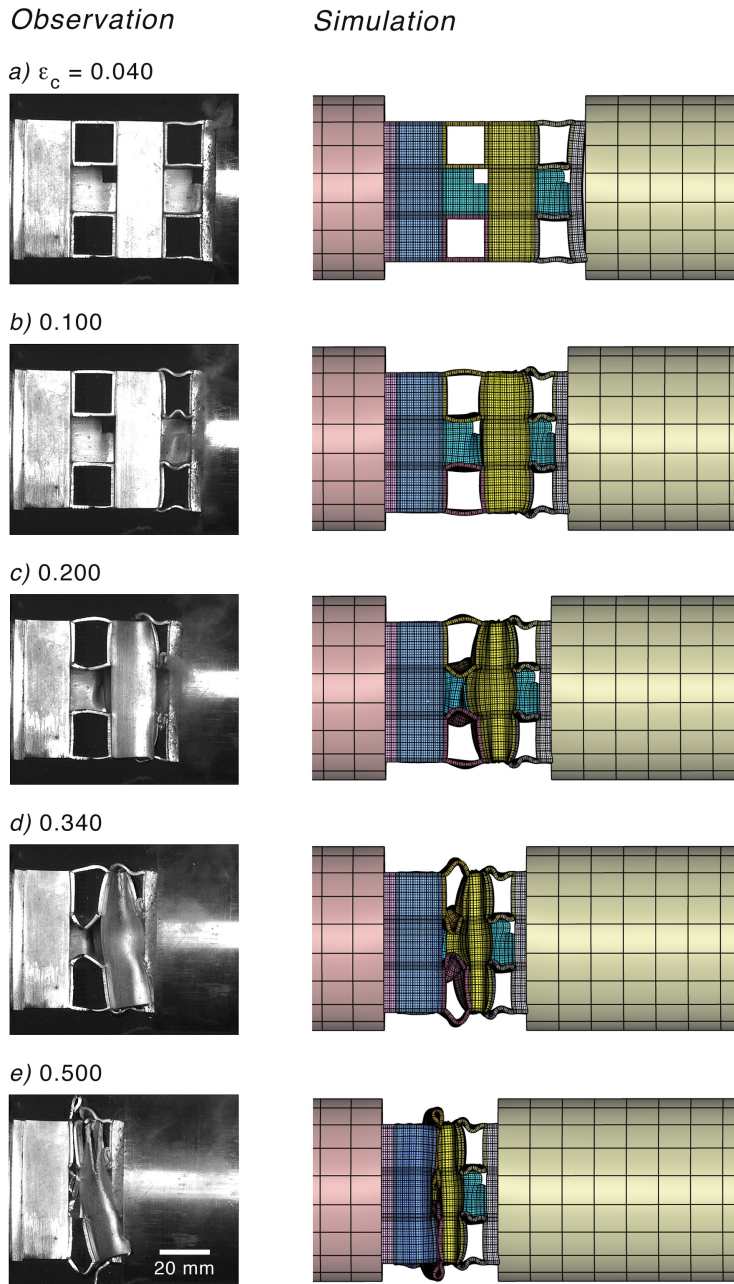


Figure 16. Observed and simulated deformation sequence for a three-dimensional specimen with a relative density of 20.1% after impact at an initial velocity $v_0 = 157 \text{ ms}^{-1}$.

The simulations indicate the initial contact stresses between the projectile and the front-face sheet increased from 764 to 1520 MPa as the impact velocity increased from 73 to 157 ms^{-1} , and greatly exceed those at the distal end of the samples; see [Figure 13\(b–d\)](#). Following striker impact at $v_0 = 73 \text{ ms}^{-1}$,

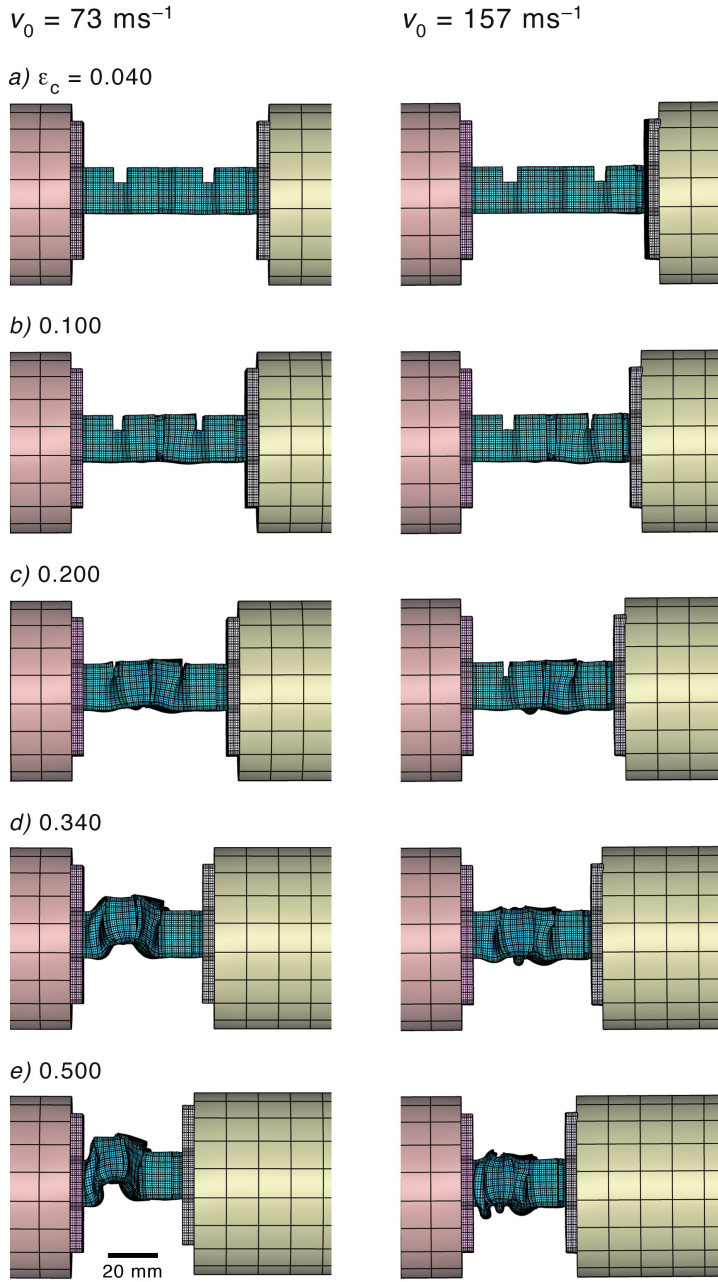


Figure 17. Deformation sequence showing the orthogonal side of the three-dimensional notched structure after the colinear tubes have been made transparent.

the three-dimensional sample was brought into equilibrium much more quickly than the one or two-dimensional cores, because of its higher mass and core strength. However, as the initial impact velocity was increased, larger amounts of energy were transferred to the specimen during initial contact, and the

contact force briefly dropped to zero for impact at $v_0 = 157 \text{ ms}^{-1}$ as sample face sheet-striker separation occurred; see [Figure 13\(d\)](#).

Three-dimensional tube cores with relative densities $\bar{\rho} = 11.6$ and 42.7% were also tested; the results are summarized in [Table 4](#). The structure with $\bar{\rho} = 11.6\%$ was observed to fail in a similar fashion as the $\bar{\rho} = 20.1\%$ structure. At the lowest impact velocity transverse (shear) displacement was present, but at the highest impact velocity the structure collapsed axially with no transverse shear, which resulted in increased flow stress. The three-dimensional cores with a relative density of 42.7% were not completely crushed during dynamic loading, even though the striker was reflected from the specimen (thereby increasing the transferred momentum and applied pressure). While the initial strength could be measured (and is given in [Table 4](#)), it was not possible to determine the densification strain or energy absorbed by this structure. Simulations indicated that the out-of-plane notched tube in the highest density structure showed no rotation, even at the lowest impact velocity, where rotation was observed in the other two structures.

5.3.2. Regular vertical tube three-dimensional case. The three-dimensional core without notches in the vertical tubes ($\bar{\rho} = 21.0\%$)⁴ was tested dynamically to determine the role of the notches upon the response of the three-dimensional structure. The measured and simulated compressive stress-strain responses for impacts at various velocities are shown in [Figure 18](#). The samples tested at impact velocities of 73 and 108 ms^{-1} exhibited several small peaks in stress during the region of plateau response like those seen in the two and three-dimensional structure with notched axial tubes. These stress peaks corresponded to the sequential collapse of three of the in-plane tube layers; see [Figure 19](#). Collapse of the fourth layer coincided with densification (in simulations, the first layer was responsible for densification). The sample tested at the highest impact velocity, as shown in [Figure 18\(d\)](#), exhibited almost no secondary peaks and had an almost ideal plateau response to a densification strain of about 0.6 (about the same as the quasistatic test).

The mechanical properties of the cores are summarized in [Table 4](#). The cores were slightly stronger than their notched counterparts, consistent with the higher strength of the unnotched out-of-plane tube. The first peak stress and densification strains were again independent of impact velocity. The average volumetric energy absorbed was 10.9 MJ/m^3 , compared to 7.8 MJ/m^3 for the average of the summed component tubes (see [Table 5](#)) indicating much less of a synergistic energy absorption effect in this three-dimensional structure. The energy absorption efficiencies range between 62 and 82% (see [Table 4](#)) for these cores, making them quite efficient.

Recall that in [Section 5.1](#) a regular tube not in perfect axial alignment with the striker underwent tube rotation and buckling with fragmentation. Stress drops were observed to accompany the fracture events. Comparison of the single tube ([Figure 8](#)) and three-dimensional ([Figure 18](#)) responses reveals significantly reduced load drops suggesting that vertical tube fragmentation was suppressed. Using the FEA postprocessor to make in-plane tubes transparent, the out-of-plane (unnotched) tube walls are shown to have concertina buckled in [Figure 15](#) as opposed to rotation, buckling, and fragmentation fracture ([Figure 9](#)). This appears to be the origin of the extra energy absorbed in the three-dimensional structures compared to their one-dimensional and $[0^\circ/90^\circ]_2$ tube components.

⁴Its density was less than the sum of the one-dimensional tube and two-dimensional structure due to variations of $\pm 0.14 \text{ mm}$ in the thickness of the tube walls.

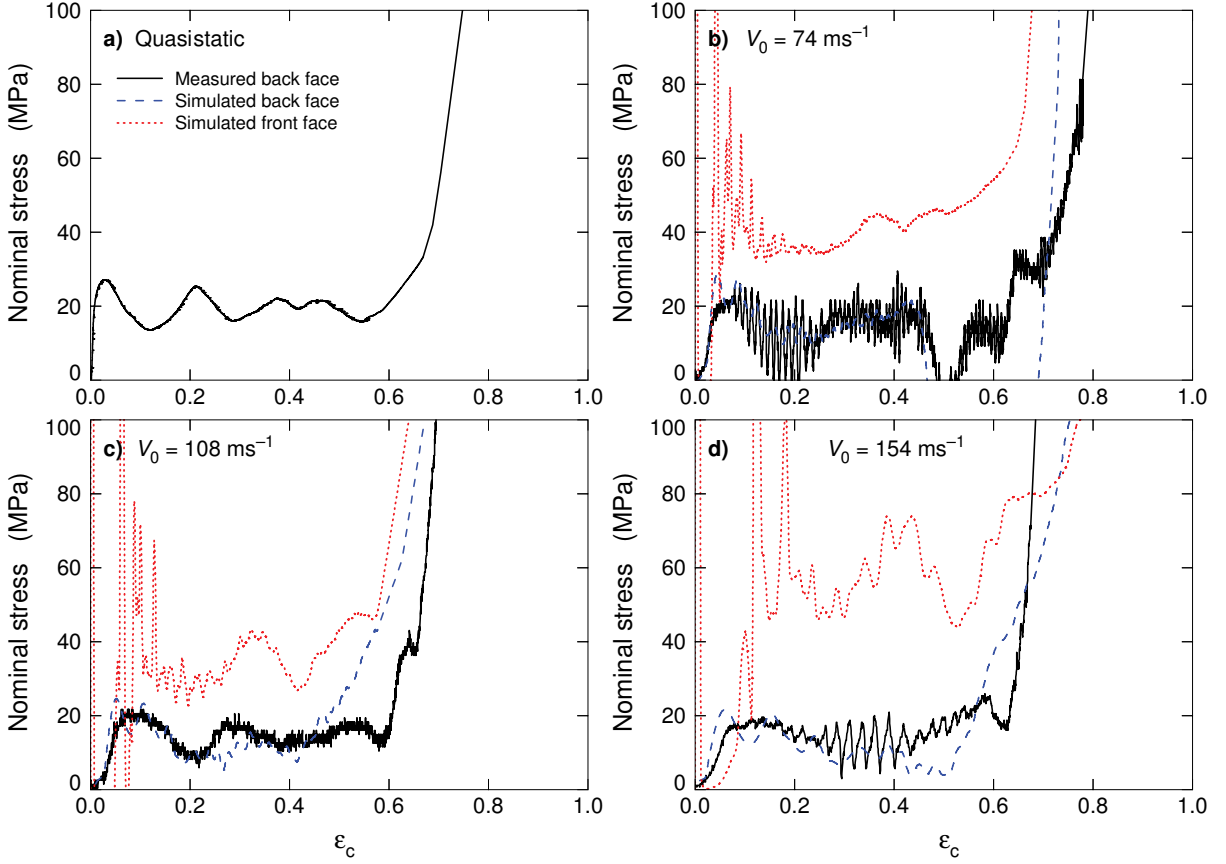


Figure 18. The measured and simulated dynamic stress versus normalized nominal strain responses of a three-dimensional tube structure that used out-of-plane tubes without notches. Its relative density was 21.0%. (a) Quasistatic response, and following impact at (b) 74 ms^{-1} , (c) 108 ms^{-1} , and (d) 154 ms^{-1} .

6. Discussion

Figure 20(a) summarizes dependence of the initial compressive peak stress, σ_p , for the three-dimensional notched structures and their components as a function of the impact velocity, v_0 , and applied strain rate, $\dot{\epsilon}_c = v_0/h$ (upper scale). The results confirm that the structures’ initial compressive strength is insensitive to the rate of loading for strain rates up to 2000 s^{-1} . Detailed observations indicate that the axial compression of single notched tubes proceeds by plastic compression of the tube walls followed by buckling at the notches and then of the tube segments between the notches; see Figures 6 and 7. The rotation of the tubes became increasingly relevant after crushing to strains of 20%, and was reduced by increasing the rate of compression, consistent with a [Calladine and English 1984] Type II structure. The suppression of the Type II behavior in rapidly compressed samples was linked with a rise in flow stress with plastic strain during plateau-region compression of single tubes and the three-dimensional structures that contained them (see Figure 13).

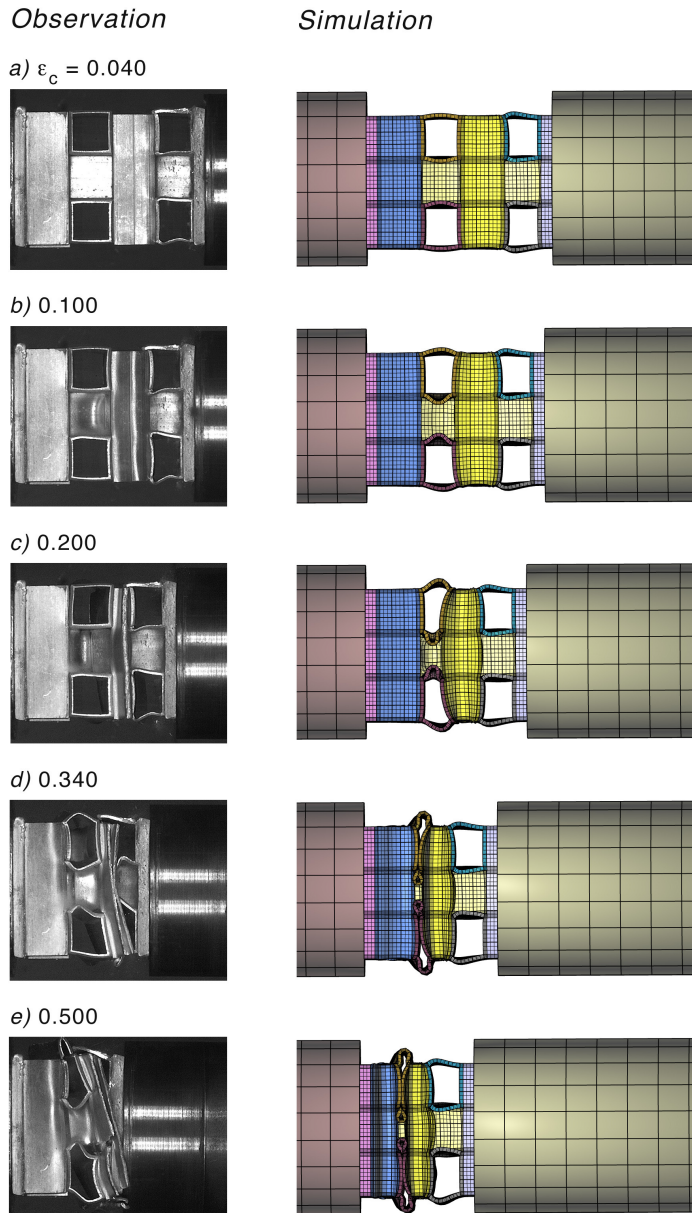


Figure 19. Observed and simulated deformation sequence for a three-dimensional specimen whose four vertical tubes had no notches in the axial aligned tube. The sample relative density was 21.0%, and it was impacted at an initial velocity $v_0 = 74 \text{ ms}^{-1}$.

The $[0/90^\circ]_2$ in-plane tube structures failed by plastic buckling of the tubes walls aligned with the crush direction, and was accompanied by three significant load drops. At low impact velocities, lateral displacement of the tubes (transverse to the loading direction) also occurred. As this lateral displacement was suppressed at higher impact velocities, the drop in load was reduced and the average stress prior to densification increased; see [Figure 10](#).

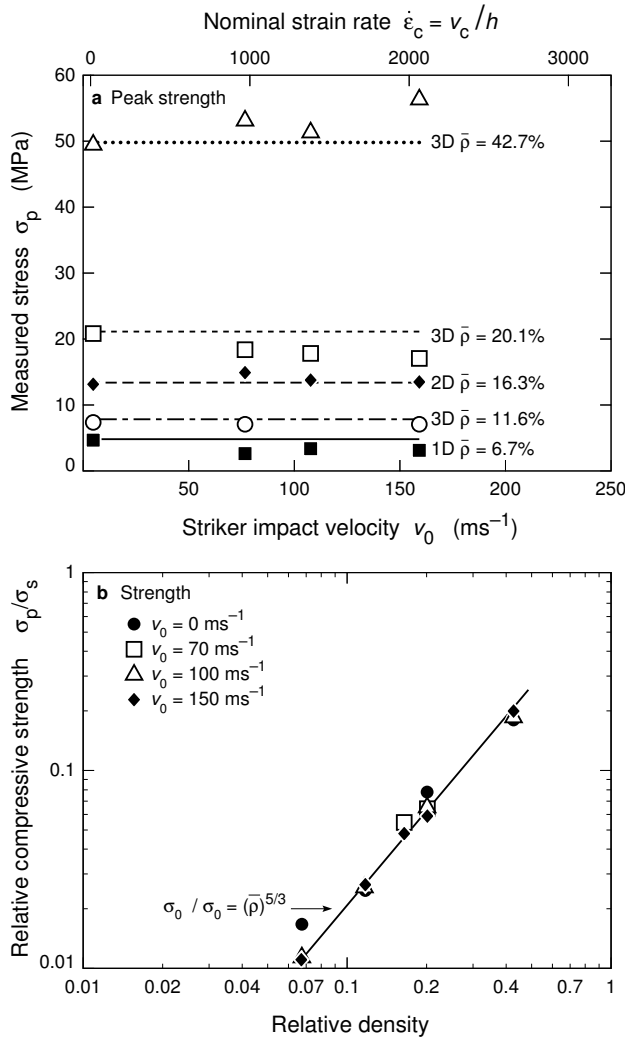


Figure 20. (a) Measured back-face stresses for the notched tube core structures as a function of impact velocity on applied strain rate for the initial stress profile peak. The horizontal dashed lines correspond to an extension of the quasistatic strength. (b) Dependence of compressive strength upon relative density with an empirical fit.

The combination of the notched vertical tubes and $[0/90^\circ]_2$ lay-up to form the three-dimensional structure resulted in an increase in plastic energy absorption that significantly exceeded the sum of the energy absorptions of the individual vertical tubes and two-dimensional lay-up; see Table 5. Analysis of the finite element simulations has revealed that it was a result of suppression of the vertical notched tubes' rotation by the in-plane tubes. The axial strain was then achieved by a greater contribution from plastic compression of the tubes' walls — a more energy-absorbing mechanism than rotation.

Removal of the notches from the vertical tubes increased the axial compressive strength of the tubes. Their mode of compression when made from an alloy in its peak aged state was highly dependent upon the orientation of tubes. The small misalignments present in experiments resulted in a low-order buckling

mode during initial deformation, followed by rotation and progressive fragmentation. Numerous load drops associated with the fragmentation were observed, and the rotation resulted in a general reduction in compression resistance. Inserting the unnotched tubes in the three-dimensional structure increased the strength of the structure over that of a similar-density three-dimensional structure containing notched tubes, and led to a synergistic effect upon the energy absorption. In this case, detailed analysis of the finite element simulations revealed that the in-plane tubes suppressed rotation and forced the vertical tubes to concertina buckle with additional energy absorption.

Figure 20(b) shows that the variation in peak strength, σ_p , of the notched three-dimensional structures with relative densities between 11 and 43% scaled by the strength of the alloy, σ_s , from which they are made. The strength exhibits a power dependence upon relative density:

$$\sigma_p/\sigma_s = (\bar{\rho})^{5/3}. \quad (4)$$

This agrees with both the experimental data and FE predictions for the structures tested quasistatically [Holloman et al. 2013]. The dynamically tested structures at all tested impact velocities scale with relative density to the power 5/3, and like the quasistatic results, this suggests the response is dominated by the out-of-plane tubes. By tailoring the in and out-of plane tube walls the three-dimensional structure can be made anisotropic and the compressive strengths will be based on the power law, (4), as shown quasistatically in [Holloman et al. 2013].

The simulation procedure used here has successfully modeled both the rear-face pressure versus compression strain response and the mechanisms of core collapse. It was therefore used to estimate the front (impact) face contact pressure which was not measured in these experiments. During an impact, the contact pressure and frontal displacement determine the work done by the impact mitigators. The simulations indicate that the ratio of the front to rear-face pressure is linearly related to the impact velocity and inversely dependent upon the relative density of the cellular structure; see Figure 21. However, the front-face pressure is much higher than that at the rear of the specimens and increases with both core density and impact velocity, suggesting that this structure may be well suited for mitigating high-intensity dynamic loads.

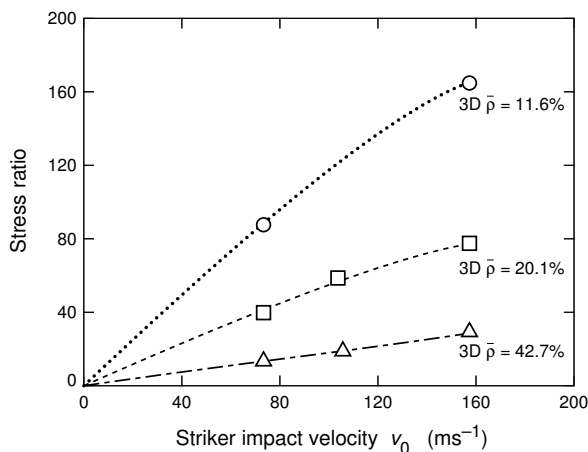


Figure 21. Simulated stress ratio based on the initial peak stress calculated for the front and back faces of the sandwich structures with notched cores.

7. Conclusion

We have fabricated aluminum 6061-T6 sandwich-panel structures with cores made from a two-dimensional $[0^\circ/90^\circ]_2$ arrangement of tubes with either notched or unnotched orthogonal tubes inserted in the out-of-plane direction. The resulting three-dimensional tube cores had relative densities between 11 and 43%. A combination of instrumented Kolsky bar impact experiments, high-speed video imaging, and finite element simulations using a rate-dependent, piecewise-linear hardening model with a von Mises multiaxial yield surface and a simplified failure criterion were used to investigate the dynamic compressive response of the three-dimensional tube core sandwich structure and the two-dimensional and out-of-plane-tubes from which they were constructed. We have found that:

- (1) A three-dimensional tube structure of a given relative density has a near-constant crush strength to a strain of about 60%. The initial compressive strength is independent of impact velocity for compression strain rates up to 2000 s^{-1} , which was verified with the simulated model to be a consequence of the rate-independent plastic response of the aluminum 6061-T6 alloy.
- (2) The core strength exhibited a power-law dependence upon relative density, given by $\sigma_p/\sigma_s = (\bar{\rho})^{5/3}$, consistent with crush strengths controlled by the buckling of tubes oriented in the applied-load direction.
- (3) The vertical tube response of the tubes was rate-dependent due to tube rotation at low impact velocities.
- (4) The vertical tube collapse mode changes when placed inside the in-plane tube lay-up, leading to a synergistic interaction in the energy absorption between the colinear aligned and vertical tubes at dynamic loading, which was also observed with quasistatic loading.
- (5) The finite element simulations reveal that the ratio of the impact to back-face stresses increased with strain rate and core density, which is a valuable result for shock load mitigation problems.

8. Acknowledgements

The authors are grateful to the U.S. Office of Naval Research (ONR grant number N00014-07-1-0764) for financial support of this research. The program manager was Dr. David Shifler.

References

- [Abramowicz and Jones 1997] W. Abramowicz and N. Jones, “Transition from initial global bending to progressive buckling of tubes loaded statically and dynamically”, *Int. J. Impact Eng.* **19**:5–6 (1997), 415–437.
- [Allen 1969] H. G. Allen, *Analysis and design of structural sandwich panels*, Pergamon, Oxford, 1969.
- [Baumeister et al. 1997] J. Baumeister, J. Banhart, and M. Weber, “Aluminium foams for transport industry”, *Mater. Des.* **18**:4–6 (1997), 217–220.
- [Bitzer 1997] T. Bitzer, *Honeycomb technology: materials, design, manufacturing, applications and testing*, 1st ed., Chapman & Hall, London, 1997.
- [Calladine and English 1984] C. R. Calladine and R. W. English, “Strain-rate and inertia effects in the collapse of two types of energy-absorbing structure”, *Int. J. Mech. Sci.* **26**:11–12 (1984), 689–701.
- [Cockcroft and Latham 1968] M. G. Cockcroft and D. J. Latham, “Ductility and workability of metals”, *J. Inst. Met.* **96**:1 (1968), 33–39.
- [Dannemann and Lankford 2000] K. A. Dannemann and J. Lankford, Jr., “High strain rate compression of closed-cell aluminium foams”, *Mater. Sci. Eng. A* **293**:1–2 (2000), 157–164.

- [Deshpande and Fleck 2000] V. S. Deshpande and N. A. Fleck, “High strain rate compressive behaviour of aluminium alloy foams”, *Int. J. Impact Eng.* **24**:3 (2000), 277–298.
- [Deshpande and Fleck 2005] V. S. Deshpande and N. A. Fleck, “One-dimensional response of sandwich plates to underwater shock loading”, *J. Mech. Phys. Solids* **53**:11 (2005), 2347–2383.
- [Dharmasena et al. 2009] K. P. Dharmasena, D. T. Queheillalt, H. N. G. Wadley, Y. C. Chen, P. Dudt, D. Knight, Z. Wei, and A. G. Evans, “Dynamic response of a multilayer prismatic structure to impulsive loads incident from water”, *Int. J. Impact Eng.* **36**:4 (2009), 632–643.
- [Dharmasena et al. 2011] K. P. Dharmasena, H. N. G. Wadley, K. Williams, Z. Xue, and J. W. Hutchinson, “Response of metallic pyramidal lattice core sandwich panels to high intensity impulsive loading in air”, *Int. J. Impact Eng.* **38**:5 (2011), 275–289.
- [Dharmasena et al. 2013] K. P. Dharmasena, H. N. G. Wadley, T. Liu, and V. S. Deshpande, “The dynamic response of edge clamped plates loaded by spherically expanding sand shells”, *Int. J. Impact Eng.* **62** (2013), 182–195.
- [Elzey and Wadley 2001] D. M. Elzey and H. N. G. Wadley, “The limits of solid state foaming”, *Acta Mater.* **49**:5 (2001), 849–859.
- [Evans et al. 2001] A. G. Evans, J. W. Hutchinson, N. A. Fleck, M. F. Ashby, and H. N. G. Wadley, “The topological design of multifunctional cellular metals”, *Prog. Mater. Sci.* **46**:3–4 (2001), 309–327.
- [Ferri et al. 2006] E. Ferri, E. Antinucci, M. Y. He, J. W. Hutchinson, F. W. Zok, and A. G. Evans, “Dynamic buckling of impulsively loaded prismatic cores”, *J. Mech. Mater. Struct.* **1**:8 (2006), 1345–1365.
- [Fyllingen et al. 2010] Ø. Fyllingen, O. S. Hopperstad, A. G. Hanssen, and M. Langseth, “Modelling of tubes subjected to axial crushing”, *Thin-Walled Struct.* **48**:2 (2010), 134–142.
- [Hanssen and Olovsson 2013] A. G. Hanssen and L. Olovsson, “IMPETUS Afea Solver”, 2013, <http://www.impetus-afea.com/solver>.
- [Hanssen et al. 2000a] A. G. Hanssen, O. S. Hopperstad, and M. Langseth, “Static and dynamic crushing of square aluminium extrusions with aluminium foam filler”, *Int. J. Impact Eng.* **24**:4 (2000), 347–383.
- [Hanssen et al. 2000b] A. G. Hanssen, L. Lorenzi, K. K. Berger, O. S. Hopperstad, and M. Langseth, “A demonstrator bumper system based on aluminium foam filled crash boxes”, *Int. J. Crashworthiness* **5**:4 (2000), 381–392.
- [Hanssen et al. 2001] A. G. Hanssen, O. S. Hopperstad, and M. Langseth, “Design of aluminium foam-filled crash boxes of square and circular cross-sections”, *Int. J. Crashworthiness* **6**:2 (2001), 177–188.
- [Holloman et al. 2013] R. L. Holloman, V. S. Deshpande, A. G. Hanssen, K. M. Fleming, J. R. Scully, and H. N. G. Wadley, “Tubular aluminum cellular structures: fabrication and mechanical response”, *J. Mech. Mater. Struct.* **8**:1 (2013), 65–94.
- [Johnson 1972] W. Johnson, *Impact strength of materials*, Edward Arnold, London, 1972.
- [Kolsky 1949] H. Kolsky, “An investigation of the mechanical properties of materials at very high rates of loading”, *Proc. Phys. Soc. B* **62**:11 (1949), 676–700.
- [Kooistra et al. 2004] G. W. Kooistra, V. S. Deshpande, and H. N. G. Wadley, “Compressive behavior of age hardenable tetrahedral lattice truss structures made from aluminium”, *Acta Mater.* **52**:14 (2004), 4229–4237.
- [Kooistra et al. 2008] G. W. Kooistra, D. T. Queheillalt, and H. N. G. Wadley, “Shear behavior of aluminum lattice truss sandwich panel structures”, *Mater. Sci. Eng. A* **472**:1–2 (2008), 242–250.
- [Maiti et al. 1984] S. K. Maiti, L. J. Gibson, and M. F. Ashby, “Deformation and energy absorption diagrams for cellular solids”, *Acta Metall.* **32**:11 (1984), 1963–1975.
- [Moongkhamklang and Wadley 2010] P. Moongkhamklang and H. N. G. Wadley, “Titanium alloy lattice structures with millimeter scale cell sizes”, *Adv. Eng. Mater.* **12**:11 (2010), 1111–1116.
- [Pingle et al. 2011] S. M. Pingle, N. A. Fleck, V. S. Deshpande, and H. N. G. Wadley, “Collapse mechanism maps for a hollow pyramidal lattice”, *Proc. R. Soc. Lond. A* **467**:2128 (2011), 985–1011.
- [Queheillalt et al. 2000] D. T. Queheillalt, H. N. G. Wadley, B. W. Choi, and D. S. Schwartz, “Creep expansion of porous Ti-6Al-4V sandwich structures”, *Metall. Mater. Trans. A* **31**:1 (2000), 261–273.
- [Queheillalt et al. 2008] D. T. Queheillalt, Y. Murty, and H. N. G. Wadley, “Mechanical properties of an extruded pyramidal lattice truss sandwich structure”, *Scr. Mater.* **58**:1 (2008), 76–79.

- [Radford et al. 2007] D. D. Radford, G. J. McShane, V. S. Deshpande, and N. A. Fleck, “Dynamic compressive response of stainless-steel square honeycombs”, *J. Appl. Mech. (ASME)* **74**:4 (2007), 658–667.
- [Reid 1993] S. R. Reid, “Plastic deformation mechanisms in axially compressed metal tubes used as impact energy absorbers”, *Int. J. Mech. Sci.* **35**:12 (1993), 1035–1052.
- [Reyes 2008] G. Reyes, “Static and low velocity impact behavior of composite sandwich panels with an aluminum foam core”, *J. Compos. Mater.* **42**:16 (2008), 1659–1670.
- [Rimoli et al. 2011] J. J. Rimoli, B. Talamini, J. J. Wetzel, K. P. Dharmasena, R. Radovitzky, and H. N. G. Wadley, “Wet-sand impulse loading of metallic plates and corrugated core sandwich panels”, *Int. J. Impact Eng.* **38**:10 (2011), 837–848.
- [Russell et al. 2010] B. P. Russell, A. Malcom, H. N. G. Wadley, and V. S. Deshpande, “Dynamic compressive response of composite corrugated cores”, *J. Mech. Mater. Struct.* **5**:3 (2010), 477–493.
- [Shahdin et al. 2009] A. Shahdin, L. Mezeix, C. Bouvet, J. Morlier, and Y. Gourinat, “Fabrication and mechanical testing of glass fiber entangled sandwich beams: a comparison with honeycomb and foam sandwich beams”, *Compos. Struct.* **90**:4 (2009), 404–412.
- [Tian et al. 2007] J. Tian, T. J. Lu, H. P. Hodson, D. T. Queheillalt, and H. N. G. Wadley, “Cross flow heat exchange of textile cellular metal core sandwich panels”, *Int. J. Heat Mass Transf.* **50**:13–14 (2007), 2521–2536.
- [Vinson 1999] J. R. Vinson, *The behavior of sandwich structures of isotropic and composite materials*, Technomic, Lancaster, PA, 1999.
- [Wadley et al. 2003] H. N. G. Wadley, N. A. Fleck, and A. G. Evans, “Fabrication and structural performance of periodic cellular metal sandwich structures”, *Compos. Sci. Technol.* **63**:16 (2003), 2331–2343.
- [Wadley et al. 2007] H. N. G. Wadley, K. P. Dharmasena, D. T. Queheillalt, Y. C. Chen, P. Dudt, D. Knight, K. Kiddy, Z. Xue, and A. Vaziri, “Dynamic compression of square honeycomb structures during underwater impulsive loading”, *J. Mech. Mater. Struct.* **2**:10 (2007), 2025–2048.
- [Wadley et al. 2013] H. N. G. Wadley, T. Børvik, L. Olovsson, J. J. Wetzel, K. P. Dharmasena, O. S. Hopperstad, V. S. Deshpande, and J. W. Hutchinson, “Deformation and fracture of impulsively loaded sandwich panels”, *J. Mech. Phys. Solids* **61**:2 (2013), 674–699.
- [Wei et al. 2008] Z. Wei, V. S. Deshpande, A. G. Evans, K. P. Dharmasena, D. T. Queheillalt, H. N. G. Wadley, Y. V. Murty, R. K. Elzey, P. Dudt, Y. C. Chen, D. Knight, and K. Kiddy, “The resistance of metallic plates to localized impulse”, *J. Mech. Phys. Solids* **56**:5 (2008), 2074–2091.
- [Xue and Hutchinson 2004] Z. Xue and J. W. Hutchinson, “A comparative study of impulse-resistant metal sandwich plates”, *Int. J. Impact Eng.* **30**:10 (2004), 1283–1305.
- [Zok et al. 2004] F. W. Zok, S. A. Waltner, Z. Wei, H. J. Rathbun, R. M. McMeeking, and A. G. Evans, “A protocol for characterizing the structural performance of metallic sandwich panels: application to pyramidal truss cores”, *Int. J. Solids Struct.* **41**:22–23 (2004), 6249–6271.
- [Zok et al. 2005] F. W. Zok, H. J. Rathbun, M. He, E. Ferri, C. Mercer, R. M. McMeeking, and A. G. Evans, “Structural performance of metallic sandwich panels with square honeycomb cores”, *Philos. Mag.* **85**:26–27 (2005), 3207–3234.

Received 27 Jul 2013. Accepted 26 Dec 2013.

RYAN L. HOLLOMAN: rlh5v@virginia.edu

Department of Materials Science and Engineering, University of Virginia, P.O. Box 400240, 351 McCormick Rd, Charlottesville, VA 22903-4240, United States

KARTHIKEYAN KANDAN: kk412@cam.ac.uk

Department of Engineering, Cambridge University, Trumpington Street, Cambridge, CB2 1PZ, United Kingdom

VIKRAM DESHPANDE: vsd20@cam.ac.uk

Department of Engineering, Cambridge University, Trumpington Street, Cambridge, CB2 1PZ, United Kingdom

HAYDN N. G. WADLEY: haydn@virginia.edu

Department of Materials Science and Engineering, University of Virginia, P.O. Box 400240, 351 McCormick Rd, Charlottesville, VA 22903-4240, United States

DYNAMIC RESPONSE OF TWIN LINED SHELLS DUE TO INCIDENT SEISMIC WAVES

J. P. DWIVEDI, V. P. SINGH AND RADHA KRISHNA LAL

The dynamic interaction of the twin shells subjected to seismic waves is investigated numerically. It is found that the three-dimensional response of twin shells may differ significantly from the two-dimensional response, and that through-soil interaction between the shells may also be significant.

1. Introduction

The dynamic response of buried pipelines and subway shells for structural stability during earthquakes is important when those structures can potentially be subjected to seismic ground motion. The amplification of seismic motions and stress concentrations may occur as a result of wave scattering around such structures. Mow and Pao [1973] were among the first to study wave diffraction around a cylindrical cavity in an infinite medium and the resulting stress concentration using wave function expansions. An analytic model was presented in [Trifunac 1972] to study horizontal polarized shear (SH) wave scattering at a semicylinder located at the boundary of a half-space. SH wave scattering for various topographies has also been studied in [Wong and Jennings 1975]. Chin et al. [1987] and Liu et al. [1991] studied the response of pipelines buried in back-filled trenches. In reality, many underground structures are constructed in close proximity and the interaction between such closely spaced structures may be significant [Okumura et al. 1992; Guan and Moore 1994]. The purpose of this paper is to investigate the three-dimensional response of a pair of lined cylindrical cavities located in a full-space subjected to incident seismic waves.

2. Governing equations

The geometry of the problem is as shown in Figure 1. The parallel twin shells, denoted I and II, are deeply buried in a viscoelastic ground material described by the shear modulus μ , mass density ρ , and Poisson's ratio σ . The material properties for the linings are described by the sets of variables μ_I , ρ_I , and σ_I and μ_{II} , ρ_{II} , and σ_{II} . For convenience, the index indicating the medium or shell lining is omitted in (2-1)–(2-9), which are valid for each of these three different materials. The displacements and stresses in these solids can be expressed in terms of potentials ϕ , ψ , and χ , which satisfy the following wave equations of motion:

$$\nabla^2 \phi + k_\alpha^2 \phi = 0, \quad k_\alpha = \frac{\omega}{\nu_L}, \quad (2-1)$$

$$\nabla^2 \psi + k_\beta^2 \psi = 0, \quad (2-2)$$

Radha Krishna Lal is the corresponding author.

Keywords: seismic waves, multiple successive reflections, shells.

$$\nabla^2 \chi + k_\beta^2 \chi = 0, \quad k_\beta = \frac{\omega}{v_L}, \tag{2-3}$$

where ω is the excitation frequency, v_L and v_T denote the longitudinal and transverse wave velocities, and ∇^2 is the Laplace operator in polar cylindrical coordinates.

The factor $e^{-i\omega(t-t_0)}$ is omitted in the text. The general solutions of (2-1), (2-2), and (2-3) take the following forms:

$$\begin{aligned} \phi(r, \theta, z) &= \sum_{n=0}^{\infty} \phi_n = \sum_{n=0}^{\infty} H_n(\alpha_L r) \begin{Bmatrix} \cos n\theta \\ \sin n\theta \end{Bmatrix} \left(\begin{Bmatrix} A \\ B \end{Bmatrix}_n e^{\pm i\gamma_L z} \right) \\ &= \sum_{n=0}^{\infty} H_n(\alpha_L r) (A_n \cos n\theta + B_n \sin n\theta) e^{\pm i\gamma_L z}, \end{aligned} \tag{2-4}$$

$$\begin{aligned} \psi(r, \theta, z) &= \sum_{n=0}^{\infty} \psi_n = \sum_{n=0}^{\infty} H_n(\alpha_T r) \begin{Bmatrix} \cos n\theta \\ \sin n\theta \end{Bmatrix} \left(\begin{Bmatrix} C \\ D \end{Bmatrix}_n e^{\pm i\gamma_T z} \right) \\ &= \sum_{n=0}^{\infty} H_n(\alpha_T r) (C_n \cos n\theta + D_n \sin n\theta) e^{\pm i\gamma_T z}, \end{aligned} \tag{2-5}$$

$$\begin{aligned} \chi(r, \theta, z) &= \sum_{n=0}^{\infty} \chi_n = \sum_{n=0}^{\infty} H_n(\alpha_T r) \begin{Bmatrix} \cos n\theta \\ \sin n\theta \end{Bmatrix} \left(\begin{Bmatrix} E \\ F \end{Bmatrix}_n e^{\pm i\gamma_T z} \right) \\ &= \sum_{n=0}^{\infty} H_n(\alpha_T r) (E_n \cos n\theta + F_n \sin n\theta) e^{\pm i\gamma_T z}, \end{aligned} \tag{2-6}$$

where H_n are the Bessel functions that satisfy the radiation conditions. Bessel functions of the first kind are used for the liners, and the outgoing wave in the medium is expressed in terms of Hankel functions

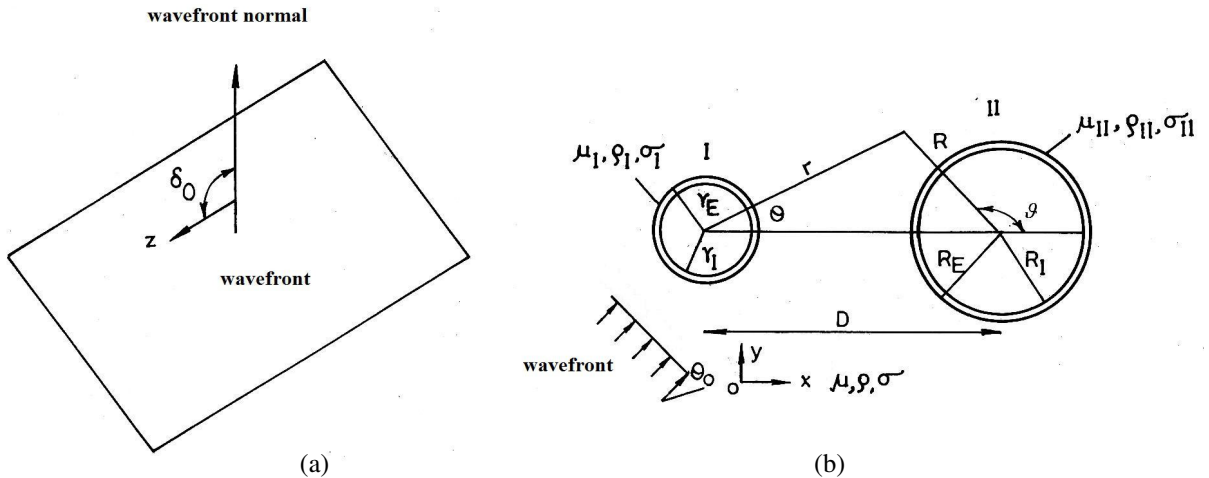


Figure 1. Geometry of the problem.

of the first kind. The wave numbers α_ν ($\nu = L, T$) are given by

$$\alpha_L = \sqrt{\frac{\omega^2}{v_L^2 - \gamma_L^2}}, \quad (2-7)$$

$$\alpha_T = \sqrt{\frac{\omega^2}{v_T^2 - \gamma_T^2}}. \quad (2-8)$$

At the interface between the linings and the medium, the continuity and equilibrium conditions will be enforced:

$$(u_r^{(I)}, u_\theta^{(I)}, u_z^{(I)}) = (u_r, u_\theta, u_z), \quad (2-9)$$

$$(u_r^{(II)}, u_\theta^{(II)}, u_z^{(II)}) = (u_r, u_\theta, u_z), \quad (2-10)$$

$$(\sigma_{rr}^{(I)}, \sigma_{r\theta}^{(I)}, \sigma_{rz}^{(I)}) = (\sigma_{rr}, \sigma_{r\theta}, \sigma_{rz}), \quad (2-11)$$

$$(\sigma_{rr}^{(II)}, \sigma_{r\theta}^{(II)}, \sigma_{rz}^{(II)}) = (\sigma_{rr}, \sigma_{r\theta}, \sigma_{rz}). \quad (2-12)$$

For the problem specified in [Figure 1](#), the wave field consists of the incident seismic waves and the waves scattered by shells I and II:

$$\phi = \phi^i + \phi^I(r, \theta, z) + \phi^{II}(R, \vartheta, z), \quad (2-13)$$

$$\psi = \psi^i + \psi^I(r, \theta, z) + \psi^{II}(R, \vartheta, z), \quad (2-14)$$

$$\chi = \chi^i + \chi^I(r, \theta, z) + \chi^{II}(R, \vartheta, z), \quad (2-15)$$

where the superscript i denotes the incident seismic wave.

2.1. Coordinate system transform. In the numerical analysis, the interaction between the two shells is considered by coordinate system transformations ([Figure 1\(b\)](#)). The coordinate transformations from (r, θ) to (R, ϑ) and from (R, ϑ) to (r, θ) are [[Watson 1944](#)]

$$H_n(\alpha_\nu r) \cos n\theta = \sum_{m=0}^{\infty} \frac{\epsilon_m}{2} (H_{n-m}(\alpha_\nu D) \pm (-1)^m H_{n+m}(\alpha_\nu D)) J_m(\alpha_\nu R) \cos m\vartheta, \quad (2-16)$$

$$H_n(\alpha_\nu r) \sin n\theta = \sum_{m=0}^{\infty} \frac{\epsilon_m}{2} (H_{n-m}(\alpha_\nu D) \pm (-1)^m H_{n+m}(\alpha_\nu D)) J_m(\alpha_\nu R) \sin m\vartheta, \quad (2-17)$$

and

$$H_n(\alpha_\nu R) \cos n\vartheta = \sum_{m=0}^{\infty} \frac{\epsilon_m}{2} (H_{m-n}(\alpha_\nu D) \pm (-1)^n H_{m+n}(\alpha_\nu D)) J_m(\alpha_\nu r) \cos m\theta, \quad (2-18)$$

$$H_n(\alpha_\nu R) \sin n\vartheta = \sum_{m=0}^{\infty} \frac{\epsilon_m}{2} (H_{m-n}(\alpha_\nu D) \pm (-1)^m H_{m+n}(\alpha_\nu D)) J_m(\alpha_\nu r) \sin m\theta, \quad (2-19)$$

where

$$\epsilon_m = \begin{cases} 1 & \text{if } m = 0, \\ 2 & \text{if } m = 1, 2, \dots \end{cases} \quad (2-20)$$

2.2. Incident seismic wave. The incident seismic wave can be expressed in terms of potentials. The incident P wave and S wave potentials can be written as

$$\phi^i = \phi_0 \exp(ik_\alpha \sin \delta_0(x \cos \theta_0) + y \sin \theta_0 + ik_\alpha z \cos \delta_0 - i\omega(t - t_0)), \tag{2-21}$$

$$\psi^i = \psi_0 \exp(ik_\beta \sin \delta_0(x \cos \theta_0) + y \sin \theta_0 + ik_\beta z \cos \delta_0 - i\omega(t - t_0)), \tag{2-22}$$

$$\chi^i = \chi_0 \exp(ik_\beta \sin \delta_0(x \cos \theta_0) + y \sin \theta_0 + ik_\beta z \cos \delta_0 - i\omega(t - t_0)), \tag{2-23}$$

where δ_0 is the angle of the wavefront normal to the z -axis (see [Figure 1\(a\)](#)), while θ_0 is the angle that the normal of the intersection between the XOY plane and the wavefront makes with the x -axis (see [Figure 1\(b\)](#)).

Expressing the wave potentials in polar coordinates yields

$$\phi^i = \phi_0 \sum_{m=0}^{\infty} \frac{\epsilon_m}{2} (i)^m J_m(k_\alpha r \sin \delta_0) (A_{0,m} \cos m\theta + B_{0,m} \sin m\theta) \exp(ik_\alpha z \cos \delta_0 - i\omega(t - t_0)), \tag{2-24}$$

$$\psi^i = \psi_0 \sum_{m=0}^{\infty} \frac{\epsilon_m}{2} (i)^m J_m(k_\beta r \sin \delta_0) (A_{0,m} \cos m\theta + B_{0,m} \sin m\theta) \exp(ik_\beta z \cos \delta_0 - i\omega(t - t_0)), \tag{2-25}$$

$$\chi^i = \chi_0 \sum_{m=0}^{\infty} \frac{\epsilon_m}{2} (i)^m J_m(k_\beta r \sin \delta_0) (A_{0,m} \cos m\theta + B_{0,m} \sin m\theta) \exp(ik_\beta z \cos \delta_0 - i\omega(t - t_0)), \tag{2-26}$$

where

$$A_{0,m} = \frac{\epsilon_m}{2} (i)^m \cos m\theta_0, \quad B_{0,m} = \frac{\epsilon_m}{2} (i)^m \sin m\theta_0, \tag{2-27}$$

and J_m is a Bessel function of the first kind. Stresses τ_{rr} , $\tau_{\theta\theta}$, and $\tau_{r\theta}$ and displacements u_r and u_θ in the medium can be evaluated in terms of potentials (for example, in [[Achenbach 1973](#)]).

The potentials in (2-13)–(2-15) must satisfy the stress-free boundary conditions at the half-space and cavity surfaces:

$$\tau_{xy} = \tau_{yy} = 0 \text{ at } y = 0, \quad \tau_{r\theta} = \tau_{rr} = 0 \text{ at } r = r_1, \quad \tau_{R\vartheta} = \tau_{RR} = 0 \text{ at } R = R_1, \tag{2-28}$$

since ψ^i , χ^i , and ϕ^i already satisfy the stress-free conditions at $y = 0$.

2.3. Method of successive reflections. The approaches of Thiruvengatachar and Viswanathan and Scheidl and Ziegler are used as follows:

- (1) The incoming wave from shell II is assumed to be zero. Using the boundary conditions, the waves in the lining and the outgoing wave in the medium are determined at shell I.
- (2) Using the boundary conditions, the waves in the lining and the outgoing wave in the medium at shell II are obtained. The incoming wave from shell I is then included using the coordinate transform of the outgoing wave at shell I.
- (3) The waves in the lining and the outgoing wave in the medium at shell I are reevaluated with the incoming wave from shell II included.
- (4) Steps (2) and (3) are repeated until the solution converges.

2.4. Convergence. Following the convergence of the method of successive reflections by Thiruvengat-achar and Vishwanathan for wave scattering by a cylinder in a half-space, the convergence of the method is now examined for the specific case of two unlined cavities. Attention is focused on the response of cavity I as a result of the incident wave boundary conditions and wave reflection between the two cavities.

Therefore, with the incoming wave from cavity II excluded, a constant k_I can be found for the upper bound of the outgoing wave coefficients due to unit incident waves:

$$(|A_n^I|, |B_n^I|, |C_n^I|, |D_n^I|, |E_n^I|, |F_n^I|) < k_I \frac{(r\alpha/2)^{2n}}{(n!)^2} (n+1), \quad n = 0, 1, 2, \dots, \quad (2-29)$$

where α is the maximum of $|\alpha_L|$ and $|\alpha_T|$.

Substituting (2-29) into (2-16) and (2-17), it is then possible to find a positive number k_D so that the following inequality holds for the incoming wave coefficients for cavity II:

$$(|a_m^{II}|, |b_m^{II}|, |c_m^{II}|, |d_m^{II}|, |e_m^{II}|, |f_m^{II}|) < k_I k_D \sum_{k=0}^{\infty} \epsilon_m \frac{(r_i \alpha/2)^{2k} (k+1)(m+k-1)!}{(D\alpha/2)^{(m+k)} (k!)^2}. \quad (2-30)$$

Similarly, the coefficients of the outgoing wave of cavity II are bounded as follows:

$$(|A_m^{II}|, |B_m^{II}|, |C_m^{II}|, |D_m^{II}|, |E_m^{II}|, |F_m^{II}|) < k_I k_D k_{II} \sum_{k=0}^{\infty} \epsilon_m \frac{(r_i R_i \alpha^2/2)^{2(k+m)} (m+k-1)!(k+1)(m+1)}{(D\alpha/2)^{(m+k)} (k!)^2 (m!)^2}. \quad (2-31)$$

The incoming wave for cavity I can be obtained from the outgoing wave from cavity II using the coordinate transform once more:

$$(|a_n^I|, |b_n^I|, |c_n^I|, |d_n^I|, |e_n^I|, |f_n^I|) < k_I k_D^2 k_{II} \sum_{m=0}^{\infty} \epsilon_n \sum_{k=0}^{\infty} \epsilon_m \frac{(r_i R_i \alpha^2/4)^{2(k+m)} (m+k-1)!(m+n-1)!(k+1)(m+1)}{(D\alpha/2)^{(2m+k+n)} (k!)^2 (m!)^2}. \quad (2-32)$$

It can be proved that the series defined by

$$k_D^n = k_D^2 \sum_{m=0}^{\infty} \epsilon_n \sum_{k=0}^{\infty} \epsilon_m \frac{(r_i R_i \alpha^2/4)^{2(k+m)} (m+k-1)!(m+n-1)!(k+1)(m+1)}{(D\alpha/2)^{(2m+k+n)} (k!)^2 (m!)^2} \quad (2-33)$$

is uniformly convergent for a given n . Hence, the outgoing wave for cavity I (with incoming wave from cavity II included) is subject to

$$(|A_n^I|, |B_n^I|, |C_n^I|, |D_n^I|, |E_n^I|, |F_n^I|) < k_I (1 + k_I k_D^n k_{II}) \frac{(r_i \alpha^2/2)^{2n}}{(n!)^2}. \quad (2-34)$$

Following m iterations of the method of successive reflections, the outgoing wave of cavity I gives

$$(|A_n^I|, |B_n^I|, |C_n^I|, |D_n^I|, |E_n^I|, |F_n^I|) < \sum_{j=0}^{\infty} k_I (k_I k_D^n k_{II}) \frac{(r_i \alpha/2)^{2n}}{(n!)^2} = k_I \frac{1 - (k_I k_D^n k_{II})^{(m+1)}}{1 - k_I k_D^n k_{II}} \frac{(r_i \alpha/2)^{2n}}{(n!)^2}. \quad (2-35)$$

The method of successive reflections therefore converges provided $k_I k_D^n k_{II} < 1$. The spacing D between the two cavities in (2-33) can be changed for a given r_i and R_i so that $k_I k_D^n k_{II} < 1$. Therefore the

procedure converges if either of the following two conditions is satisfied:

- (1) The wavelength is long enough or there is sufficient spacing between the two cavities.
- (2) The $k_I k_D^n k_{II} < 1$ values for the dominant terms (for example, $n = 2$) are particularly small ($k_I k_D^n k_{II} \ll 1$).

It is remarkable to note that, in some specific problems, the expected divergence may also be removed by a large number of iterations of the technique applied in this paper.

3. Numerical study

3.1. Geometry. The response of the twin lined shells to seismic ground motion is clearly a function of a considerable number of geometrical and material properties. In order to simplify this study, the response will be examined for shells of equal radius ($r_i = R_i$) and with identical linings ($r_e = R_e, \mu = \mu_I = \mu_{II}$). The Poisson's ratios for the medium and liners are 0.30 and 0.35, respectively. Furthermore, the center-to-center spacing of the shells will be taken as $D = 3.50r_i, 4.50r_i$, or ∞ , and the liner thickness, $r_e - r_i = r_i/8$, and the incident seismic waves examined will be parallel to either the YOZ ($\theta_0 = \pi/2$) or the XOZ ($\theta_0 = 0$) plane. The two shells have axes parallel to z , so that for $\theta_0 = \pi/2$ the shells have symmetric response about the YOZ plane and only one shell response needs to be reported. Alternatively, for $\theta_0 = 0$ the shell responses are different but symmetric about the horizontal diameters. For all the results presented, the displacements and stresses are normalized by k_β and μk_β^2 , respectively.

3.2. Incident S wave: interaction between the shells. To examine the interaction of the two shells, Figure 2 shows predictions of the normalized hoop stress for shells at three different spacings, $D/r_i = 3.50, 4.50$, and ∞ , and for two different incident angles, $\delta_0 = \pi/2$ and $\delta_0 = \pi/3$. To determine the effect of the frequency of the seismic ground motion, a range of normalized vibration frequencies $a_0 = \omega r_i / v_T$ is considered.

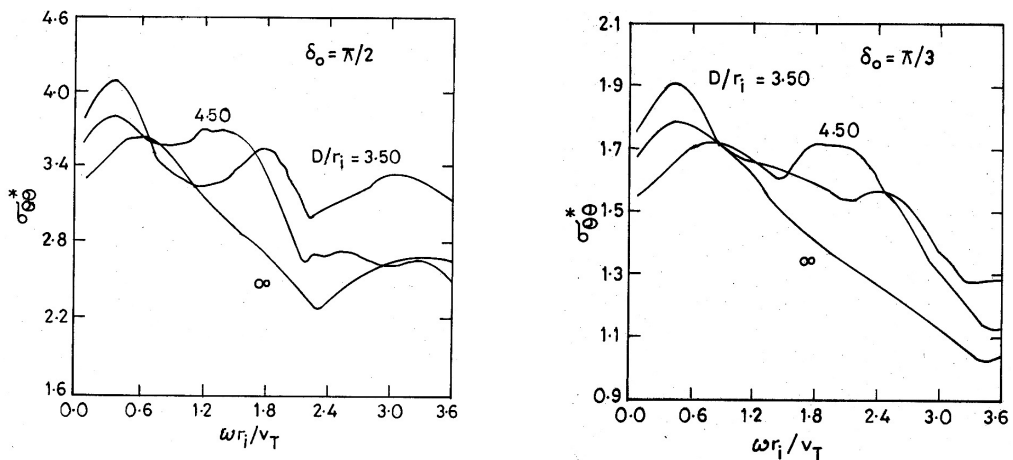


Figure 2. Maximum stress versus normalized frequency: response to incident S waves at the inside surface of the liner, at position $z = 0$ ($\theta_0 = \pi/2, \mu/\mu_m = 3$) for $\delta_0 = \pi/2$ (left) and $\delta_0 = \pi/3$ (right).

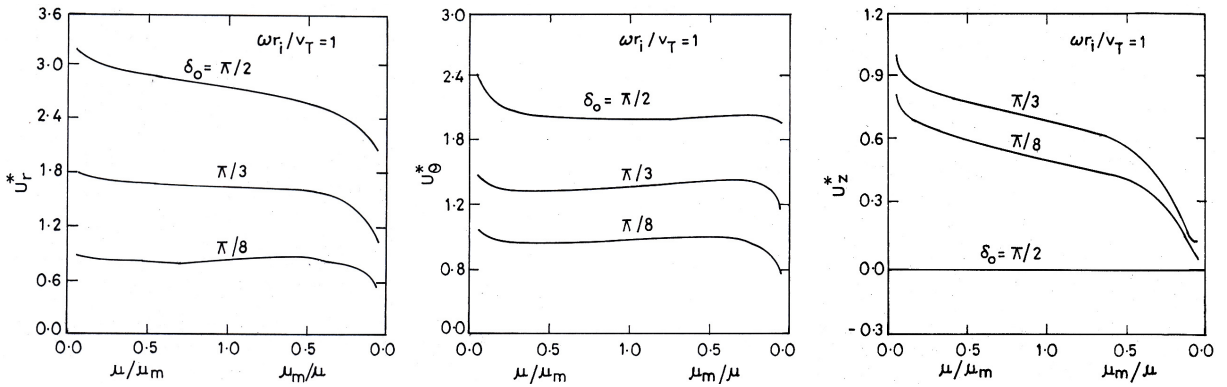


Figure 3. Maximum displacements U_r^* (left), U_θ^* (middle), and U_z^* (right) versus normalized frequency: response to incident S waves at the outside surface of the liner, at position $z = 0$ ($\theta_0 = 0$, $D/r_i = 3.50$).

At low vibration frequency, $a_0 < 0.5$, the shell-to-shell interaction for all three shell spacings is insignificant. As normalized frequency a_0 increases, however, the shell response becomes significantly influenced by the spacing. For $0.5 < a_0 < 2.5$, the hoop stress $\sigma_{\theta\theta}^*$ is up to 35% less for an isolated shell $D/r_i = \infty$ than for $D/r_i = 3.50, 4.50$. For shells with $D < 3r_i$, the increase in hoop stress due to through-soil interaction is expected to be even more important.

3.3. Incident S wave: influence of lining modulus. To examine the influence of lining design, **Figure 3** shows solutions for the maximum normalized displacements U_r^* , U_θ^* , and U_z^* for the specific normalized frequency $a_0 = 1$, for a range of modular ratios μ/μ_m and for three different incident angles δ_0 . **Figure 4** shows solutions for the maximum normalized stresses $\sigma_{\theta\theta}^*$ and $\sigma_{\theta z}^*$ for the specific normalized frequency $a_0 = 1$, for a range of modular ratios μ/μ_m and for three different incident angles δ_0 .

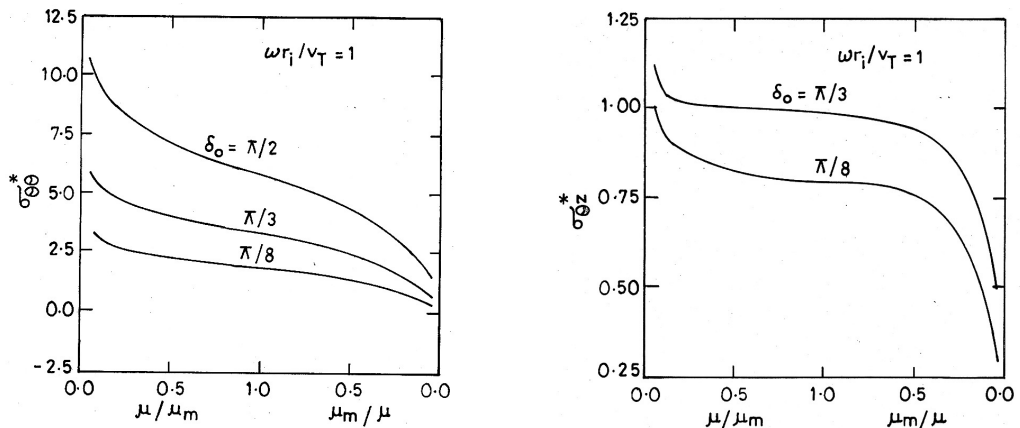


Figure 4. Maximum normalized stresses $\sigma_{\theta\theta}^*$ (left) and $\sigma_{\theta z}^*$ (right) versus normalized frequency: response to incident S waves at the inside surface of the liner, at position $z = 0$ ($\theta_0 = 0$, $D/r_i = 3.50$).

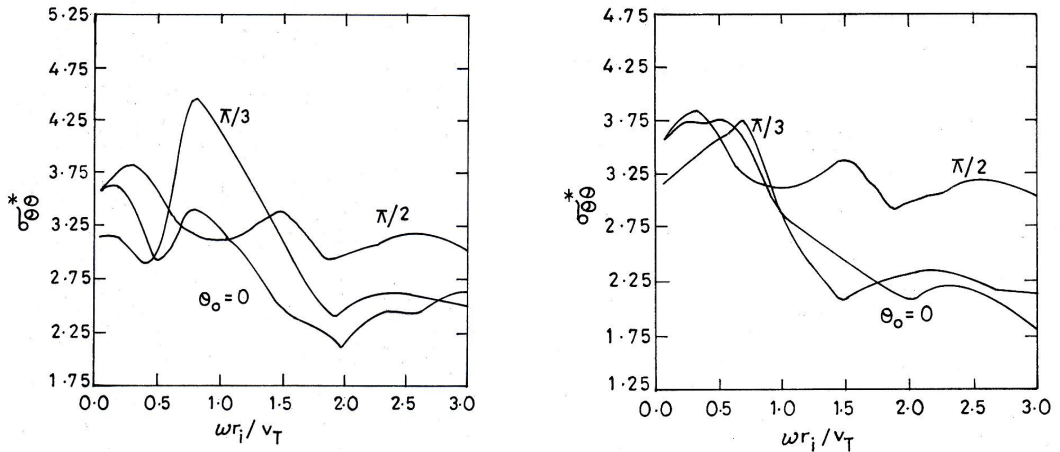


Figure 5. Maximum stress versus normalized frequency: response to incident S waves at the inside surface of the liner, at position $z = 0$ ($\delta_0 = \pi/2$, $\mu/\mu_m = 3$) for shells I (left) and II (right).

The normalized radial and circumferential displacements are the greatest responses under plane strain conditions, $\delta_0 = \pi/2$. They peak at low modulus ratio, μ/μ_m , but remain nearly constant when μ/μ_m ranges from 0.25 to 4. Normalized longitudinal displacement also decreases monotonically as μ/μ_m increases, but is generally more sensitive to any changes in the modular ratio.

Normalized stress amplitudes $\sigma_{\theta\theta}^*$ and $\sigma_{\theta z}^*$ at the inner surface of the lining all steadily decrease as the surrounding modulus, μ_m , decreases relative to that of liners μ . All values tend towards zero as modular ratio μ_m/μ approaches zero. As noted for the normalized displacement, the two-dimensional loading condition $\delta_0 = \pi/2$ induces the greatest stress. Circumferential stresses $\sigma_{\theta\theta}^*$ are largest in magnitude.

3.4. Incident S wave: influence of incident angle θ_0 . The behavior of the two shells is now examined under the plane strain condition ($\delta_0 = \pi/2$) with incident angles $\theta_0 = 0, \pi/3$, and $\pi/2$, and a range of vibration frequencies. The shells are spaced at distance $D/r_i = 3.50$ and have a lining modulus three times that of the ground medium ($\mu/\mu_m = 3$). Figure 5 shows the amplitude of the normalized stress $\sigma_{\theta\theta}^*$ for shells I and II.

For an isolated shell, the response is independent of the incident angle θ_0 . However, for these closely spaced shells, the response is significantly affected by the orientation of the incoming wave. Firstly, Figure 5 clearly shows that the effect of the incident angle θ_0 is frequency dependent. The circumferential stress $\sigma_{\theta\theta}^*$ of shell I has the greatest amplitude when $\theta_0 = \pi/3$ at the normalized frequency $a_0 = 0.8$. For larger values of normalized frequency, $a_0 > 1.5$, the responses are less frequency dependent and the vertically moving seismic wave ($\theta_0 = \pi/2$) induces the highest hoop stresses in both shells. For shell II the peak stress occurs when $0.2 < a_0 < 0.8$, but is not quite as great and is less dependent on θ_0 .

3.5. Incident P wave. Figure 6 shows normalized radial, circumferential, and longitudinal displacements for $\theta = \pi/2$, for three incident wave angles δ_0 and a range of the modular ratios. The trends are similar to those observed earlier for shell response to shear waves, but with stress and displacement amplitudes somewhat smaller. The response increases as the modular ratio increases. Figure 7 shows

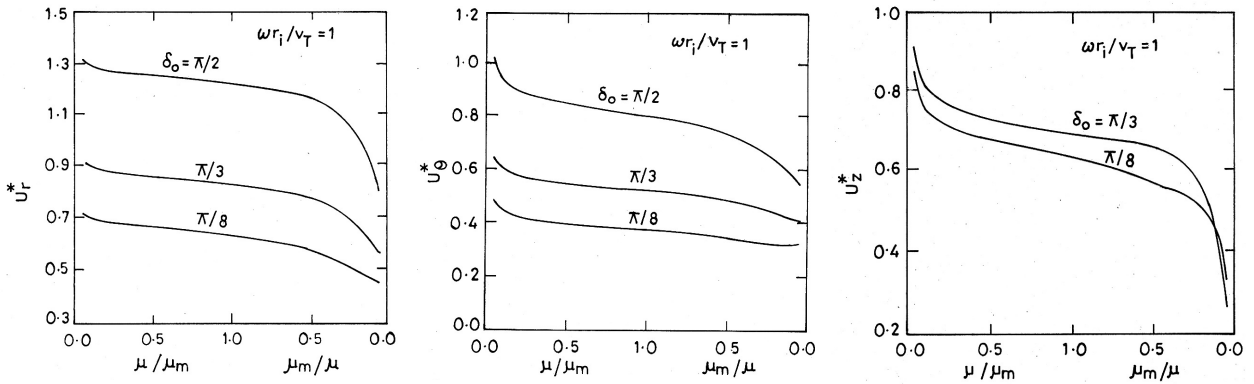


Figure 6. Maximum displacements U_r^* (left), U_θ^* (middle), and U_z^* (right) versus normalized frequency: response to incident P waves at the outside surface of the liner, at position $z = 0$ ($\theta_0 = \pi/2$, $D/r_i = 3.50$).

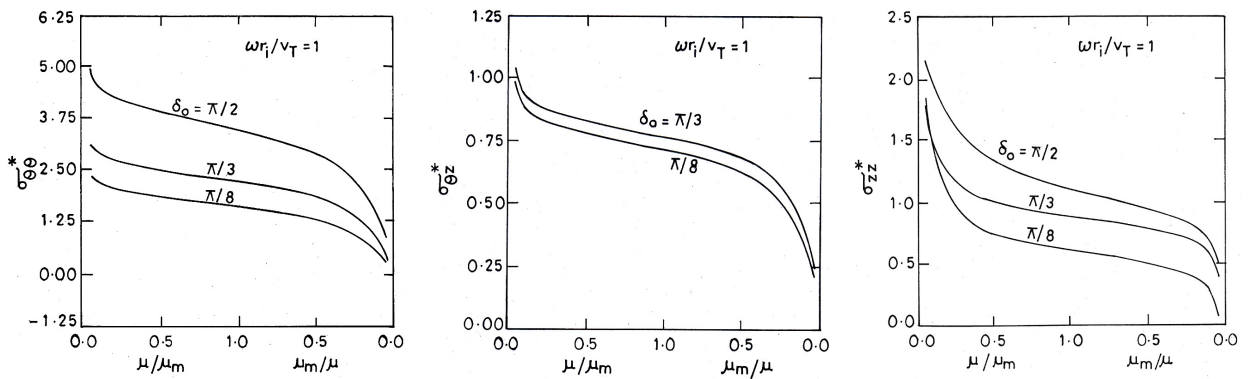


Figure 7. Maximum stresses $\sigma_{\theta\theta}^*$ (left), $\sigma_{\theta z}^*$ (middle), and σ_{zz}^* (right) versus normalized frequency; response to incident P waves at the inside surface of the liner, at position $z = 0$ ($\theta_0 = 0$, $D/r_i = 3.50$).

solutions for maximum normalized stresses $\sigma_{\theta\theta}^*$, $\sigma_{\theta z}^*$, and σ_{zz}^* for the specific normalized frequency $a_0 = 1$, for a range of modular ratios μ/μ_m and three different incident angles δ_0 . Compared to the normalized displacement amplitudes, the stresses are more sensitive to changes in the modular ratios.

3.6. Incident P wave: interaction between the shells. The interaction between the shells is shown in Figure 8 different angles, $\delta_0 = \pi/2$ and $\pi/4$. Unlike the prediction made for the shell response to an S wave, the hoop stress $\sigma_{\theta\theta}^*$ decreases rapidly as the frequency is increased. The through-soil interaction between the shells is not as significant as it is for an incident S wave. At most frequencies, the stress predictions for the closely spaced shells are higher than those for an isolated shell, though the difference is not very significant.

3.7. Incident P wave: influence of incident angle. Figure 9 shows the hoop stress response for shells I and II. The peak hoop stress is produced for an incident angle $\delta_0 = 0$ and a normalized frequency $a_0 = 1$.

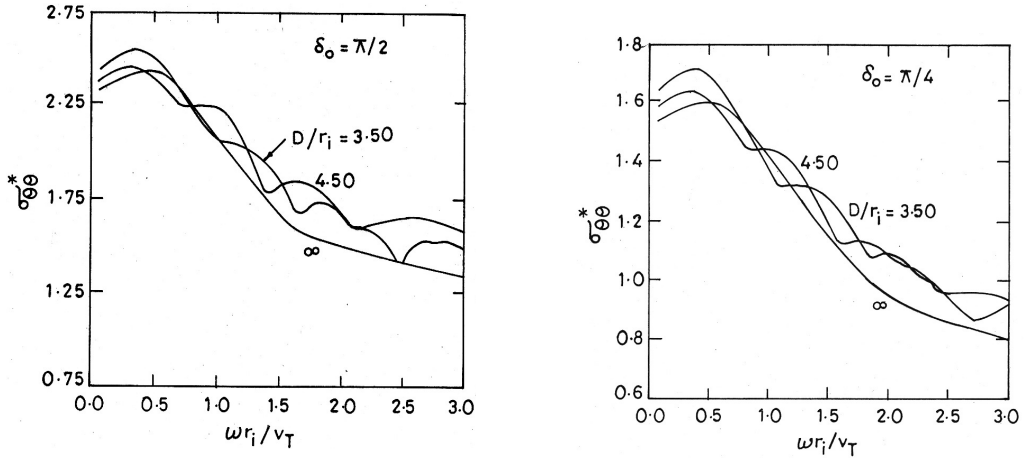


Figure 8. Maximum stress versus normalized frequency: response to incident P waves at the inside surface of the liner, at position $z = 0$ ($\theta_0 = \pi/2$, $\mu/\mu_m = 3$) for $\delta_0 = \pi/2$ (left) and $\delta_0 = \pi/4$ (right).

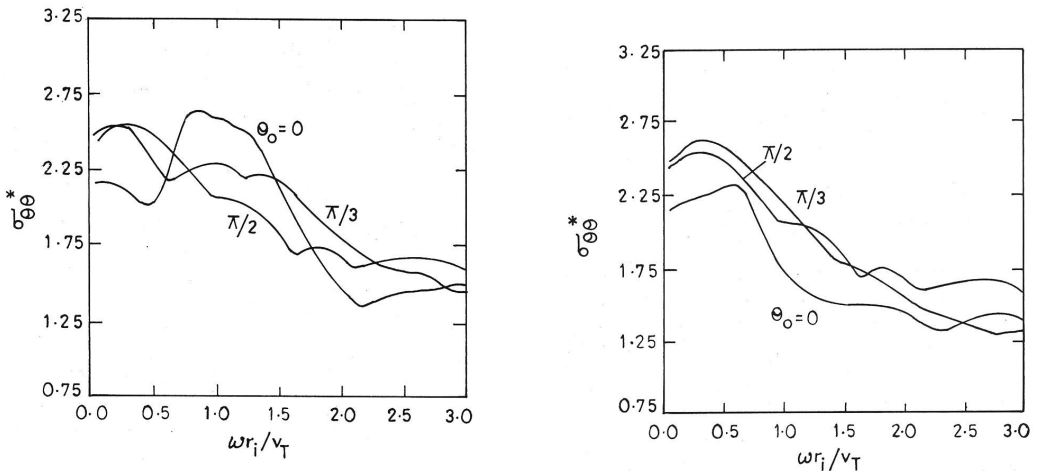


Figure 9. Maximum stress versus normalized frequency; response to incident P waves at the inside surface of the liner, at position $z = 0$ ($\delta_0 = \pi/2$, $\mu/\mu_m = 3$, and $D/r_i = 3.50$) for shells I (left) and II (right).

However, less response is induced in shell II for incident angle $\theta_0 = 0$ since it is shielded by shell I (shell II is in the “shadow” of shell I).

Acknowledgments

The authors are grateful to the referee for valuable suggestions and comments for the improvement of this paper. The authors also thank Prof. P. C. Upadhyay, former head of the Department of Mechanical Engineering, Indian Institute of Technology (Banaras Hindu University), Varanasi, for his kind help in the preparation of this paper.

References

- [Achenbach 1973] J. D. Achenbach, *Wave propagation in elastic solids*, North-Holland Series in Applied Mathematics and Mechanics **16**, North-Holland, Amsterdam, 1973.
- [Chin et al. 1987] Y. F. Chin, R. K. N. D. Rajapakse, A. H. Shah, and S. K. Datta, “Dynamics of buried pipes in back-filled trench”, *Soil Dyn. Earthq. Eng.* **6**:3 (1987), 158–163.
- [Guan and Moore 1994] F. Guan and I. D. Moore, “Three-dimensional dynamic response of twin cavities due to traveling loads”, *J. Eng. Mech. (ASCE)* **120**:3 (1994), 637–651.
- [Liu et al. 1991] S. W. Liu, A. H. Shah, S. K. Datta, and K. R. Khair, “Dynamic response of pipelines buried in back-filled trenches”, *J. Press. Vessel Technol. (ASME)* **113**:3 (1991), 429–436.
- [Mow and Pao 1973] C.-C. Mow and Y.-H. Pao, *The diffraction of elastic waves and dynamic stress concentrations*, Crane Russak, New York, 1973.
- [Okumura et al. 1992] T. Okumura, N. Takewaki, K. Shimizu, and K. Fukutake, “Dynamic response of twin circular tunnels during earthquakes”, pp. 181–191 in *Proceedings of the 4th US–Japan workshop on earthquake disaster prevention for lifeline systems* (Los Angeles, 1991), edited by R. T. Euchi, NIST Special Publication **840**, US Department of Commerce, Gaithersburg, MD, 1992.
- [Trifunac 1972] M. D. Trifunac, “Scattering of plane SH waves by a semi-cylindrical canyon”, *Earthq. Eng. Struct. Dyn.* **1**:3 (1972), 267–281.
- [Watson 1944] G. N. Watson, *A treatise on the theory of Bessel functions*, Cambridge University, 1944.
- [Wong and Jennings 1975] H. L. Wong and P. C. Jennings, “Effects of canyon topography on strong ground motion”, *Bull. Seismol. Soc. Am.* **65**:5 (1975), 1239–1257.

Received 7 Sep 2013. Revised 28 Dec 2013. Accepted 26 Jan 2014.

J. P. DWIVEDI: jpd@bhu.ac.in

Department of Mechanical Engineering, Indian Institute of Technology (Banaras Hindu University), Varanasi 221005, India

V. P. SINGH: vp_singh56@yahoo.co.in

Department of Mechanical Engineering, Indian Institute of Technology (Banaras Hindu University), Varanasi 221005, India

RADHA KRISHNA LAL: radhakrishna773@gmail.com

Department of Mechanical Engineering, Indian Institute of Technology (Banaras Hindu University), Varanasi 221005, India

SOLUTIONS OF THE VON KÁRMÁN PLATE EQUATIONS BY A GALERKIN METHOD, WITHOUT INVERTING THE TANGENT STIFFNESS MATRIX

HONGHUA DAI, XIAOKUI YUE AND SATYA N. ATLURI

Large deflections of a simply supported von Kármán plate with imperfect initial deflections, under a combination of in-plane loads and lateral pressure, are analyzed by a semianalytical global Galerkin method. While many may argue that the dominance of the finite element method in the marketplace may make any other attempts to solve nonlinear plate problems to be redundant and obsolete, semi- and precise analytical methods, when possible, simply serve as benchmark solutions if nothing else. Also, since parametric variations are simpler to access through such analytical methods, they are more useful in studying the physics of the phenomena. In the present method, the Galerkin scheme is first applied to transform the governing nonlinear partial differential equations of the von Kármán plate into a system of general nonlinear algebraic equations (NAEs) in an explicit form. The Jacobian matrix, the tangent stiffness matrix of the system of NAEs, is *explicitly derived*, which speeds up the Newton–Raphson iterative method if it is used. The present global Galerkin method is compared with the incremental Galerkin method, the perturbation method, the finite element method and the finite difference method in solving the von Kármán plate equations to compare their relative accuracies and efficiencies. Buckling behavior and jump phenomenon of the plate are detected and analyzed. Besides the classical Newton–Raphson method, an entirely novel series of scalar homotopy methods, which do not need to invert the Jacobian matrix (the tangent stiffness matrix), even in an elastostatic problem, and which are insensitive to the guesses of the initial solution, are introduced. Furthermore, we provide a comprehensive review of the newly developed scalar homotopy methods, and incorporate them into a uniform framework, which renders a clear and concise understanding of the scalar homotopy methods. In addition, the performance of various scalar homotopy methods is evaluated through solving the Galerkin-resulting NAEs. The present scalar homotopy methods are advantageous when the system of NAEs is very large in size, when the inversion of the Jacobian may be avoided altogether, when the Jacobian is nearly singular, and the sensitivity to the initially guessed solution as in the Newton–Raphson method needs to be avoided, and when the system of NAEs is either over- or under-determined.

1. Introduction

Analysis of large deflections of square and rectangular plates is one of the most studied engineering problems in the structural community, with many engineering applications including in aircraft structures, shipbuilding, bridges, and spaceships. The thin plates used in aircraft construction are subjected to lateral loads from the pressurized cabin or from the lift on the wings, and to edge loading due to bending of the fuselage and wings. The skin plates of a ship bottom are subjected to a significant water pressure, and to

Keywords: von Kármán plate equations, initial imperfection, global Galerkin method, nonlinear algebraic equations, scalar homotopy methods, buckling behavior.

the edge loading owing to bending of the hull. Plate bending problems are also applicable to spaceships, where the outer plates may undergo lateral pressures and in-plane loadings.

The classical Kirchhoff theory for linear plate bending is accurate only for small deflection problems ($w \leq 0.2$ thickness) ignoring the middle surface strains and the corresponding in-plane stresses. As the external force increases, the lateral deflection may be relatively large ($w \geq 0.3$ thickness). In this scenario, the stretching of the middle surface of the plate should be considered and correspondingly the membrane forces arising from this stretching play a role in carrying lateral loads. The extension to large deformations was first provided by von Kármán in a seminal work [1910], wherein the nonlinear terms are retained in the kinematic relationships to account for a significantly large deflection of the plate (w is comparable with plate thickness or larger but remains small with respect to other dimensions of the plate). This leads to a pair of coupled nonlinear fourth-order equations for the transverse displacement, and the stress function for the in-plane stress resultants. Inasmuch as the nonlinear terms are included in the coupled PDEs, closed form solutions for the nonlinear problem do not exist.

The first attempt to solve the von Kármán plate equations by a semianalytical method is attributed to Way [1939], who analyzed a geometrically nonlinear clamped rectangular plate via an energy method to obtain approximate solutions. Levy [1942a; 1942b] applied a Fourier series method to solve a simply supported rectangular plate under combined edge compression and lateral loading. Then Levy [1944] and Woolley et al. [1946] analyzed long rectangular plates with simply supported edges and clamped edges respectively by a similar approach. Okada, Oshima and Fukumoto [Okada et al. 1979] applied the Rayleigh–Ritz method to a simply supported long rectangular plate (length/width = 3 and 4) under hydrostatic pressure, and discussed various buckling behaviors. Ueda, Rashed and Paik [Ueda et al. 1987] proposed an incremental Galerkin method by solving stepwise the linearized form of the von Kármán plate equations of the simply supported rectangular plate. The incremental Galerkin method was then applied to solve stiffened ship plates [Paik et al. 2001]. Large deflection of a simply supported plate was also analyzed in [Shen 1989] using a perturbation method and in [Bert et al. 1989] using a differential quadrature method. These semianalytical methods have respective drawbacks in that they may be too complex mathematically, or require large amounts of computational efforts, or have a slow convergence rate of the solution. Readers are advised to see [Chia 1980] for a comprehensive review.

With the development of modern digital computers, numerical methods based on domain discretization took over the difficult task. Brown and Harvey [1969] used the finite difference method to carry out the analysis of large deflections of rectangular plates subjected to a combination of lateral pressure and edge loading. Some of the earlier finite element implementations for large deformations were conducted in [Brebbia and Connor 1969] and [Bergan and Clough 1973], and involved conventional displacement based elements with the strain energy expressed in terms of the three displacement components. The stress based finite element method was proposed in [Punch and Atluri 1986]. A boundary element approach was proposed to investigate static, dynamic and buckling behavior of thin flat plates in [O’Donoghue and Atluri 1987]. Although these numerical methods can be employed to solve the von Kármán plate equations accurately and are more flexible than the semianalytical methods with respect to various boundary conditions and geometries, *these domain discretization methods would require several orders of magnitude more degrees of freedom than semianalytical approaches*. Therefore, the computational burden is comparatively heavy. Also, semianalytical methods will provide the needed benchmark solutions with minimal computational cost, to judge the accuracies of the many fully numerical methods

using spatial discretization based on simple polynomials locally.

In this paper a simply supported rectangular plate with initial imperfections, under a combination of in-plane and out of plane loads, is analyzed by the global Galerkin method. The present method is applied directly to the von Kármán equations to derive a system of cubic order fully coupled NAEs with as many unknowns as desired. Then the resulting system of NAEs is solved by an algebraic equation solver, such as the Newton–Raphson method. Previously, Dai, Paik and Atluri [Dai et al. 2011a] applied the global Galerkin method to the von Kármán plate, and derived the Galerkin-resulting system of NAEs explicitly. However, the explicit expression for Jacobian matrix (the so-called “tangent-stiffness” matrix) was not obtained, and should be calculated symbolically at each step. As a contribution of the present study, we derive the explicit expression of the Jacobian matrix (or the tangent stiffness matrix) of the resulting NAEs, so that the iterative methods, which require the numerical inversion of the Jacobian matrix, may be applied more efficiently. Eliminating the symbolic operations makes the computational efficiency much more improved than that in [Dai et al. 2011a], as will be verified in numerical illustrations.

The global Galerkin method is compared with the incremental Galerkin method, the perturbation method, the finite element method and the finite difference method in solving the von Kármán plate equations under a combination of in-plane and out-of-plane loads to test its accuracy and efficiency. In addition, the buckling behavior and jump phenomenon of the plate are detected and analyzed numerically.

Another topic of this study is to review a recently proposed class of scalar homotopy methods for solving NAEs. Conventionally, the Newton–Raphson method is popularly used to find successively better approximations to the solutions of a real valued nonlinear system. The Newton–Raphson method converges remarkably quickly provided that the initial guess is sufficiently close to the solution. However, the Newton–Raphson method in general requires the inversion of the Jacobian matrix in each iterative step, it is sensitive to the initial guess, and the accuracy of the solution cannot be guaranteed if nearly singular or ill-conditioned Jacobian matrix is encountered. When the Jacobian (tangent stiffness) matrix becomes singular, as in limit load problems, researchers over the past three decades have devised enhancements to the Newton–Raphson method, such as the arclength method. In this paper we present more elegant algorithms which do not involve the inversion of the Jacobian and which are simpler to use when the Jacobian is nearly singular.

We introduce a series of scalar homotopy methods based on the Newton scalar homotopy function. The general form of the Newton homotopy methods is used to incorporate all the existing homotopy methods in a uniform framework. Besides, the present paper provides a concise and clear interpretation for the scalar homotopy methods, and the efficiencies of the various methods are tested through using them to solve the Galerkin-resulting system of NAEs. The presented scalar homotopy methods overcome the several known drawbacks of the Newton–Raphson method:

- (1) They can be applied more efficiently than the Newton–Raphson method, when the unknown vector to be solved from the NAEs tends to be large (even through we have limited our study in this paper to only 40 nonlinear algebraic equations).
- (2) They completely avoid the need for the inversion of the Jacobian matrix either numerically or analytically (which is impossible in most cases).
- (3) They perform much better than the Newton–Raphson method, when the Jacobian matrix is nearly singular, or is severely ill-conditioned.

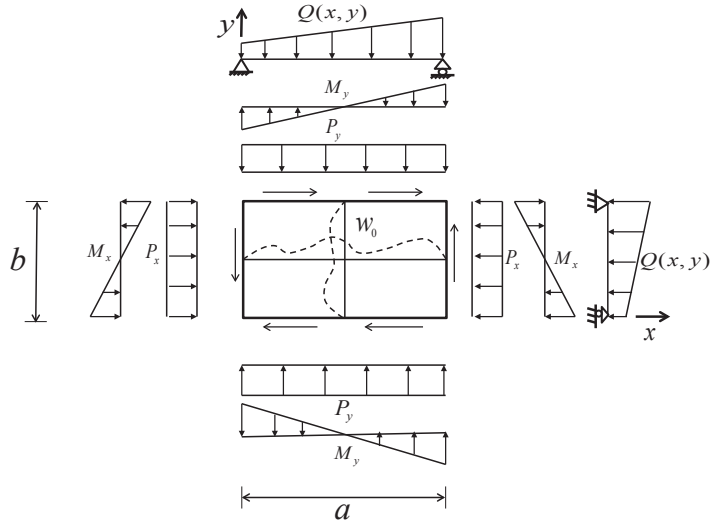


Figure 1. A rectangular plate with initial deflection and general in-plane and lateral loads.

- (4) They are insensitive to the guess of the initial solution vector, unlike the Newton–Raphson method.
- (5) They can solve either over-determined or under-determined systems of NAEs.

The paper is organized as follows. In [Section 2](#), the global Galerkin method is used to transform the governing PDEs into a system of NAEs. The explicit form of the Jacobian matrix of the NAEs is also derived. In [Section 3](#), various NAE solvers are introduced. A series of Newton homotopy methods are illustrated and classified into continuous-type Newton homotopy and iterative-type Newton homotopy methods. Consequently all the existing Newton homotopy methods are incorporated into a corresponding uniform framework. Moreover, features of the solvers are discussed. We note that [Section 3](#) can stand alone for researchers who are interested in the new NAE solvers. Researchers who focus on the semianalytical methods or nonlinear behavior of the plate may skip this part. Numerical experiments are carried out in [Section 4](#). Finally, we draw some conclusions about the present global Galerkin method and the NAE solvers in [Section 5](#).

2. Governing equations and the Galerkin method

The elastic large deflection response of a plate with initial deflection is governed by two PDEs, which are named von Kármán equations. One of them represents the equilibrium condition in the transverse direction, and the other represents the compatibility condition of in-plane strains. The PDEs are as follows:

$$\phi \equiv D\nabla^4 w - t[\varphi_{,yy}(w + w_0)_{,xx} + \varphi_{,xx}(w + w_0)_{,yy} - 2\varphi_{,xy}(w + w_0)_{,xy}] - Q = 0, \tag{1a}$$

$$\nabla^4 \varphi = E[w_{,xy}^2 - w_{,xx}w_{,yy} + 2w_{0,xy}w_{,xy} - w_{0,xx}w_{,yy} - w_{0,yy}w_{,xx}]. \tag{1b}$$

In the above, w_0 is the given initial transverse displacement; w is the additional transverse displacement; Q is the lateral pressure acting on the plate; φ is the Airy stress function governing the in plane stress

resultants and t is the plate thickness.

$$\nabla^4 = \frac{\partial^4}{\partial x^4} + 2\frac{\partial^4}{\partial x^2\partial y^2} + \frac{\partial^4}{\partial y^4}, \quad D = \frac{Et^3}{12(1-\nu)^2}, \quad (2)$$

where D is the flexural rigidity, and ∇^4 is the well known biharmonic operator; E and ν are Young's modulus and Poisson's ratio. The subscripts $_{,x}$ and $_{,y}$ stand for $\partial/\partial x$ and $\partial/\partial y$.

Stress σ_x in the x direction, σ_y in the y direction and shear stress τ_{xy} in xy plane may be expressed as

$$\sigma_x = \varphi_{,yy}, \quad \sigma_y = \varphi_{,xx}, \quad \tau_{xy} = \varphi_{,xy}.$$

We emphasize that, in using the Galerkin method, we need to solve the Airy stress function φ first from the (1b), and then apply the Galerkin approach to (1a), which is different from the Rayleigh–Ritz method where the air stress function φ and even the governing equations are not required. Rayleigh–Ritz method based on Lagrangian equations is simple in application but computationally expensive since more freedoms are expected by Rayleigh–Ritz method than by Galerkin method, because the deflections of all three directions are required to be assumed. In this study, we derive the explicit expressions of the φ and then the resulting NAEs, so that researchers can avoid lengthy algebra and enjoy the advantage of the Galerkin method. The geometry and general loading conditions of the plate is plotted in Figure 1.

In solving the governing equations, the added deflection w due to the applied load, and the initial deflection w_0 should satisfy the boundary conditions at four edges. All four edges are assumed to be simply supported, and the boundary conditions of the plate are

$$\begin{aligned} w = 0, \quad w_{,yy} + \nu w_{,xx} = 0, \quad \text{at } y = 0 \text{ and } y = b, \\ w = 0, \quad w_{,xx} + \nu w_{,yy} = 0, \quad \text{at } x = 0 \text{ and } x = a. \end{aligned}$$

2.1. Application of the Galerkin method. To satisfy the boundary conditions, the initial deflection w_0 and the added deflection function w can be normally assumed in double Fourier series,

$$w_0 = \sum_{m=1}^M \sum_{n=1}^N A_{0mn} \sin \frac{m\pi x}{a} \sin \frac{n\pi y}{b}, \quad (3)$$

$$w = \sum_{m=1}^M \sum_{n=1}^N A_{mn} \sin \frac{m\pi x}{a} \sin \frac{n\pi y}{b}, \quad (4)$$

where A_{0mn} and A_{mn} are the known and unknown coefficients, respectively. The present simply supported plate can be solved with various patterns of external loads. The conditions of the combined loads, namely, biaxial loads, biaxial in-plane bending and edge shear are given as follows:

$$\int_0^b \varphi_{,yy} t \, dy = P_x, \quad \int_0^b \varphi_{,yy} t \left(y - \frac{b}{2}\right) dy = M_x \quad \text{at } x = 0 \text{ and } x = a, \quad (5a)$$

$$\int_0^a \varphi_{,xx} t \, dx = P_y, \quad \int_0^a \varphi_{,xx} t \left(x - \frac{a}{2}\right) dx = M_y \quad \text{at } y = 0 \text{ and } y = b, \quad (5b)$$

$$\varphi_{,xy} = -\tau \quad \text{at all four edges.} \quad (5c)$$

Then the homogenous solution φ_h for the Airy stress function φ should satisfy the condition of the combined loads acting on the plate. Considering the loading conditions, we can easily find φ_h , by assuming φ_h as cubic polynomials in x and y . Substituting φ_h into (5) we can obtain,

$$\varphi_h = -P_x \frac{y^2}{2bt} - \sigma_{rx} \frac{y^2}{2} - P_y \frac{x^2}{2at} - \sigma_{ry} \frac{x^2}{2} - M_x \frac{y^2(2y-3b)}{b^3t} - M_y \frac{x^2(2x-3a)}{a^3t} - \tau_{xy}xy. \quad (6)$$

The following notations are introduced to abbreviate the expressions involving the sine or cosine terms:

$$\sin \frac{m\pi x}{a} \equiv sx(m), \quad \cos \frac{m\pi x}{a} \equiv cx(m), \quad \sin \frac{n\pi y}{b} \equiv sy(n), \quad \cos \frac{n\pi y}{b} \equiv cy(n).$$

To find the particular solution φ_p that should satisfy (1b), one ought to substitute w and w_0 into the right side of (1b), thus obtaining

$$\begin{aligned} \nabla^4 \varphi_p = \frac{E\pi^4}{4a^2b^2} \sum_{m=1}^M \sum_{n=1}^N \sum_{k=1}^K \sum_{l=1}^L \left\{ [A_{mn}A_{kl}ml(nk-ml) - A_{kl}A_{0mn}(nk-ml)^2] cx(m+k)cy(n+l) \right. \\ \left. + [A_{mn}A_{kl}ml(nk+ml) + A_{kl}A_{0mn}(nk+ml)^2] cx(m+k)cy(n-l) \right. \\ \left. + [A_{mn}A_{kl}ml(nk+ml) + A_{kl}A_{0mn}(nk+ml)^2] cx(m-k)cy(n+l) \right. \\ \left. + [A_{mn}A_{kl}ml(nk-ml) - A_{kl}A_{0mn}(nk-ml)^2] cx(m-k)cy(n-l) \right\}. \quad (7) \end{aligned}$$

Consequently, motivated by the form of the right-hand side of (7), the particular solution φ_p for the Airy stress function is assumed as

$$\begin{aligned} \varphi_p = \frac{E\pi^4}{4a^2b^2} \sum_{m=1}^M \sum_{n=1}^N \sum_{k=1}^K \sum_{l=1}^L \left\{ B_1(m, n, k, l) cx(m+k)cy(n+l) + B_2(m, n, k, l) cx(m+k)cy(n-l) \right. \\ \left. + B_3(m, n, k, l) cx(m-k)cy(n+l) + B_4(m, n, k, l) cx(m-k)cy(n-l) \right\}. \quad (8) \end{aligned}$$

Upon substituting (8) into (1b), the coefficients B_i , $i = 1, 2, 3, 4$ can be readily calculated; they are not written out for saving space. Then, substituting the B_i into (8), we obtain the particular solution φ_p :

$$\begin{aligned} \varphi_p = \frac{E\alpha^2}{4} \sum_{m=1}^M \sum_{n=1}^N \sum_{k=1}^K \sum_{l=1}^L \left\{ \frac{A_{mn}A_{kl}ml(nk-ml) - A_{kl}A_{0mn}(nk-ml)^2}{[(m+k)^2 + (n+l)^2]^2} cx(m+k)cy(n+l) \right. \\ \left. + \frac{A_{mn}A_{kl}ml(nk+ml) + A_{kl}A_{0mn}(nk+ml)^2}{[(m+k)^2 + (n-l)^2]^2} cx(m+k)cy(n-l) \right. \\ \left. + \frac{A_{mn}A_{kl}ml(nk+ml) + A_{kl}A_{0mn}(nk+ml)^2}{[(m-k)^2 + (n+l)^2]^2} cx(m-k)cy(n+l) \right. \\ \left. + \frac{A_{mn}A_{kl}ml(nk-ml) - A_{kl}A_{0mn}(nk-ml)^2}{[(m-k)^2 + (n-l)^2]^2} cx(m-k)cy(n-l) \right\}. \quad (9) \end{aligned}$$

Then, the Airy stress function φ can be expressed as

$$\varphi = \varphi_h + \varphi_p. \quad (10)$$

It is evident from Equations (6), (9) and (10) that φ is a second-order function with regard to the unknown deflection coefficients A_{mn} . To compute the unknown coefficients, the global Galerkin method

is applied to the equilibrium (1a):

$$\iiint_V \phi(x, y, z) s_x(i) s_y(j) dx dy dz = 0. \tag{11}$$

Upon substituting (10) into (1a), and then (1a) to (11) after a lengthy derivation, we obtain a system of third-order (cubic) coupled NAEs, with respect to the unknown coefficients, the explicit expression of the nonlinear system of algebraic equations is

$$\begin{aligned} & \sum \sum A_{mn} \cdot D\pi^4 \left(\frac{m^2}{a^2} + \frac{n^2}{b^2} \right)^2 H_{01}(i, j, m, n) \\ & + \sum \sum \sum \sum \sum \sum A_{mn} A_{kl} A_{rs} \cdot (-t) \frac{E\alpha^2 \pi^4}{4a^2 b^2} (H_1 + H_2 + H_3 + H_4 - 2H_9 - 2H_{10} - 2H_{11} - 2H_{12}) \\ & + \sum \sum \sum \sum A_{mn} A_{kl} \cdot (-t) \frac{E\alpha^2 \pi^4}{4a^2 b^2} \sum \sum A_{0rs} (H_1 + H_2 + H_3 + H_4 - 2H_9 - 2H_{10} - 2H_{11} - 2H_{12}) \\ & + \sum \sum \sum \sum A_{kl} A_{rs} \cdot (-t) \frac{E\alpha^2 \pi^4}{4a^2 b^2} \sum \sum A_{0mn} (H_6 + H_7 - H_5 - H_8 + 2H_{13} - 2H_{14} - 2H_{15} + 2H_{16}) \\ & + \sum \sum A_{kl} \cdot (-t) \frac{E\alpha^2 \pi^4}{4a^2 b^2} \sum \sum \sum \sum A_{0mn} A_{0rs} (H_6 + H_7 - H_5 - H_8 + 2H_{13} - 2H_{14} - 2H_{15} + 2H_{16}) \\ & + \sum \sum A_{mn} \cdot (-t) \left\{ \frac{m^2 \pi^2}{a^2} \left[\left(\frac{P_x}{bt} + \sigma_{rx} - \frac{6}{b^2 t} M_x \right) H_{01}(i, j, m, n) + \frac{12}{b^3 t} M_x H_{03}(i, j, m, n) \right] \right. \\ & \quad + \frac{n^2 \pi^2}{b^2} \left[\left(\frac{P_y}{at} + \sigma_{ry} - \frac{6}{a^2 t} M_y \right) H_{01}(i, j, m, n) + \frac{12}{a^3 t} M_y H_{02}(i, j, m, n) \right] \\ & \quad \left. + \frac{2\tau \pi^2}{ab} mn \cdot H_{04}(i, j, m, n) \right\} \\ & + \sum \sum A_{0mn} \cdot (-t) \left\{ \frac{m^2 \pi^2}{a^2} \left[\left(\frac{P_x}{bt} + \sigma_{rx} - \frac{6}{b^2 t} M_x \right) H_{01}(i, j, m, n) + \frac{12}{b^3 t} M_x H_{03}(i, j, m, n) \right] \right. \\ & \quad + \frac{n^2 \pi^2}{b^2} \left[\left(\frac{P_y}{at} + \sigma_{ry} - \frac{6}{a^2 t} M_y \right) H_{01}(i, j, m, n) + \frac{12}{a^3 t} M_y H_{02}(i, j, m, n) \right] \\ & \quad \left. + \frac{2\tau \pi^2}{ab} mn \cdot H_{04}(i, j, m, n) \right\} \\ & - Q \cdot H_{00}(i, j) = 0, \tag{12} \end{aligned}$$

where for simplicity the coefficient matrix $H_1(i, j, m, n, k, l, r, s)$ is denoted by H_1 and so forth, and all the summations above are carried out over the dummy indexes m, n, k, l, r, s , and i, j are free indexes. All the coefficient matrices can be obtained by performing integration over the whole volume of the plate, whose expressions are provided in the Appendix of [Dai et al. 2011a]. We can write the resulting

algebraic system (12) neatly in matrix form:

$$\mathbf{K}_t \mathbf{A}_t + \mathbf{K}_s \mathbf{A}_s + \mathbf{K}_f \mathbf{A}_f + \mathbf{C} = \mathbf{0}, \quad (13)$$

where \mathbf{C} is a constant column matrix, \mathbf{K}_f , \mathbf{K}_s and \mathbf{K}_t are the first-, second- and third-order coefficient matrices — the dimensions (number of rows \times number of columns) of these matrices being

$$MN \times (MN)^3 \text{ for } \mathbf{K}_t, \quad MN \times (MN)^2 \text{ for } \mathbf{K}_s, \quad MN \times MN \text{ for } \mathbf{K}_f, \quad MN \times 1 \text{ for } \mathbf{C},$$

— and where \mathbf{A}_f , \mathbf{A}_s and \mathbf{A}_t are the first-, second- and third-order unknown vectors.¹

2.2. An explicit derivation of the Jacobian matrix (tangent stiffness matrix) for the von Kármán plate.

Up to now, the NAEs are obtained, and can be solved by applying NAE solvers. However, in most of the cases, the Jacobian matrix of the derived system of NAEs is required to enable the iterative procedures in the course of using the algebraic equation solvers. In our previous work, we only derived the explicit form of algebraic system. The Jacobian matrix to this system is not derived explicitly. Therefore, we resort to symbolic operations embedded in the Matlab to calculate the Jacobian matrix at each iteration. Although very accurate solutions were achieved in [Dai et al. 2011a] via this scheme, we admit that the computational efforts are very heavy. In the present work, we derive the explicit form of the Jacobian matrix to eliminate this drawback. It should be emphasized that the explicit form of the Jacobian matrix of the NAEs resulting from the von Kármán plate PDEs is provided for the first time in literature. This Jacobian matrix needs to be inverted in each iterative step in the Newton–Raphson method, but such an inversion is not necessary in any of the scalar homotopy methods presented in this paper.

The resulting algebraic system (13) can be written in a general form as

$$\mathbf{F}(\mathbf{A}) = \mathbf{0}, \quad (14)$$

or, particularly

$$F_{ij}(A_{pq}) = 0, \quad i, p = 1, 2, \dots, M; j, q = 1, 2, \dots, N. \quad (15)$$

It should be noted that F_{ij} does not represent a matrix. It is used to simply denote that there are $M \times N$ equations, with the $[(j-1)N+i]$ -th equation being denoted by F_{ij} . Similarly, A_{pq} represents the $[(q-1)N+p]$ -th unknown coefficient.

$$B_{u,v} = \frac{\partial F_{ij}}{\partial A_{pq}}, \quad (16)$$

where the $B_{u,v}$ is the u -th row and v -th column of \mathbf{B} with $u = (j-1)N+i$, $v = (q-1)N+p$. There are eight terms in (12), the first six terms are associated with the unknown coefficients and the last two terms are constant with regard to unknowns. The Jacobian matrix \mathbf{B} of (12) is derived term by term as follows.

$$\frac{\partial F_{ij}^1}{\partial A_{pq}} = D\pi^4 \left(\frac{p^2}{a^2} + \frac{q^2}{b^2} \right)^2 H_{01}(i, j, p, q).$$

¹The second- and third-order unknown vectors are vectors devised in [Dai et al. 2011a; 2011b] for obtaining the matrix equation (13).

$$\begin{aligned} \frac{\partial F_{ij}^2}{\partial A_{pq}} &= \sum \sum \sum \sum A_{kl} A_{rs} \times (-t) \frac{E\alpha^2\pi^4}{4a^2b^2} (H_1 + H_2 + H_3 + H_4 - 2H_9 - 2H_{10} - 2H_{11} - 2H_{12}) \\ &+ \sum \sum \sum \sum A_{mn} A_{rs} \times (-t) \frac{E\alpha^2\pi^4}{4a^2b^2} (H_1 + H_2 + H_3 + H_4 - 2H_9 - 2H_{10} - 2H_{11} - 2H_{12}) \\ &+ \sum \sum \sum \sum A_{mn} A_{kl} \times (-t) \frac{E\alpha^2\pi^4}{4a^2b^2} (H_1 + H_2 + H_3 + H_4 - 2H_9 - 2H_{10} - 2H_{11} - 2H_{12}), \end{aligned}$$

the matrices H_i in the first, second and third line being evaluated, respectively, as follows:

$$H(i, j, p, q, k, l, r, s), \quad H(i, j, m, n, p, q, r, s), \quad H(i, j, m, n, k, l, p, q).$$

$$\begin{aligned} \frac{\partial F_{ij}^3}{\partial A_{pq}} &= \sum \sum A_{kl} \times (-t) \frac{E\alpha^2\pi^4}{4a^2b^2} \sum \sum A_{0rs} (H_1 + H_2 + H_3 + H_4 - 2H_9 - 2H_{10} - 2H_{11} - 2H_{12}) \\ &+ \sum \sum A_{mn} \times (-t) \frac{E\alpha^2\pi^4}{4a^2b^2} \sum \sum A_{0rs} (H_1 + H_2 + H_3 + H_4 - 2H_9 - 2H_{10} - 2H_{11} - 2H_{12}), \end{aligned}$$

where the matrices H_i in the first and second lines are $H(i, j, p, q, k, l, r, s)$ and $H(i, j, m, n, p, q, r, s)$, respectively.

$$\begin{aligned} \frac{\partial F_{ij}^4}{\partial A_{pq}} &= \sum \sum A_{rs} \times (-t) \frac{E\alpha^2\pi^4}{4a^2b^2} \sum \sum A_{0mn} (H_6 + H_7 - H_5 - H_8 + 2H_{13} - 2H_{14} - 2H_{15} + 2H_{16}) \\ &+ \sum \sum A_{kl} \times (-t) \frac{E\alpha^2\pi^4}{4a^2b^2} \sum \sum A_{0mn} (H_6 + H_7 - H_5 - H_8 + 2H_{13} - 2H_{14} - 2H_{15} + 2H_{16}), \end{aligned}$$

where the matrices H_s in the first and second line are $H(i, j, m, n, p, q, r, s)$ and $H(i, j, m, n, k, l, p, q)$, respectively.

$$\frac{\partial F_{ij}^5}{\partial A_{pq}} = (-t) \frac{E\alpha^2\pi^4}{4a^2b^2} \sum \sum \sum \sum A_{0mn} A_{0rs} (H_6 + H_7 - H_5 - H_8 + 2H_{13} - 2H_{14} - 2H_{15} + 2H_{16}).$$

$$\begin{aligned} \frac{\partial F_{ij}^6}{\partial A_{pq}} &= (-t) \left\{ \frac{p^2\pi^2}{a^2} \left[\left(\frac{P_x}{bt} + \sigma_{rx} - \frac{6}{b^2t} M_x \right) H_{01} + \frac{12}{b^3t} M_x H_{03} \right] \right. \\ &\quad \left. + \frac{q^2\pi^2}{b^2} \left[\left(\frac{P_y}{at} + \sigma_{ry} - \frac{6}{a^2t} M_y \right) H_{01} + \frac{12}{a^3t} M_y H_{02} \right] + \frac{2\tau\pi^2}{ab} pq H_{04} \right\}, \end{aligned}$$

where the matrices depend on (i, j, p, q) . Therefore, the Jacobian matrix is

$$B_{u,v} = \frac{\partial F_{ij}}{\partial A_{pq}} = \sum_{k=1}^6 \frac{\partial F_{ij}^k}{\partial A_{pq}}. \quad (17)$$

Consequently, with the explicit form of the system of NAEs and its Jacobian matrix, the present problem can be solved readily by using various NAE solvers. In the course of solving a system of NAEs, the Jacobian matrix is usually necessary. Normally, the numerical approximation of the Jacobian matrix is calculated in each iteration step via numerical difference techniques. The explicitly derived Jacobian

matrix may significantly accelerate the computing rate of the algebraic solver [Dai et al. 2014a]. The effect of using the explicitly derived Jacobian matrix rather than the numerically calculated one on the computational efficiency has been intensively analyzed in [Dai et al. 2014b] in a two-degree-of-freedom airfoil problem. It was demonstrated that using the explicit Jacobian matrix can be roughly two orders of magnitude faster.

3. Methods for nonlinear algebraic equations

The numerical solution of linear or nonlinear, well-conditioned or ill-conditioned, and underdetermined or overdetermined algebraic equations is one of the main aspects of computational mechanics. In many practical nonlinear engineering problems, methods such as the finite element method, boundary element method, finite volume method, the meshless method, global Galerkin method, Rayleigh–Ritz method, etc., eventually lead to a system of nonlinear algebraic equations (NAEs). Many numerical methods used in computational mechanics, as illustrated in [Atluri 2005] lead to the solution of a system of linear algebraic equations for a linear problem, and of a system of NAEs for a nonlinear problem.

A system of nonlinear algebraic equations is

$$F_i(x_j) = 0, \quad i, j = 1, 2, \dots, n. \quad (18)$$

Solvers for this set of NAEs are introduced below. In the section of numerical experiments, they are applied to solve the resulting algebraic system from the implementation of the Galerkin method to von Kármán plate equations.

3.1. Newton method and preliminary work. The most famous method for solving nonlinear algebraic equations is the Newton–Raphson method, or Newton method, which is given algorithmically as

$$\mathbf{x}_{k+1} = \mathbf{x}_k - \mathbf{B}_k^{-1} \mathbf{F}_k, \quad (19)$$

where we use $\mathbf{x} := x_1, x_2, \dots, x_n$ and $\mathbf{F} := F_1, F_2, \dots, F_n$ to represent the vectors, \mathbf{B} is the $n \times n$ Jacobian matrix with its (i, j) entry given by $\partial F_i / \partial x_j$, and \mathbf{x}_{k+1} is the $(k+1)$ -th iteration for the unknown vector \mathbf{x} . *Newton method is advantageous in that it converges quadratically fast, provided that the initial “guesses” for the solution are within a certain radius of convergence.* However, sometimes Newton method suffers from its sensitiveness to initial “guesses”, and the computational burden/accuracy of inverting the Jacobian matrix when the Jacobian matrix is singular or severely ill-conditioned.

Hirsch and Smale [1979] derived a “continuous Newton method” governed by the differential equation

$$\dot{\mathbf{x}}(t) = -\mathbf{B}^{-1} \mathbf{F}(\mathbf{x}), \quad (20)$$

$$\mathbf{x}(0) = \mathbf{a}, \quad (21)$$

where $\mathbf{a} \in \mathbb{R}^n$. It should be noted that applying a forward Euler scheme to (20) leads to the classical Newton method. Therefore, the continuous Newton method is just the iterative form of Newton method written in the ODE form. The performance does not improve much as compared with the classical Newton method.

Until very recently Newton-type methods are the only choice for solving NAEs, where the inverse of Jacobian matrix is inevitable. To eliminate the need for inverting a matrix in the iteration procedure, a

straightforward first-order ODE system,

$$\dot{\mathbf{x}}(t) = -\mathbf{F}(\mathbf{x}), \quad (22)$$

$$\mathbf{x}(0) = \mathbf{a}, \quad (23)$$

was used [Ramm 2004]. However, iteration procedure arising out of the integration of (22) is very sensitive to the initial guess, and converges very slowly. Liu and Atluri [2008] proposed a fictitious time integration method (FTIM) in the form of a system of ODEs as

$$\dot{\mathbf{x}}(t) = -\frac{\nu}{q(t)}\mathbf{F}(\mathbf{x}), \quad (24)$$

where ν is a nonzero parameter and $q(t)$ is required to be a monotonically increasing function of t . In their approach, the term $\nu/q(t)$ plays the role of speeding up the convergence. It is noted that an elementary version of the continuation method similar to the FTIM was introduced in [Kane and Levinson 1985].

However, both the methods of FTIM and that in [Ramm 2004] are not rigorously derived mathematically. Interestingly, we can see that both of them do not need the Jacobian matrix, let alone its inversion. However, according to authors' experience, they are extremely sensitive to initial guesses, and converge much more slowly than the Newton method. Therefore both methods are not recommended unless the Jacobian matrix cannot be obtained or involved.

Atluri, Liu and Kuo [Atluri et al. 2009] proposed a modified Newton method (MNM), which is in fact a combination of the continuous Newton method and the FTIM and the finite difference technique, for solving nonlinear algebraic equations avoiding the inverse of the Jacobian matrix. The MNM is given as

$$\frac{d\mathbf{x}_i}{d\tau} = -\frac{\nu}{1+\tau}(1-s_i)\mathbf{B}_i \frac{\mathbf{x}_i - \mathbf{x}_{i-1}}{\Delta s} + \mathbf{F}_i = \mathbf{0}, \quad i = 1, \dots, m, \quad (25)$$

where $s = 1 - e^{-\tau}$ is a new variable, and $s \in [0, 1)$ is divided into m subintervals with $\Delta s = 1/m$. Numerical examples of [Atluri et al. 2009] showed that the MNM converges faster than the FTIM in some problems. However, the convergence rate still cannot compare with that of the Newton method. In addition, the ODE system (25) of the MNM is m times larger than the FTIM and the continuous Newton method, which makes the integration much more expensive.

Liu, Yeih, Kuo and Atluri [Liu et al. 2009] developed a scalar homotopy method, which transforms the original NAEs into an equivalent system of ODEs. The scalar homotopy method is totally distinguished from the aforementioned FTIM, MNM methods because the FTIM and MNM are based on (24), which is not a strictly derived relation but rather an intuition.

In solving nonlinear algebraic equations, the homotopy method represents a way to enhance the convergence from a local convergence to a global convergence. Previously, all the homotopy methods are based on the construction of a vector homotopy function, $\mathbf{H}(\mathbf{x}, t)$ which serves the objective of continuously transforming a function $\mathbf{G}(\mathbf{x})$ into $\mathbf{F}(\mathbf{x})$ by introducing a homotopy parameter t . The homotopy parameter t can be treated as a time-like fictitious variable, and the homotopy function can be any continuous function such that: $\mathbf{H}(\mathbf{x}, 0) = \mathbf{G}(\mathbf{x})$ and $\mathbf{H}(\mathbf{x}, 1) = \mathbf{F}(\mathbf{x})$.

Two kinds of homotopy functions are popularly used. The fixed-point homotopy function can be written as

$$\mathbf{H}(\mathbf{x}, t) = t\mathbf{F}(\mathbf{x}) + (1-t)(\mathbf{x} - \mathbf{x}_0) = 0, \quad (26)$$

and the Newton homotopy function is

$$\mathbf{H}(\mathbf{x}, t) = t\mathbf{F}(\mathbf{x}) + (1-t)[\mathbf{F}(\mathbf{x}) - \mathbf{F}(\mathbf{x}_0)] = 0, \quad (27)$$

where \mathbf{x}_0 is the given initial values and $t \in [0, 1]$. Motivated by the above vector homotopy function (26), Liu et al. [2009] proposed a fixed-point scalar homotopy function

$$h(\mathbf{x}, t) = \frac{1}{2}t\|\mathbf{F}(\mathbf{x})\|^2 + \frac{1}{2}(t-1)\|\mathbf{x} - \mathbf{x}_0\|^2 = 0, \quad (28)$$

Then $\mathbf{x} = \mathbf{x}(t)$ is assumed in [Liu et al. 2009]. Differentiating (28) on both sides with respect to t yields

$$\frac{1}{2}[\|\mathbf{F}(\mathbf{x})\|^2 + \|\mathbf{x} - \mathbf{a}\|^2] + [t\mathbf{B}^T\mathbf{F} - (1-t)(\mathbf{x} - \mathbf{a})] \cdot \dot{\mathbf{x}} = 0. \quad (29)$$

Also, $\dot{\mathbf{x}}$ needs to be parallel to the gradient of the above scalar homotopy function, such that the trajectory of \mathbf{x} can be equivalent to seeking of $h(\mathbf{x}, t) = 0$. Thus,

$$\dot{\mathbf{x}} = -\lambda \frac{\partial h}{\partial \mathbf{x}}. \quad (30)$$

Therefore, using Equations (28)–(30) the scalar homotopy method (SHM) is derived as

$$\dot{\mathbf{x}} = -\frac{1}{2} \frac{\|\mathbf{F}(\mathbf{x})\|^2 + \|\mathbf{x} - \mathbf{a}\|^2}{\|t\mathbf{B}^T\mathbf{F} - (1-t)(\mathbf{x} - \mathbf{a})\|^2} [t\mathbf{B}^T\mathbf{F} - (1-t)(\mathbf{x} - \mathbf{a})]. \quad (31)$$

The SHM is the first scalar homotopy method, and it is based on the fixed point scalar homotopy function. This method is proved to be less sensitive to initial guess, it has an acceptable convergence rate [Liu et al. 2009]. Systems of over/under determined algebraic equations, or systems being sensitive to initial guesses, or systems whose Jacobian matrix is ill-conditioned, can be solved by the SHM method better than by the Newton method.

3.2. Continuous Newton homotopy methods. In this study, we introduce a series of continuous algorithms based on the Newton homotopy function. The general form of the Newton homotopy methods incorporates all the existing homotopy methods in a uniform framework.

The Newton homotopy function (27) can be written as

$$\mathbf{H}(\mathbf{x}, t) = \mathbf{F}(\mathbf{x}) + (t-1)\mathbf{F}(\mathbf{x}_0) = 0. \quad (32)$$

Similar to the process in SHM, we can transform the vector Newton homotopy function into a scalar form as follows:

$$h(\mathbf{x}, t) = \frac{1}{2}\|\mathbf{F}(\mathbf{x})\|^2 + \frac{1}{2}(t-1)\|\mathbf{F}(\mathbf{x}_0)\|^2 = 0. \quad (33)$$

Equation (33) holds for all $t \in [0, 1]$. To motivate this study, we first consider a fictitious time function $Q(t)$, $t \in [0, \infty)$, where t is the fictitious time and $Q(t)$ has to satisfy that $Q(t) > 0$, $Q(0) = 1$, and $Q(t)$ is a monotonically increasing function of t , and $Q(\infty) = \infty$. Then we introduce the proposed fictitious time function $Q(t)$ into (33) and have a generalized scalar Newton homotopy function

$$h(\mathbf{x}, t) = \frac{1}{2}\|\mathbf{F}(\mathbf{x})\|^2 - \frac{1}{2Q(t)}\|\mathbf{F}(\mathbf{x}_0)\|^2 = 0, \quad (34)$$

Using the fictitious time function, $Q(t)$, when the fictitious time $t = 0$ and $t = \infty$, we can obtain

$$h(\mathbf{x}, t = 0) = \frac{1}{2} \|\mathbf{F}(\mathbf{x})\|^2 - \frac{1}{2} \|\mathbf{F}(\mathbf{x}_0)\|^2 = 0 \Leftrightarrow \mathbf{F}(\mathbf{x}) = \mathbf{F}(\mathbf{x}_0), \quad (35)$$

$$h(\mathbf{x}, t = \infty) = \frac{1}{2} \|\mathbf{F}(\mathbf{x})\|^2 = 0 \Leftrightarrow \mathbf{F}(\mathbf{x}) = 0. \quad (36)$$

Clearly, the tracking of a solution path for the proposed scalar Newton homotopy function is equivalent to the fictitious time varying from zero to infinity. Multiplying both sides of (34) by $Q(t)$ we have

$$h(\mathbf{x}, t) = \frac{1}{2} Q(t) \|\mathbf{F}(\mathbf{x})\|^2 - \frac{1}{2} \|\mathbf{F}(\mathbf{x}_0)\|^2 = 0, \quad (37)$$

We expect $h(\mathbf{x}, t)$ to be an invariant manifold in the space of (\mathbf{x}, t) for a dynamical system $h(\mathbf{x}(t), t)$ to be specified further. With the assumption of $Q(t) > 0$, the manifold defined is continuous, and thus the following operation of differential carried out on the manifold makes sense. As a consistency condition, by taking the time differential of (37) with respect to t and considering $\dot{\mathbf{x}} = \dot{\mathbf{x}}(t)$, we have

$$\frac{1}{2} \dot{Q}(t) \|\mathbf{F}(\mathbf{x})\|^2 + Q(t) (\mathbf{B}^T \mathbf{F}) \cdot \dot{\mathbf{x}} = 0. \quad (38)$$

To transform the original NAEs to ODEs, $\dot{\mathbf{x}}$ should be specified like $\dot{\mathbf{x}} = \lambda \mathbf{u}$. It should be emphasized that there are a variety of choices for the form of $\dot{\mathbf{x}} = \lambda \mathbf{u}$. Various Newton homotopy methods may generate from selections of \mathbf{u} . Initially, we assume

$$\dot{\mathbf{x}} = \lambda \mathbf{u}. \quad (39)$$

Substituting (39) into (38) yields

$$\lambda = - \frac{\dot{Q}(t) \|\mathbf{F}(\mathbf{x})\|^2}{2Q(t) \mathbf{F}^T \mathbf{B} \mathbf{u}}, \quad (40)$$

where, λ is a scalar. Plugging λ into (39), we have

$$\dot{\mathbf{x}} = - \frac{\dot{Q}(t) \|\mathbf{F}(\mathbf{x})\|^2}{2Q(t) \mathbf{F}^T \mathbf{B} \mathbf{u}} \mathbf{u}, \quad (41)$$

Equation (41) is the general form equation for the continuous Newton homotopy methods. A class of continuous Newton homotopy methods can be obtained from this general equation by reasonably choosing different driving vector \mathbf{u} . It is found that a fictitious time function is introduced in (41) which is a mathematically equivalent n (if t is implicit) or $n + 1$ (if t is explicit) dimensional dynamical system to the original algebraic equation system. The solution for the original algebraic equation can be obtained by applying numerical integration to the equivalent dynamical ODEs.

The fictitious time function $Q(t)$ should be specified before applying the numerical integration. $Q(t)$, as discussed above, should be a monotonically increasing function of t . There are many choices for $Q(t)$. According to [Ku et al. 2009], we can choose

$$Q(t) = e^{\frac{v}{1-m} [(1+t)^{1-m} - 1]}, \quad (42)$$

so that

$$\frac{\dot{Q}(t)}{Q(t)} = \frac{v}{(1+t)^m}, \quad 0 < m \leq 1. \quad (43)$$

We make (42) the first choice of $Q(t)$. A simpler, intuitive choice of the fictitious time function is

method	driving vector \mathbf{u}	$Q(t)$
DNM1	$\mathbf{B}^{-1}\mathbf{F}$	choice 1
DNM2	$\mathbf{B}^{-1}\mathbf{F}$	choice 2*
MBECA1	$\mathbf{B}^T\mathbf{F}$	choice 1
MBECA2	$\mathbf{B}^T\mathbf{F}$	choice 2
DJIFM1	\mathbf{F}	choice 1
DJIFM2	\mathbf{F}	choice 2

Table 1. A summary of continuous Newton homotopy methods.

$$Q(t) = e^t, \quad (44)$$

which makes $\dot{Q}(t)/Q(t) = 1$. This is labeled as the second choice of $Q(t)$.

Finally the general form continuous Newton homotopy method has been derived as (41) with a specified $Q(t)$ in (42) or (44). Integrating this system of ODEs, one can arrive at the stable solution of the ODEs, which is the solution of the original nonlinear algebraic system.

Different choices of the driving vector \mathbf{u} in the general Equation (41) lead to different kinds of continuous Newton homotopy methods. See Table 1 for a summary of methods.

Interestingly, if we choose $Q(t) = e^{2t}$, that is, choice 2*, instead of $Q = e^t$ for the DNM2, we obtain

$$\dot{\mathbf{x}} = -\mathbf{B}^{-1}\mathbf{F}, \quad (45)$$

which turns out to be exactly the continuous Newton method by Hirsch and Smale [1979]. Applying the forward Euler scheme to (45), we have

$$\mathbf{x}_{k+1} = \mathbf{x}_k - \mathbf{B}_k^{-1}\mathbf{F}_k, \quad (46)$$

which is the classical Newton method.

It can be seen from Table 1 that DNMs are different from the other continuous Newton homotopy methods in that the inverse of the Jacobian matrix is involved. The DNM2 and DNM1 should be regarded as the Newton method and a variant Newton method respectively. However, the DNMs [Ku et al. 2011; Ku and Yeih 2012] are more flexible than the Newton method, since the dynamical system of the DNMs can be with different choices of $Q(t)$ and numerical integration methods, while the Newton method is a special case with $Q(t) = e^{2t}$ and the forward Euler method. It is expected that proper selections of $Q(t)$ and integration method may improve the convergence performance.

The MBECAs and the DJIFMs do not involve the inversion of Jacobian matrix. The MBECA1 turns out to be exactly the same as the ECSHA, which is applied in [Dai et al. 2011a].

There are three types of continuous Newton homotopy methods as introduced above. All the three methods are based on the driving vector \mathbf{u} where there is only one vector in \mathbf{u} . To be extended, we can assume \mathbf{u} to be constructed by two vectors, such as \mathbf{F} and $\mathbf{B}^T\mathbf{F}$, or \mathbf{F} and its normal vector \mathbf{P} , or $\mathbf{B}^T\mathbf{F}$ and its normal vector \mathbf{P}^* . To derive the new methods, the only thing to do is to replace the \mathbf{u} in (41). In this study, unless otherwise specified, we use the forward Euler method to perform the integration for the continuous Newton homotopy methods. The performance of the continuous Newton homotopy methods is tested in numerical examples.

3.3. Iterative Newton homotopy methods. Subsequently, Liu and his coworkers developed a series of purely iterative Newton homotopy methods, where $Q(t)$ no longer needs to be specified. Similar to the continuous Newton homotopy methods, these iterative Newton homotopy methods can also be incorporated into a uniform framework.

To derive the purely iterative methods, the general equation (41) of the continuous Newton homotopy methods is first discretized into a discrete time dynamics via the forward Euler method:

$$\mathbf{x}(t + \Delta t) = \mathbf{x}(t) - \beta \frac{\|\mathbf{F}(\mathbf{x})\|^2}{\mathbf{F}^T \mathbf{B} \mathbf{u}} \mathbf{u}, \quad (47)$$

where

$$\beta = q(t) \Delta t \quad \text{and} \quad q(t) = \frac{\dot{Q}(t)}{2Q(t)}. \quad (48)$$

Then, we differentiate \mathbf{F} with respect to t , and obtain

$$\dot{\mathbf{F}} = \mathbf{B} \dot{\mathbf{x}} = -q(t) \frac{\|\mathbf{F}\|^2}{\|\mathbf{B}^T \mathbf{F}\|^2} \mathbf{A} \mathbf{F}, \quad (49)$$

where $\mathbf{A} = \mathbf{B} \mathbf{B}^T$. Similarly, we use the forward Euler scheme to integrate (49) and get

$$\mathbf{F}(t + \Delta t) = \mathbf{F}(t) - \beta \frac{\|\mathbf{F}(\mathbf{x})\|^2}{\mathbf{F}^T \mathbf{B} \mathbf{u}} \mathbf{u}. \quad (50)$$

Considering that formula (37) is an invariant manifold in time and letting $C = \frac{1}{2} \|\mathbf{F}(\mathbf{x}_0)\|^2$, we can get

$$\|\mathbf{F}(t)\|^2 = \frac{2C}{Q(t)}, \quad (51)$$

$$\|\mathbf{F}(t + \Delta t)\|^2 = \frac{2C}{Q(t + \Delta t)}, \quad (52)$$

since the defined manifold should be invariant with time. Squaring both sides of (50) and using Equations (51) and (52) we can obtain

$$\frac{C}{Q(t + \Delta t)} = \frac{C}{Q(t)} - 2\beta \frac{C}{Q(t)} + \beta^2 \frac{C}{Q(t)} \frac{\|\mathbf{F}\|^2}{(\mathbf{F}^T \mathbf{B} \mathbf{u})^2} \|\mathbf{B} \mathbf{u}\|^2. \quad (53)$$

After some simple algebra, the following scalar equation is obtained:

$$a_0 \beta^2 - 2\beta + 1 - s = 0, \quad (54)$$

where

$$a_0 := \frac{\|\mathbf{F}\|^2 \|\mathbf{B} \mathbf{u}\|^2}{\|\mathbf{F}^T \mathbf{B} \mathbf{u}\|^2}, \quad s = \frac{Q(t)}{Q(t + \Delta t)} = \frac{\|\mathbf{F}(t + \Delta t)\|^2}{\|\mathbf{F}(t)\|^2}. \quad (55)$$

It worth noting that s can be used as a quantity to assess the convergence property of the iterative Newton homotopy methods, and $a_0 \geq 1$ according to the Cauchy–Schwarz inequality

$$\|\mathbf{F} \cdot (\mathbf{B} \mathbf{u})\| \leq \|\mathbf{F}\| \|\mathbf{B} \mathbf{u}\|. \quad (56)$$

From (54), we can take the solution of β to be

$$\beta = \frac{1 - \sqrt{1 - (1 - s)a_0}}{a_0}. \quad (57)$$

To ensure $1 - (1 - s)a_0 \geq 0$, let

$$1 - (1 - s)a_0 = \gamma^2 \geq 0, \quad (58)$$

$$s = 1 - \frac{1 - \gamma^2}{a_0}, \quad (59)$$

and from (57) it follows that

$$\beta = \frac{1 - \gamma}{a_0}. \quad (60)$$

From Equations (47), (55) and (60) we can obtain the algorithm

$$\mathbf{x}(t + \Delta t) = \mathbf{x}(t) - (1 - \gamma) \frac{\mathbf{F}^T \mathbf{B} \mathbf{u}}{\|\mathbf{B} \mathbf{u}\|^2} \mathbf{u}, \quad (61)$$

where

$$-1 < \gamma < 1 \quad (62)$$

is a parameter to be chosen by user. Equation (61) is the general form of the iterative Newton homotopy methods.

Using Equations (55), (59) and (62) we derive that

$$\frac{\|\mathbf{F}(t + \Delta t)\|}{\|\mathbf{F}(t)\|} = \sqrt{s} < 1, \quad (63)$$

which means that the residual error is absolutely decreased. This property guarantees that the algorithm in (61) is absolutely convergent to the true solution, and a smaller s implies a faster convergence rate.

Recall that the continuous Newton homotopy methods involve the fictitious time function, and the dynamical system (41) should be integrated in time, step by step. Conversely, the iterative Newton homotopy methods are purely iterative, and do not require a specification of $Q(t)$. Different choices of the driving vector \mathbf{u} in the general Equation (61) will lead to different iterative Newton homotopy methods as summarized in Table 2, wherein $\mathbf{R} = \mathbf{B}^T \mathbf{F}$, $\mathbf{C} = \mathbf{B}^T \mathbf{B}$.

The RNBA is the first iterative Newton homotopy method, which employs one vector \mathbf{R} in the driving vector \mathbf{u} . Later, a series of iterative Newton homotopy methods employing two vectors in the driving vector are developed. The OVDA uses $\mathbf{u} = \alpha \mathbf{F} + \beta \mathbf{R}$, and the dividing parameters α and β are determined by letting $\partial s / \partial \alpha = 0$ and $\beta = 1 - \alpha$.

Liu, Dai and Atluri [2011a; 2011b] proposed the OIA/ODVs and the OIAs. The main difference between the OIA/ODVs, OIAs and the OVDA is that two orthogonal vectors instead of the couple of \mathbf{F} and \mathbf{R} are used to constitute the driving vector. Numerical examples in [Liu et al. 2011a; 2011b] illustrated that OIA/ODVs and OIAs have a better performance than the OVDA in solving their selected problems, while this is not always the case. Numerical examples of this study indicate that the OIAs and the OVDA are comparable in terms of convergence rate, while the OIA/ODVs converge more slowly. In particular, the OIA/ODV[R] is several times slower than the OIAs and the OVDA. So the OIAs are believed to be superior to the OIA/ODVs.

method	driving vector \mathbf{u}	\mathbf{P} (or \mathbf{P}^*)	parameter optimization scheme
RNBA [Liu and Atluri 2011b]	\mathbf{R}	*	*
OVDA [Liu and Atluri 2011a]	$\alpha \mathbf{F} + \beta \mathbf{R}$	*	$\partial s / \partial \alpha = 0, \beta = 1 - \alpha$
OIA/ODV[R] [Liu et al. 2011a]	$\alpha \mathbf{R} + \beta \mathbf{P}$	$\mathbf{R} - \frac{\ \mathbf{R}\ ^2}{\mathbf{R}^T \mathbf{C} \mathbf{R}} \mathbf{C} \mathbf{R}$	$\partial s / \partial \alpha = \partial s / \partial \beta = 0$
OIA/ODV[F] [Liu et al. 2011a]	$\alpha \mathbf{F} + \beta \mathbf{P}^*$	$\mathbf{F} - \frac{\ \mathbf{F}\ ^2}{\mathbf{F}^T \mathbf{C} \mathbf{F}} \mathbf{C} \mathbf{F}$	$\partial s / \partial \alpha = \partial s / \partial \beta = 0$
OIA(R) [Liu et al. 2011b]	$\alpha \mathbf{R} + \beta \mathbf{P}$	$\mathbf{F} - \frac{\mathbf{R} \cdot \mathbf{F}}{\ \mathbf{R}\ ^2} \mathbf{R}$	$\partial s / \partial \alpha = \partial s / \partial \beta = 0$
OIA(F) [Liu et al. 2011b]	$\alpha \mathbf{F} + \beta \mathbf{P}^*$	$\mathbf{R} - \frac{\mathbf{R} \cdot \mathbf{F}}{\ \mathbf{F}\ ^2} \mathbf{F}$	$\partial s / \partial \alpha = \partial s / \partial \beta = 0$
LOIA [Liu and Atluri 2012]	$\alpha \mathbf{F} + \mathbf{R}$	*	$\partial s / \partial \alpha = 0, \beta = 1 - \alpha$
GOIA [Liu and Atluri 2012]	$\alpha \mathbf{F} + \mathbf{R}$	*	global minimum of s

Table 2. A summary of iterative Newton homotopy methods.

It can be seen from Table 2 that the LOIA is essentially similar to the OVDA method, so only the OVDA is evaluated via numerical experiments. For more details about the Newton homotopy methods, one is recommended to refer to related references in Table 2.

4. Numerical examples

In this section, examples concerning the solution of von Kármán nonlinear plate equations, for a plate undergoing various kinds of loads are provided to verify the present method as well as to evaluate the novel algebraic equation solvers. The Young's modulus and Poisson's ratio are $E = 205.8 \times 10^9$ and $\nu = 0.3$, unless otherwise specified. For NAE solvers, the parameter $\gamma = 0.3$ and the stop criterion $\epsilon = 10^{-4}$ are fixed throughout the paper.

In some examples, the external loads are applied in terms of critical values P_{ocr} or τ_{cr} . The critical values of P_{ocr} and τ_{cr} for a plate depend on its supporting pattern as well as length versus width ratio. For a simply supported plate with $a/b = 1$ or 2, the critical values are given as follows

$$\sigma_{\text{ocr}} = 4 \times \frac{\pi^2 D}{b^2 t}, \quad \frac{a}{b} = 1, 2,$$

$$\tau_{\text{cr}} = k \times \frac{\pi^2 D}{b^2 t}, \quad k = 9.34 \text{ if } \frac{a}{b} = 1; k = 6.6 \text{ if } \frac{a}{b} = 2,$$

where $\sigma_{\text{ocr}} = P_{\text{ocr}}/(bt)$. For more types of supporting forms and length/width ratios, one may refer to Chapter 9 of [Timoshenko 1961].

4.1. A square plate under uniaxial compression. In this example, a simply supported square plate under uniaxial compression is analyzed. The dimensions of this plate are $a = 1, b = 1, t = 0.009$, where a, b, t represent length, width and thickness respectively. All dimensions in this study are in meters unless

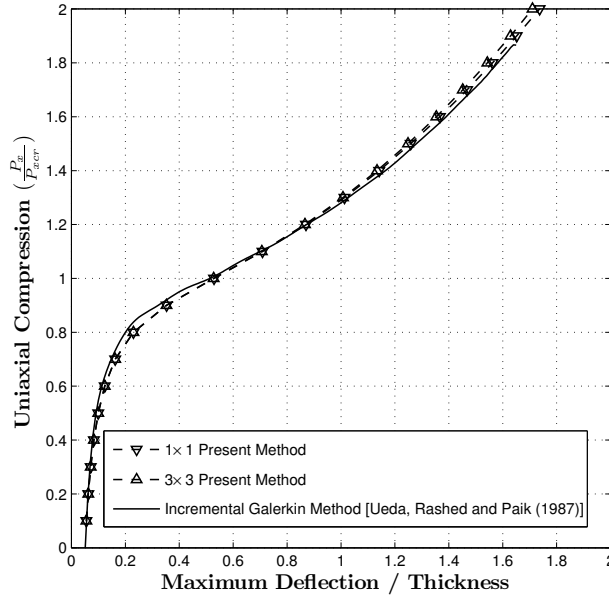


Figure 2. Deflection versus compression loads.

otherwise mentioned. The initial deflection is specified as $A_{0mn} = 0.45 \times 10^{-3}$. P_{cr} is the critical compression causing buckling of plate.

To examine the accuracy of the present global Galerkin method, a case of the incremental Galerkin method developed by Ueda, Rashed and Paik [Ueda et al. 1987] is used to compare with the present method. Figure 2 plots the load-deflection relationships obtained at different load levels. The compression load acting on the plate varies from 0.1 to 2 with load step being 0.1. Therefore, there are 20 load steps and hence 20 sets of NAEs to solve. For the first load step, the initial values are chosen as a set of small values rather freely, since the expected solution is small. In addition to the first load step, the initial values to start the NAE solver are obtained through a load marching procedure, where the solution of the previous load step is used as the initials of the current load step.

It can be seen from Figure 2 that the results of the present Galerkin method and the incremental Galerkin method are in very good agreement. Figure 2 also reveals that the present method with nine term (3×3) deflection function (labeled as 3×3 present method) agrees very well with the 1×1 present method. In the square plate case, 1×1 present method is quite accurate owing to the similarity between the one half wave plate deflection and the 1×1 deflection function, which indicates solving the simply supported square plate is extremely economic via the present global Galerkin method. Numerical calculations throughout the paper are performed in Matlab on a personal computer with an Intel core i5 CPU.

4.1.1. Comparative performance of various NAE solvers. Another purpose of the present study is to evaluate the various kinds of NAE solvers. We employ the 3×3 present method to solve the von Kármán plate problem. Thus, a system of nine NAEs is obtained. Table 3 provides the computational information for solving the resulting system of NAEs via various kinds of solvers. The number of iterations, computing time, and time per iteration (TPI) are listed in Table 3, from which we can see that DNM2, that is,

method	time(s)	iterations	TPI(s)
SHM	2923.9	184679	0.0158
MBECA1	289.9	19144	0.0151
MBECA2	859.7	56758	0.0151
DNM1	1.9	76	0.0255
DNM2	1.7	72	0.0233
DJIFM1	26.9	1849	0.0145
DJIFM2	51.8	3419	0.0152
OVDA	20.2	999	0.0202
OIA/ODV[R]	317.4	16142	0.0197
OIA/ODV[F]	26.5	1341	0.0198
OIA(R)	20.2	1020	0.0198
OIA(F)	20.1	1001	0.0201
GOIA	19.6	980	0.0200

Table 3. Example 1: 3×3 present method.

the classical Newton method, and its variant DNM1 are the fastest ones. It implies that the best driving vector should employ the inverse of the Jacobian matrix. However, since the DNM1 and DNM2 require calculating the inverse of the Jacobian matrix, the TPIs of them are expected to be larger than those of the other methods, which is justified in Table 3. It is emphasized that the larger TPIs do not influence much the computational costs due to the relatively smaller size of the Jacobian matrix. However, when the number of NAEs is very large, the initial “guesses” of solution are not easy to generate, and when the Jacobian matrix is nearly singular or severely ill-conditioned, the advantages of the scalar homotopy methods such as the GOIA which does not need to invert the Jacobian matrix start becoming apparent.

The FTIM and MNM are applied to the present case; however, neither gives a convergent solution. The preliminary SHM based on the fixed-point homotopy function converges several times more slowly than the Newton homotopy methods based on the Newton homotopy function. In general, the number of iterations of the iterative methods of the lower part table is smaller than that of the continuous methods of the upper part table. However the OIA/ODV[R] is verified to be an exceptional case in the family of iterative methods, which costs ten more times iterations than its counterpart OIA/ODV[F]. The iterative Newton homotopy methods cost less iterations than the continuous Newton homotopy methods in general. *As shown in Table 3, the OVDA, the OIAs and the GOIA are comparable, and promise to be the best Jacobian-inverse-free methods; they may play an important role in solving a nonlinear problem whose initial guess is hard to choose, when Jacobian matrix is ill-conditioned or nearly singular, when the number of NAEs tends to be very large and when the system of NAEs is overdetermined or underdetermined.*

4.2. A rectangular plate under uniaxial compression. A simply supported rectangular plate under uniaxial compression is considered. Its dimensions are $a = 1.68$, $b = 0.98$ and $t = 0.011$. The initial deflection is given by $A_{011} = 1.1 \times 10^{-3}$ and $A_{021} = 0.22 \times 10^{-3}$. The present Galerkin method is applied to solve this rectangular plate. Besides, the analysis is also carried out by the FEM using rectangular,

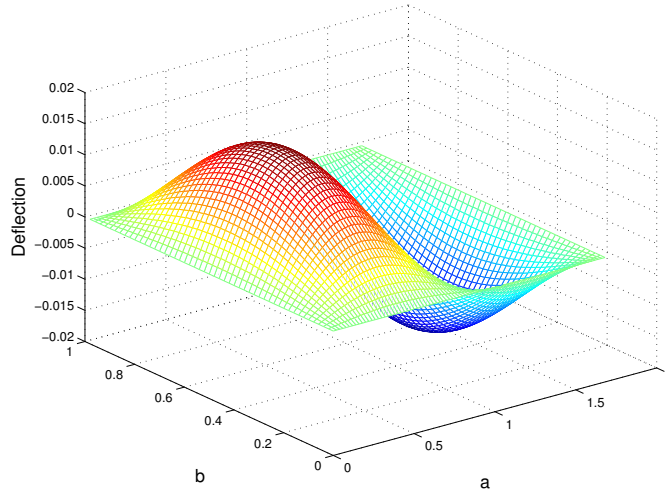


Figure 3. Deformation of a rectangular plate under uniaxial compression: load = 2.

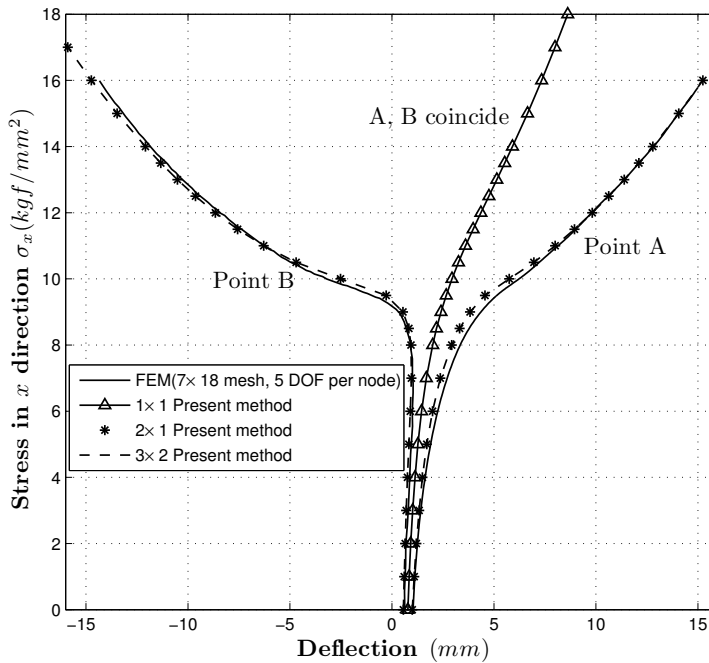


Figure 4. Stress σ_x versus deflection of point A and B, for the present Galerkin method and the finite element method.

four node, and nonconforming plate elements with five degrees freedom at each node; 7×18 elements for half of the plate.

Figure 3 provides the deformation of the rectangular plate. Figure 4 displays curves that plot the stress σ_x against the deflection of two points A $(0.25a, 0.5b)$ and B $(0.75a, 0.5b)$. It reveals that the results

of the present method and that of the FEM are in good agreement, which confirms the accuracy of the present method.

Comparing the solutions by the present methods in Figure 4, we see that the global Galerkin method with 1×1 term deflection function cannot provide an acceptable solution, Physical intuition tells us that the deformation of the plate cannot be described by one term deflection function anyway. It can be seen from Figure 3 that the deformation of the plate has two half waves in the x direction; therefore at least two terms should be used in x direction. The result of 2×1 present method is in a very good agreement with the result of FEM. Figure 4 also displays that solutions by 3×2 and 2×1 present methods are overlapped, which indicates that present method with only a few modes can provide a very accurate solution for the simply supported von Kármán plate under uniaxial compression.

4.2.1. Performance of solvers. The 3×2 present method is used to solve the rectangular plate, and the computation information for various solvers for solving the Galerkin-resultant NAEs is provided in Table 4.

In accordance with Example 1 (Table 3), the DNM1 and DNM2 involved with the inverse of the Jacobian matrix have larger TPIs, while the total computing time and consumed iterations of the DNMs are much more cheap. The reason is that the usage of \mathbf{B}^{-1} provides the best descent direction to reduce residuals (hence requiring fewer iterations), and the time consumption of inverting the current Jacobian matrix is not expensive. Although in the present case the slightly different TPIs are not sufficient to reverse the overall performance of the Newton method and the homotopy methods. It is reasonable to expect that when the size of Jacobian is very large, the Newton method would suffer from a larger TPI. Also, the iterative Newton homotopy methods are computationally cheaper than the continuous-type methods in general, except the OIA/ODV[R].

method	time(s)	iterations	TPI(s)
MBECA*	600.7	11208	0.0536
MBECA1	39.4	12555	0.0031
MBECA2	63.3	20537	0.0031
DNM1	0.51	109	0.0047
DNM2	0.55	114	0.0048
DJIFM1	4.6	1424	0.0032
DJIFM2	5.9	1861	0.0032
OVDA*	53.2	633	0.0840
OVDA	2.3	663	0.0035
OIA/ODV[R]	20.4	6336	0.0032
OIA/ODV[F]	2.9	866	0.0033
OIA(R)	2.2	636	0.0034
OIA(F)	2.3	659	0.0034
GOIA	2.3	665	0.0035

Table 4. Example 2: 3×2 present method.

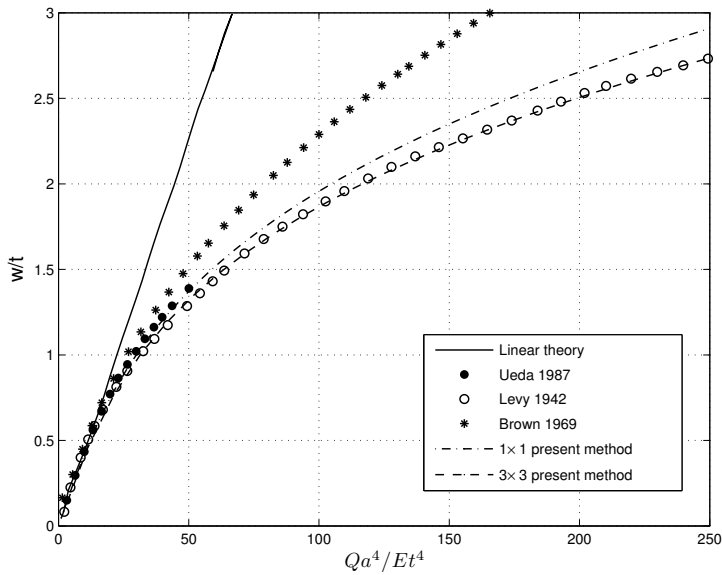


Figure 5. Square plate: central deflection versus lateral pressure.

In addition, the MBECA* [Dai et al. 2011a] (or named ECSHA) and the OVDA* [Dai et al. 2011b] using symbolic calculations of the Jacobian matrix at each iteration are also listed in Table 4. We see that inclusion of the symbolic operations slightly improves the performance of the solvers in terms of the consumed number of iterations, because using symbolic operations can avoid the cut-off errors which inherently exist in numerical calculations. Nevertheless, the TPIs of MBECA* and OVDA* are about ten times larger than those of the MBECA and OVDA, which indicates that the contribution of deriving the explicit Jacobian matrix is of significant importance. Table 4 shows that the GOIA, the OIAs and the OVDA are the most efficient Jacobian-inverse-free methods. Next to the above three methods are the OIA/ODV[F] and the DJIFMs; the OIA/ODV[R] and the MBECAs are several orders of magnitude more expensive. It is found that Newton homotopy methods having a driving vector with \mathbf{F} inside are superior to those where \mathbf{F} is not included.

4.3. A square/rectangular plate subjected to lateral load. A square plate, with geometry $a = b = 1$ and $t = 0.009$, subjected to a uniformly distributed lateral load Q is considered in this example without initial imperfections.

It indicates in Figure 5 that the present method is quite accurate in solving a plate under lateral load through a comparison with the incremental Galerkin method [Ueda et al. 1987], and Levy's method. The result of 1×1 present method agrees well with that of 3×3 present method. We conclude that for a square plate, the present method with very few terms can be reasonably accurate, due to the similarity between the real plate deflection and the one half-wave bulge of the assumed function.

Figure 5 also gives the result via a finite difference method proposed by Brown and Harvey [1969]. It is seen that there is a discrepancy between the present method and the finite difference method. The differences between the solutions, which may be attributed to two different sets of boundary conditions, both of which might be loosely described as simply supported, indicate the importance of specifying

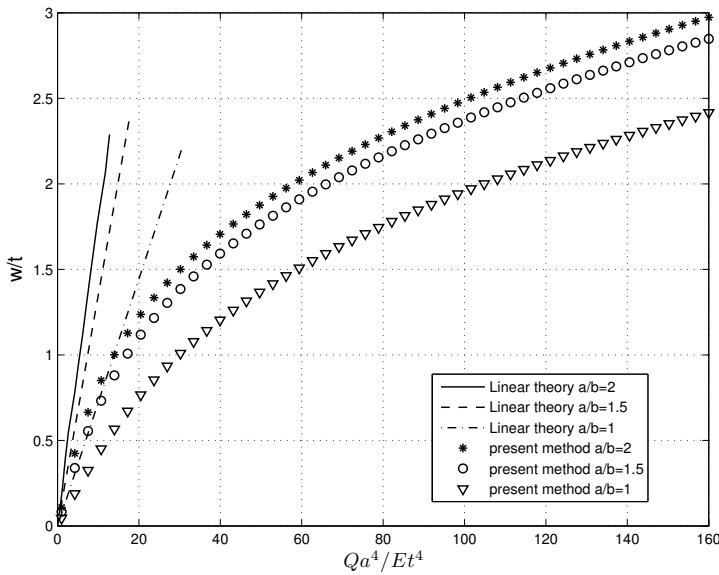


Figure 6. Maximum deflection versus lateral pressure for a range of length/width ratios.

plate number	a/b	b/t	E (GPa)	ν	Q	P_x
1	1	50	205.8	0.30	varies	$0.60P_{xcr}$
2	3	66.7	204.8	0.33	29400 (Pa)	varies
3	3	66.7	204.8	0.33	49000 (Pa)	varies
4	3	74.7	214.6	0.33	$1.43\left(\frac{Qb^4}{Et^4}\right)$	varies
5	3	74.7	214.6	0.33	$4.28\left(\frac{Qb^4}{Et^4}\right)$	varies

Table 5. Geometries and material properties of plates.

all four boundary conditions. In a further study, we are trying to replace the loose simply supported conditions used in [Levy 1942b; Ueda et al. 1987; Paik et al. 2001; Dai et al. 2011a] by strict simply supported conditions using the present method.

Figure 6 shows the deflection-load relationships for various length/width ratios, and the results by the linear theory are also provided. It can be seen that increasing the ratio of length versus width will lead to a larger plate deflection, which is in accord with physical intuition. Under the same load situation, we expect that an infinite large length/width ratio causes the largest deflection of a plate.

4.4. A square/rectangular plate subjected to lateral pressure combined with uniaxial compression.

First, a square plate subjected to lateral pressure combined with uniaxial compression is considered. The x -direction compression acting on the plate is a constant (see plate 1 in Table 5), and the lateral pressure acting on the plate increases as shown in Figure 7. The geometric and material properties are listed in Table 5, and the initial deflection is zero. For comparison purpose, this plate has also been analyzed via

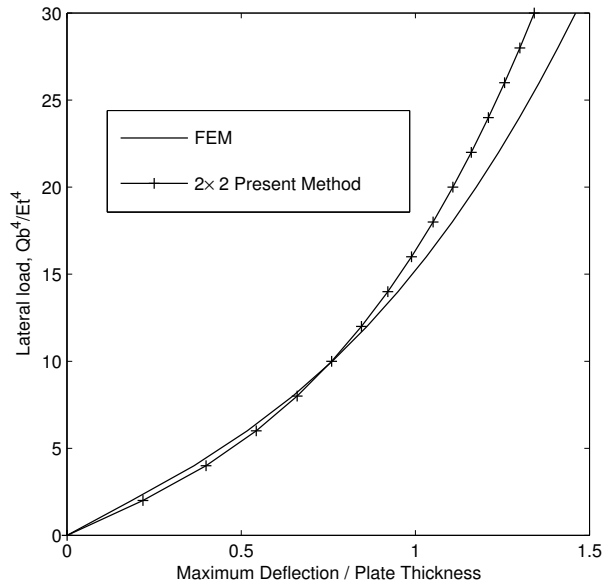


Figure 7. Square plate 1: maximum deflection versus lateral pressure by the present method and the FEM.

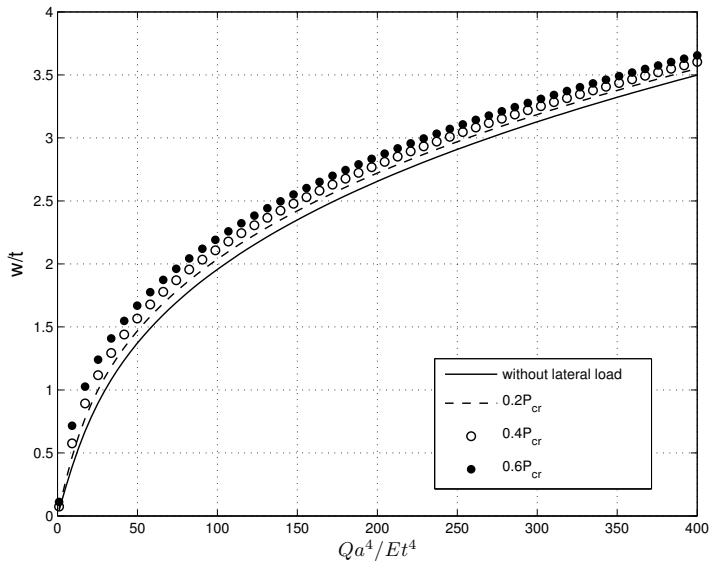


Figure 8. Square plate 1: maximum deflection versus lateral pressure for a range of edge compressions.

FEM in ANSYS (brick element with eight node and three degrees freedom at each node, $50 \times 50 \times 1$ elements for the whole volume).

It is seen from [Figure 7](#) that the results of the present method are quite in accordance with those of the FEM when the lateral pressure is below approximate 15. As the lateral pressure increases further, the discrepancy between the two methods increases.

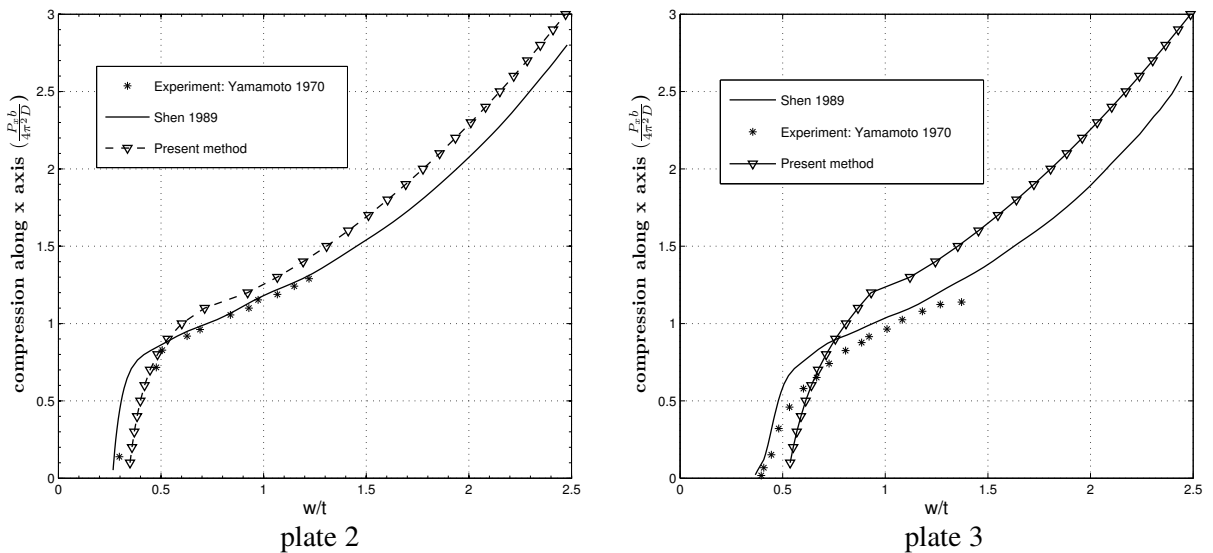


Figure 9. Uniaxial compression versus maximum deflection with a constant lateral pressure by the present method, the perturbation method [Shen 1989] and the experiment [Yamamoto et al. 1970]. Axial load versus deflection: plate 2 (left) and plate 3 (right).

Figure 8 shows the deflection versus lateral pressure curves for square plate 1 under a range of edge compressions. It indicates that as the edge loading increases the plate deflection increases accordingly under the same lateral pressure.

In the first case of plate 1, the axial compression is kept constant and the lateral pressure is increased incrementally. We also analyze the cases, rectangular plates 2–5, wherein the lateral pressure is exerted first and kept constant, and x -direction compression is increased gradually.

Figure 9 shows the comparisons of the load-deflection relationships by the present method, the perturbation method [Shen 1989], and the experiment results [Yamamoto et al. 1970]. We see that the present method approximately agrees with the perturbation method and the experiment. The present method is more closer to the experiment than the perturbation method when the compression is relatively low. However, as the load increases, the deflection by the present method is smaller than that of the perturbation method and the experiment. The discrepancy between the present method and the experiment is approximately a constant value, larger than the discrepancy between the perturbation method and the experiment. The present method is simpler than the perturbation method in [Shen 1989]. Because in [Shen 1989], the Galerkin method is used to first convert lateral pressure into an initial deflection, and then governing equations are studied using a perturbation method, taking deflection as its perturbation parameter.

Figure 10 displays the deflection-axial load relations for a range of lateral pressures. The curves are computed through a load-marching procedure wherein the solution of the previous load step is used as the initial of the current load step. In Figure 10, both forward marching and backward marching paths are plotted. It can be seen that with the increase of the lateral pressure, a hysteresis phenomenon may occur. In this case, $Q = 3.7$ has no hysteresis while $Q = 4$ has hysteresis; so the buckling behavior of

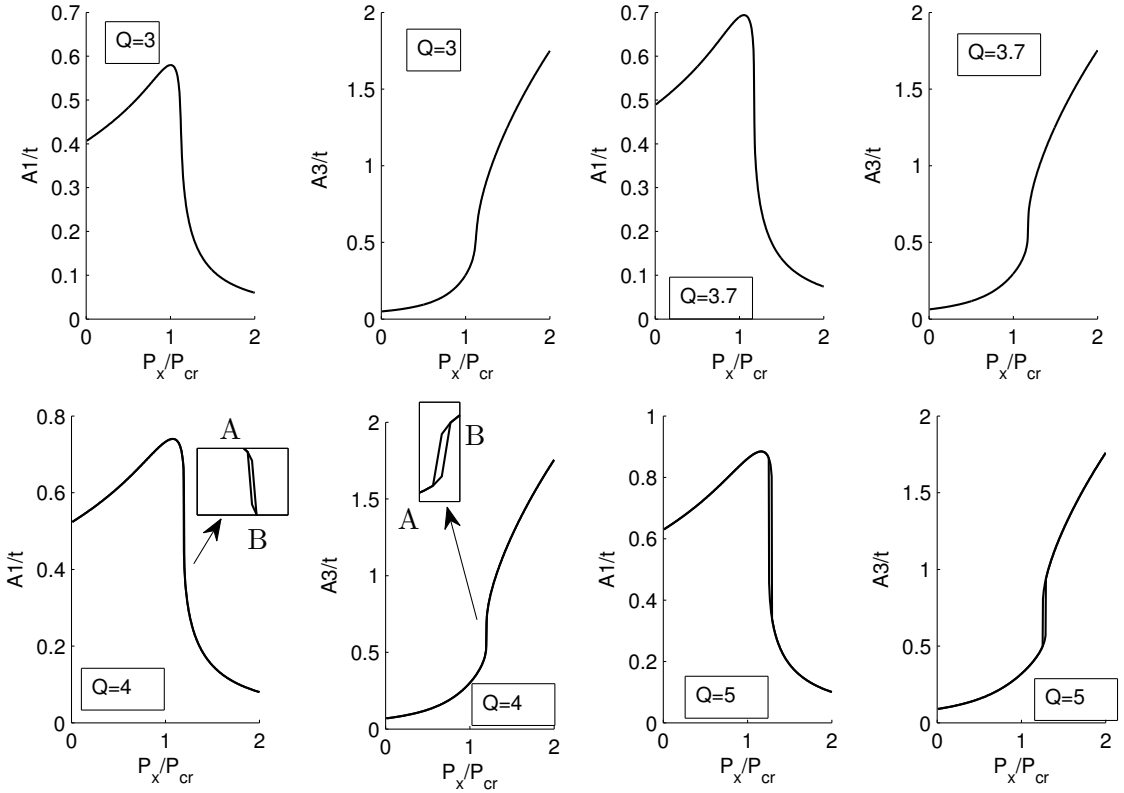


Figure 10. The deflection versus axial load relationships for a range of lateral loading Q s: $Q = 3, 3.7$, no hysteresis; $Q = 4, 5$, hysteresis occurs.

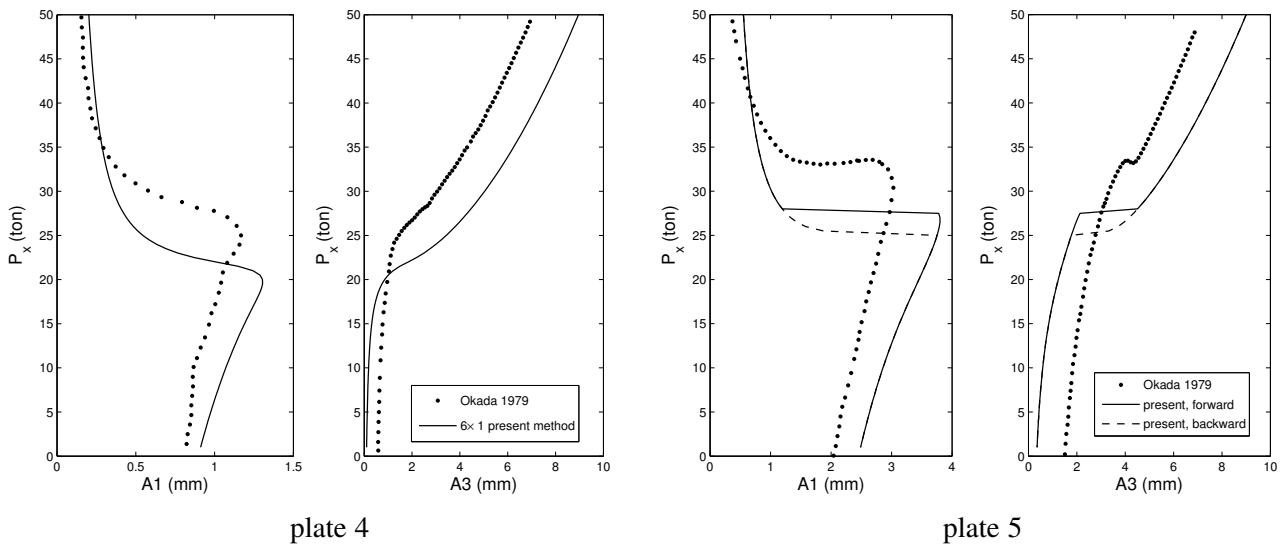


Figure 11. Axial load versus deflection: comparison between present method and [Okada et al. 1979]: not buckling (plate 4); buckling (plate 5).

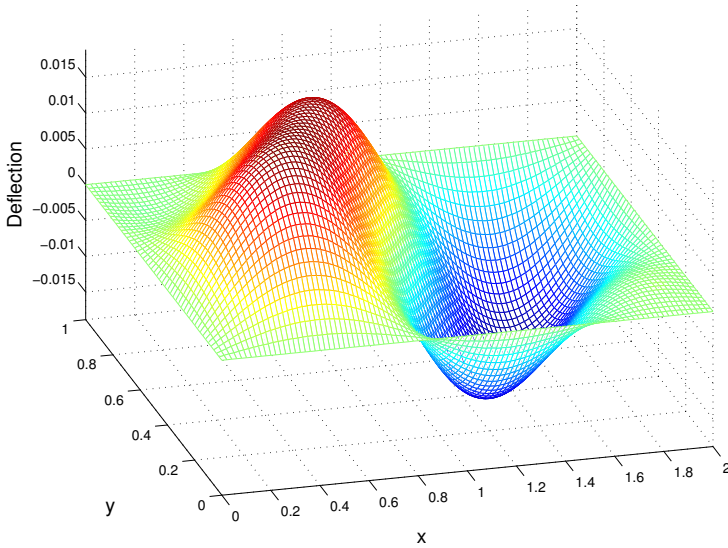


Figure 12. Deformation of a rectangular plate under uniaxial compression $P_x = 0.65 P_{xcr}$ (applied first and keep constant) and shear $\tau = 2\tau_{cr}$ (applied gradually).

the plate occurs at between $Q = 3.7$ and $Q = 4$. By a refined estimation, we determined that $Q^* = 3.75$ is the buckling critical value detected by the present method, which is very close to the critical value 3.7 given in [Okada et al. 1979].

When the lateral pressure is small ($Q \leq Q^* = 3.75$), the buckling does not occur; that is, there is neither the bifurcation point nor the unstable paths on the deflection-axial load curves. In fact, the deformation varies continuously towards the deflection form of triple bulges with the large value of A_3 , with the increase of the edge compression from the single bulge deflection form.

When the lateral pressure is large ($Q > Q^* = 3.75$), the buckling occurs at a certain edge compression (the load at point A in Figure 10). In this case, the plate can show a jump behavior from a single bulge deformation form to a three bulges deformation form once the edge pressure reaches the critical value. In addition, an external stimulus to the plate may switch the deflection form of the plate when edge pressure is in between load of point A and load of point B, because in this interval (hysteresis area) this system has two stable states either of which is physically realizable.

Figure 11 provides the solutions for plates 4 and 5 by the present method and the Rayleigh–Ritz method [Okada et al. 1979]. It can be seen that both methods can detect the critical buckling points. However, there exists a discrepancy between the two methods. Similar to the case in Section 4.3, the differences between the solutions are due to the different sets of boundary conditions, although both of which might be loosely described as simply supported.

4.5. A rectangular plate subjected to shear and uniaxial compression. A rectangular plate under shear stress and uniaxial compression is analyzed with dimensions being $a = 2$, $b = 1$ and $t = 0.009$. The uniaxial compression $P_x = 0.65 P_{xcr}$ is exerted first and kept constant. The shear stress is applied incrementally from $0.1\tau_{cr}$ to $2\tau_{cr}$ with a step size $0.1\tau_{cr}$. The final deformation of the plate is shown in Figure 12.

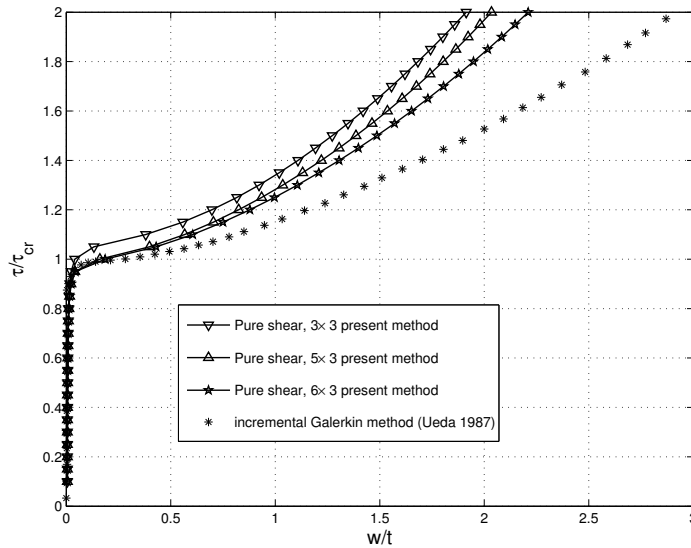


Figure 13. Comparisons of load-deflection curves as given by present global Galerkin method and the incremental Galerkin method [Ueda et al. 1987] under a pure shearing load.

Load-deflection curves of the rectangular plate under pure shearing load are plotted in Figure 13 via the present method and the incremental Galerkin method. It is shown that the present method is in accord with the incremental Galerkin method. The addition of terms in the assumed deflection function can generate a more accurate result if the result of the incremental Galerkin method is taken as a benchmark. Also, we can see that the deflection calculated by the present method is smaller than the incremental Galerkin method in general. It can be seen that the buckling critical value for the plate is about $\tau \approx \tau_{cr}$, since there is no extra force acting on the plate and the initial imperfection is very slight so that it does not influence much.

Load-deflection curves of the plate under combined uniaxial and shearing loadings are given in Figure 14. A similar conclusion can be obtained as the above pure shearing case. There is a discrepancy between the results of the present method and the incremental Galerkin method. As the number of terms in the deflection function increases, the difference between the present method and the incremental method decreases. It shows from Figure 14 that the critical shearing value for the plate buckling decreases from the theoretical value τ_{cr} of the pure shearing condition to approximately half of τ_{cr} of the combined load condition. It illustrates that the uniaxial compression acting on the plate can degrade the critical value for shearing buckling. Plus, with rectangular plates, more terms in the longitudinal direction are required such that the real deflection shape of the plate can be satisfactorily described.

4.5.1. Comparison of solvers. The consumed computing efforts via different solvers are provided in Table 6, where eight term (4×2) deflection function is used in the present Galerkin method.

We see that the DNM2, that is, classical Newton method, is the fastest method both in terms of iteration numbers and computational time. The DNM1, a variant Newton method, is comparable with the Newton method. The DNMs are regarded as Newton-type methods, since they involve with the

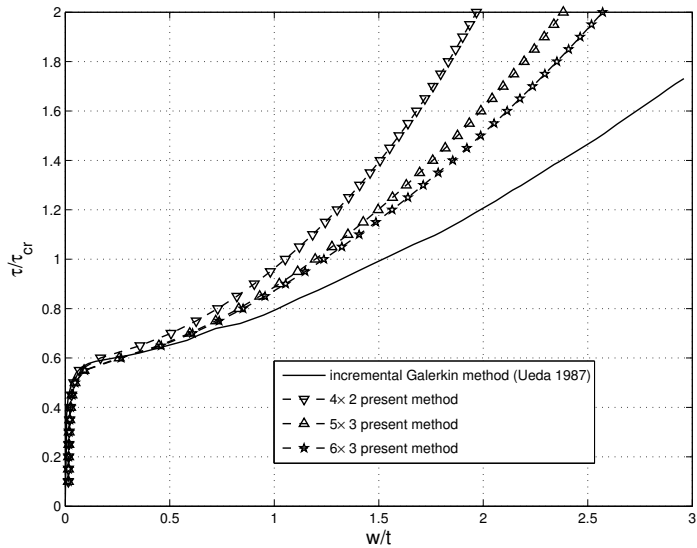


Figure 14. Comparisons of load-deflection curves as given by present global Galerkin method and the incremental Galerkin method [Ueda et al. 1987] under uniaxial compression combined with a shearing load.

method	time(s)	iterations	TPI
MBECA1	174.07	17394	0.0100
MBECA2	159.4	15938	0.0100
DNM1	5.28	472	0.0112
DNM2	5.05	457	0.0111
DJIFM1	35.68	3479	0.0103
DJIFM2	21.81	2143	0.0102
OVDA	12.96	1298	0.0100
OIA/ODV[R]	95.03	9655	0.0098
OIA/ODV[F]	16.19	1689	0.0096
OIA(R)	12.93	1300	0.0099
OIA(F)	12.94	1300	0.0100
GOIA	12.94	1300	0.0100

Table 6. Example 5: 4×2 present method.

inverse of Jacobian matrix. The TPIs of the DNM1 and DNM2 are larger than those of other methods, which can be explained by the need for inverting Jacobian matrix. In general, the iterative methods are several times faster than the continuous methods except the OIA/ODV[R]. However owing to the small size of the Jacobian matrix, the TPIs of DNMs are only slightly larger. Therefore the DNMs, which

converge quadratically fast, are preferable choices for solving the current Galerkin-resultant system of NAEs which involve only a small number of nonlinear equations.

The prominent Jacobian-inverse-free methods, for example, OVDA, the OIAs and the GOIA, can be employed in solving nonlinear problems whose initial guess is hard to choose, whose Jacobian matrix is ill-conditioned or nearly singular, when the number of equations tends to be very large, and when the system of equations is either over or under determined.

5. Conclusion

In this paper a global Galerkin method is presented for solving the simply supported initially imperfect von Kármán plate under a combination of in-plane and lateral loads. The coupled nonlinear differential equations are transformed into a system of NAEs via the global Galerkin method. The explicit form of the Jacobian matrix (“tangent stiffness” matrix) of the NAEs is derived to eliminate the symbolic calculations involved in solving the NAEs. Plates subjected to uniaxial compression, or lateral pressure, or a combination of axial compression and lateral pressure, or a combination of shear stress and axial compression, are investigated by the present global Galerkin method in numerical examples. Large deflections of plate under different loading conditions are analyzed, and nonlinear phenomena such as the buckling behavior and the jump phenomenon are discussed. The present method is validated to be in agreement with the perturbation method, the incremental Galerkin method, the finite difference method, the finite element method and the experiments.

The present method is extremely advantageous provided that the deflection shape of a plate can be accurately expressed by the deflection function with a few terms. Numerical experiments indicate that the computing effort of the present method would be very economic when less than forty terms are considered in the assumed deflection function. Also, because of the extremely high accuracy provided at a very modest cost, the global Galerkin method may also provide the much needed highly accurate benchmark solutions against which other numerical methods may be validated. While distributed loads are treated in the present paper using the Galerkin method and trigonometric basis functions, (nonlinear) plates subjected to concentrated loads at arbitrary locations will be treated in a forthcoming paper using radial basis functions [Atluri 2005] and a spatial collocation or a Galerkin method. The resulting NAEs for these point load problems can be solved by the same methods as in the present paper.

On the other hand, a series of scalar homotopy methods (mainly the Newton homotopy methods), which do not need to invert the Jacobian matrix, are reviewed and used to solve the Galerkin-resulting system of NAEs. The performance of each method is evaluated. The GOIA, the OIAs and the OVDA promise to be the best Jacobian-inverse-free methods hitherto. A general form equation is proposed to incorporate all the existing scalar Newton homotopy methods in a uniform framework. Interestingly, the classical Newton method (labeled DNM2 in paper) can be generated from this general dynamical system under a certain condition.

Acknowledgement

This study is financially supported by the Doctorate Foundation of Northwestern Polytechnical University (CX201305), the Chinese NSF (11172235), and the Doctor Subject Foundation of the Ministry of Education of China (20106102110018).

References

- [Atluri 2005] S. N. Atluri, *Methods of computer modeling in engineering and the sciences, I: A unified treatment of finite volume, finite element, field-boundary element, meshless, and boundary methods*, Tech Science Press, Forsyth, GA, 2005.
- [Atluri et al. 2009] S. N. Atluri, C.-S. Liu, and C.-L. Kuo, “A modified Newton method for solving non-linear algebraic equations”, *J. Marine Sci. and Tech.* **17**:3 (2009), 238–247.
- [Bergan and Clough 1973] P. G. Bergan and R. W. Clough, “Large deflection analysis of plates and shallow shells using the finite element method”, *Int. J. Numer. Methods Engin.* **5** (1973), 543–556.
- [Bert et al. 1989] C. W. Bert, S. K. Jang, and A. G. Striz, “Nonlinear bending analysis of orthotropic rectangular plates by the method of differential quadrature”, *Comput. Mech.* **5**:2-3 (1989), 217–226.
- [Brebbia and Connor 1969] C. Brebbia and J. Connor, “Geometrically nonlinear finite-element analysis”, *J. Engng. Mech. Div. (ASCE)* **95** (1969), 463–483.
- [Brown and Harvey 1969] J. C. Brown and J. M. Harvey, “Large deflections of rectangular plates subjected to uniform lateral pressure and compressive edge loading”, *J. Mech. Engin. Sci.* **11**:3 (1969), 305–317.
- [Chia 1980] C. Y. Chia, *Nonlinear analysis of plates*, McGraw-Hill, New York, NY, 1980.
- [Dai et al. 2011a] H. H. Dai, J. K. Paik, and S. N. Atluri, “The global nonlinear Galerkin method for the analysis of elastic large deflections of plates under combined loads: a scalar homotopy method for the direct solution of nonlinear algebraic equations”, *Comput. Mater. Continua* **23**:1 (2011), 69–99.
- [Dai et al. 2011b] H. H. Dai, J. K. Paik, and S. N. Atluri, “The global nonlinear Galerkin method for the solution of von Karman nonlinear plate equations: an optimal and faster iterative method for the direct solution of nonlinear algebraic equations $F(\mathbf{x}) = \mathbf{0}$, using $\mathbf{x} = \lambda [\alpha \mathbf{F} + (1 - \alpha) \mathbf{B}^T \mathbf{F}]$ ”, *Comput. Mater. Continua* **23**:2 (2011), 155–185.
- [Dai et al. 2014a] H. H. Dai, X. K. Yue, J. P. Yuan, and S. N. Atluri, “A time domain collocation method for studying the aeroelasticity of a two dimensional airfoil with a structural nonlinearity”, *J. Comput. Phys.* **270** (2014), 214–237.
- [Dai et al. 2014b] H. H. Dai, X. K. Yue, J. P. Yuan, and D. Xie, “A fast harmonic balance technique for periodic oscillations of an aeroelastic airfoil”, 2014. Submitted for publication in *J. Fluids Struct.*
- [Hirsch and Smale 1979] M. W. Hirsch and S. Smale, “On algorithms for solving $f(x) = 0$ ”, *Comm. Pure Appl. Math.* **32**:3 (1979), 281–313.
- [Kane and Levinson 1985] T. R. Kane and D. A. Levinson, *Dynamics, theory and applications*, McGraw-Hill, New York, NY, 1985.
- [Ku and Yeih 2012] C.-Y. Ku and W. Yeih, “Dynamical Newton-like methods with adaptive stepsize for solving nonlinear algebraic equations”, *Comput. Mater. Continua* **31**:3 (2012), 173–200.
- [Ku et al. 2009] C.-Y. Ku, W. Yeih, C.-S. Liu, and C.-C. Chi, “Applications of the fictitious time integration method using a new time-like function”, *CMES Comput. Model. Eng. Sci.* **43**:2 (2009), 173–190.
- [Ku et al. 2011] C.-Y. Ku, W. Yeih, and C.-S. Liu, “Dynamical Newton-like methods for solving ill-conditioned systems of nonlinear equations with applications to boundary value problems”, *CMES Comput. Model. Eng. Sci.* **76**:2 (2011), 83–108.
- [Levy 1942a] S. Levy, “Bending of rectangular plates with large deflections”, technical report 737, National Advisory Committee for Aeronautics, 1942, <http://naca.central.cranfield.ac.uk/reports/1942/naca-report-737.pdf>.
- [Levy 1942b] S. Levy, “Bending of rectangular plates with large deflections”, technical note 846, National Advisory Committee for Aeronautics, 1942, <http://www.dtic.mil/dtic/tr/fulltext/u2/a800848.pdf>.
- [Levy et al. 1944] S. Levy, D. Goldenberg, and G. Zibritosky, “Simply supported long rectangular plate under combined axial load and normal pressure”, technical note 949, National Advisory Committee for Aeronautics, 1944, <http://digital.library.unt.edu/ark:/67531/metadc59844/m1/1/>.
- [Liu and Atluri 2008] C.-S. Liu and S. N. Atluri, “A novel time integration method for solving a large system of non-linear algebraic equations”, *CMES Comput. Model. Eng. Sci.* **31**:2 (2008), 71–83.
- [Liu and Atluri 2011a] C.-S. Liu and S. N. Atluri, “An iterative algorithm for solving a system of nonlinear algebraic equations, $F(\mathbf{x}) = \mathbf{0}$, using the system of ODEs with an optimum α in $\dot{\mathbf{x}} = \lambda [\alpha \mathbf{F} + (1 - \alpha) \mathbf{B}^T \mathbf{F}]$; $B_{ij} = \partial F_i / \partial x_j$ ”, *CMES Comput. Model. Eng. Sci.* **73**:4 (2011), 395–431.

- [Liu and Atluri 2011b] C.-S. Liu and S. N. Atluri, “Simple ‘residual-norm’ based algorithms, for the solution of a large system of non-linear algebraic equations, which converge faster than the Newton’s method”, *CMES Comput. Model. Eng. Sci.* **71**:3 (2011), 279–304.
- [Liu and Atluri 2012] C.-S. Liu and S. N. Atluri, “A globally optimal iterative algorithm using the best descent vector $\dot{\mathbf{x}} = \lambda[\alpha_c \mathbf{F} + \mathbf{B}^T \mathbf{F}]$, with the critical value α_c , for solving a system of nonlinear algebraic equations $\mathbf{F}(\mathbf{x}) = \mathbf{0}$ ”, *CMES Comput. Model. Eng. Sci.* **84**:6 (2012), 575–602.
- [Liu et al. 2009] C.-S. Liu, W. Yeih, C.-L. Kuo, and S. N. Atluri, “A scalar homotopy method for solving an over/under-determined system of non-linear algebraic equations”, *CMES Comput. Model. Eng. Sci.* **53**:1 (2009), 47–72.
- [Liu et al. 2011a] C.-S. Liu, H.-H. Dai, and S. N. Atluri, “Iterative solution of a system of nonlinear algebraic equations $\mathbf{F}(\mathbf{x}) = 0$, using $\dot{\mathbf{x}} = \lambda[\alpha \mathbf{R} + \beta \mathbf{P}]$ or $\dot{\mathbf{x}} = \lambda[\alpha \mathbf{F} + \beta \mathbf{P}^*]$ \mathbf{R} is a normal to a hyper-surface function of \mathbf{F} , \mathbf{P} normal to \mathbf{R} , and \mathbf{P}^* normal to \mathbf{F} ”, *CMES Comput. Model. Eng. Sci.* **81**:3-4 (2011), 335–363.
- [Liu et al. 2011b] C.-S. Liu, H.-H. Dai, and S. N. Atluri, “A further study on using $\dot{\mathbf{x}} = \lambda[\alpha \mathbf{R} + \beta \mathbf{P}]$ ($\mathbf{P} = \mathbf{F} - \mathbf{R}(\mathbf{F} \cdot \mathbf{R})/\|\mathbf{R}\|^2$) and $\dot{\mathbf{x}} = \lambda[\alpha \mathbf{F} + \beta \mathbf{P}^*]$ ($\mathbf{P}^* = \mathbf{R} - \mathbf{F}(\mathbf{F} \cdot \mathbf{R})/\|\mathbf{F}\|^2$) in iteratively solving the nonlinear system of algebraic equations $\mathbf{F}(\mathbf{x}) = \mathbf{0}$ ”, *CMES Comput. Model. Eng. Sci.* **81**:2 (2011), 195–228.
- [O’Donoghue and Atluri 1987] P. E. O’Donoghue and S. N. Atluri, “Field/boundary element approach to the large deflection of thin flat plates”, *Comput. Struct.* **27**:3 (1987), 427–435.
- [Okada et al. 1979] H. Okada, K. Oshima, and Y. Fukumoto, “Compressive strength of long rectangular plates under hydrostatic pressure”, *J. Soc. Naval Arch. Japan* **146**:1 (1979), 270–280.
- [Paik et al. 2001] J. K. Paik, A. K. Thayamballi, and B. Ju Kim, “Large deflection orthotropic plate approach to develop ultimate strength formulations for stiffened panels under combined biaxial compression/tension and lateral pressure”, *Thin-Walled Struct.* **39**:3 (2001), 215–246.
- [Punch and Atluri 1986] E. F. Punch and S. N. Atluri, “Large displacement analysis of plates by a stress-based finite element approach”, *Comput. Struct.* **24**:1 (1986), 107–117.
- [Ramm 2004] A. G. Ramm, “Dynamical systems method for solving operator equations”, *Commun. Nonlinear Sci. Numer. Simul.* **9**:4 (2004), 383–402.
- [Shen 1989] H. S. Shen, “Postbuckling behaviour of rectangular plates under combined loading”, *Thin-walled Struct.* **8**:3 (1989), 203–216.
- [Timoshenko 1961] S. P. Timoshenko, *Theory of elastic stability*, 2nd ed., McGraw-Hill Book Co., New York, 1961.
- [Ueda et al. 1987] Y. Ueda, M. H. Rashed, and J. K. Paik, “An incremental Galerkin method for plates and stiffened plates”, *Comput. Struct.* **27**:1 (1987), 147–156.
- [Von Kármán 1910] T. Von Kármán, “Festigkeitsprobleme im maschinenbau”, *Encykl. Math. Wiss.* **4** (1910), 314–385.
- [Way 1939] S. Way, “Uniformly loaded, clamped, rectangular plates with large deflection”, pp. 123–128 in *Proceedings of the Fifth International Congress of Applied Mechanics* (Cambridge, MA), Wiley, Cambridge, MA, 1939.
- [Woolley et al. 1946] R. M. Woolley, J. N. Correick, and S. Levy, “Clamped long rectangular plate under combined axial load and normal pressure”, technical note 1047, National Advisory Committee for Aeronautics, 1946, <http://www.dtic.mil/dtic/tr/fulltext/u2/a800975.pdf>.
- [Yamamoto et al. 1970] Y. Yamamoto, N. Matsubara, and T. Murakami, “Buckling of plates subjected to edge thrusts and lateral pressure”, *J. Soc. Naval Arch. Japan* **127** (1970), 171–179. In Japanese.

Received 16 Oct 2013. Revised 8 Mar 2014. Accepted 7 Apr 2014.

HONGHUA DAI: daihonghua@gmail.com

College of Astronautics, Northwestern Polytechnical University, Xi’an 710072, China

XIAOKUI YUE: xkyue@nwpu.edu.cn

College of Astronautics, Northwestern Polytechnical University, Xi’an 710072, China

SATYA N. ATLURI: satluri@uci.edu

Center for Aerospace Research and Education, University of California, Irvine, Irvine, CA 92697, United States

BIMATERIAL LATTICES WITH ANISOTROPIC THERMAL EXPANSION

MARINA M. TOROPOVA AND CRAIG A. STEEVES

Bimaterial lattices with anisotropic thermal expansion consist of nonidentical cells comprising a skewed triangle made of one material surrounding an unskewed triangle made of a second material. The two materials have differing individual coefficients of thermal expansion. The variation in skew angles makes the thermal expansion of the cell anisotropic. Being composed of anisotropic nonidentical cells, the assembled lattice is also anisotropic and can be designed to have different coefficients of thermal expansion on its top and bottom surfaces. Such lattices can be used as transition elements or adapters to avoid thermal-expansion mismatch between two parts of a structure made of materials with different coefficients of thermal expansion and subjected to temperature changes. In the present paper, three nonlinear algebraic equations linking skew angles with the coefficients of thermal expansion in three directions of a cell are derived, the design of several lattices is performed, the algorithm of lattice design is elaborated, and some examples are presented.

1. Introduction

Often structures that are used in aerospace, civil engineering, and microelectronics experience large temperature changes. If connected components of such structures are made of materials with different coefficients of thermal expansion (CTE), they experience mechanical stresses due to thermal-expansion mismatch. To eliminate thermal stresses, the parts of the structure with differing CTEs, herein referred to as the substrates, can be connected to each other through special transition elements or adapters with anisotropic CTE. Using composite structures with graded CTEs for joining purposes is not a new concept. For example, Yousefiani et al. [2009a; 2009b] applied it to design a layered injector-chamber attachment component in rocket engines. In the first of these papers they suggested joining approaches such as welding, brazing, or solid-state bonding to produce a graded-CTE layered composite. In the second, they used build-up (bottom-up) fabrication approaches such as metal deposition or powder metallurgy to produce a graded-CTE layered composite preform, which was consolidated and heat-treated to create the graded-CTE integrated composite billet of near net shape. In [Dang 2008], the composite adapters with graded CTE were components of a precision optical assembly to prevent lens misalignment. The adapter material comprised multiple thin composite material layers, each possessing a CTE slightly different from its two adjacent layers, bonded to form an adapter with CTE gradually varying in the direction perpendicular to the bonding interfaces. Such adapters will bend when subjected to temperature changes, and deformations of the system must be permitted or thermal stresses will arise if the bending is suppressed. Also, their mechanical properties can be substantially anisotropic, leading to the reduction of overall stiffness and strength. An alternative to graded systems is a compliant system, where differential

Funding was provided through Natural Sciences and Engineering Research Council Strategic Project Grant 413357-11.

Keywords: composite lattices, graded coefficient of thermal expansion, thermal-mismatch adapters.

thermal expansion is accommodated by connectors with low stiffness. This has the disadvantage of reducing the overall stiffness of the structure.

Here, we suggest a way for joining dissimilar parts of a structure using planar composite lattices with anisotropic CTE: one edge of the lattice has CTE that matches the material of the first substrate, and the opposite edge of the lattice has a CTE matching the second substrate. In designing such lattices, we rely on [Sigmund and Torquato 1996; Lakes 1996; Gibiansky and Torquato 1997; Sigmund and Torquato 1997; Jefferson et al. 2009; Steeves et al. 2007; Lehman and Lakes 2013], where it was demonstrated that a lattice with a desirable isotropic CTE can be constructed from cells incorporating two materials with widely differing individual CTEs and empty space. A lattice cell consisting of a skewed triangle of low-CTE material surrounding a triangle of high-CTE material combines high stiffness, simple shape, and ability to reach desirable CTE [Steeves et al. 2007]. In [Steeves et al. 2007; Berger et al. 2011], a pin-jointed lattice consisting of these cells is shown to be nearly optimally stiff: the mechanical response of this type of lattice is dominated by stretching rather than bending. Such lattices are structurally robust and can be relatively easily manufactured. Gdoutos et al. [2013] designed, fabricated, and tested thermally stable metastructures consisting of the cells suggested in [Steeves et al. 2007]. These structures were finely and coarsely tuned by varying the CTE of the constituent materials and the unit cell geometry. The microscale unit cells were composed of aluminum and titanium and were assembled over a large area to create thin low-CTE foils.

In this work, the lattice concept created by Steeves et al. is used to design a lattice adapter with anisotropic CTE. To be anisotropically tunable, each cell can have six different skew angles and therefore have anisotropic thermal expansion. Also, the cells in the lattice are not identical. As a result, the whole lattice has anisotropic and graded net CTE. In this paper, the anisotropic thermal expansion of the lattice is analyzed and the equations connecting the cell skew angles with CTE in three directions are derived. These equations are used to find desirable skew angles for the design of each cell. Then the design of the whole lattice is performed: three CTEs in each cell are found as functions of the CTEs of the substrates. A system for choosing the lattice materials that can provide such CTEs is discussed. Design examples then show how the choice of materials influences the skewness of the cells. This anisotropic-lattice concept eliminates both of the problems with other adapter concepts: the lattice remains stiff at all times, and if pin-connected, differential thermal deformations of the substrates are accommodated without generating any thermal stresses either in the lattice or the substrates. Moreover, the anisotropic lattices presented here are scale independent and can be extended to three-dimensional geometries.

2. Formulation of the problem

Consider two adjoining planar parts of a structure; name them Substrate 1 and Substrate 2. Suppose that Substrates 1 and 2 are made of materials with different CTEs A_1 and A_2 , respectively. We would like to join these plates by a planar interfacial one-row lattice that has the CTE of the first substrate A_1 on the edge connected to the first plate and the CTE of the second substrate A_2 on the edge adjacent to the second plate; this eliminates thermal stresses in the substrates during thermal excursions. In addition, the lattice itself should experience no internal thermal stresses during temperature changes. For this purpose, we use the lattice with cells described in [Steeves et al. 2007]: it is based on a virtual triangle ACE and consists of a skewed triangle $ABCDEF$ made of a material with lower CTE α_1 and connected with an

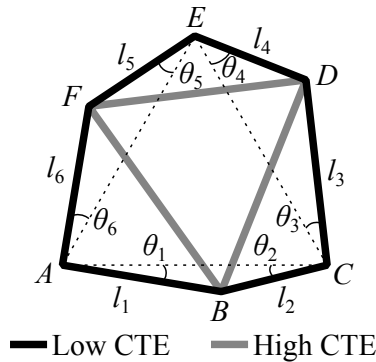


Figure 1. One cell of a lattice. The members AB , BC , CD , DE , EF , and AF have low CTE, depicted in black. The members BD , DF , and BF have higher CTE, depicted in gray. The equilateral triangle upon which the cell is based is shown as a dashed line. The skew angles, θ_1 , θ_2 , θ_3 , θ_4 , θ_5 , and θ_6 , are the angles by which the unit cell strut orientation differs from those of an equilateral triangle.

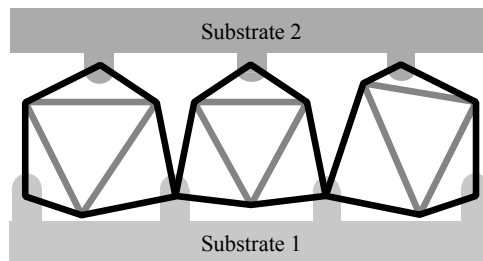


Figure 2. A planar anisotropic lattice connecting two substrates with different CTE. The lattice has net anisotropic CTE, and each individual cell has net anisotropic CTE.

internal unskewed triangle BDF made of a material with higher CTE α_2 (Figure 1). The internal triangle BDF is pin-jointed to the skewed triangle. Adjacent cells of the lattice, connected at A , C , and E , also have pin-joints between each other and with the substrates (Figure 2) such that the whole structure is free of bending and thermal stresses.

The triangle ACE is equilateral [Steeves et al. 2007]: $AC = L_1$, $CE = L_2$, $AE = L_3$, and $L_1 = L_2 = L_3 = L$. Unlike the lattice described in [Steeves et al. 2007], the skew angles θ_1 , θ_2 , θ_3 , θ_4 , θ_5 , and θ_6 and the lengths of members $l_1 = AB$, $l_2 = BC$, $l_3 = CD$, $l_4 = DE$, $l_5 = EF$, and $l_6 = AF$ may be different. As a result, AC , CE , and AE can expand differently when temperature changes: $dL_1 = \bar{\alpha}_1 L_1 dT$, $dL_2 = \bar{\alpha}_2 L_2 dT$, and $dL_3 = \bar{\alpha}_3 L_3 dT$, where T is temperature and $\bar{\alpha}_i$, $i = 1, 2, 3$, are the CTEs of the cell along AC , CE , and AE , respectively.

By choosing the angles θ_i , $i = 1, 2, 3, 4, 5, 6$, we can influence the change of dL_1 , dL_2 , and dL_3 in each cell and provide different changes of distances between vertices of the cells and hence different CTEs on the bottom and top levels of the lattice (Figure 3). To design such a lattice, we need first to obtain relations between CTEs $\bar{\alpha}_i$, $i = 1, 2, 3$, and angles θ_j , $j = 1, 2, 3, 4, 5, 6$.

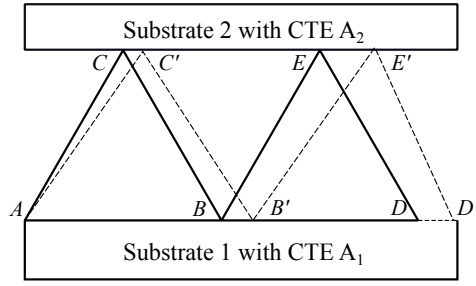


Figure 3. Lattice design: base equilateral triangles of two cells. During thermal expansion, the original points translate from, for example, B to B' . The lattice cell must be designed to accommodate the changing distances between the points.

3. General formulae

The undeformed lengths of the constituent members of a cell (Figure 1) are

$$\begin{aligned} l_1 &= L_1 f_1(\theta_1, \theta_2), & l_2 &= L_1 f_2(\theta_1, \theta_2), & l_3 &= L_2 f_3(\theta_3, \theta_4), \\ l_4 &= L_2 f_4(\theta_3, \theta_4), & l_5 &= L_3 f_5(\theta_5, \theta_6), & l_6 &= L_3 f_6(\theta_5, \theta_6), \end{aligned} \quad (1)$$

where

$$\begin{aligned} f_1 &= \frac{\sin \theta_2}{\sin(\theta_1 + \theta_2)}, & f_2 &= \frac{\sin \theta_1}{\sin(\theta_1 + \theta_2)}, & f_3 &= \frac{\sin \theta_4}{\sin(\theta_3 + \theta_4)}, \\ f_4 &= \frac{\sin \theta_3}{\sin(\theta_3 + \theta_4)}, & f_5 &= \frac{\sin \theta_6}{\sin(\theta_5 + \theta_6)}, & f_6 &= \frac{\sin \theta_5}{\sin(\theta_5 + \theta_6)}. \end{aligned}$$

From (1), we obtain the differential relations

$$\begin{aligned} \frac{1}{L} dl_1 \left(1 - \frac{\bar{\alpha}_1}{\alpha_1}\right) &= f'_{1\theta_1} d\theta_1 + f'_{1\theta_2} d\theta_2, & \frac{1}{L} dl_2 \left(1 - \frac{\bar{\alpha}_1}{\alpha_1}\right) &= f'_{2\theta_1} d\theta_1 + f'_{2\theta_2} d\theta_2, \\ \frac{1}{L} dl_3 \left(1 - \frac{\bar{\alpha}_2}{\alpha_1}\right) &= f'_{3\theta_3} d\theta_3 + f'_{3\theta_4} d\theta_4, & \frac{1}{L} dl_4 \left(1 - \frac{\bar{\alpha}_2}{\alpha_1}\right) &= f'_{4\theta_3} d\theta_3 + f'_{4\theta_4} d\theta_4, \\ \frac{1}{L} dl_5 \left(1 - \frac{\bar{\alpha}_3}{\alpha_1}\right) &= f'_{5\theta_5} d\theta_5 + f'_{5\theta_6} d\theta_6, & \frac{1}{L} dl_6 \left(1 - \frac{\bar{\alpha}_3}{\alpha_1}\right) &= f'_{6\theta_5} d\theta_5 + f'_{6\theta_6} d\theta_6, \end{aligned} \quad (2)$$

where $f'_{i\theta_j}$, $i, j = 1, 2, 3, 4, 5, 6$, is a partial derivative of the function f_i with respect to the angle θ_j .

The length of three members of the internal triangle can be expressed as

$$\begin{aligned} FB &= l_7 = (L_1^2 f_1^2 + L_3^2 f_6^2 - 2L_1 L_3 f_1 f_6 \cos A')^{1/2}, \\ BD &= l_8 = (L_1^2 f_2^2 + L_2^2 f_3^2 - 2L_1 L_2 f_2 f_3 \cos B')^{1/2}, \\ DF &= l_9 = (L_2^2 f_4^2 + L_3^2 f_5^2 - 2L_2 L_3 f_4 f_5 \cos C')^{1/2}, \end{aligned} \quad (3)$$

where

$$A' = \theta_1 + \theta_6 + 60^\circ, \quad B' = \theta_2 + \theta_3 + 60^\circ, \quad \text{and} \quad C' = \theta_4 + \theta_5 + 60^\circ.$$

From (3), we can find dl_i , $i = 7, 8, 9$, as

$$\begin{aligned} dl_7 &= a_7 dl_7 + b_7 d\theta_1 + c_7 d\theta_2 + d_7 d\theta_5 + e_7 d\theta_6, \\ dl_8 &= a_8 dl_8 + b_8 d\theta_1 + c_8 d\theta_2 + d_8 d\theta_3 + e_8 d\theta_4, \\ dl_9 &= a_9 dl_9 + b_9 d\theta_3 + c_9 d\theta_4 + d_9 d\theta_5 + e_9 d\theta_6, \end{aligned} \quad (4)$$

where

$$\begin{aligned} a_7 &= \frac{l_1}{l_7^2} (l_1 - l_6 \cos A') \frac{\bar{\alpha}_1}{\alpha_2} + \frac{l_6}{l_7^2} (l_6 - l_1 \cos A') \frac{\bar{\alpha}_3}{\alpha_2}, \\ b_7 &= \frac{\partial l_7}{\partial \theta_1} = \frac{L}{l_7} (l_1 - l_6 \cos A') f'_{1\theta_1} + \frac{l_1 l_6}{l_7} \sin A', \\ c_7 &= \frac{\partial l_7}{\partial \theta_2} = \frac{L}{l_7} (l_1 - l_6 \cos A') f'_{1\theta_2}, \\ d_7 &= \frac{\partial l_7}{\partial \theta_5} = \frac{L}{l_7} (l_6 - l_1 \cos A') f'_{6\theta_5}, \\ e_7 &= \frac{\partial l_7}{\partial \theta_6} = \frac{L}{l_7} (l_6 - l_1 \cos A') f'_{6\theta_6} + \frac{l_1 l_6}{l_7} \sin A'. \end{aligned} \quad (5)$$

The coefficients a_8 , b_8 , c_8 , d_8 , and e_8 can be obtained from previous formulae by replacing l_1 , l_6 , l_7 , $\bar{\alpha}_1$, $\bar{\alpha}_3$, f_1 , f_6 , θ_1 , θ_2 , θ_5 , θ_6 , and A' by l_3 , l_2 , l_8 , $\bar{\alpha}_2$, $\bar{\alpha}_1$, f_3 , f_2 , θ_3 , θ_4 , θ_1 , θ_2 , and B' , respectively. Similarly, the coefficients a_9 , b_9 , c_9 , d_9 , and e_9 can be obtained from (5) by replacing l_1 , l_6 , l_7 , $\bar{\alpha}_1$, $\bar{\alpha}_3$, f_1 , f_6 , θ_1 , θ_2 , θ_5 , θ_6 , and A' by l_5 , l_4 , l_9 , $\bar{\alpha}_3$, $\bar{\alpha}_2$, f_5 , f_4 , θ_5 , θ_6 , θ_3 , θ_4 , and C' , respectively.

Then expressing $d\theta_i$ through dl_i from (2), substituting them into (4), and performing all necessary transformations, we obtain three nonlinear equations linking the six skew angles θ_i with three normalized thermal-expansion coefficients along the lines AC , CE , and AE in the skewed triangle:

$$\begin{aligned} \left(\frac{\bar{\alpha}_1}{\alpha_1} - 1\right) \frac{f_1 \cos(\theta_1 + \theta_2) + f_2}{\sin \theta_2} + \left(\frac{\bar{\alpha}_3}{\alpha_1} - 1\right) \frac{f_6 \cos(\theta_5 + \theta_6) + f_5}{\sin \theta_5} &= \frac{1}{\sin A'} \left(1 - \frac{\alpha_2}{\alpha_1}\right) \left(\frac{f_1}{f_6} + \frac{f_6}{f_1} - 2 \cos A'\right), \\ \left(\frac{\bar{\alpha}_1}{\alpha_1} - 1\right) \frac{f_2 \cos(\theta_1 + \theta_2) + f_1}{\sin \theta_1} + \left(\frac{\bar{\alpha}_2}{\alpha_1} - 1\right) \frac{f_3 \cos(\theta_3 + \theta_4) + f_4}{\sin \theta_4} &= \frac{1}{\sin B'} \left(1 - \frac{\alpha_2}{\alpha_1}\right) \left(\frac{f_2}{f_3} + \frac{f_3}{f_2} - 2 \cos B'\right), \\ \left(\frac{\bar{\alpha}_3}{\alpha_1} - 1\right) \frac{f_5 \cos(\theta_5 + \theta_6) + f_6}{\sin \theta_6} + \left(\frac{\bar{\alpha}_2}{\alpha_1} - 1\right) \frac{f_4 \cos(\theta_3 + \theta_4) + f_3}{\sin \theta_3} &= \frac{1}{\sin C'} \left(1 - \frac{\alpha_2}{\alpha_1}\right) \left(\frac{f_4}{f_5} + \frac{f_5}{f_4} - 2 \cos C'\right). \end{aligned} \quad (6)$$

The equations (6) are scale-independent, contain the ratio α_2/α_1 as a parameter, and couple three normalized CTEs in a cell $\bar{\alpha}_1/\alpha_1$, $\bar{\alpha}_2/\alpha_1$, and $\bar{\alpha}_3/\alpha_1$. If the skew angles are known, these three CTEs

can be calculated using the following formulae:

$$\frac{\bar{\alpha}_1}{\alpha_1} = 1 + \frac{\Delta_1}{\Delta}, \quad \frac{\bar{\alpha}_2}{\alpha_1} = 1 + \frac{\Delta_2}{\Delta}, \quad \text{and} \quad \frac{\bar{\alpha}_3}{\alpha_1} = 1 + \frac{\Delta_3}{\Delta}, \quad (7)$$

where

$$\begin{aligned} \Delta &= c_{11}c_{22}c_{33} + c_{21}c_{32}c_{13}, \\ \Delta_1 &= F_1c_{22}c_{33} + F_2c_{13}c_{32} - F_3c_{22}c_{13}, \\ \Delta_2 &= F_2c_{11}c_{33} + F_3c_{13}c_{21} - F_1c_{21}c_{33}, \\ \Delta_3 &= F_3c_{11}c_{22} + F_1c_{21}c_{32} - F_2c_{11}c_{32}, \end{aligned} \quad (8)$$

$$\begin{aligned} c_{11} &= \sin \theta_5 \sin(\theta_5 + \theta_6)(\sin \theta_2 \cos(\theta_1 + \theta_2) + \sin \theta_1), \\ c_{13} &= \sin \theta_2 \sin(\theta_1 + \theta_2)(\sin \theta_5 \cos(\theta_5 + \theta_6) + \sin \theta_6), \\ c_{21} &= \sin \theta_4 \sin(\theta_3 + \theta_4)(\sin \theta_1 \cos(\theta_1 + \theta_2) + \sin \theta_2), \\ c_{22} &= \sin \theta_1 \sin(\theta_1 + \theta_2)(\sin \theta_4 \cos(\theta_3 + \theta_4) + \sin \theta_3), \\ c_{32} &= \sin \theta_6 \sin(\theta_5 + \theta_6)(\sin \theta_3 \cos(\theta_3 + \theta_4) + \sin \theta_4), \\ c_{33} &= \sin \theta_3 \sin(\theta_3 + \theta_4)(\sin \theta_6 \cos(\theta_5 + \theta_6) + \sin \theta_5), \end{aligned} \quad (9)$$

$$\begin{aligned} F_1 &= \frac{1}{\sin A'} \left(1 - \frac{\alpha_2}{\alpha_1} \right) (\sin^2 \theta_2 \sin^2(\theta_5 + \theta_6) + \sin^2 \theta_5 \sin^2(\theta_1 + \theta_2) \\ &\quad - 2 \cos A' \sin \theta_2 \sin \theta_5 \sin(\theta_1 + \theta_2) \sin(\theta_5 + \theta_6)), \\ F_2 &= \frac{1}{\sin B'} \left(1 - \frac{\alpha_2}{\alpha_1} \right) (\sin^2 \theta_1 \sin^2(\theta_3 + \theta_4) + \sin^2 \theta_4 \sin^2(\theta_1 + \theta_2) \\ &\quad - 2 \cos B' \sin \theta_1 \sin \theta_4 \sin(\theta_1 + \theta_2) \sin(\theta_3 + \theta_4)), \\ F_3 &= \frac{1}{\sin C'} \left(1 - \frac{\alpha_2}{\alpha_1} \right) (\sin^2 \theta_3 \sin^2(\theta_5 + \theta_6) + \sin^2 \theta_6 \sin^2(\theta_3 + \theta_4) \\ &\quad - 2 \cos C' \sin \theta_3 \sin \theta_6 \sin(\theta_3 + \theta_4) \sin(\theta_5 + \theta_6)). \end{aligned} \quad (10)$$

On the other hand, in design of anisotropic lattices, we need to solve the inverse problem of finding the skew angles when the values of three CTEs in each cell are known. In this case, three equations (6) are insufficient and it is possible to impose additional conditions on the lattice or optimize the lattice structure using various criteria. If instead we make the simplification $\theta_1 = \theta_2 = t_1$, $\theta_3 = \theta_4 = t_2$, and $\theta_5 = \theta_6 = t_3$ (Figure 4), the equations (6) take the form

$$\begin{aligned} \left(\frac{\bar{\alpha}_1}{\alpha_1} - 1 \right) \cot t_1 + \left(\frac{\bar{\alpha}_3}{\alpha_1} - 1 \right) \cot t_3 &= G_1, \\ \left(\frac{\bar{\alpha}_1}{\alpha_1} - 1 \right) \cot t_1 + \left(\frac{\bar{\alpha}_2}{\alpha_1} - 1 \right) \cot t_2 &= G_2, \\ \left(\frac{\bar{\alpha}_2}{\alpha_1} - 1 \right) \cot t_2 + \left(\frac{\bar{\alpha}_3}{\alpha_1} - 1 \right) \cot t_3 &= G_3, \end{aligned} \quad (11)$$

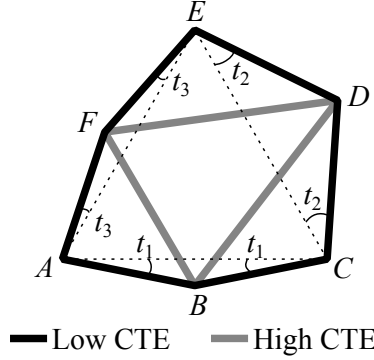


Figure 4. A cell with three skew angles. The original six skew angles are replaced by $\theta_1 = \theta_2 = t_1$, $\theta_3 = \theta_4 = t_2$, and $\theta_5 = \theta_6 = t_3$.

where

$$G_1 = \frac{1}{\sin A''} \left(1 - \frac{\alpha_2}{\alpha_1} \right) \left(\frac{\cos t_1}{\cos t_3} + \frac{\cos t_3}{\cos t_1} - 2 \cos A'' \right),$$

$$G_2 = \frac{1}{\sin B''} \left(1 - \frac{\alpha_2}{\alpha_1} \right) \left(\frac{\cos t_1}{\cos t_2} + \frac{\cos t_2}{\cos t_1} - 2 \cos B'' \right),$$

$$G_3 = \frac{1}{\sin C''} \left(1 - \frac{\alpha_2}{\alpha_1} \right) \left(\frac{\cos t_2}{\cos t_3} + \frac{\cos t_3}{\cos t_2} - 2 \cos C'' \right)$$

and $A'' = t_1 + t_3 + 60^\circ$, $B'' = t_1 + t_2 + 60^\circ$, and $C'' = t_2 + t_3 + 60^\circ$.

From (11), $\bar{\alpha}_i/\alpha_1$, $i = 1, 2, 3$, can be found as

$$\begin{aligned} \frac{\bar{\alpha}_1}{\alpha_1} &= 1 + \frac{G_1 + G_2 - G_3}{2} \tan t_1, \\ \frac{\bar{\alpha}_2}{\alpha_1} &= 1 + \frac{G_2 + G_3 - G_1}{2} \tan t_2, \\ \frac{\bar{\alpha}_3}{\alpha_1} &= 1 + \frac{G_1 + G_3 - G_2}{2} \tan t_3. \end{aligned} \quad (12)$$

From (12), it is seen that if any $t_i = 0$, $i = 1, 2, 3$, then $\bar{\alpha}_i = \alpha_1$ and the two other skew angles do not influence it. Conversely, if $\bar{\alpha}_i = \alpha_1$, then the two skew angles adjacent to this side must be equal to zero.

If all angles in (6) are equal to θ , the cell is isotropic with a constant coefficient of thermal expansion in all directions equal to $\bar{\alpha}$ and these three equations can be transformed into the equation for the expansion coefficient obtained in [Steeves et al. 2007]:

$$\frac{\bar{\alpha}}{\alpha_1} = \frac{1 - 0.5(\alpha_2/\alpha_1) \sin(2\theta)(1/\sqrt{3} + \tan \theta)}{1 - 0.5 \sin(2\theta)(1/\sqrt{3} + \tan \theta)}. \quad (13)$$

In the isotropic configuration, the maximum of the function $\bar{\alpha}/\alpha_1$ is reached at $\theta = -15^\circ$; the function decreases at $-15^\circ < \theta < 90^\circ$ (see Figure 5). For design considerations, to avoid overlapping the cells, we consider skew angles in the range $[-15^\circ, 30^\circ]$. In this range of skew angle, all values of three normalized CTEs presented by the formulae (12) belong to the interval $\Omega \equiv [\bar{\alpha}(30^\circ)/\alpha_1, \bar{\alpha}(-15^\circ)/\alpha_1]$ that depends

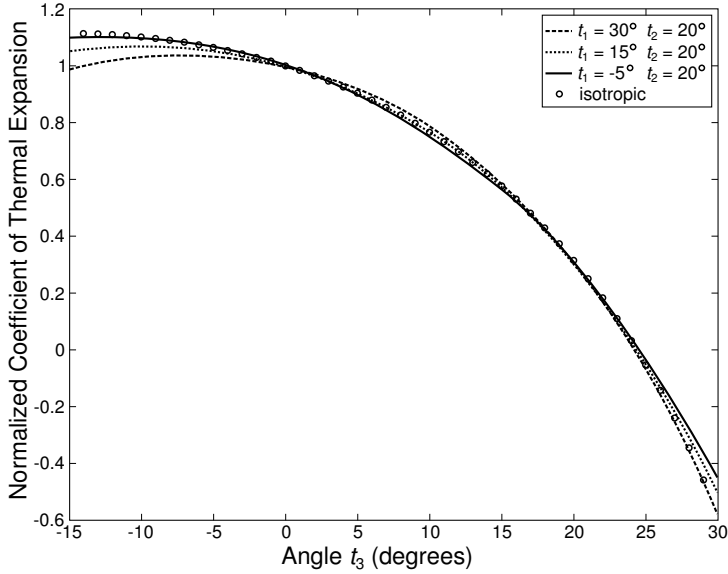


Figure 5. The influence of two skew angles on $\bar{\alpha}_3/\alpha_1$ for $\alpha_2/\alpha_1 = 2.581$, which corresponds to the ratio of the CTEs of aluminum and titanium.

on the ratio α_2/α_1 (Figure 6). Here, $\bar{\alpha}/\alpha_1$ is calculated from (13). Figure 5 plots the behavior of $\bar{\alpha}_3/\alpha_1$ via t_3 at three different sets of values $t_1 = 30^\circ$, $t_2 = 20^\circ$; $t_1 = 15^\circ$, $t_2 = 20^\circ$; and $t_1 = -5^\circ$, $t_2 = 20^\circ$ and the ratio $\alpha_2/\alpha_1 = 2.581$, which corresponds to the ratio of the CTEs of aluminum and titanium. These do not coincide with the isotropic case, which means that an arbitrary set of three values from Ω is not necessarily a solution of the equations (11). In other words, the condition

$$\frac{\bar{\alpha}_1}{\alpha_1}, \frac{\bar{\alpha}_2}{\alpha_1}, \frac{\bar{\alpha}_3}{\alpha_1} \in \Omega$$

is necessary but not sufficient for the existence of the solution of the equations (11). For example, while the maximum for $t_1 = -5^\circ$, $t_2 = 20^\circ$ coincides with the maximum for the isotropic case, $t_1 = 15^\circ$, $t_2 = 20^\circ$ has a maximum at $t_3 = -10^\circ$ and $t_1 = 30^\circ$, $t_2 = 20^\circ$ has a maximum at $t_3 = -5^\circ$. Hence, in the latter two cases, we need to search for solutions in the interval $[-10^\circ, 30^\circ]$ and $[-5^\circ, 30^\circ]$, respectively. Also, the maxima in the three cases are different, so it is not possible to attain the same maximum $\bar{\alpha}_3$.

In Figure 6, it is seen that the interval Ω increases with respect to the ratio α_2/α_1 . The higher values of normalized CTEs can be reached at negative unequal skew angles $\theta_1 \neq \theta_2$, $\theta_3 \neq \theta_4$, and $\theta_5 \neq \theta_6$. This case will be illustrated in Section 6, Problem 5.

4. Lattice design

In this section, planar, one-row lattices are considered. We can design lattices by designating the points on the substrates to which the lattice will be attached and following those points as the temperature changes. This will provide the changes in the lengths of the sides of the equilateral triangles upon which the lattice cells are based, to which the changing lengths of the lattice cells must be matched. For example, Figure 3 shows the base triangles of two cells. Suppose the point A is fixed. When temperature changes, the other

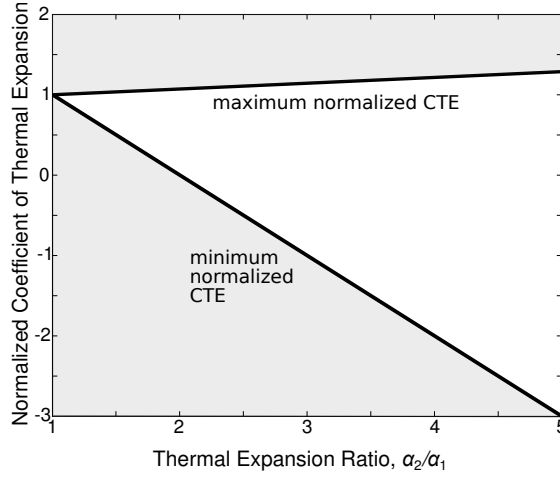


Figure 6. Upper and lower boundaries of the normalized CTE, giving the range Ω , as a function of the ratio α_2/α_1 .

points B , C , D , and E move to the positions B' , C' , D' , and E' , respectively. The new distances AB' , $B'D'$, and $C'E'$ can be expressed in terms of the side length L and three unknown CTEs of each cell. The following four conditions on the shape of the lattice after temperature changes are sufficient to find them:

- (1) the distances between vertices connected to Substrate 1 must be equal to $L(1 + A_1dT)$,
- (2) the distances between vertices connected to Substrate 2 must be equal to $L(1 + A_2dT)$,
- (3) the height of each triangle must remain constant, i.e., not depend on temperature, and
- (4) the lattice must have a line of symmetry.

The third condition is arbitrary: the relative approach or retreat of the substrates depends upon the materials and the configuration of the overall structure. Here, constant H is chosen although $\Delta H > 0$ and $\Delta H < 0$ may equivalently be selected.

Using these conditions and deriving formulae for $\bar{\alpha}_i$, $i = 1, 2, 3$, we neglect terms with $\bar{\alpha}_i^2$ (which is reasonable because $\bar{\alpha}_i$ are small). As a result, the formulae for $\bar{\alpha}_1$, $\bar{\alpha}_2$, and $\bar{\alpha}_3$ in each cell of two-cell, three-cell, and n -cell lattices as functions of the CTEs of substrates A_1 and A_2 are obtained.

To work with several cells, denote $\alpha_{i1} = \bar{\alpha}_1$, $\alpha_{i2} = \bar{\alpha}_2$, and $\alpha_{i3} = \bar{\alpha}_3$, where i is the number of the cell in the row (the skeleton of a lattice is depicted in Figure 7). For example, $i = 1$ for cell ABC and $i = 2$ for BDE . Along AB and BD , $j = 1$; along BC and DE , $j = 2$; and along AC and BE , $j = 3$.

Consider a lattice consisting of two cells ABC and BDE (Figure 7). The lattice is pin-joined at A , B , and D to a substrate with CTE A_1 while at points C and E it is pin-joined to a substrate with CTE A_2 . At the initial state, $AB = BC = AC = BD = DE = BE = L$. When the temperature changes, the lengths of these segments become $L(1 + \alpha_{ij}dT)$. The first substrate and the bottom level of the lattice have the same CTE (Condition (1)), $\alpha_{11} = \alpha_{21} = A_1$. Similarly, when temperature changes, the distance between points C and E changes following the formula $L(1 + A_2dT)$ (Condition (2)). Denote $FB = x$. Then for the first cell,

$$L^2(1 + \alpha_{12}dT)^2 - x^2 = L^2(1 + \alpha_{13}dT)^2 - (L(1 + \alpha_{11}dT) - x)^2.$$

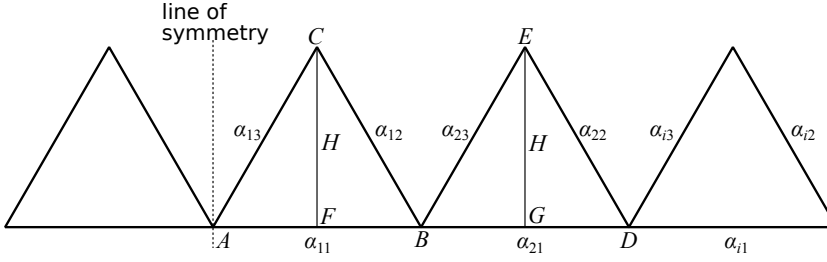


Figure 7. Designation of CTEs in a multicell lattice. Note that the lines do not represent actual cell members; these lines refer to the virtual equilateral triangles upon which the cells are based, shown in Figure 1 as dashed lines. The cell vertices are A to E while the midpoints on the lower face of the cell are F and G . H is the height of the cells. If the lattice has a line of symmetry, it would exist as the dashed line with additional cells to the left.

Neglecting terms with α_{ij}^2 , we get

$$x = 0.5L(1 + (\alpha_{11} + 2\alpha_{12} - 2\alpha_{13})dT).$$

Using this formula, we can find from the second cell that

$$BG = 0.5L(1 + (\alpha_{21} - 2\alpha_{22} + 2\alpha_{23})dT).$$

Thus, when temperature changes, the distance between points C and E changes according to the rule

$$CE = L(1 + (\alpha_{12} - \alpha_{13} - \alpha_{22} + \alpha_{23} + A_1)dT).$$

Hence,

$$A_2 = \alpha_{12} - \alpha_{13} - \alpha_{22} + \alpha_{23} + A_1.$$

Also, we would like to design a lattice that does not expand along FC and GE so that the lattice cell height H remains constant when temperature changes (Condition (3)). Applying the approach used above, we can write, for example, for the first cell

$$\begin{aligned} (H + dH)^2 &= L^2(1 + \alpha_{12}dT)^2 - 0.25L^2(1 + (2\alpha_{12} - 2\alpha_{13} + \alpha_{11})dT)^2 \\ &= (0.5\sqrt{3}L(1 + \frac{2}{3}(\alpha_{12} + \alpha_{13} - 0.5\alpha_{11})dT))^2. \end{aligned}$$

Thus, the CTE along cell heights FC and GE is $\alpha_H = \frac{2}{3}(\alpha_{12} + \alpha_{13} - 0.5\alpha_{11})$. In this case,

$$\alpha_{12} + \alpha_{13} - 0.5\alpha_{11} = 0.$$

Finally, for more uniform deformation of the lattice, symmetry can be imposed through $\alpha_{12} = \alpha_{23}$ and $\alpha_{13} = \alpha_{22}$ (Condition (4)).

For a lattice consisting of two symmetric cells, three CTEs in each cell can be found as functions of the CTEs of the substrates

$$\begin{aligned}\alpha_{11} &= \alpha_{21} = A_1, \\ \alpha_{12} &= \alpha_{23} = 0.25A_2, \\ \alpha_{13} &= \alpha_{22} = 0.5A_1 - 0.25A_2.\end{aligned}\tag{14}$$

All values must belong to the interval Ω , and the CTEs, α_1 and α_2 , of the two materials that comprise the lattice are restricted by the following inequalities:

$$\begin{aligned}\alpha_2 + A_1 &> 2\alpha_1, \\ \alpha_2 + 0.25A_2 &> 2\alpha_1, \\ \alpha_2 + 0.5A_1 - 0.25A_2 &> 2\alpha_1, \\ \alpha_2 + 12.93\alpha_1 &> 13.93A_1, \\ \alpha_2 + 12.93\alpha_1 &> 3.48A_2, \\ \alpha_2 + 12.93\alpha_1 &> 6.97A_1 - 3.48A_2.\end{aligned}\tag{15}$$

From (15), it follows that, in the particular case when the lattice is made of the same materials as the substrates ($\alpha_1 = A_1$ and $\alpha_2 = A_2$), the ratio of the lattice material CTEs must lie in the range $2 < \alpha_2/\alpha_1 < 5.20875$.

For a three-cell lattice, we obtain similar formulae:

$$\begin{aligned}\alpha_{11} &= \alpha_{21} = \alpha_{31} = A_1, \\ \alpha_{12} &= \alpha_{33} = 0.5A_2 - 0.25A_1, \\ \alpha_{13} &= \alpha_{32} = 0.75A_1 - 0.5A_2, \\ \alpha_{22} &= \alpha_{23} = 0.25A_1.\end{aligned}\tag{16}$$

The conditions on the CTEs of the materials comprising the lattice are:

$$\begin{aligned}\alpha_2 + 0.25A_1 &> 2\alpha_1, \\ \alpha_2 + 0.5A_2 - 0.25A_1 &> 2\alpha_1, \\ \alpha_2 + 0.75A_1 - 0.5A_2 &> 2\alpha_1, \\ \alpha_2 + 12.93\alpha_1 &> 13.93A_1, \\ \alpha_2 + 12.93\alpha_1 &> 6.97A_2 - 3.48A_1, \\ \alpha_2 + 12.93\alpha_1 &> 10.45A_1 - 6.97A_2.\end{aligned}\tag{17}$$

From (17), it follows that, if $\alpha_1 = A_1$ and $\alpha_2 = A_2$, $2.5 < \alpha_2/\alpha_1 < 2.7515$. This is a very narrow range with few candidate materials, so for the lattices consisting of three or more cells, choosing lattice materials different from the substrate materials is nearly obligatory. Aluminum and titanium are a rare combination of common substrate materials that can be connected by a three-cell lattice of the same materials.

If the lattice contains $2n$ cells, $n = 2, 3, 4, \dots$, and is symmetrical with respect to the vertical line passing through one of the bottom vertices (see the line of symmetry in [Figure 7](#)), the formulae for cells lying to the right of the symmetry line are

$$\begin{aligned}\alpha_{i1} &= A_1, \\ \alpha_{i2} &= 0.5i A_1 - 0.25(2i - 1)A_2, \\ \alpha_{i3} &= 0.25(2i - 1)A_2 - 0.5(i - 1)A_1,\end{aligned}\tag{18}$$

where $i = 1, 2, \dots, n$.

The conditions for the lattice materials are

$$\begin{aligned}\alpha_2 + A_1 &> 2\alpha_1, \\ \alpha_2 - 0.25A_2 + 0.5A_1 + 0.5i(A_2 - A_1) &> 2\alpha_1, \\ \alpha_2 + 12.93\alpha_1 &> 13.93A_1, \\ \alpha_2 + 12.93\alpha_1 + 6.97i(A_2 - A_1) &> 3.48A_2.\end{aligned}\tag{19}$$

Two additional analogous conditions define the maximum number of cells that the lattice made of these materials can contain:

$$\begin{aligned}n &< \frac{2\alpha_2 + 0.5A_2 - 4\alpha_1}{A_2 - A_1}, \\ n &< \frac{0.5A_2 + 0.14\alpha_2 + 1.86\alpha_1 - A_1}{A_2 - A_1}.\end{aligned}\tag{20}$$

If we need to design a lattice of more complex shape or just a lattice without the vertical line of symmetry or consisting, for example, of an odd number of cells, the formulae for the cells' CTEs and the lattice-material selection can be obtained in similar way. If two substrates are connected by a one-row lattice with three cells or more, they also can be connected by a lattice containing two or more rows. This may be advantageous if a lattice possessing a particular ratio of width to height is preferable.

5. General algorithm of lattice design

Assembling all the reasoning presented in the previous sections, this algorithm is effective for lattice-tailoring:

- (1) Choose the initial number of cells in the lattice.
- (2) Using the formulae (14), (16), or (18), find the CTEs α_{ij} in all cells of the lattice as functions of the substrate CTEs A_1 and A_2 .
- (3) Choose the materials of the lattice accounting for the relations (15), (17), (19), or (20), and find the ratio α_2/α_1 .
- (4) Check the existence of solutions to equations (6) at calculated values of normalized CTEs of the current cell $\bar{\alpha}_i/\alpha_1 = \alpha_{ij}/\alpha_1$, $i = 1, 2, 3$, and the chosen ratio of α_2/α_1 .
- (5) If the solution exists, find the skew angles of the current cell. Then repeat the previous step with the next cell of the lattice.

- (6) If the solution does not exist, there are three options:
 - (a) Choose lattice materials with a higher value of the ratio α_2/α_1 .
 - (b) Use unequal negative skew angles adjacent to the cell members in order to provide a wider range of cell CTEs.
 - (c) Reduce the number of cells in the lattice.
- (7) After Step (6), repeat Step (4).
- (8) The lattice design halts when this procedure is performed for all cells in the lattice. If the lattice can be successfully designed, it may be possible to increase the number of units cells and redesign the lattice, beginning at Step (1).

The initial number of lattice cells is determined heuristically, accounting for the geometry of the substrates and the difference between their CTEs. The larger the difference, the fewer cells the lattice can contain. **Problem 6** from the next section will illustrate this. The final number of cells is determined through Step (6)(c) in the design algorithm.

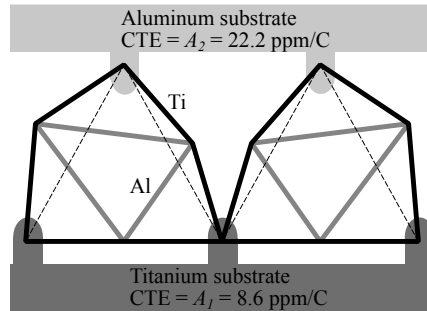


Figure 8. Problem 1: Two-cell aluminum-titanium lattice to connect aluminum and titanium substrates.

6. Examples

Problem 1. This is an example of connecting titanium and aluminum substrates by a two-cell lattice made also of titanium and aluminum. So $\alpha_1 = A_1 = 8.6$ ppm/C, $\alpha_2 = A_2 = 22.2$ ppm/C, and $\alpha_2/\alpha_1 = 2.58$. For these values of α_1 and α_2 , $\Omega = [-0.581, 1.1135]$. From (14), we find $\alpha_{11}/\alpha_1 = \alpha_{21}/\alpha_1 = A_1/\alpha_1 = 1$, $\alpha_{12}/\alpha_1 = \alpha_{23}/\alpha_1 = 0.25A_2/\alpha_1 = 0.64535$, and $\alpha_{13}/\alpha_1 = \alpha_{23}/\alpha_1 = 0.5A_1/\alpha_1 - 0.25A_2 = -0.14535$. All values of α_{ij} belong to Ω . Now using formulae (11), the skew angles in the left cell can be calculated as $t_1 = 0.0^\circ$, $t_2 = 12.9^\circ$, and $t_3 = 27.1^\circ$ (Figure 8).

In the problem of the two-cell lattice connecting titanium and aluminum substrates, the inequalities (15) define a region of allowable values of α_1 and α_2 ; the region is plotted in Figure 9. For this case, the third and fourth inequalities in (15) are the strongest. Their intersection provides a minimum of $\alpha_2 = 17.14$ ppm/C with corresponding $\alpha_1 = 7.94$ ppm/C.

The utility of the lattice adapter can be illustrated by this example. For comparison, a bimetallic strip consisting of titanium and aluminum layers of the same thickness welded together and uniformly heated to 100°C will be bent due to thermal-expansion mismatch [Timoshenko 1925]. The maximum stress during heating of this bimetallic strip [Timoshenko 1925] is 70.5 MPa. A pinned lattice adapter experiences no thermal distortion or thermal stress.

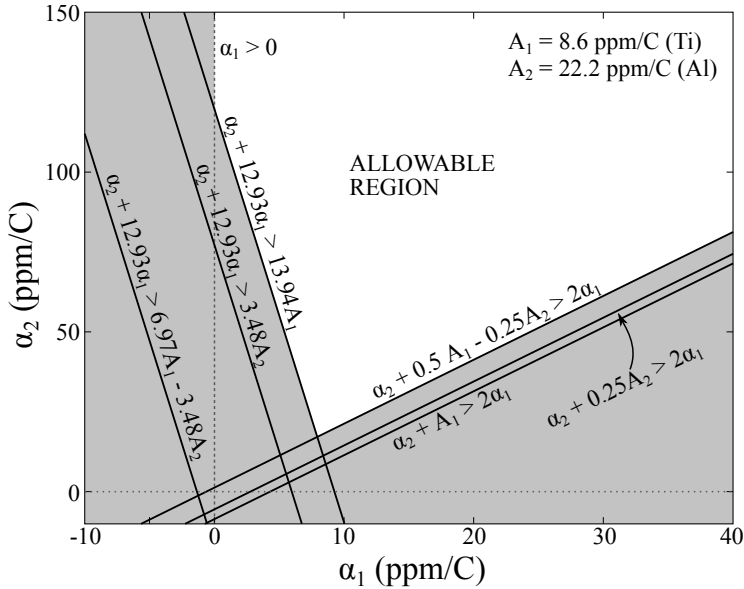


Figure 9. Problem 1: The white region indicates the ranges for the CTEs of the lattice materials that can be used to design the lattice for **Problem 1**. The lines defining the allowable region are the inequalities in (15). Note the difference in the scales of the two axes; for small or moderately large values of α_1 , large values of α_2 are implied.

Problem 2. The same lattice materials can be used to connect other substrates that have CTEs that are more widely different, for example, zirconium and lead. In this case, $A_1 = 5.7$ ppm/C and $A_2 = 28$ ppm/C with $\Omega = [-0.581, 1.1135]$. Then $\alpha_{11}/\alpha_1 = \alpha_{21}/\alpha_1 = A_1/\alpha_1 = 0.66279$, $\alpha_{12}/\alpha_1 = \alpha_{23}/\alpha_1 = 0.25A_2/\alpha_1 = 0.81395$, and $\alpha_{13}/\alpha_1 = \alpha_{23}/\alpha_1 = 0.5A_1/\alpha_1 - 0.25A_2 = -0.48256$. Again, α_{ij} belong to Ω . The skew angles for the left cell are $t_1 = 12.71^\circ$, $t_2 = 8.65^\circ$, and $t_3 = 30.48^\circ$ (Figure 10). It is seen that skew angles of the lattice cells are greater than those from **Problem 1**. We have allowed $t_3 > 30^\circ$ because these are the exterior sides of the lattice, and hence, there are no adjacent cells to cause interference. It does however make impossible the addition of further cells.

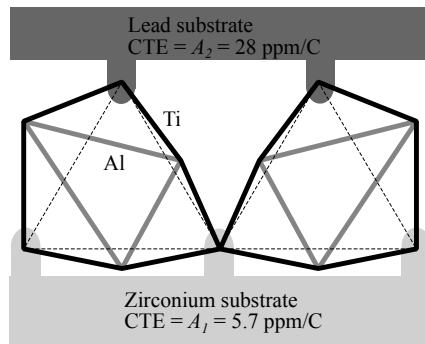


Figure 10. Problem 2: Two-cell aluminum-titanium lattice to connect zirconium and lead substrates.

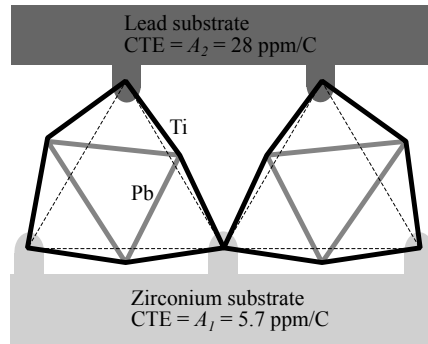


Figure 11. Problem 3: Two-cell lead-titanium lattice to connect zirconium and lead substrates.

Problem 3. We can connect the same substrates as in [Problem 2](#) using other materials for the lattice, for example, titanium and lead. While these materials are unlikely candidates for lattice construction, their widely differing CTEs make them good example materials. In this case, $\alpha_1 = 8.6$ ppm/C, $\alpha_2 = 28.0$ ppm/C, and $\alpha_2/\alpha_1 = 3.25$. A_1 and A_2 and therefore the values of α_{ij} have the same values as in [Problem 2](#). For this combination of lattice materials, $\Omega = [-1.256, 1.162]$. All values of α_{ij} belong to Ω . From formulae (11), the skew angles in the left cell can be calculated as $t_1 = 10.0^\circ$, $t_2 = 6.5^\circ$, and $t_3 = 25.7^\circ$ ([Figure 11](#)). In this lattice, the ratio α_2/α_1 is greater than in the lattices of the previous problems, which is why the lattice cells are less skewed.

Problem 4. In this problem, we design a three-cell aluminum-titanium lattice connecting aluminum and titanium substrates. It is possible because the ratio of CTEs of the substrates satisfies $2.5 < \alpha_2/\alpha_1 < 2.7515$. Using formulae (16), we find $\alpha_{11}/\alpha_1 = \alpha_{21}/\alpha_1 = \alpha_{31}/\alpha_1 = 1$, $\alpha_{12}/\alpha_1 = \alpha_{33}/\alpha_1 = 1.04$, $\alpha_{13}/\alpha_1 = \alpha_{32}/\alpha_1 = -0.54$, and $\alpha_{22}/\alpha_1 = \alpha_{23}/\alpha_1 = 0.25$. The skew angles for the first cell on the left are $t_1 = 0.0^\circ$, $t_2 = -3.0^\circ$, and $t_3 = 32.6^\circ$. The skew angles for the second cell are $t_1 = 0.0^\circ$, $t_2 = 21.0^\circ$, and $t_3 = 21.0^\circ$ ([Figure 12](#)). Here, although $\alpha_2/\alpha_1 \in \Omega$, this ratio is very close to the minimum boundary of Ω . That is why t_3 in the first cell on the left and t_2 in last cell on the right are greater than 30° . In this case, it is admissible because these skew angles do not cause overlapping with adjoining lattice cells but force a limit to the number of cells in this lattice to be three.

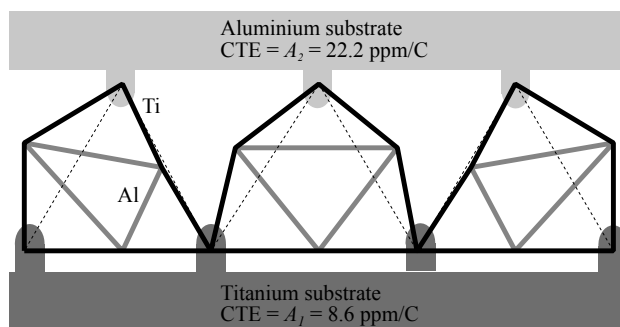


Figure 12. Problem 4: Three-cell titanium-aluminum lattice to connect titanium and aluminum substrates.

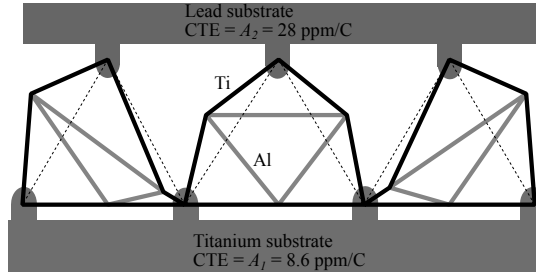


Figure 13. Problem 5: Three-cell titanium-aluminum lattice to connect titanium and lead substrates. The available range of thermal expansion is expanded by allowing the six skew angles to be independent.

Problem 5. Suppose there is a need to connect titanium and lead substrates by a three-cell titanium-aluminum lattice. From formulae (16), we have $\alpha_{11}/\alpha_1 = \alpha_{21}/\alpha_1 = \alpha_{31}/\alpha_1 = 1$, $\alpha_{12}/\alpha_1 = \alpha_{33}/\alpha_1 = 1.375$, $\alpha_{13}/\alpha_1 = \alpha_{32}/\alpha_1 = -0.875$, and $\alpha_{22}/\alpha_1 = \alpha_{23}/\alpha_1 = 0.25$. For the chosen lattice materials, $\Omega = [-0.581, 1.1135]$. As we can see, $\alpha_{12}/\alpha_1 = \alpha_{33}/\alpha_1 \notin \Omega$ and $\alpha_{13}/\alpha_1 = \alpha_{32}/\alpha_1 \notin \Omega$. To overcome this for α_{12}/α_1 , we can use negative nonsymmetric skew angles $\theta_3 \neq \theta_4$, and for α_{13}/α_1 , we can use symmetric angles greater than 30° ; this will not lead to the overlapping of the cells because these skew angles are adjacent to the external sides of the lattice. The skew angles for the second cell are the same as in Problem 4. The solution for the first cell on the left is not unique; for example, the skew angles that satisfy (6) may be $\theta_1 = \theta_2 = 0.0^\circ$, $\theta_3 = -30.0^\circ$, $\theta_4 = -6.2^\circ$, and $\theta_5 = \theta_6 = 35.3^\circ$. Figure 13 is a sketch of the lattice.

Problem 6. If the substrate materials have CTEs that are relatively similar ($A_2/A_1 \lesssim 2$), we can design a lattice consisting of four cells and more. For example, suppose we would like to connect titanium ($A_1 = 8.6$ ppm/C) and stainless-steel ($A_2 = 17.3$ ppm/C) substrates with an aluminum-titanium lattice. For such materials, the maximum total number of cells in the lattice according to inequalities (20) is 4. Using formulae (18), we have $\alpha_{11}/\alpha_1 = \alpha_{21}/\alpha_1 = 1$, $\alpha_{12}/\alpha_1 = 0.5A_1/\alpha_1 - 0.25A_2/\alpha_1 = 0.03$, $\alpha_{13}/\alpha_1 = 0.25A_2/\alpha_1 = 0.5$, $\alpha_{22}/\alpha_1 = A_1/\alpha_1 - 0.75A_2/\alpha_1 = -0.5$, and $\alpha_{23}/\alpha_1 = 0.75A_2/\alpha_1 - 0.5A_1/\alpha_1 = 1.0$. Now, using (11), for Cell 1, $t_1 = 0.0^\circ$, $t_2 = 24.6^\circ$, and $t_3 = 16.1^\circ$. For Cell 2, $t_1 = 0.0^\circ$, $t_2 = 32.0^\circ$, and $t_3 = 0.0^\circ$ (Figure 14). Two other cells are symmetric with respect to the vertical line passing through the middle of the lattice. Note that, if the second substrate is made from ferritic stainless steel with CTE $A_2 = 9.9$ ppm/C, then the maximum number of the cells in the lattice would be 22.

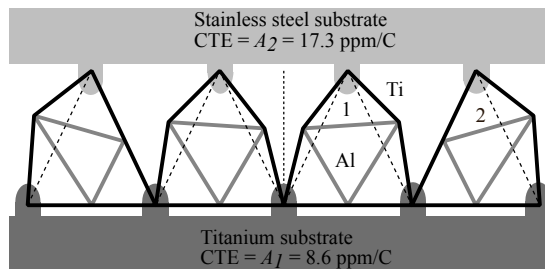


Figure 14. Problem 6: Four-cell aluminum-titanium lattice for stainless steel and titanium substrates.

The solutions to the problems considered above show that, the more the substrates' CTEs differ, the more the lattice cells are skewed. On the other hand, the higher the ratio of CTEs of the lattice materials, the less the cells of the lattice are skewed. Also, different skew angles adjacent to the same side of the cell can provide a wider range of CTEs compared to corresponding skew angles equal to each other.

7. Conclusion

The anisotropic planar lattices described in this paper provide a structural option for connecting materials with differing CTEs without generating thermal stresses during temperature excursions. Each cell is composed of internal and external triangles made of materials with different CTEs and pin-connected at three locations. The internal triangle is regular whereas the external triangle is deformed with varying skew angles. As a consequence of the variation in skew angles in a single cell, the cells have anisotropic CTEs. Combining cells with anisotropic CTEs into a pin-jointed lattice provides the capability to achieve desirable, and differing, CTEs on the bottom and top edges of the lattice. Such lattices can therefore be used as transition elements between two parts of a structure (substrates) with different CTEs, and as a result, the whole structure will be free of thermal stresses. Additionally, these lattices are relatively stiff; the isotropic variants are nearly optimally stiff for a structure of this nature [Steeves et al. 2007]. Alternative options for adapters for thermal mismatch mitigation either induce thermal stresses and curvatures or are very compliant.

The design strategy described herein provides a systematic process for choosing the geometric configuration of a single-row lattice that connects substrates of known materials. In particular, guidance on the choice of the materials that would be appropriate to connect the substrates is given, based upon the CTEs of the substrate materials. The design process for single rows of lattice can be extended to multiple rows if that provides a preferable aspect ratio for the adapter. A key limitation to this lattice system is that there are stringent limits on the maximum number of cells that can be used. As the difference between the substrate CTEs increases, the maximum number of lattice cells is reduced because the total deflections that must be accommodated increase with lattice length. An option for mitigating this limitation is to use multirow lattices and permit rotation of the lattice cells. Such topics are the subject of ongoing research.

References

- [Berger et al. 2011] J. Berger, C. Mercer, R. M. McMeeking, and A. G. Evans, "The design of bounded biomaterial lattices that combine low thermal expansion with high stiffness", *J. Am. Ceram. Soc.* **94**:S1 (2011), S42–S54.
- [Dang 2008] C. H. Dang, "Coefficient of thermal expansion adaptor", US Patent No. 2008/0160274 A1, 2008, Available at <http://www.google.com/patents/US20080160274>.
- [Gdoutos et al. 2013] E. Gdoutos, A. A. Shapiro, and C. Daraio, "Thin and thermally stable periodic metastructures", *Exp. Mech.* **53**:9 (2013), 1735–1742.
- [Gibiansky and Torquato 1997] L. V. Gibiansky and S. Torquato, "Thermal expansion of isotropic multiphase composites and polycrystals", *J. Mech. Phys. Solids* **45**:7 (1997), 1223–1252.
- [Jefferson et al. 2009] G. Jefferson, T. A. Parthasarathy, and R. Kerans, "Tailorable thermal expansion hybrid structures", *Int. J. Solids Struct.* **46**:11–12 (2009), 2372–2387.
- [Lakes 1996] R. S. Lakes, "Cellular solid structures with unbounded thermal expansion", *J. Mater. Sci. Lett.* **15**:6 (1996), 475–477.
- [Lehman and Lakes 2013] J. Lehman and R. S. Lakes, "Stiff lattices with zero thermal expansion and enhanced stiffness via rib cross section optimization", *Int. J. Mech. Mater. Des.* **9**:3 (2013), 213–225.

- [Sigmund and Torquato 1996] O. Sigmund and S. Torquato, “Composites with extremal thermal expansion coefficients”, *Appl. Phys. Lett.* **69**:21 (1996), 3203–3205.
- [Sigmund and Torquato 1997] O. Sigmund and S. Torquato, “Design of materials with extreme thermal expansion using a three-phase topology optimization method”, *J. Mech. Phys. Solids* **45**:6 (1997), 1037–1067.
- [Steeves et al. 2007] C. A. Steeves, S. L. dos Santos e Lucato, M. He, E. Antinucci, J. W. Hutchinson, and A. G. Evans, “Concepts for structurally robust materials that combine low thermal expansion with high stiffness”, *J. Mech. Phys. Solids* **55**:9 (2007), 1803–1822.
- [Timoshenko 1925] S. P. Timoshenko, “Analysis of bi-metal thermostats”, *J. Opt. Soc. Am.* **11**:3 (1925), 233–255.
- [Yousefiani et al. 2009a] A. Yousefiani, J. M. Comfort, J. G. Vollmer, and M. L. Hand, “Joined composite structures with a graded coefficient of thermal expansion for extreme environment applications”, US Patent No. 2009/0266870 A1, 2009, Available at <http://www.google.com/patents/US20090266870>.
- [Yousefiani et al. 2009b] A. Yousefiani, J. G. Vollmer, M. L. Hand, and J. M. Comfort, “Built-up composite structures with a graded coefficient of thermal expansion for extreme environment applications”, US Patent No. 2009/0269497 A1, 2009, Available at <http://www.google.com/patents/US20090269497>.

Received 13 Dec 2013. Revised 7 Feb 2014. Accepted 25 Mar 2014.

MARINA M. TOROPOVA: toropova@utias.utoronto.ca

Institute for Aerospace Studies, University of Toronto, 4925 Dufferin Street, Toronto, ON M4H 5T6, Canada

CRAIG A. STEEVES: csteeves@utias.utoronto.ca

Institute for Aerospace Studies, University of Toronto, 4925 Dufferin Street, Toronto, ON M4H 5T6, Canada

ORIGIN AND EFFECT OF NONLOCALITY IN A COMPOSITE

STEWART A. SILLING

A simple demonstration of nonlocality in a heterogeneous material is presented. By analysis of the microscale deformation of a two-component layered medium, it is shown that nonlocal interactions necessarily appear in a homogenized model of the system. Explicit expressions for the nonlocal forces are determined. The way these nonlocal forces appear in various nonlocal elasticity theories is derived. The length scales that emerge involve the constituent material properties as well as their geometrical dimensions. A peridynamic material model for the smoothed displacement field is derived. It is demonstrated by comparison with experimental data that the incorporation of nonlocality in modeling improves the prediction of the stress concentration in an open-hole tension test on a composite plate.

1. Introduction

In typical engineering analysis, the elastic response of a heterogeneous material is treated by applying the classical solid mechanics equations with smoothed (often called “homogenized” or “effective”) material properties. These properties can be thought of as those that would be measured using a laboratory test specimen much larger than any internal length scale in the material. For example, we perform an unconfined compression test on a sample of concrete about 15 cm in diameter and measure the total force as a function of displacement at the ends. We divide the relative displacement at the ends by the specimen length and call the result the “strain”. We divide the force by the cross-sectional area and call the result the “stress”. The ratio of stress to strain is defined to be the Young’s modulus of the material, which is then treated as homogeneous for purposes of finite element modeling of a structure.

This approximation is adequate for many applications. However, it ignores the reality of how a load applied on the surface of a concrete body is transmitted internally. Concrete is a heterogeneous material. It consists of small rocks (aggregate) of length scale about 2 cm held together by a weaker material (cement or paste). Since the aggregate inclusions may be in contact with each other, or nearly so, the actual force distribution within the material follows a tortuous path through the aggregate particles and their points of contact. This results in a quantitative and qualitative disparity between the local equations of solid mechanics theory using smoothed material properties and the way the material really behaves. Nonlocality in a random medium such as concrete has been treated in a number of references, for example [Willis 1985; Drugan and Willis 1996; Drugan 2003].

In the early 1980s, Bažant pioneered the application of nonlocal modeling to materials with damage. He demonstrated by a simple example that nonlocality is a necessary property of the elastic response in a material containing distributed defects [Bažant 1991]. In the same general spirit, the present paper

Sandia is a multiprogram laboratory operated by Sandia Corporation, a Lockheed Martin Company, for the United States Department of Energy’s National Nuclear Security Administration under contract DE-AC04-94AL85000.

Keywords: composite, laminate, elasticity, nonlocality, peridynamics.

derives nonlocal interactions that are implied by the use of a smoothed displacement field to model a heterogeneous microstructure. Unlike Bažant's analysis, the discussion here omits cracks and damage, and treats only the elastic response of the composite.

Nonlocality also arises in the study of plasticity, in which the finite sizes of dislocations and the distances between them interacts with the geometry of the system, as in the formation of geometrically necessary dislocations. Strain gradient models of plasticity, which incorporate a kind of weak nonlocality, have been developed to model such effects [Fleck et al. 1994; Bassani et al. 2000]. Much of the nonlocal literature concerns nonlocal operations on a damage variable, particularly its beneficial effects in reducing mesh dependence in numerical modeling [Bažant 1991; de Borst et al. 1995; Geers et al. 1999; Germain et al. 2007]. In a heterogeneous elastic material with a periodic microstructure, it has also long been recognized that nonlocal interactions may arise as a result of homogenization [Beran and McCoy 1970a; 1970b; Gambin and Kröner 1989; Boutin 1996; Bellieud and Bouchitté 1998; Fish et al. 2002; Cherednichenko et al. 2006; Chakraborty 2007]. Ben-Amoz [1975; 1976] and Ardiç, Santare, and Chou [Ardiç et al. 1989] incorporated aspects of nonlocality in models of composite material elasticity.

A large body of literature on nonlocal elasticity, much of which is highly mathematical, has been developed over the past five decades. In spite of this, nonlocal models are generally not adopted in the computational and analytical methods that engineers commonly use for applications. A typical analyst simply does not see why there should be nonlocal forces in a material at any scale above the molecular. Casual observers may conclude that, in spite of any benefits in regularizing finite element simulations, and regardless of compelling evidence from mathematical proofs, nonlocal models are not justified physically.

What apparently has been lacking in the nonlocal literature is a convincing *mechanical* picture of nonlocal interactions. In the present work, we consider how nonlocality arises in a specific, relatively simple heterogeneous system, based only on simple mechanical concepts. The micromechanical model uses only the standard equations of solid mechanics, yet it is shown that nonlocality appears in the global model derived from it. It is demonstrated that nonlocality arises from the decision to model the composite in terms of a smoothed displacement field, rather than arising from direct physical interactions across a finite distance. The nonlocal interaction forces can be included in the displacement equations of motion in various nonlocal theories. This example also permits us to compute how mesoscale geometrical dimensions combine with material properties to determine the length scale that applies in the nonlocal model.

2. Microscale model of a composite

Consider a composite material composed of alternating layers of stiff (s) and compliant (c) materials (Figure 1). The two constituent materials have the same density. The layers have thickness $2h_s$ and $2h_c$. Let E_s and E_c denote the Young's moduli and μ_s and μ_c the shear moduli of the materials. It is assumed that

$$E_s \gg E_c, \quad \mu_s \gg \mu_c.$$

Only the displacements u_s and u_c in the x -direction, that is, parallel to the layers, appear in the following approximate analysis.

The following analysis is based on a "shear-lag" model of the transfer of forces between the materials [Nairn 1997]. It is assumed that because of the disparity in elastic constants, u_s is independent of y . The



Figure 1. Composite composed of alternating stiff and compliant layers.

following ansatz is adopted: in the compliant material, a displacement field of the form

$$u_c(x, y) = u_s(x) + (h_c^2 - y^2)w(x) \tag{2-1}$$

is assumed, where w is a continuous function and $y = 0$ is located at the midplane of a typical compliant layer (Figure 2). The shear traction on either surface of any compliant layer is found from

$$\tau(x) = \mu_c \frac{\partial u_c}{\partial y}(x, -h_c) = 2\mu_c h_c w(x). \tag{2-2}$$

In the absence of body forces, a force balance on the cross-section of a stiff layer yields

$$h_s \sigma'_s(x) + \tau(x) = 0, \tag{2-3}$$

where σ_s is the normal stress and a prime denotes d/dx . Using (2-2), (2-3), and the Hooke's law expression

$$\sigma_s = E_s u'_s,$$

the force balance on the stiff layers may be rewritten as

$$E_s h_s u''_s(x) + 2\mu_c h_c w(x) = 0. \tag{2-4}$$

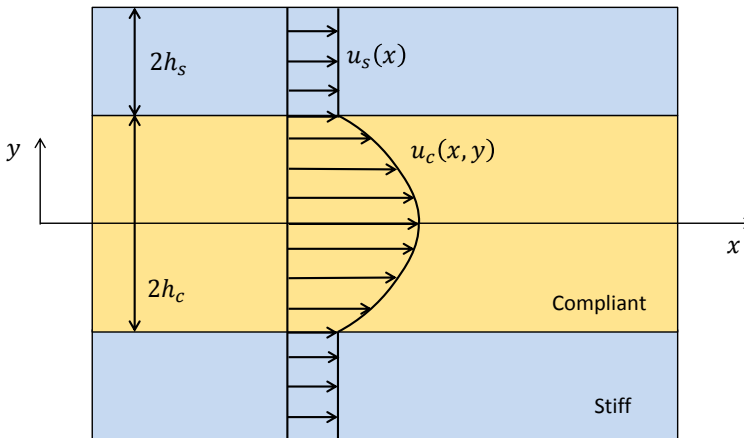


Figure 2. Axial displacement fields in the composite layers.

3. Equilibrium of a smoothed displacement field

Define the smoothed (homogenized) displacement field to be the average at any x over a cross-section through the layers:

$$\bar{u}(x) = \frac{1}{h_s + h_c} \left[h_s u_s(x) + \int_0^{h_c} u_c(x, y) dy \right].$$

Using (2-1), this evaluates to

$$\bar{u}(x) = u_s(x) + \alpha w(x), \quad (3-1)$$

where

$$\alpha = \frac{2h_c^3}{3(h_s + h_c)}. \quad (3-2)$$

Using (3-1) and (3-2), we remove u_s from the force balance (2-4) and obtain

$$\bar{u}''(x) = \alpha w''(x) - \frac{2\mu_c h_c}{E_s h_s} w(x). \quad (3-3)$$

Our immediate objective is to analyze the forces in the composite for a prescribed \bar{u} function. If \bar{u} is prescribed, then (3-3) is a nonhomogeneous second-order linear ordinary differential equation (ODE) for w . The homogeneous part of the solution to this ODE (that is, for \bar{u} either constant or a linear function of x) is

$$w_h(x) = A e^{\lambda x} + B e^{-\lambda x},$$

where

$$\lambda = \sqrt{\frac{2\mu_c h_c}{\alpha E_s h_s}} = \sqrt{\frac{3\mu_c (h_s + h_c)}{E_s h_s h_c^2}}, \quad (3-4)$$

and where A and B are arbitrary constants.

Of particular interest is the choice of prescribed \bar{u}'' given by

$$\bar{u}''(x) = \Delta(x), \quad (3-5)$$

where Δ is the Dirac delta function. Kinematically, this choice means that the homogenized strain field \bar{u}' is given by the Heaviside step function

$$\bar{u}'(x) = H(x)$$

(see Figure 3). For this choice, the solution, denoted $-G$, to the ODE (3-3) is

$$w(x) = -G(x), \quad G(x) = k e^{-\lambda|x|}, \quad (3-6)$$

where

$$k = \frac{1}{2\alpha\lambda}. \quad (3-7)$$

The easiest way to confirm that (3-6) and (3-7) provide a solution to (3-3) and (3-5) is to observe that by integrating (3-3) from 0^- to 0^+ , the jump in \bar{u}' at the origin is given by

$$[\bar{u}'] = \alpha[w'] - \frac{2\mu_c h_c}{E_s h_s} \int_{0^-}^{0^+} w(x) dx. \quad (3-8)$$

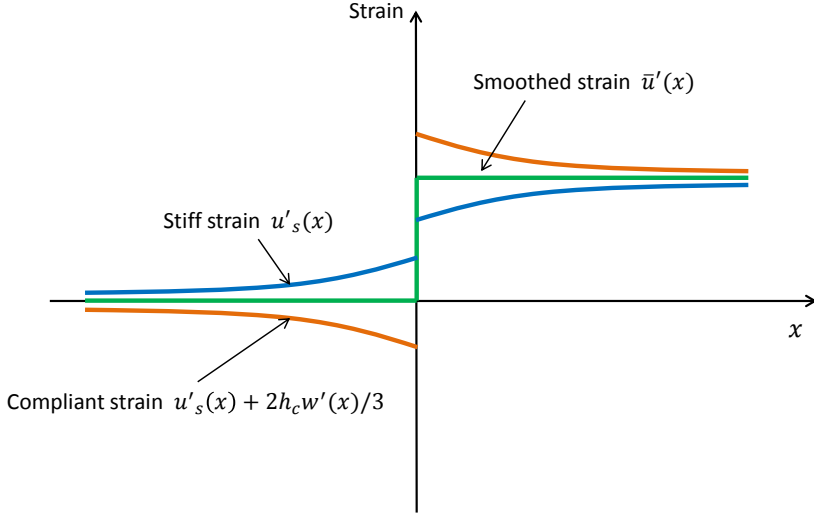


Figure 3. Strain fields in the stiff and compliant layers resulting from a prescribed smoothed displacement field in which there is a jump in strain at $x = 0$.

By (3-6), w is bounded (as well as continuous) everywhere, so the last term vanishes. Differentiation of w yields

$$w'(x) = k\lambda(2H(x) - 1)e^{-\lambda|x|}.$$

Evidently this implies $[w'] = 2k\lambda$. So, using (3-7), the jump condition (3-8) is satisfied.

Because the ODE (3-3) is linear, and because of the properties of the Dirac delta function, for an arbitrary prescribed function \bar{u} , (3-6) implies

$$w(x) = - \int_{-\infty}^{\infty} \bar{u}''(p)G(x-p) dp. \quad (3-9)$$

Next we compute the homogenized normal stress $\bar{\sigma}$ in the composite. From a force balance on a cross-section through the point x , this stress is found to be

$$\bar{\sigma}(x) = \frac{1}{h_s + h_c} \left[h_s \sigma_s(x) + \int_0^{h_c} \sigma_c(x, y) dy \right], \quad (3-10)$$

with

$$\sigma_s(x) = E_s u'_s(x), \quad \sigma_c(x) = E_c u'_c(x).$$

Carrying out the integration in (3-10) using (2-1) and (3-1) leads to

$$\bar{\sigma}(x) = \bar{E} \bar{u}'(x) - \gamma w'(x), \quad (3-11)$$

where

$$\bar{E} = \frac{E_s h_s + E_c h_c}{h_s + h_c}, \quad (3-12)$$

$$\gamma = \alpha \bar{E} - \frac{2E_c h_c^3}{3(h_s + h_c)} = \frac{2h_s h_c^3 (E_s - E_c)}{3(h_s + h_c)^2}. \quad (3-13)$$

Rewriting (3-11) using (3-9) and (3-13) leads to

$$\bar{\sigma}(x) = \bar{E} \bar{u}'(x) + \gamma \int_{-\infty}^{\infty} \bar{u}''(p) G'(x-p) dp. \quad (3-14)$$

Note that w no longer appears explicitly in this expression for the homogenized stress. The nonlocality inherent in modeling heterogeneous materials using a smoothed displacement field is now evident: values of \bar{u} remote from x contribute to the stress at x . This is a type of strong nonlocality. A more suggestive version of (3-14) may be obtained by integrating the last term by parts:

$$\bar{\sigma}(x) = \bar{E} \bar{u}'(x) + \gamma \int_{-\infty}^{\infty} \bar{u}'(p) G''(x-p) dp. \quad (3-15)$$

Differentiating (3-6) twice yields

$$G''(x) = k\lambda^2 e^{-\lambda|x|} - 2k\lambda\Delta(x) \quad (3-16)$$

$$= \lambda^2 G(x) - 2k\lambda\Delta(x). \quad (3-17)$$

Substituting (3-17) into (3-15), using the properties of the Dirac delta function, and using (3-7), (3-12), and (3-13) to simplify the constants yields

$$\bar{\sigma}(x) = E_c \bar{u}'(x) + \gamma \lambda^2 \int_{-\infty}^{\infty} \bar{u}'(p) G(x-p) dp. \quad (3-18)$$

This expression is similar to the nonlocal stress used in Eringen's nonlocal theory [Eringen and Edelen 1972], because it involves taking a weighted average of strain.

4. Nonlocal equations of motion

Next we investigate how the nonlocal forces in the homogenized model appear in nonlocal equations of motion. With this goal in mind, we evaluate the acceleration at x at a given time t . From the linear momentum balance in the absence of body forces, using the assumption that $\rho_s = \rho_c$, our expression for the net normal stress (3-18) implies

$$\rho \ddot{u}(x) = \bar{\sigma}'(x) = E_c \bar{u}''(x) + \gamma \lambda^2 \int_{-\infty}^{\infty} \bar{u}'(p) G'(x-p) dp.$$

Integrating the last term by parts,

$$\rho \ddot{u}(x) = E_c \bar{u}''(x) + \gamma \lambda^2 \int_{-\infty}^{\infty} \bar{u}(p) G''(x-p) dp.$$

Using (3-16) in the last term, and introducing a body force field b according to d'Alembert's principle, yields

$$\rho \ddot{u}(x) = E_c \bar{u}''(x) + \gamma k \lambda^4 \int_{-\infty}^{\infty} (\bar{u}(p) - \bar{u}(x)) e^{-\lambda|x-p|} dp + b(x). \quad (4-1)$$

In this form, the model is similar to the nonlocal theory proposed by DiPaola, Failla, and Zingales [2009]. This form, like that of Kröner [1967], retains both local and nonlocal terms.

The peridynamic model seeks to eliminate any reference to strain, because one of its goals is to avoid using spatial derivatives of the deformation, thus making the theory compatible with discontinuities in displacement. The general form of the peridynamic equation of motion in one dimension [Silling 2000; Silling and Lehoucq 2010] is given by

$$\rho \ddot{u}(x) = \int_{\mathcal{H}_x} f(p, x, t) dp + b(x), \quad (4-2)$$

where \mathcal{H}_x is a neighborhood of x called the *family* of x . The radius of \mathcal{H}_x , which is called the *horizon*, can be either finite or infinite. The function f is called the *bond force density*. It can depend quite generally on the deformation of the family through suitable material models, including the effects of nonlinearity and damage. The peridynamic model is nonlocal because the family has nonzero size.

In linearized peridynamics [Silling 2010], the equation of motion (4-2) can be approximated by the following expression, which is formally the same as in the nonlocal theories of Kunin [1982; 1983] and Rogula [1982]:

$$\rho \ddot{u}(x) = \int_{\mathcal{H}_x} C(x, p)(u(p) - u(x)) dp + b(x), \quad (4-3)$$

where C is a function called the *micromodulus*. The equation of motion (4-1) that was derived from the microstructural model of a composite has strong similarities to the linearized peridynamic expression (4-3). Both equations contain strongly nonlocal terms; in (4-1) the horizon is infinite, although a reasonable approximation would be to cut off the nonlocal interactions outside a distance r where the weighting term $e^{-\lambda r}$ is sufficiently small.

A local term involving u'' does not appear in the peridynamic equation (4-3). However, with the goal of representing this term in (4-1), it can be approximated by short-range interactions by using the same sort of manipulations used above. Using integration by parts, the following identities hold:

$$u''(x) = \int_{-\infty}^{\infty} u''(p) \Delta(x-p) dp = \int_{-\infty}^{\infty} u'(p) \Delta'(x-p) dp = \int_{-\infty}^{\infty} u(p) \Delta''(x-p) dp. \quad (4-4)$$

Using the approximation

$$\Delta(x) \approx \phi(x) := \frac{\tau e^{-\tau|x|}}{2},$$

where τ is a large constant, we compute from (4-4)

$$\begin{aligned} u''(x) &= \int_{-\infty}^{\infty} u(p) \Delta''(x-p) dp \approx \int_{-\infty}^{\infty} u(p) \phi''(x-p) dp \\ &= \int_{-\infty}^{\infty} u(p) \left(\frac{\tau^3 e^{-\tau|x-p|}}{2} - \tau^2 \Delta(x-p) \right) dp = \frac{\tau^3}{2} \int_{-\infty}^{\infty} (u(p) - u(x)) e^{-\tau|x-p|} dp. \end{aligned}$$

Thus, our model for the smoothed composite displacement field, (4-1), can be approximated to any level of accuracy by choosing a sufficiently large τ in the following model:

$$\rho \ddot{\bar{u}}(x) = \int_{\mathcal{H}_x} \left(\frac{E_c \tau^3}{2} e^{-\tau|x-p|} + \gamma k \lambda^4 e^{-\lambda|x-p|} \right) (\bar{u}(p) - \bar{u}(x)) dp + b(x). \quad (4-5)$$

This is the peridynamic model (4-3) with the choice of micromodulus function given by

$$C(x, p) = \frac{E_c \tau^3}{2} e^{-\tau|x-p|} + \gamma k \lambda^4 e^{-\lambda|x-p|}.$$

The foregoing discussion illustrates many of the key properties in understanding the role of nonlocality in the modeling of continua:

- Nonlocality is introduced by making the *modeling decision* to describe the problem using a smoothed displacement field rather than the detailed microstructural fields.
- Although the underlying microstructural model (in terms of the u_s and u_c fields) is local, the resulting smoothed model (in terms of \bar{u}) is nonlocal.
- Expressions called *bond force densities* in the peridynamic model of the form

$$C(x, p)(\bar{u}(p) - \bar{u}(x))$$

do not necessarily represent a direct nonlocal *physical* interaction (such as electrostatic forces) between p and x .

- The applicable *length scale* in the nonlocal term, $1/\lambda$, depends not only on the geometrical length scales (h_s and h_c), but also on the constituent material properties E_s and μ_c . If $E_s \gg \mu_c$, then this length scale can greatly exceed the layer thicknesses. This result is consistent with the computations by Pipes and Pagano [1970] which show that edge effects on the stresses in plies can extend over distances that substantially exceed the ply thicknesses.
- A peridynamic model can contain multiple length scales; in the case of the composite model in (4-5) these are $1/\lambda$ and $1/\tau$.
- By considering a displacement field of the form

$$\bar{u}(x) = \varepsilon_0 x + \frac{\beta}{2} x^2,$$

where β is a constant, and applying (4-1), one finds that the quadratic term leads to an acceleration at $x = 0$ given by

$$\ddot{\bar{u}}(0) = \frac{4\beta\gamma k \lambda}{\rho}.$$

Since this acceleration is positive whenever the strain gradient β is positive, this result means that positive strain gradient tends to increase the force on x . This is suggestive of experimental results that show stresses in real materials increase as the strain gradient is increased [Fleck et al. 1994].

The analogous *local* model for the composite in terms of the smoothed displacement field is

$$\rho \ddot{\bar{u}}(x) = \bar{E} \bar{u}''(x) + b(x),$$

where \bar{E} is given by (3-12). Comparing this with (4-1), evidently the local term $\bar{E}\bar{u}''$ is replaced by a different local term $E_c\bar{u}''$ plus a nonlocal term. It is possible that a more detailed microstructural model, for example, a submicrostructural model that considers the features *within* each of the layers such as individual fibers, would further resolve the local term in (4-1). Based on the patterns emerging in the above derivations, it is plausible that a hierarchy of N such submodels could be derived, resulting in a micromodulus of the form

$$C(x, p) = C_1(x, p; \lambda_1) + C_2(x, p; \lambda_2) + \dots + C_N(x, p; \lambda_N),$$

where each C_i represents interactions with length scale $1/\lambda_i$. By inference from (4-5), such terms might have the form

$$C_i(x, p; \lambda_i) = a_i e^{\lambda_i|x-p|},$$

where the a_i are constants.

5. Nonlocality at the macroscale

As noted in the previous section, the operative length scale in a heterogeneous material system depends on the constituent material properties as well as the geometrical length scale. However, the macroscale geometry of a body also combines with material properties to provide additional length scales. For example, consider the classic problem of an anisotropic plate under tension containing an open hole of radius r (Figure 4). In the local theory, the stress σ_{yy} as a function of position x along the midplane was derived analytically by Lekhnistskii [1968]:

$$\sigma_{yy} = \frac{\sigma_\infty}{2} \left\{ 2 + \left(\frac{r}{x}\right)^2 + 3\left(\frac{r}{x}\right)^4 + (2-n) \left[5\left(\frac{r}{x}\right)^6 - 7\left(\frac{r}{x}\right)^8 \right] \right\}, \tag{5-1}$$

where

$$n = \sqrt{2 \left(\frac{E_1}{E_2} - \nu_{12} \right) + \frac{E_1}{G_{12}}},$$

where the subscripts 1 and 2 denote the loading direction and transverse direction, respectively. From this, the stress concentration at the edge of the hole is found to be

$$K_{\pi/2} = 1 + n.$$

The parameter n tends to increase in anisotropic materials, particularly those that have greater stiffness in the loading (y) direction. In addition to changing the stress concentration at the edge, anisotropy also changes the rate at which the stress decays with distance from the edge. Denote by r_0 the radius at which the stress in the classical solution drops off to half of its value at the edge, that is,

$$\frac{\sigma_{yy}(r_0)}{\sigma_{yy}(r)} = \frac{1}{2}.$$

Typical values of r_0 determined from (5-1) are given in Table 1. (Similar decay distance parameters play an important role in certain laminate failure models that implicitly recognize nonlocality [Whitney and Nuismer 1974; Ko 1985] by including an explicit length scale.)

Material	n	$K_{\pi/2}$	r_0/r
Isotropic	2	3	1.52
Fabric ply	4.16	5.16	1.13
Unidirectional ply	10	11	1.07

Table 1. Stress concentration and decay distance near an open hole in a plate.

Thus, in a unidirectional ply, the stress decays to half its value at the edge over a distance of only 7% of the hole radius. If the hole radius is $r = 2.5$ mm, then this distance is $r_0 - r = 0.175$ mm, which is on the order of a typical ply thickness.

To put this result in the context of our previous discussion of length scales and nonlocality in heterogeneous media, suppose we compute the length scale implied by (3-4) with $h_c = h_s = 0.1$ mm, $\mu_c = 4$ GPa, and $E_s = 150$ GPa. The resulting length scale for nonlocal interactions due to transfer of shear load between the constituent materials is

$$\frac{1}{\lambda} = \sqrt{\frac{E_s h_s h_c^2}{3\mu_c (h_s + h_c)}} = 0.25 \text{ mm.}$$

Comparing this with our stress concentration decay distance (0.175 mm), the two values are similar. From this similarity, evidently nonlocality in a homogenized model due to the exchange of forces between the materials could play an important role in modeling the problem.

Toubal, Karama, and Lorrain [Toubal et al. 2005] measured the stress in a fabric composite laminate near an open hole as a function of position along the midplane of the specimen. They used an electronic speckle pattern interferometry measurement technique. This technique provides noncontact strain data with a spatial resolution of about 0.5 mm. Their measurements showed that the actual stress concentration is much lower than what is predicted by the analytical results from the local theory [Lekhnist'skiĭ 1968]. Does nonlocality explain this difference?

To investigate this possibility, the peridynamic computational model Emu [Silling and Askari 2005] was applied to try to reproduce the measured stress concentration reported in [Toubal et al. 2005]. The material model used in the peridynamic computations was similar to that used in [Xu et al. 2008]. In this material model, peridynamic bonds parallel to the fibers have much greater stiffness than bonds in any other direction.

In the experiment, the hole diameter was 5.0 mm, and the specimen width was 25 mm. The specimen contained six plies, all epoxy reinforced by carbon fabric, with a total thickness of 2.28 mm. The ply laminate properties were $E_1 = 51$ GPa, $E_2 = 50$ GPa, $\nu_{12} = 0.06$, and $G_{12} = 3.24$ GPa. Since all the plies were identical in the experiment, shear forces between the plies are not significantly involved in the problem. Therefore, for purposes of estimating the nonlocal interaction distance $1/\lambda$, the applicable geometric length scale is the fabric tow width. In other words, each tow acts like one of the layers in the microstructural model developed in Section 2. This view is supported by the X-ray diffraction studies [Davies et al. 2008] which show that in the vicinity of an open hole, the fabric tows deform more or less uniformly across the width of each tow. Under this assumption, and setting $h_c = h_s = 1.25$ mm, which is a typical value for tow width, one finds from (3-4) that $1/\lambda = 2.0$ mm. In the computational model, the mesh spacing was 0.32 mm and the peridynamic horizon was 2.0 mm.

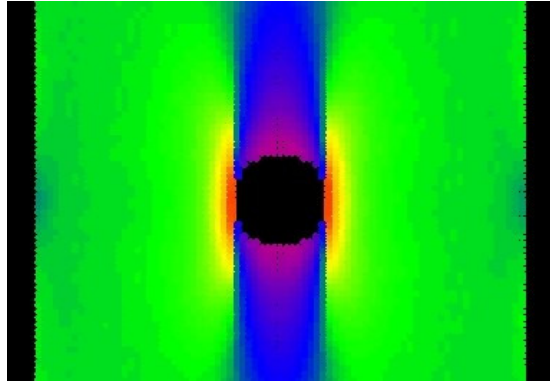


Figure 4. Stress contours in a simulated open-hole tension test in a composite. Note the large stress gradients.

As shown in Figure 4, the predicted contours of σ_{yy} (the normal stress in the loading direction) show strong gradients in the vicinity of the hole. In fact, there are large gradients above and below the hole as well, due primarily to the relatively small shear modulus G_{12} , which is characteristic of fiber and fabric-reinforced composites. In an isotropic material such as a typical metal, the contours of stress would be more diffuse. Figure 5 shows a comparison between the optically measured stress σ_{yy} and the local theory of anisotropic media [Toubal et al. 2005]. The figure also shows the results from the peridynamic computational model. The results in this figure suggest that nonlocality helps improve the agreement

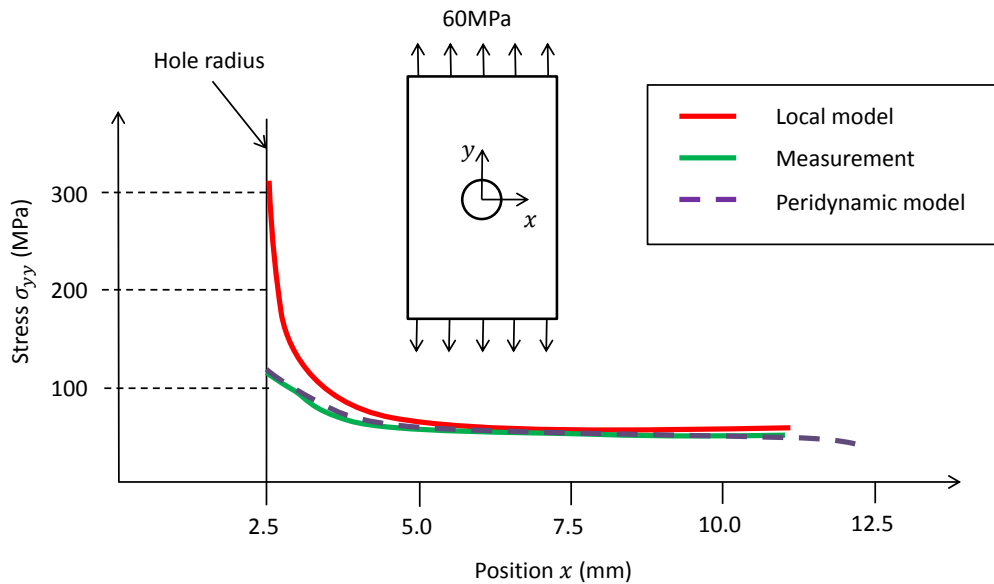


Figure 5. Comparison of stress along the midplane in an open-hole tension test on a fabric-reinforced composite. The local theory overpredicts the stress concentration compared with optically measured data [Toubal et al. 2005]. The peridynamic model offers improved agreement, apparently due to nonlocality.

between a continuum model and measured data for stress concentrations in composites. This also helps explain why failure criteria in composites that rely solely on the predicted stress in the local theory tend to under-predict the failure load in open-hole tension and compression tests: these criteria are based on an over-prediction of the stress concentration [Soutis et al. 1991].

6. Conclusions

The purpose of this work is to show how a nonlocal model arises when we make the modeling decision to use a smoothed displacement field, rather than a detailed microstructural description. By considering the micromechanics of a layered composite under uniaxial stress, it was shown that nonuniformity of the displacement field across any cross-section leads to nonlocality in a homogenized model. The nonlocal effects appear only when the strain in the smoothed displacement field is nonconstant (that is, when a strain gradient is present). The nonlocal interactions, in this special case, can be represented using different nonlocal models, including those of Eringen and Kröner, as well as peridynamics. The peridynamic micromodulus function for the nonlocal interactions can be determined explicitly, although there is some arbitrariness in the kernel used to approximate the local term that appears in the peridynamic equation of motion. The length scale $1/\lambda$ in the peridynamic model is determined not only by the microscale geometry of the composite, but also by the material properties of the constituent materials. In the peridynamic expression that was derived, interactions between material points separated by a finite distance necessarily occur, even though there are no direct physical interactions between these points in the microstructure.

In summary, nonlocality is not just a property of the physical system; it is also a property of the fields we choose to model the system with.

References

- [Ardiç et al. 1989] E. S. Ardiç, M. H. Santare, and T.-W. Chou, “Stress fields in a composite material by means of a non-classical approach”, *Int. J. Eng. Sci.* **27**:11 (1989), 1397–1405.
- [Bassani et al. 2000] J. L. Bassani, A. Needleman, and E. van der Giessen, “Plastic flow in a composite: a comparison of nonlocal continuum and discrete dislocation predictions”, *Int. J. Solids Struct.* **38**:5 (2000), 833–853.
- [Bažant 1991] Z. P. Bažant, “Why continuum damage is nonlocal: Micromechanics arguments”, *J. Eng. Mech. (ASCE)* **117**:5 (1991), 1070–1087.
- [Bellieud and Bouchitté 1998] M. Bellieud and G. Bouchitté, “Homogenization of elliptic problems in a fiber reinforced structure: Nonlocal effects”, *Ann. Scuola Norm. Sup. Pisa Cl. Sci. (4)* **26**:3 (1998), 407–436.
- [Ben-Amoz 1975] M. Ben-Amoz, “On wave propagation in laminated composites, I: Propagation parallel to the laminates”, *Int. J. Eng. Sci.* **13** (1975), 43–56.
- [Ben-Amoz 1976] M. Ben-Amoz, “A dynamic theory for composite materials”, *Z. Angew. Math. Phys.* **27** (1976), 83–99.
- [Beran and McCoy 1970a] M. J. Beran and J. J. McCoy, “Mean field variations in a statistical sample of heterogeneous linearly elastic solids”, *Int. J. Solids Struct.* **6** (1970), 1035–1054.
- [Beran and McCoy 1970b] M. J. Beran and J. J. McCoy, “The use of strain gradient theory for analysis of random media”, *Int. J. Solids Struct.* **6** (1970), 1267–1275.
- [de Borst et al. 1995] R. de Borst, J. Pamin, R. H. J. Peerlings, and L. J. Sluys, “On gradient-enhanced damage and plasticity models for failure in quasi-brittle and frictional materials”, *Comput. Mech.* **17**:1–2 (1995), 130–141.
- [Boutin 1996] C. Boutin, “Microstructural effects in elastic composites”, *Int. J. Solids Struct.* **33**:7 (1996), 1023–1051.

- [Chakraborty 2007] A. Chakraborty, “Wave propagation in anisotropic media with non-local elasticity”, *Int. J. Solids Struct.* **44**:17 (2007), 5723–5741.
- [Cherednichenko et al. 2006] K. D. Cherednichenko, V. P. Smyshlyaev, and V. V. Zhikov, “Non-local homogenized limits for composite media with highly anisotropic periodic fibres”, *Proc. Roy. Soc. Edinburgh Sect. A* **136**:1 (2006), 87–114.
- [Davies et al. 2008] R. J. Davies, S. J. Eichhorn, J. A. Bennett, C. Riekel, and R. J. Young, “Analysis of the structure and deformation of a woven composite lamina using X-ray microdiffraction”, *J. Mater. Sci.* **43**:20 (2008), 6724–6733.
- [Di Paola et al. 2009] M. Di Paola, G. Failla, and M. Zingales, “Physically-based approach to the mechanics of strong non-local linear elasticity theory”, *J. Elasticity* **97**:2 (2009), 103–130.
- [Drugan 2003] W. J. Drugan, “Two exact micromechanics-based nonlocal constitutive equations for random linear elastic composite materials”, *J. Mech. Phys. Solids* **51**:9 (2003), 1745–1772.
- [Drugan and Willis 1996] W. J. Drugan and J. R. Willis, “A micromechanics-based nonlocal constitutive equation and estimates of representative volume element size for elastic composites”, *J. Mech. Phys. Solids* **44**:4 (1996), 497–524.
- [Eringen and Edelen 1972] A. C. Eringen and D. G. B. Edelen, “On nonlocal elasticity”, *Int. J. Eng. Sci.* **10** (1972), 233–248.
- [Fish et al. 2002] J. Fish, W. Chen, and G. Nagai, “Non-local dispersive model for wave propagation in heterogeneous media: one-dimensional case”, *Int. J. Numer. Methods Eng.* **54**:3 (2002), 331–346.
- [Fleck et al. 1994] N. A. Fleck, G. M. Muller, M. F. Ashby, and J. W. Hutchinson, “Strain gradient plasticity: Theory and experiment”, *Acta Metall. Mater.* **42**:2 (1994), 475–487.
- [Gambin and Kröner 1989] B. Gambin and E. Kröner, “Higher-order terms in the homogenized stress-strain relation of periodic elastic media”, *Phys. Status Solidi B* **151**:2 (1989), 513–519.
- [Geers et al. 1999] M. G. D. Geers, R. de Borst, and T. Peijs, “Mixed numerical-experimental identification of non-local characteristics of random-fibre-reinforced composites”, *Compos. Sci. Technol.* **59**:10 (1999), 1569–1578.
- [Germain et al. 2007] N. Germain, J. Besson, and F. Feyel, “Composite layered materials: anisotropic nonlocal damage models”, *Comput. Methods Appl. Mech. Eng.* **196**:41–44 (2007), 4272–4282.
- [Ko 1985] W. L. Ko, “Stress concentration around a small circular hole in the HiMAT composite plate”, Technical Memorandum 86038, NASA, 1985.
- [Kröner 1967] E. Kröner, “Elasticity theory of materials with long range cohesive forces”, *Int. J. Solids Struct.* **3** (1967), 731–742.
- [Kunin 1982] I. A. Kunin, *Elastic media with microstructure, I: One-dimensional models*, Springer Series in Solid-State Sciences **26**, Springer, Berlin, 1982.
- [Kunin 1983] I. A. Kunin, *Elastic media with microstructure, II: Three-dimensional models*, Springer Series in Solid-State Sciences **44**, Springer, Berlin, 1983.
- [Lekhnistskiĭ 1968] G. Lekhnistskiĭ, *Anisotropic plates*, Gordon & Breach, New York, 1968.
- [Nairn 1997] J. A. Nairn, “On the use of shear-lag methods for analysis of stress transfer in unidirectional composites”, *Mechanics of Materials* **26**:2 (1997), 63–80.
- [Pipes and Pagano 1970] R. B. Pipes and N. J. Pagano, “Interlaminar stresses in composite laminates under uniform axial extension”, *J. Compos. Mater.* **4** (1970), 538–548.
- [Rogula 1982] D. Rogula, *Nonlocal theory of material media*, CISM Courses and Lectures **268**, Springer, Berlin, 1982.
- [Silling 2000] S. A. Silling, “Reformulation of elasticity theory for discontinuities and long-range forces”, *J. Mech. Phys. Solids* **48**:1 (2000), 175–209.
- [Silling 2010] S. A. Silling, “Linearized theory of peridynamic states”, *J. Elasticity* **99**:1 (2010), 85–111.
- [Silling and Askari 2005] S. A. Silling and E. Askari, “A meshfree method based on the peridynamic model of solid mechanics”, *Comput. Struct.* **83**:17–18 (2005), 1526–1535.
- [Silling and Lehoucq 2010] S. A. Silling and R. B. Lehoucq, “Peridynamic theory of solid mechanics”, *Adv. Appl. Mech.* **44** (2010), 73–168.
- [Soutis et al. 1991] C. Soutis, N. A. Fleck, and P. A. Smith, “Failure prediction technique for compression loaded carbon fibre-epoxy laminate with open holes”, *J. Compos. Mater.* **25**:11 (1991), 1476–1498.

- [Toubal et al. 2005] L. Toubal, M. Karama, and B. Lorrain, “Stress concentration in a circular hole in composite plate”, *Composite Structures* **68**:1 (2005), 31–36.
- [Whitney and Nuismer 1974] J. M. Whitney and R. J. Nuismer, “Stress fracture criteria for laminated composites containing stress concentrations”, *J. Compos. Mater.* **8**:3 (1974), 253–265.
- [Willis 1985] J. R. Willis, “The nonlocal influence of density variations in a composite”, *Int. J. Solids Struct.* **21** (1985), 805–817.
- [Xu et al. 2008] J. Xu, E. Askari, O. Weckner, and S. Silling, “Peridynamic analysis of impact damage in composite laminates”, *J. Aerosp. Eng. (ASCE)* **21**:3 (2008), 187–194.

Received 31 Jan 2014. Accepted 23 Feb 2014.

STEWART A. SILLING: sasilli@sandia.gov

Multiscale Science Department, Sandia National Laboratories, P.O. Box 5800, MS-1322, Albuquerque, NM 87185-1322, United States

SUBMISSION GUIDELINES

ORIGINALITY

Authors may submit manuscripts in PDF format online at the Submissions page. Submission of a manuscript acknowledges that the manuscript is original and has neither previously, nor simultaneously, in whole or in part, been submitted elsewhere. Information regarding the preparation of manuscripts is provided below. Correspondence by email is requested for convenience and speed. For further information, write to contact@msp.org.

LANGUAGE

Manuscripts must be in English. A brief abstract of about 150 words or less must be included. The abstract should be self-contained and not make any reference to the bibliography. Also required are keywords and subject classification for the article, and, for each author, postal address, affiliation (if appropriate), and email address if available. A home-page URL is optional.

FORMAT

Authors can use their preferred manuscript-preparation software, including for example Microsoft Word or any variant of $\text{T}_{\text{E}}\text{X}$. The journal itself is produced in $\text{L}^{\text{A}}\text{T}_{\text{E}}\text{X}$, so accepted articles prepared using other software will be converted to $\text{L}^{\text{A}}\text{T}_{\text{E}}\text{X}$ at production time. Authors wishing to prepare their document in $\text{L}^{\text{A}}\text{T}_{\text{E}}\text{X}$ can follow the example file at www.jomms.net (but the use of other class files is acceptable). At submission time only a PDF file is required. After acceptance, authors must submit all source material (see especially Figures below).

REFERENCES

Bibliographical references should be complete, including article titles and page ranges. All references in the bibliography should be cited in the text. The use of $\text{BibT}_{\text{E}}\text{X}$ is preferred but not required. Tags will be converted to the house format (see a current issue for examples); however, for submission you may use the format of your choice. Links will be provided to all literature with known web locations; authors can supply their own links in addition to those provided by the editorial process.

FIGURES

Figures must be of publication quality. After acceptance, you will need to submit the original source files in vector format for all diagrams and graphs in your manuscript: vector EPS or vector PDF files are the most useful. (EPS stands for Encapsulated PostScript.)

Most drawing and graphing packages—Mathematica, Adobe Illustrator, Corel Draw, MATLAB, etc.—allow the user to save files in one of these formats. Make sure that what you're saving is vector graphics and not a bitmap. If you need help, please write to graphics@msp.org with as many details as you can about how your graphics were generated.

Please also include the original data for any plots. This is particularly important if you are unable to save Excel-generated plots in vector format. Saving them as bitmaps is not useful; please send the Excel (.xls) spreadsheets instead. Bundle your figure files into a single archive (using zip, tar, rar or other format of your choice) and upload on the link you been given at acceptance time.

Each figure should be captioned and numbered so that it can float. Small figures occupying no more than three lines of vertical space can be kept in the text (“the curve looks like this:”). It is acceptable to submit a manuscript with all figures at the end, if their placement is specified in the text by means of comments such as “Place Figure 1 here”. The same considerations apply to tables.

WHITE SPACE

Forced line breaks or page breaks should not be inserted in the document. There is no point in your trying to optimize line and page breaks in the original manuscript. The manuscript will be reformatted to use the journal's preferred fonts and layout.

PROOFS

Page proofs will be made available to authors (or to the designated corresponding author) at a Web site in PDF format. Failure to acknowledge the receipt of proofs or to return corrections within the requested deadline may cause publication to be postponed.

